UNIVERSITÀ DELLA CALABRIA
Dipartimento di MECCANICA
DOTTORATO DI RICERCA IN INGEGNERIA MECCANICA
CICLO XXIII (2008-2010)

(DENOMINAZIONE DEL SETTORE): ING-IND/14

Development and Testing of Plasma Sprayed Coatings for High-Temperature Applications

By Giovanni Di Girolamo

A Dissertation submitted in partial fulfilment of the requirements for the Doctoral Research degree in Mechanical Engineering

Doctoral Research Director
Prof. Sergio Rizzuti

Supervisor
Prof. Leonardo Pagnotta

Candidate
Dr. Giovanni Di Girolamo

INDEX

Introduction and objectives

This doctoral thesis is the result of three years of researches and experiments performed at University of Calabria and related to the field of Mechanical Engineering. The theme of this experimental work concerns “Surface and Coatings Technology” for high-temperature applications in aerospace and energy conversion industry.

In particular, this work is focused on the study, the development and the characterization of advanced metallic and ceramic coatings fabricated by Air Plasma Spraying (APS) for thermal barrier coating (TBC) applications. These coatings are typically used for protection of Ni-based hot section components of aircraft and land-based turbine engines from heat, oxidation, thermal fatigue and hot corrosion.

In the last decades, the refinement of superalloys composition, as well as the development of superalloys with directional grain growth and single crystal superalloys, have provided significant improvements to the resistance and the durability of turbine metal components. However, the presence of oxygen and molten salts in combustion environment, such as sulphates, chlorides and vanadates, involves much severe operating conditions and usually leads to a rapid degradation of their surface, reducing their durability and increasing the costs for maintenance or substitution.

To this purpose, the application of a protective coating can substantially enhance the lifetime of metal components as well as their functional properties. Indeed, a ceramic coating is typically able to maintain the temperature of the component surface low enough to retain the starting properties within acceptable bounds during long-term service. Moreover, at the end of coating service life, produced by spallation, the underlying component is reusable. Indeed, it can be easily recovered, cleaned and recoated, thus involving a significant economic saving. Actually, the full potential of thermal barrier coatings is only partially exploited. However, further new applications are expected in the near future. Indeed, there is a constant demand

for increased performance, energy saving and reduced environmental impact. To this purpose, four-generation turbine engines will operate at temperatures higher than those actually experienced in actual ones (approximately in the range between 900 °C and 1100 °C). Such temperatures are above the capability of metal components.

Therefore, the application of an upper ceramic coating represents the best technological solution in order to increase the engine efficiency, through an increase of the inlet gas temperature or a significant reduction of the cooling air flow from the compressor. As known, metal components as turbine blades are typically cooled by an internal air cooling system (see Fig. 1) and this involves considerable service costs. Lower fuel consumption and emissions of NO_x and carbon monoxide into the atmosphere are also expected by the application of a ceramic TBC on metallic component surface.

In this context, intense and detailed researches about new materials and coatings are needed, as well as a comprehensive knowledge of the microstructural, thermal and mechanical properties of conventional thermal barrier coatings and the study of their evolution during high-temperature exposure in harsh operating environments.

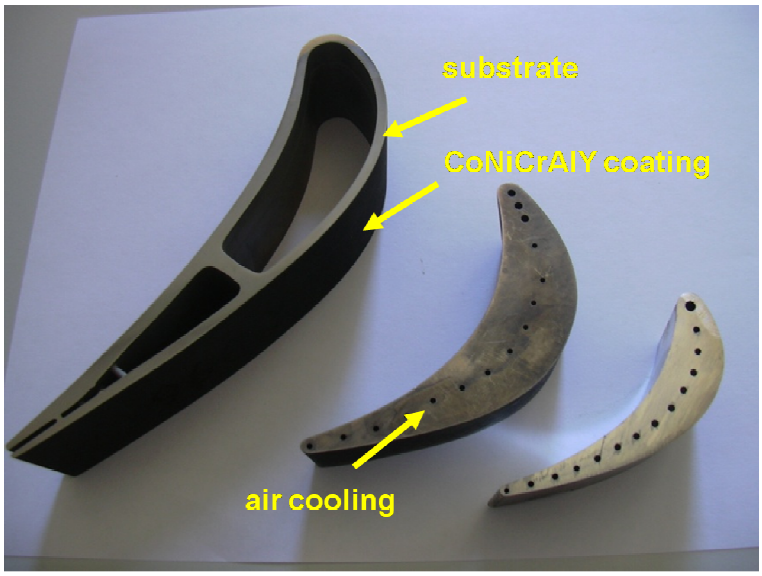

Figure 1 – Some examples of coated and uncoated turbine blades.

Air Plasma Spraying is a cost-effective technique for the fabrication of metal coatings and porous ceramic thermal barrier coatings with unique microstructure and well-determined functional properties. This technology uses a plasma gas stream to melt and accelerate powder particles toward a substrate where they impact and solidify, thus gradually forming a coating.

The present work is focused on the study and the development of metallic and ceramic coatings which can have a high valence in short-run industrial applications. To this purpose, commercially available materials have been processed in order to fabricate coatings with enhanced microstructural, thermal and mechanical properties.

So, Air Plasma Spraying has been employed to fabricate CoNiCrAlY metallic coatings with reduced porosity and low degree of oxidation. CoNiCrAlY coatings are commonly used to protect metal hot section components of turbine engines from oxidation and hot corrosion, frequently in conjunction with an upper ceramic thermal barrier coating (TBC). When used as an intermediate layer, CoNiCrAlY coating plays a significant role on the durability of the same TBC. Firstly, it allows to reduce the mismatch between the thermal expansion coefficient values of the substrate and the TBC, since a too large gap can generate high interfacial shear stresses during thermal cycling, producing the nucleation and the propagation of cracks and accelerating TBC spallation. Secondly, it creeps at high temperature, so that it is able to accommodate thermal strains and to reduce interfacial shear stresses. Thirdly, it provides higher resistance to oxidation and hot corrosion to the substrate, since most ceramic TBCs are transparent to the oxygen and permeable by corrosive agents, due to their open porosity. The propagation of oxygen during high-temperature exposure promotes the formation of a thermally grown oxide (TGO) layer whose thickness grows with increasing the exposure time and can induce TBC delamination and failure.

It should be noted that metal coatings are commonly manufactured by using other thermal spraying processes, such as Vacuum Plasma Spraying or High-Velocity Oxygen Fuel

Spraying. Vacuum Plasma Spraying allows to reduce the interaction between the sprayed metal particles and the surrounding oxygen, due to very low oxygen content in the pre-evacuated spraying chamber, thus reducing in-flight particles oxidation during processing. In turn, HVOF involves higher velocity of deposition, reducing the residence time of the sprayed particles in the flame prior to their impact on the cold substrate and leading to coatings with very low porosity and high bonding strength. However, these systems are less flexible and more expensive than Air Plasma Spray. A few works have been published about CoNiCrAlY coatings fabricated by APS.

To this purpose, CoNiCrAlY coatings with enhanced microstructural and mechanical properties were fabricated by APS. The evolution of their microstructural and mechanical properties has been investigated after early-stage high-temperature oxidation. It is worth noting that in literature the mechanical properties of as-sprayed MCrAlY (M = Co, Ni) coatings are marginally reported and mainly referred to as-produced coatings, while oxidation tests have been mainly performed with the purpose to study the phase changes promoted by high-temperature exposure. As better discussed in the next sections, early-stage oxidation produced a partial densification of the microstructure, thus improving the mechanical properties (hardness and elastic modulus), while the oxidation mainly occurred at the coating top-surface. So, this densification is desirable because makes the coatings more resistant to oxygen penetration.

Yttria partially stabilized zirconia (YSZ) was studied as reference material for TBCs, in addition to new alternative materials such as ceria-yttria co-stabilized zirconia (CYSZ) and nanostructured YSZ. This choice can be easily explained. Indeed, at the moment, zirconia-based materials offer the best compromise between the most relevant microstructural and thermo-mechanical properties demanded to TBC materials. The use of rare earth oxides (ceria) to stabilize zirconia in the tetragonal or cubic form represents an important

technological solution and, therefore, the properties of CYSZ coatings have been extensively investigated and compared to those of YSZ ones. The aim of these experiments was to fabricate coatings with improved microstructural, thermal and mechanical properties, to analyze in detail some aspects not well-investigated in literature and to study the evolution of the functional properties using advanced methodologies of testing and characterization. So, the most important features which affect coatings in-service performance, such as elastic modulus, hardness, thermal expansion coefficient (CTE) and heat capacity, were extensively investigated. To this purpose, porosity and elastic modulus play an important role on the heat transfer to the substrate and on the strain tolerance of the TBC, respectively. Static (Nanoindentation) and dynamic techniques were employed for the determination of the elastic properties of plasma sprayed coatings; a resonant method, known as the Impulse Excitation Technique (IET), was used to measure the Young's modulus in conjunction with a bi-layer specimen configuration (substrate and coating). The knowledge of thermal expansion coefficient is fundamental for TBCs designers, because a high CTE mismatch between coating and substrate can induce crack formation and propagation, leading to TBC delamination and failure. Heat capacity, together to the thermal diffusivity and density, in turn influences the thermal conductivity and the rate of thermal heat transfer from coating surface to the substrate.

As described in the next sections, CYSZ and YSZ coatings with high hardness, low elastic modulus, well-determined porosity (~10-12 %) and enhanced thermal properties (high CTE and low heat capacity) were obtained.

In this context, on the basis of the direct experience of any famous industrial turbine manufacturers and users, the main mechanisms that govern TBC degradation during service have been extensively investigated and thus the evolution of the microstructural and the mechanical properties has been studied after high-temperature post-treatments. Therefore,

free-standing YSZ and CYSZ TBCs were thermally aged at temperature higher than 1300 °C for different times.

To this purpose, high-temperature phase changes and sintering phenomena are known as the main factors which affect the durability of thermal barrier coatings and have to be extensively investigated by TBC designers in order to obtain high-reliability data which can be rapidly transferred to the industrial field.

For example, it is worth noting that upon slow cooling from service conditions to room temperature, some phase transitions may occur in zirconia-based TBC system. As an example, the monoclinic transformation is notoriously accompanied by a volume change (from 4 to 9 %) and can promote TBC cracking and lifetime reduction.

Moreover, high-temperature exposure can produce the closure of finer pores and microcracks embedded in TBC microstructure, leading to the partial densification of the same porous microstructure and to a corresponding increase in Young's modulus and, according to the level of stiffening, to a reduction of the strain tolerance. Sintering also affects the thermal transport properties of a ceramic thermal barrier coating, increasing the thermal conductivity. It should be noted that in literature the sintering kinetics of state-of-the-art yttria partially stabilized zirconia (YSZ) coatings has been mainly investigated, but many aspects about the evolution of coatings properties have not been highlighted. So, the sintering behaviour of YSZ and CYSZ coatings has been investigated. Sintering produced a decrease of porosity volume and a corresponding increase of hardness and elastic modulus. Moreover, it has been generally reported that CTE and heat capacity are not affected by high-temperature sintering. On the contrary, significant changes were noticed for both YSZ and CYSZ coatings. As annealing time increased an increase in heat capacity was noticed for YSZ coatings, while a decrease was noticed for CYSZ ones.

Due to the increasing interest in nanostructured ceramic materials, some preliminary experiments about nanostructured zirconia coatings have been also performed in order to study their basic microstructural features and looking at future studies and research projects. Based on these preliminary investigations, further experiments will be performed in order to optimize the most important plasma spraying parameters which influence the final properties of nanostructured coatings. Indeed, their processing requires an accurate control, in the purpose to fabricate coatings with well-determined microstructural and mechanical properties. The nanostructured powders are typically composed of porous agglomerates of nanoparticles, which can be partially or totally melted during processing, thus producing a unique microstructure characterized by both well-melted and partially melted areas. If the powder particles are totally melted the coating behaves as a microstructured one. So, differently from microstructured powders, the melting degree of nanostructured powders becomes a key factor to be controlled, even if this is not easy as well as it is not easy to measure quantitatively the differences in microstructure and mechanical properties for these coatings.

The work described in this thesis was carried out at Department of Mechanical Engineering of Calabria University and ENEA Brindisi Research Centre. In particular, the Air Plasma Spray (APS) equipment installed at ENEA Brindisi Research Centre was used for spraying trials and coatings fabrication. The microstructural characterization was carried out at ENEA, using various techniques such as X-ray Diffraction (XRD), Optical Microscopy and Scansion Electron Microscopy (SEM), Image Analysis (IA), Thermal Analysis, Dilatometry, Differential Scanning Calorimetry (DSC) and other techniques and equipments for preparation, testing and characterization of coatings and materials, available at ENEA National Centres. An experimental set-up, arranged at Department of Mechanical Engineering of University of Calabria, has been studied and adapted for determining the elastic properties of as-sprayed coatings by Impulse Excitation Technique (IET). A cooperation with National

Centre of Advanced Tribology of Southampton (nCATS) was initiated and allowed to perform Nanoindentation (NI) tests on samples and coatings. The results demonstrated that this advanced and unique testing methodology is very useful to study the evolution of mechanical properties of plasma sprayed coatings after high-temperature treatments.

In order to help the reader, this work has been divided in four chapters, so that the structure can be summarized as follows.

Chapter 1 reports a bibliographic study about the employment of Thermal Spraying technology to produce coatings for multi-functional applications. This technology is very cost-effective and flexible, since it allows to process a wide variety of materials, such as metals, ceramics and composites. For completeness, all the commercially available Thermal Spray methods are presented, as well as the main characteristics of the coatings which can be fabricated and used in several industrial fields. Great attention is obviously focused on ceramic thermal barrier coatings produced by Air Plasma Spraying, so that detailed information about standard and novel materials for TBCs are given. It should be noted that many studies about advanced materials (often produced at laboratory scale) are not definitive and, thus, further investigations are needed. The characteristics of Air Plasma Spray processing and the mechanism of coatings formation are also presented, as well as the methodologies commonly used for their mechanical testing and microstructural characterization.

Chapter 2 describes the experimental procedures followed for the development, fabrication and testing of metallic and ceramic coatings. The details about APS equipment employed for coatings fabrication and the properties of raw materials are reported, as well as the experimental conditions at which the coatings were fabricated and tested and the technical data of the apparatus employed.

Chapter 3 reports the main results about the microstructural, mechanical and thermal properties of plasma sprayed metallic and ceramic coatings, in as-sprayed conditions and after high-temperature exposure. The results obtained are discussed and compared to the data available in literature.

In Chapter 4 the most significant experimental results discussed in the previous chapter are summarized and validated. A comparative analysis between the experimental results and the corresponding data reported in literature is carried out, taking into consideration applications, materials and equipments. Some interesting ideas for coming researches and experiments are also reported.

1. Thermally Sprayed Coatings for Engineering Applications: Status of the Art

1.1 Industrial Demand for Surface Coatings

Surface coatings are commonly used to protect a wide variety of engineering components from high temperature, oxidation, corrosion and wear, and to tailor their surface functional properties for a lot of industrial applications. As known, the outer surface of mechanical components may be subjected to damaging or degradation when operating in severe service conditions, due to the interaction with other components or harsh environments. These particular conditions may be responsible for unexpected component failure and reduced lifetime. The demand for more performant components which are suitable to operate for long times in severe environments, implies the development of advanced materials characterized by enhanced strenght, toughness, hardness and, at the same time, the development and the validation of new processes of manufacturing. It should be noted that, in any applications, the use of structural materials with enhanced physical and mechanical properties may result very expensive and, sometimes, technically unsatisfactory. As an example, solid advanced ceramics represent an attractive solution to fabricate components for high temperature applications, such as gas turbine blades and vanes. However, actually, their brittleness and their unreliable behaviour involve significant limitations and, thus, further studies are required in order to validate their use in real applications. Meanwhile, other available technological solutions have to be carefully considered and employed. To this purpose, the application of surface coatings represents a technologically suitable and cost-effective solution, since it allows to tailor the component surface to withstand in harsh environments, by enhancing of its capability, and to extend the lifetime, without compromising the original characteristics. Thermal Spraying is an attractive, easy, reliable and cost-effective technique to fabricate high quality coatings with unique design, well-determined microstructural and mechanical features

and with thicknesses typically ranging from tens of micrometers to some millimetres [1]. Several typologies of materials can be processed to form coatings, such as ceramics, metals and ceramic-metals (cermet) composites. The rapid deposition rates typically involve low processing costs. An other significant advantage should be highlighted. It is well-known that the end of the coating lifetime is determined by its failure, produced by partial or total delamination from the substrate. The replacement of the underlying component is not always required. Indeed, the damaged coating can be stripped off from the component surface; this last surface may be re-prepared and re-coated by applying of a new coating. Otherwise, if the coating has been partially delaminated, Thermal Spraying can be used to restore the starting dimensions of the mechanical component (especially for metallic coatings).

In Thermal Spraying a heat source is used to heat the starting material, in form of powder, wire or rod, above its melting point. The molten and atomized particles are then accelerated toward a substrate and, on impact, their solidification produces the gradual formation of a coating. Powder particles can show various shape, morphology and size, depending on the corresponding process manufacturing (fused and crushed, spray-dried, sintered, etx). Moreover, they can be spherical, hollow spherical or angular. Their intrinsic characteristics influence their flowability and their melting degree which affects the microstructural and the mechanical properties of the final coatings [1].

Thermal spray processes are commonly used for a wide variety of applications in many industrial fields, such as in aerospace, automotive, power generation, biomedical, glass manufacturing, corrosion of marine and land-based infrastructures, fabrication of electronic devices, petrochemical and paper industry. The industrial interest implies future researches about new typologies of coatings, as well as new techniques for coatings deposition and new methods for characterization and testing.

1.2 Thermal Spray History

Thermal Spraying processes have been firstly used for repairing and dimensional restoration of worn or damaged machine components. The first Thermal Spray equipment was patented by Schoop between 1882 and 1889. A modified oxy-acetylene welding torch was used as heat source. The powder particles were caught up in the hot expanding jet flow, heated and accelerated toward the substrate. The molten droplets impact the substrate surface, spread and solidified, promoting the build up of a solid coating [1].

Around 1908 Schoop patented an Electric Arc Spray system for deposition of metal coatings. Schoop introduced some improvements in the equipment and in process control in comparison with the previous system. During the World Wear II, the cylinders of radial piston engines in military aircrafts had typically coated with aluminium by Combustion Wire Spraying [1].

However, only around 1940s the introduction of the first Plasma Spray by Reinecke gave a significant improvement to the technology. Thermal Spraying allowed to melt various materials by means of a plasma jet, which yielded to higher temperature and higher particle speed than those achieved through the previous systems. However, Thermal Spray industry had not a great diffusion until the late 1950s. Then, it had a significant growth, by means of the great contribute of the aircraft and diesel engine applications. Its gradual growth has been determined by means of the development and the introduction of new systems such as Detonation Gun and High Velocity Oxygen Fuel (HVOF), new process control equipments and new feedstock materials. The first ceramic coating used as thermal barrier coating (TBC) has been a coating of calcia stabilized zirconia in 1960s, applied on turbine components and compressor blades and vanes [1].

1.3 Coatings Engineered for Industrial Applications

By means of their intrinsic characteristics, thermally sprayed coatings are very promising for functional applications in many industrial fields.

Metals, ceramics (metal oxides or not oxides), intermetallics (TiAl, NiAl), thermoplastic polymers, composite and cermets can be sprayed by using different Thermal Spray processes.

The microstructural, thermo-mechanical and anti-wear properties of thermally sprayed coatings may be tailored on the basis of given applications, by an accurate selection of the starting materials and of the most appropriate thermal spray process. Typical applications include thermal barrier coatings (TBCs) for aircraft, land based gas turbine engines and diesel engines, abradable and abrasive coatings for hot components of gas turbines, anti-corrosion coatings used in chemical industry, biomedical coatings for implant prostheses, electrical conductive or insulating coatings and wear resistant coatings for protection of steel mechanical components against abrasive and adhesive wear and erosion [1].

The main characteristics of these coatings will be reported in the next sections. To this purpose, the attention will be mainly focused on the coatings which can be successfully fabricated by Plasma Spraying process. Obviously, for other applications there are more proper manufacturing processes. As an example, thermally sprayed coatings can commonly show anisotropic properties and may show lower bonding strenght, loading capacity and impact resistance than other coatings deposited by using different techniques and processes. However, their quality is very high and the benefit-cost ratio is very high when compared to other technological processes.

1.3.1 Microstructured Coatings

1.3.1.1 Thermal Barrier Coatings

Thermal Barrier Coatings (TBCs) represent the most promising industrial application of thermally sprayed coatings. Ni-based super-alloys are currently used for manufacturing of hot-sections components of aircrafts and land-based gas turbine engines, such as first-stage turbine blades and vanes, transition pieces and combustion chamber tiles. During their service these components are notoriuosly exposed to high temperature and operate in highly oxidizing and corrosive environments. In the actual turbines, the temperatures on the metal surface are in the range from 900 °C to 1100 °C. The hot gas temperatures may exceed the temperature capability of Ni-based superalloys, especially for next generation gas turbine engines. Moreover, these components are addressed to operate in harsh environments, where high temperature and oxidation can provide significant problems. In addition, the presence of aggressive agents, such as sulphates, chlorides and vanadates, often contained in low grade fuels, may enable much severe hot corrosion, considerably reducing the resistance and the lifetime of metal components. From 1950, Ni-based superalloys have been used in different form and chemical compositions, in the purpose to improve their respective thermo-mechanical and anti-corrosion properties. Figure 1.1 illustrates the temperature capability of gas turbine engine components versus year, by considering the evolution of Ni-superalloys and the benefit associated to the application of a TBC. The first wrought superalloys have been replaced by cast materials characterized by higher creep and oxidation resistance, and then by directionally solidified materials. Recently, single crystal alloys have been considered as promising candidates for manufacturing of last generation turbine blades and vanes. The addition of rhenium in the composition of Ni-based superalloys allows to increase their creep strength [2]. Further improvements have been obtained in the design of the internal cooling channels into the blades. However, above 1100 °C the Ni-superalloys have to be protect

against oxidation and high temperature. Therefore, new concepts in materials and components manufacturing have been identified and developed.

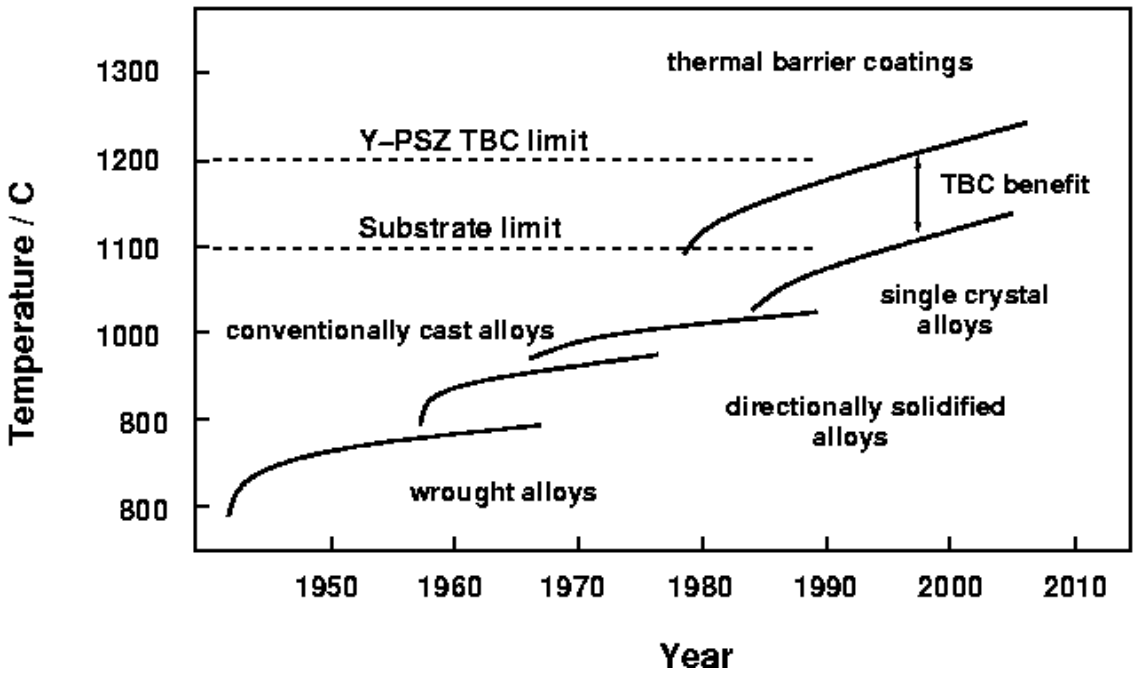

Figure 1.1 – Historical evolution of materials and design for turbine engines hot components.

Ceramic materials notoriously show high resistance at high temperatures, as well as other interesting thermo-mechanical properties. However, structural ceramics show not reliable properties, thus their use for fabrication of complex turbine components is currently object of accurate studies. Indeed, it is well-known that ceramics are very brittle and liable to fracture by mechanical and thermal shocks. Current studies are mainly addressed to enhance their toughness. However, the properties of metals and ceramics can be properly combined by the development of TBCs, giving them the most proper design for a given application. Indeed, the application of a protective porous ceramic layer is able to thermally insulate component surface, by a reduction of the heat transfer from hot gases to the underlying material, and to improve the temperature capability and durability. It is strongly suggested when severe in-service conditions are expected. Today, thermal barrier coatings are generally applied to

respond to this demand. However, the growing demand for energy reduction, less fuel consumption and less environmental impact, resulting in less emissions of CO_2 and NO_x into the atmosphere, require higher performance for advanced turbines of next generation and, therefore, a significant increase of their operating temperature, in a range between 150 °C and 200 °C, and correspondingly in their efficiency. Moreover, it is well known that gas turbine components are currently cooled by an internal cooling system or a film cooling, which reduce metal surface temperature by up to about 150 °C. Unfortunately, this cooling system results very expensive and thus more cheap and performant alternatives should be developed.

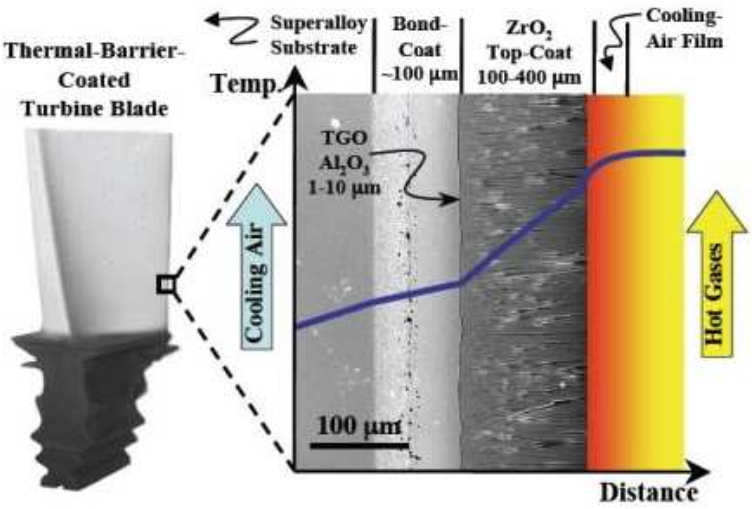

Figure 1.2 – Design of a thermal barrier coating applied on a turbine blade.

To this purpose, the application of a TBC would allow to reduce the requirements for the cooling system, in terms of lower cooling air flow and higher efficiency or, at constant cooling air flow, lower metal surface temperature and consequently higher lifetime. The TBCs operate under a temperature gradient by cooling. Indeed, the application of a TBC allows to tolerate a ΔT through the thickness, maintaining the underlying component at lower temperature. The TBCs may be developed and engineered in order to accommodate high temperature gradients and, to this purpose, thick barrier coatings, *i.e.* with thickness higher

than 1 mm, can be applied, especially in the case of combustion chamber components and diesel engine components. This is an important possibility, even if a higher thickness reflects in higher stresses during deposition and during service. The formation of significant cracks can increase the probability of a premature spallation and failure of the TBC. Moreover, the geometrical and dimensional requirements for the coated component can limit the thickness of the protective layer. As an example, the total thickness of a TBC applied on a stationary turbine blade is generally around 500 μm or less. Figure 1.2 shows a typical thermal barrier coating applied on an turbine blade. The TBC is composed of a dual layer, an inner metal layer, deposited by High Velocity Oxygen Fuel on the superalloy substrate, and an upper ceramic layer deposited by Electron Beam Vapour Deposition (EB-PVD).

In diesel engines TBCs are used to protect pistons, valves and piston fire decks from heat, high-temperature oxidation, corrosion against fuel contaminants and thermal shocks. They are applied with the purpose to improve the fuel efficiency or to allow the use of heavier grade fuel oils [3]. The application of a TBC provides lower peak combustion temperatures and a decrease of the emissions (NO_x and CO) and of particulate.

It is worth noting that in diesel engines the maximum service temperature is of about 800 °C and the cycle lasts only a fraction of a second. Otherwise, aircraft turbines exhibit thermal cycles of several hours at higher temperatures (> 950-1000 °C). The thermal cycles of the stationary turbines last from several hours for peak-load up to 1 year at base-load operation. Thereby, the corresponding mechanisms of degradation of the TBC can be different.

Several techniques are suitable to manufacture TBCs. Plasma Spraying (PS) and Electron-Beam Physical Vapor Deposition (EB-PVD) are widely used to this purpose.

TBCs began to be studied since 1960s. In the last years the researches have been mainly focused on the study and on testing of promising materials for TBCs which could substitute and improve the in-service performance and the durability of typical 7-8 wt.% yttria-partially

stabilized zirconia (YSZ). YSZ TBCs have been used for more than 30 years in many industrial fields, since they offer a satisfactory performance and a good combination between the main requirements that a TBC has to satisfy in a lot of high-temperature applications. Zirconia is notoriously characterized by high thermal expansion coefficient, low thermal conductivity, phase stability to relatively high temperature, high strength, high thermal shock resistance and high fracture toughness. Firstly, pure zirconia had been proposed as TBC material. Unfortunately, it shows a phase transition which is deleterious for the durability of a TBC. It should be remembered that the equilibrium form of zirconia is monoclinic at temperature less than 1170 °C. Between 1170 °C and 2370 °C it is tetragonal, while it is cubic at temperatures higher 2370 °C [4,5].

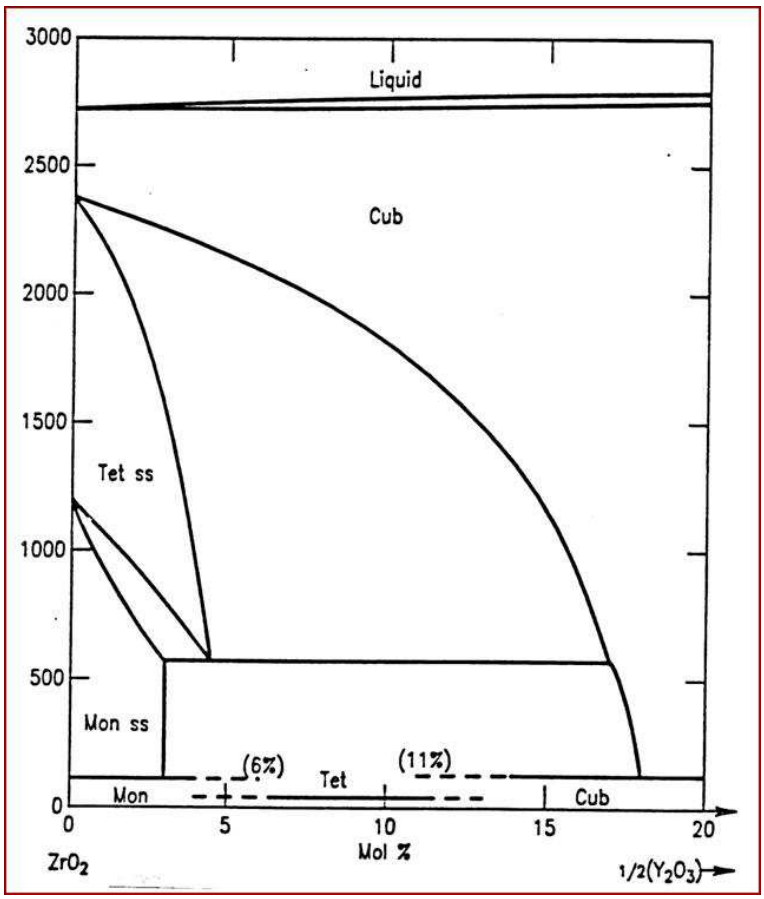

Figure 1.2 - Phase diagram for ZrO_2-Y_2O_3 compositions.

It has been demonstrated that the addition of one or more stabilizer oxides to pure zirconia allows to stabilize this last one in its cubic or tetragonal form. The introduction of a stabilizer implies the introduction of several vacancies within the original structure. It has been reported that yttria fully stabilized zirconia coatings exhibit lower lifetime under thermal cycling than partially stabilized zirconia ones [6]. Thereby, the amount of the stabilizer oxide has to be properly optimized, in order to allow a controlled phase change during high-temperature exposure. Indeed, the monoclinic transition is notoriously accompanied by a volume change and can promote the formation of significant cracks. Various zirconia stabilizer oxides, such as CaO, MgO, Y_2O_3, CeO_2, are currently used. Figure 1.3 shows the binary phase diagram for Zirconia-Yttria compositions.

It should be noted that the materials candidates for TBCs development have to satisfy some basic requirements, such as **low thermal conductivity**, a **thermal expansion coefficient** close to that of metal substrate, **high melting point and temperature capability**, **phase stability** between room temperature and operating temperature, a **low Young's modulus**, a chemical compatibility with substrate and **a low sintering rate** of the porous microstructure at high temperature. Thermal conductivity is a basic properties, because it influences the heat transfer from the coating surface to the substrate. The thermal expansion coefficient (CTE) is an other important thermophysical property, because the lifetime of the TBC is highly related to the strain level and, then, to the difference in CTE values of the overlapped layers. Microstructural and mechanical properties, such as density (< 7.5 gcm^{-3}) and hardness (> 6 GPa) are in turn important. The elastic modulus influences the residual stresses level and the strain tolerance capacity. A porous microstructure typically possesses a low Young's modulus and high strain tolerance. The hardness is strongly related to wear and abrasion resistance. The density and the deposited thickness can influence the weight of the component. Thereby, in aircraft engines thin coatings with low thermal conductivity are preferable, whereas thicker

coatings are more suitable for land-based turbine applications. The coating thickness may be set on the basis of the geometrical requirements and in the purpose to obtain the desired thermal insulation. The choice of the material and of the design for a thermal barrier coating is strongly related to the real application it is addressed to. As above reported, yttria partially stabilized zirconia (YSZ) is the most common material used for TBCs. However, it can show an insufficient performance, mainly in land-based turbine and diesel engines, where low-quality fuels are typically used. The contaminants (Na_2SO_4, V_2O_5) make notably severe the operating environment and are able to produce a premature failure of the TBC by hot-corrosion. Therefore, alternative solutions and further investigations are needed, in order to process and analyze new advanced materials with lower thermal conductivity, high hot-corrosion resistance, high phase stability and long-term thermal cycling resistance.

Since a few data about alternative thermally sprayed TBCs are reported in literature, the selection of alternative materials is generally made by considering the properties of bulk materials showing the same chemical composition. The effect of thermal spray processing on the resulting coatings properties have to be carefully investigated

The TBCs are commonly engineered following a well-known design. In diesel engines, the ceramic layer is directly applied on metal substrate, whereas in the turbine engine components an intermediate metallic bond coat is applied before ceramic thermal barrier coating.

This metallic coating (MCrALY, where M = Ni, Co) has to exhibit a high chemical compatibility with the substrate material. It has been demonstrated that it may play an important role on the lifetime of the TBC. Firstly, its application provides a rough surface for mechanical bonding of the upper TBC and, thus, it increases the interfacial adhesion between the substrate and the same TBC, since these last ones are notoriuously characterized by a high mismatch between their respective thermal expansion coefficient values. A large gap would be able to produce high interfacial shear stresses during in-service thermal cycling, thus

promoting the growth and the propagation of cracks which lead to the spallation and, finally, to the TBC failure [7,8,9]. As known, the failure of a TBC is involved by delamination, which in turn results from nucleation and propagation of cracks at the interface. Secondly, the bond coat protects the substrate, since it provides high resistance to oxidation and hot-corrosion, because the ceramic materials used for TBCs are generally transparent to oxygen and, since they were characterized by both open and closed porosities, they result permeable by oxygen and other aggressive agents. The intermediate coating is usually deposited by thermal spraying. The spraying in atmospheric environment can induce increased oxidation of the powder particles surface and result in the presence of oxides within the coating microstructure. Thereby, it would be better to spray metallic powders by using Vacuum Plasma Spraying (VPS) or High Velocity Oxy Fuel (HVOF) systems, which better insulate the sprayed particles from oxygen or reduce the time of interaction between particles and surrounding air, respectively. The effect of oxidation may be controlled and reduced in both cases. HVOF system allows to fabricate denser coatings, being this result more appreciated, since a denser coating represents a better barrier to oxygen and other contaminants. Detonation Gun and Cold Spraying represent other interesting technical options. However, in many cases, Plasma Spraying may be successfully used to deposit high quality metal and cermet (ceramic-metal) coatings by a proper coice of the spraying parameters or by arranging simple shrouding devices in order to reduce the effect of oxidation and decarburization, respectively [10].

1.3.1.2 Environmental Barrier Coatings (EBCs)

Silicon-based ceramic matrix composites (CMC) are the most promising materials for hot section structural components in advanced and low emission turbine engines, due to their high oxidation resistance. However, it has been found that the volatilization of the protective silica

layer in water vapour environments produces a significant drop in their performance, correspondingly reducing their service life. According to recent studies, Environmental Barrier Coatings (EBCs) represent an attractive technological solution to protect the outer surface of these components and to extend the temperature capability of CMC liners and vanes in combustion environments [11]. Mullite is a promising material for EBCs, due to its thermal expansion coefficient close to that of Silicon Carbide (SiC) substrates, resulting in high thermal cycling lifetime [12]. Plasma sprayed mullite coatings show low porosity, but typically contain a large amount of amorphous phase due to the high cooling rate of the melted particles during deposition. The in-service re-crystallization of amorphous mullite can promote the development of cracks within the coating, due to the volume contraction associated to the phase transition. The amount and the size of these cracks can strongly influence the coating performance. Moreover, mullite also suffers high temperature silica volatilization in water vapour environments. To this purpose, the development of more appropriate multilayered environmental barrier coatings seem to be the best future solution.

1.3.1.3 Anti-wear Coatings

Several types of friction and wear modes are known and, therefore, functional coatings can be developed and fabricated in order to respond to well-determined industrial demands. To this aim, thermally sprayed coatings can be applied to protect the surfaces of machine components from abrasive wear, adhesive wear and surface fatigue wear.

Abrasive wear occurs when hard particles, such as metal debris or dust, entrapped between the rubbing surfaces, promotes enhanced abrasion of the same surfaces. This phenomenon can occur at relatively high temperature. Alumina (Al_2O_3), Chromia (Cr_2O_3) and Tungsten Carbide-Cobalt (WC-Co) coatings are usually applied for this type of applications [13,14].

Adhesive wear occurs when two solid surfaces slide against each other during their relative motion, producing the removal of material from one surface. So, the detached fragments adhere to the other surface. This wear mode commonly occurs in many mechanical components, such as piston guides and bronze bearings, especially when the lubrication between the surfaces is inadequate. To this purpose, soft bearing coatings can be applied to embed abrasive fragments and to allow the deformation for alignment of bearing surfaces. These coatings are usually applied to babbitt bearings and piston guides. Otherwise, hard bearing coatings are more resistant to adhesive wear and are used for more severe applications, such as in piston rings and fuel pump rotors. Alumina-Titania (Al_2O_3-TiO_2) and Tungsten Carbide-Cobalt coatings (WC-Co) are typically addressed to these applications.

Surface fatigue wear is produced by repeated loading and unloading cycles, which promote high stresses on a surface and, without a constant removal of particles, can generate cracks and large fractures. The detachment of large fragments reduces the lifetime of the component.

Fretting is an example of fatigue wear between two surfaces in contact, determined by repeated cyclic stresses. Fretting commonly occurs in both lower and higher temperature sections of turbine engines. Components exposed at high temperature are typically subjected to severe wear, because their surfaces can not be lubricated. The wear generates particulate debris. The erosion is promoted by the interaction between the surface and the particles which impact at high velocity.

Cermet coatings combine wear resistance and thermal properties and their application in both hot and cold sections of engines can extend the component life to several months or years.

Chromium Carbide in a matrix of Nickel Chromium (Cr_3C_2-NiCr) and Tungsten Carbide-Cobalt are commonly applied to enhance the erosion resistance of rocker arms, piston rings, cylinder lines, compressor air seals, exhaust fans and valve seats. The former is used in hot sections, whereas the latter in cold sections (< 540 °C), because its properties drop as the

temperature increases. In cermets, the hardness of WC grains and the ductility of metal binder, which cements the brittle phases avoiding the brittle fracture, are properly combined and provide high wear resistance. TiC is an other cermet materials, suitable for high-temperature applications, due to its high hardness and low friction coefficient.

Atmospheric plasma spraying of carbide-based coatings typically produces increased decarburization. High temperature and oxidizing atmosphere promote the growth of brittle crystalline and amorphous phases along primary WC, due to the carbide dissolution in the metal binder and decarburization. This leads to a reduction of their wear resistance [15]. Therefore, carbides are preferably deposited by VPS, HVOF or Detonation Gun, where lower temperature, high particles velocity and the spraying environment are able to reduce carbides dissolution [13,14]. However, recent studies have demonstrated that by a proper choice of the spraying parameters (plasma gas mixture, standoff distance and plasma enthalpy), high-performance plasma sprayed WC-Co coatings may be successfully fabricated, since they are characterized by hardness, toughness and wear resistance comparable to the same coatings deposited by VPS or HVOF [10].

1.3.1.4 Anti-corrosion Coatings

Corrosion may be divided in hot corrosion between gases and solid surfaces and atmospheric corrosion.

Hot corrosion commonly affects hot components of gas turbines and diesel engines. To the purpose, MCrAlY and ceramic coatings are usually applied. Further details will be discussed later, since hot corrosion has to be carefully considered in the development of thermal barrier coatings.

Otherwise, several infrastructures have to be protected against atmospheric and water corrosion, such as electrical conduits, bridges, ship holds and tanks, ship pylons, storage tanks

for oils and fuels, antennae, wind towers, offshore structures, petrochemical pumps and valves. To the purpose, thermally sprayed coatings have been used since the 1930s in U.S. and then they have had a gradual growth. Thermally sprayed coatings are able to substitute traditional metal paints or organic coatings, due to their higher effectiveness and lower cost, predictable life and higher abrasion resistance. Typical coatings that can be applied include metal coatings made of aluminium, aluminium metal-matrix composites, zinc, molybdenum and nickel-chromium, chemically inert ceramics and polymers [1]. A significant factor has to be remarked with respect to both hot and cold corrosion. Indeed, some microstructural features observable in thermally sprayed coatings, such as pores and splat boundaries, play an important role on their corrosion resistance, as well as the chemical inertness of the material to the operating environment. Coming from this point of view, HVOF coatings would be preferable, due their very low porosity. However, a sealant could be used to close the open porosity of plasma sprayed coatings, in order to better insulate the surface of the coated component. This sealant, organic or not organic, may be applied by using other deposition techniques, such as Sol-Gel, Impregnation or Slurry Coating.

Severe corrosion can be promoted by molten glass in glass industry, where TBCs can be deposited on combustion chambers, heat exchangers and other hot components.

1.3.1.5 Abradable Coatings

Abradable seals coatings are applied on the surface of aircraft turbine engine components, in the purpose to reduce bypass flow of hot combustion gases or cold compressor gases through the spaces between the rotating blade tips and the stator. These coatings provide a good sealing of the gas path and, therefore, can notably improve the efficiency of the engine [1]. Obviously, the abradable coatings have to satisfy some basic requirements, in order to accommodate high-speed blade tip rubs, induced during the start-up and the next operating

conditions, and to provide wear protection to both stationary and rotating components. Thereby, they have to resist to abrasion and spallation during rubbing. However, they have not to be too harder, because they could damage the blade tips promoting accelerated wear. To this aim, polymers, soft metals and abradable ceramic coatings with particular compositions are usually applied.

1.3.1.6 Biomedical Coatings

Biomedical coatings are usually divided in bioactive and biocompatible coatings, which are used for implant prostheses, orthopaedic devices and dental implants.

Biocompatible coatings are porous titanium coatings compatible with the human bone and they are usually applied on titanium alloys prostheses.

Bioactive coatings, including tricalcium phosphate and hydroxyapatite $Ca_{10}(PO_4)_6(OH)_2$ coatings are usually applied to the implant before the implantation in the human body. They are dynamic interfaces between titanium alloy implants and osteoblast cells. These coatings exhibit characteristics similar to those of the natural bone and their strong activity with the bone tissue promotes a good bonding. So, many implants are put in the human body and here fixed without any adhesive, allowing the bone tissue to grow into the open porosity of the biocompatible coating. Both biocompatible and bioactive coatings allow a faster patient recovery and extend the implant life. High purity is required for these particular applications.

1.3.1.7 Other Coatings and Applications

Electrically insulating coatings are commonly used in electronic devices for high frequency applications. It should be also mentioned that thermally sprayed porous coatings are suitable for fabrication of power generation components, as components of solid oxide fuel cells.

Electromagnetic coatings can be found in capacitors, inductors, resistors, automotive electronics and waveguide devices for microwave applications.

1.3.2 Nanostructured Coatings

The above reported coatings, which herein are identified as “conventional”, are usually deposited starting from micronsized powder particles. However, nanosized particles could be thermally processed to manufacture “nanostructured” coatings having the same composition of the conventional ones. Nanostructured materials are an attractive solution for a wide range of functional applications, by means of their enhanced mechanical properties associated to the reduction of the grain size. Plasma spray is suitable for fabrication of nanostructured coatings, because the thermal effects may be contained by an accurate choice of the spraying parameters during deposition and correspondingly at least a part of the starting nanostructure can be retained in the final coatings. Due to their low mass, nanoparticles possess low flowability and can not be successfully carried by a gas stream. Indeed, a low mass implies a low momentum. Therefore, they are commonly agglomerated in micronsized particles by spray drying and then sintered. In order to preserve the original nanostructure these agglomerates have to be not fully melted during plasma spraying. Their melting degree influences the amount of retained nanosized areas within the coating. By controlling the amount of retained nanostructures or nanozones embedded in the coating microstructure, nanostructured ceramic coatings can be engineered for a given application, as described in detail in a recent paper [16]. It should be noted that a low melting degree can also lead to coatings characterized by low cohesive strength. The melting degree depends on the temperature of the particles into the plasma jet. Plasma temperature and enthalpy have to be carefully controlled, in order to melt only the outer surface of the agglomerated particles, thus leaving their core unmelted.

A few nanostructured agglomerated powders for thermal spraying are commercially available (ZrO_2-$7Y_2O_3$, Al_2O_3-$13TiO_2$, TiO_2, WC-Co). The first ones were introduced in commerce in the early 2000s. Actually, these products are produced in small quantities, thus yielding to high manufacturing costs. Further researches could justify higher production volume and make their manufacturing very cost-effective, especially if the expected superior performance of nanostructured coatings should be demonstrated in comparison with the conventional ones having the same composition.

These coatings can show a typical bimodal microstructure, characterized by fully melted areas which surround and cement partially or unmelted areas, which resemble the morphology of the powder feedstock. The thermal effects associated to plasma spraying can determine a controlled grain growth. Otherwise, when feedstock particles are fully melted, the nanostructure is destroyed and the coating tends to behave as a conventional one.

As mentioned above, nanostructured coatings can be engineered for several applications. Firstly, nanostructured materials are potential for advanced thermal barrier coatings. Their thermo-mechanical properties have been studied in previous works, even if a few investigations have been made and further studies are then required**.** It has been found that nanostructured zirconia coatings show higher creep rate than the conventional ones, implying more rapid stress relaxation at high temperature [17]. However, nanostructured coatings exhibit higher fracture toughness and, much probably, lower elastic modulus due to the presence of retained nanoparticles. These factors promote lower tendency to crack propagation and a better stresses accommodation during high temperature service, respectively. Nanostructured YSZ coatings show higher thermal shock resistance than the conventional ones, in terms of number of cycles to failure [18,19]. This enhancement can be associated to their high porosity. Indeed, the nanostructured areas embedded in coating microstructure retain the intrinsic porosity of the feedstock. It has been found that

nanostructured and conventional coatings approximately exhibit similar hardness. The bimodal microstructure of nanostructured coatings could or not could result in a bimodal distribution of the mechanical properties, depending on the melting degree of the agglomerated particles and on the indentation loads used during mechanical tests [13,20].

Long term exposures at temperatures higher than 1300 °C can promote the sintering of the porous microstructure and the growth of the grain size. Lima *et al.* [21] have recently reported that nanostructured coatings can be properly engineered to counteract the sintering effects, due to their bimodal microstructure characterized by areas with different sintering rate. The results reported in literature are preliminary and further investigations are needed, in order to achieve a good control on the spraying process and on the final properties of the nanostructured coatings.

Moreover, nanostructured alumina-titania coatings are promising candidates for anti-wear applications, due to their high abrasion and sliding wear resistance, substantially higher than those of the conventional ones [16]. The high wear resistance can be related to higher crack propagation resistance, since retained porous nanozones act as a barrier to crack propagation.

Nanostructured Tungsten Carbide-Cobalt coatings have been also proposed for anti-wear applications, due to their high fracture toughness and wear resistance. They are commonly sprayed by VPS or HVOF, because Atmospheric.Plasma Spraying can yield to enhanced decarburization, thus resulting in lower wear resistance [22,23].

Due to their unique microstructure, nanostructured highly friable coatings can be fabricated by retaining a high content of nanostructured areas and, therefore, they are particularly promising as abradable coatings for high temperature applications in turbine engines.

Again, the distribution and the amount of the nanostructured areas within the coating microstructure can also favour the bioactivity level of biomedical coatings via biomimetism.

1.4 Thermal Spraying Equipments for Coatings Fabrication

As reported, Thermal Spraying is widely used in many industrial fields for several applications. Thermally sprayed coatings may be developed and fabricated by means of different Thermal Spraying processes. In the current work, the attention will be mainly focused on TBCs, and thus other alternative techniques for coatings deposition will be briefly mentioned in this section, such as Electron Beam Physical Vapour Deposition (EB-PVD) and Chemical Vapour Deposition (CVD). It should be noted that these last technologies are usually used to apply thin coatings, whereas Thermal Spraying is more suitable for rapid deposition of thicker coatings on mechanical components with complex shape and large size. The thickness can approximately vary from tens of micrometers to some millimeters.

Thermal Spraying has been widely used since 1960s to fabricate TBCs on combustion chamber components. Thermal Spraying is an easy and cost effective process to fabricate coatings of a wide variety of materials without producing high thermal distortion of the underlying substrate and without changing the mechanical properties of its original surface.

Many different thermal spraying equipments are commercially available, such as Flame Spray, Electric Arc Spray and Plasma Spraying, depending on the heat source, input energy, feedstock type (powder, wire or rod) and spraying environment. Each process possesses its own characteristics and can be addressed to well-determined industrial applications, since it yields to different materials as well as microstructures tailored for particular operating conditions.

1.4.1 Flame Spraying Process

Flame Spray includes Flame Spray, Wire Flame, High Velocity Oxy-Fuel (HVOF) and Detonation Gun (D-Gun). Flame Spray and Wire Flame are similar and only differ in the starting material they are able to process, *i.e.* powders or wires.

In Wire Flame, an oxy-fuel flame is employed as heat source in order to melt the starting material. As illustrated in Figure 1.4, the wire is axially introduced through the rear of the nozzle into the flame at the nozzle exit, atomized by an expanding air stream and propelled toward the substrate. Fuel-oxygen ratio and total gas flow rate have to be adjusted to achieve the desired thermal energy level. This adjustment allows to make the flame either oxidizing or reducing, depending on the feedstock material to be processed. Low melting point feedstock materials, such as some metals and polymers, can be sprayed by using this equipment. Wire Flame is a cheap system, which achieves moderate deposition rates. Howewer, both low particle velocities, typically less than 200 m/s, and low temperatures result in coatings characterized by relatively low bond strength and high porosity [1].

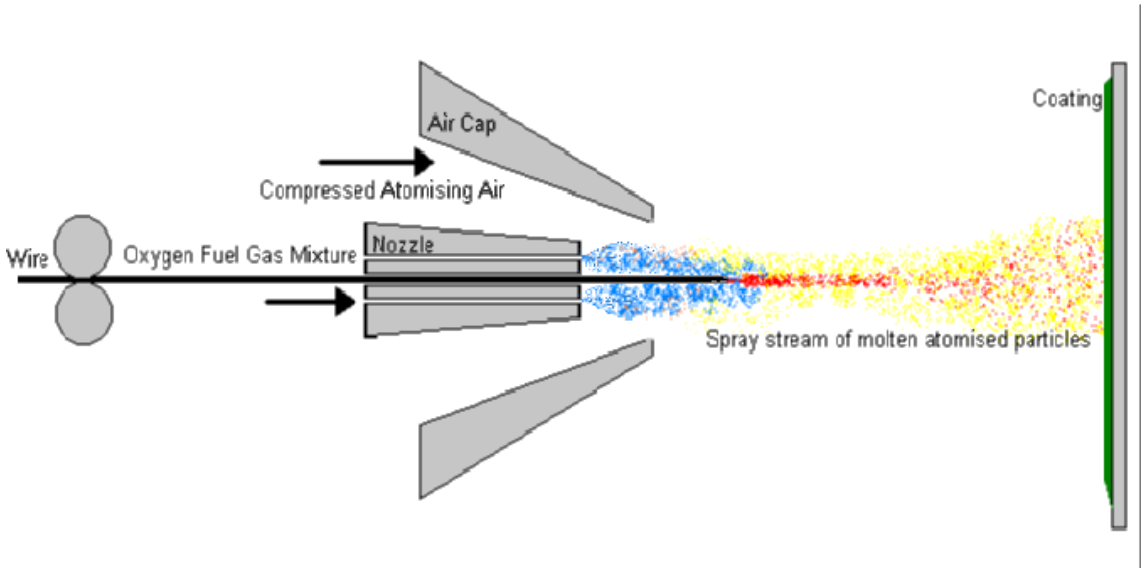

Figure 1.4 – Wire Flame Spraying.

HVOF (High Velocity Oxy Fuel) was invented in 1958 by Union Carbide (Praxair Surface Technologies, Inc.). However, it became available and commercially significant only in 1980s. An oxy-fuel burner with an advanced nozzle design technology is used to accellerate the gas-particle stream in order to achieve a particle velocity around 600 m/s. An internal

combustion jet is generated by reaction between oxygen and a gas fuel at temperatures from 2500 to 3000 °C. Propylene, propane or hydrogen are currently used as gas fuels. The combustion occurs inside a high pressure chamber, where a supersonic flame gas stream of approximately 2000 m/s is generated through a confined cooled convergent-divergent nozzle. As schematized in Figure 1.5, the powder particles are injected into the gas jet and here heated and propelled toward the substrate [1].

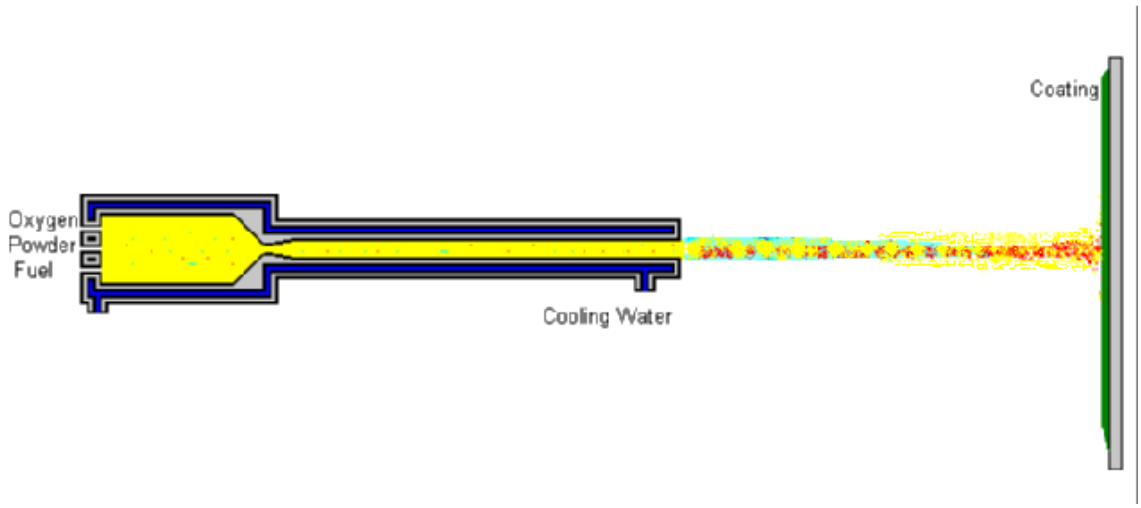

Figure 1.5 – High Velocity Oxygen Fuel (HVOF) Spraying.

HVOF coatings typically show high bond strength and high density, since their porosity can result less than 1%. The system allows to obtain higher particle velocity and lower particle temperature those achieved in common plasma spraying, thus providing lower particle overheating and preventing increased oxidation or decarburization, which can take place during spraying of metal and cermet particles, respectively. Thereby, denser coatings can be easily manufactured. The noise levels are very high (>130 db) and the deposition rates are moderate. The system is not appropriate to deposit ceramic coatings for TBCs. On the contrary, coatings with reduced porosity are desiderable for anti-wear and anti-corrosion

applications. Compared to Flame Spray, higher enthalpy of HVOF results in higher thermal stresses and higher oxidation of gun components, combustion chamber and nozzle.

Detonation Gun produces high thermal and kinetic energy jets, by confining the combustion between oxygen and fuel (acetylene) within a barrel, as illustrated in Figure 1.6. A spark plug is used for the ignition of the gas mixture, producing a controlled explosion that propagates down the length of the barrel where the powder particles are injected [1]. High temperature and pressure are used to melt and accelerate the powder particles, giving them high speed and kinetic energy, thus resulting in denser and harder coatings characterized by low oxidation level and enhanced wear resistance. Nitrogen is used to purge the barrel, between successive detonations. The cycle of purging, injection and detonation is repeated at the frequency from 3 to 6 Hz.

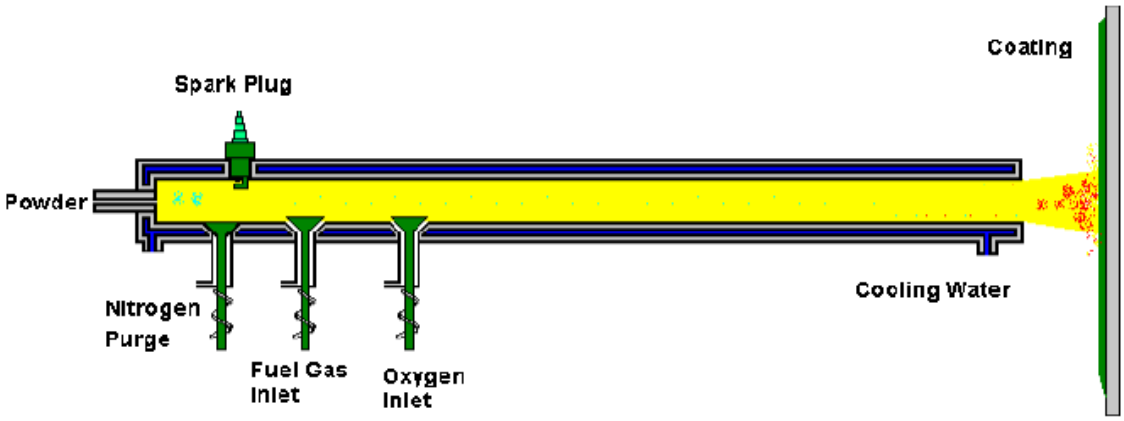

Figure 1.6 - Detonation Gun Sparying.

The frequency and noise levels (145 dB) associated to detonation spraying require that this equipment has to be confined through acoustical enclosures. Detonation gun is particularly used to spray carbide coatings, due to the reducing atmosphere of the confined combustion

zone in the barrel and due to the shorter dwell time of the sprayed particles in the hottest flame zone.

HVOF is similar to Detonation Gun. Indeed it has an extended internal-confined combustion chamber. Unlike Detonation Gun, HVOF operates on a continuous steady-state basis.

1.4.2 Wire Arc Spraying Process

It was developed by M.Schoop in 1910, but the process did not gain wide commercial acceptance until the early 1960s.

As shown in Figure 1.7, two consumable metal wire electrodes connected to a high direct-current power source are fed into the gun and meet, establishing an electric arc in the gap between the wire tips as the wire tips are continuously fed together. The wires are melted directly by the arc, so the thermal efficiency and the deposition rate are noticeably higher than those of other thermal spraying processes. A high velocity air jet located behind the intersection of the wires shears away the molten metal that continuously forms as the wires are fed into the arc and melted. The air jet atomizes the material into fine droplets which are propelled toward the substrate, where they impact, flatten and solidify [1]. It should be noted that the droplets are already molten when the material is picked up and entrained in the jet and, unlike other Thermal Spraying processes, the particles begin to cool after leaving the arc region. The substrate heating is rather limited and, therefore, the process is much suitable to deposit coatings on low melting point substrates, such as polymers and glasses. Short distances and high air flows have to be used to reduce the in-flight oxidation of the sprayed particles. Alternatively, an inert gas may be used. Wire Arc Spray is often limited to conductive materials that may be formed into wires. It is more appropriate for the deposition of any typologies of metal coatings, such as aluminium, copper, steel and zinc, used for protection of building structures from atmospheric or sea-water corrosion.

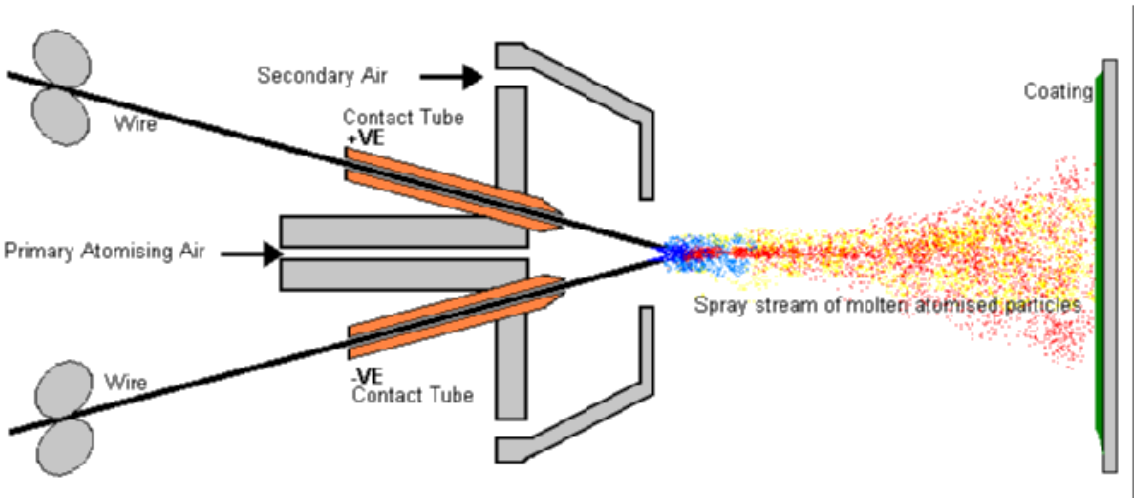

Figure 1.7 – Wire Arc Spraying.

1.4.3 Plasma Spraying Process

Plasma Spraying include Atmospheric Plasma Spraying (APS), Vacuum Plasma Spraying (VPS) and Radio-Frequency Plasma Spraying, which yield to coatings characterized by different microstructure and functional properties.

The plasma is produced by transferring energy into an inert gas until the energy level is sufficient to ionize the gas, allowing the electrons and ions to act independently of one another. The plasma state is achieved when, under an electric field, arc current can be sustained as the free electrons move through the ionized gas. Once the energy input is removed, the electrons and the ions recombine, releasing heat energy. This process, illustrated in Figure 1.8, is accompanied by high enthalpy. In direct current plasma arc spray, the plasma gun combines an axially aligned thoriated tungsten cathode and a water-cooled copper anode-nozzle, which constricts and spatially stabilizes the arc and accelerates the expanding super-heated gases at temperature up to 12000 °C. The cathode relies on conduction and the high melting point of tungsten to survive the high-temperature arc. Water cooling prevents melting and minimizes cathode and nozzle erosion. Plasma forming gas mixture is introduced through

the gun and enters the arc chamber through a gas injector that imparts a spin or vortex flow. The vortex stabilizes the arc at the cathode tip in the low-pressure region of the vortex and rotates the arc root at the anode. The arc gases are re-heated as they pass around and through the arc. Then they expand radially and axially, accelerating as they expand and exit through the nozzle. The powder particles are fed by an inert gas and injected by an external injector in the plasma jet. The hot gas jet entrains the powder particles which are heated to molten or semimolten state and accellerated toward the substrate. When they impact the substrate, they are flattened and form splats which solidify at high cooling rate and thus produce the build up of a coating with lamellar structure. Within lamellae columnar grains can be detected, typically smaller than those commonly observed in EB-PVD coatings. Coarser particles, especially for high melting point materials, can be partially melted, whereas very small particles, characterized by much lower momentum, can not penetrate the jet.

The substrate temperature can be controlled by optimizing the plasma temperature and enthalpy and by arranging an appropriate cooling system. When metal powders have to be processed, an inert gas shrouding may be also used to provide an inert atmosphere surrounding the jet at the exit of the gun and to reduce the interaction between the plasma jet and the air environment, and thus the oxidation of in-flight droplet surface. Both temperature and velocity of the sprayed particles, as well as the stand-off distance between the plasma torch and the substrate, can influence the level of oxidation.

High-melting point materials can be deposited at relatively high velocity (200-400 m/s), leading to coatings with good bonding strength [1].

Plasma spraying is suitable to spray less or more dense coatings, by modifying particle temperature and velocity. Plasma spraying may be arranged and optimized for fabrication of coatings with high porosity and, consequently, high strain tolerance and low thermal conductivity with respect to EB-PVD coatings. The thermal conductivity is strongly related to

both intrinsic porosity and thermal conductivity of the starting powder, depending on the chemical composition, and to the main microstructural features of as-sprayed coatings, such as pores and microcracks, which act as a barrier against the heat transfer through the coating thickness.

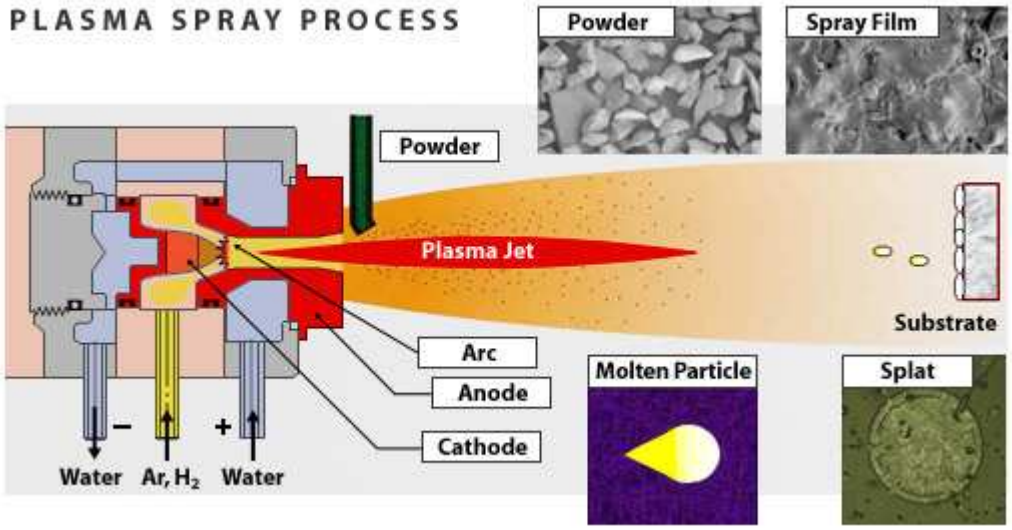

Figure 1.8 – Mechanism of coating formation in Atmospheric Plasma Spraying.

From 1960s to 1980s high attention has been focused on the development of spraying systems operating in controlled atmosphere, in the purpose to minimize the detrimental effects of oxidation and decarburization occurring during thermal spraying of metals and cermets, respectively.

VPS or LPPS (Vacuum Plasma Spraying or Low-Pressure Plasma Spraying) was introduced in 1974. Unlike most common plasma spraying processes, this process uses a modified plasma torch which operates in a chamber at low pressure in the range between 0.1 and 0.5 atm, involving an increased plasma expansion. Therefore, the plasma jet is broader and extended than in air plasma spray, resulting in a large and uniform spray pattern. The use of a convergent-divergent nozzle provides higher gas velocity [1]. Higher particle speed implies shorter residence time of the sprayed particles in the plasma jet and, together to better plasma

jet insulation from surrounding environment, reduces the effect of oxidation of metal particles in comparison with atmospheric plasma spraying. So, denser coatings can be fabricated, characterized by lower content of oxides and higher cohesive strenght. The residual stresses are also lower than in atmospheric plasma spraying, and a higher substrate preheating capability is obtained. Oxygen contamination can not be totally avoided, even if the oxygen content is more related to surface oxides on the powder particles than to the partial pressure of oxygen in the low-pressure environment of the chamber. The oxidation can be further reduced by spraying larger particles, since larger size implies a reduced surface-area-to-volume ratio. VPS process is less indicated for spraying of ceramic powders, due to their shorter dwell time and less degradation than in atmospheric plasma spraying. To this purpose, ceramic feedstocks with smaller particles should be manufactured and this would be very expensive. VPS system is more expensive, less versatile and efficient than APS and, thus, it is recommended only when the benefits in coating performance outweight the price disadvantage. Therefore, in the last years alternative more cost-effective systems have been employed. As an example, an inert-chamber plasma spray has been proposed in order to combine many of the benefits of APS and VPS, by using an inert gas environment at atmospheric pressure.

Radiofrequency (RF) Plasma Spray is an other plasma spraying system. It has been commercially available since the 1960s, but did not see much commercial exposure until the 1990s. RF torch uses an induction coil to produce an oscillating RF field in the range from 450 kHz to 4 MHz in a reactor tube, which couples to and inductively heats the plasma arc gas stream. The RF energy initially creates a glow discharge within the coil, which quickly cascades to an elongated toroidal electrodeless arc-type discharge. The arc is confined by a water-cooled quartz reactor. Arc gas or gas mixture are fed into the reactor to create a discharge that does not touch the quartz tube. The RF field and boundary layer also help to

keep the arc from contacting and melting the quartz. Water-cooled powder injector tubes are required to penetrate the plasma wall, because powder particles do not have enough inertia to penetrate the plasma [1]. Once injected, the particles are heated in the plasma jet and propelled toward the exit. This equipment is more suitable to melt coarser particle in atmospheric environment by means of higher dwell times.

1.4.4 Cold Spraying Process

The cold spraying system has been developed and patented in 1990s by Alkimov *et al.* [24,25,26]. This process shows unique characteristics and it can be explained as follows. The process gas is introduced in a manifold system containing a gas heater and a powder feeder, as shown in Figure 1.9.

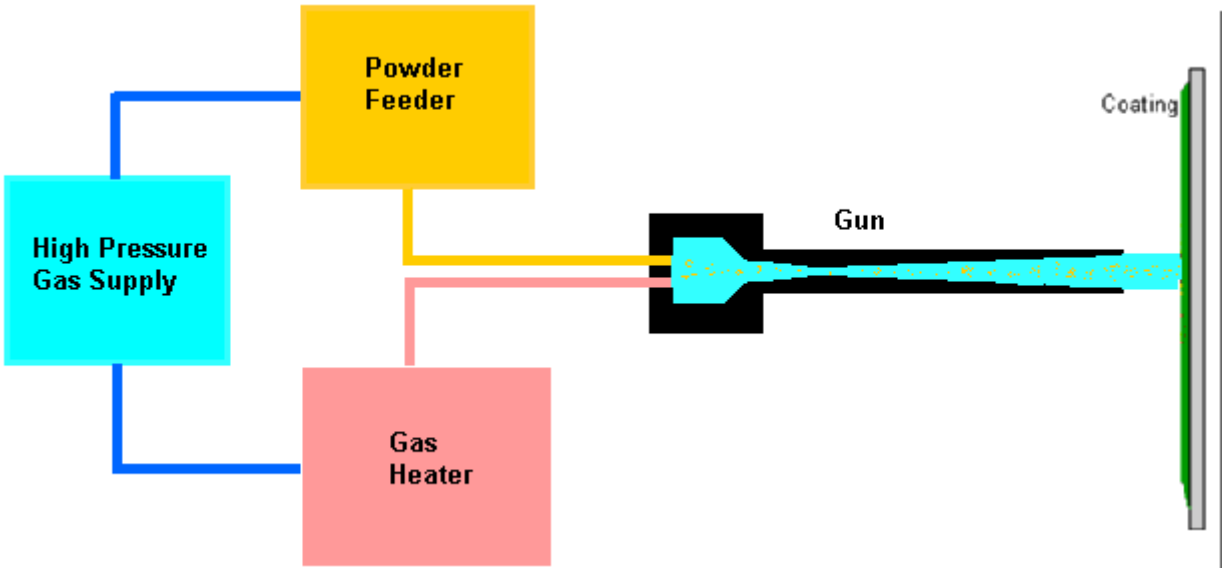

Figure 1.9 – Cold Spraying Process.

The pressurized gas is heated to a given temperature, typically up to 700 °C, by using a coil of an electrically resistance-heated tube. The gas heating is addressed to produce a higher sonic flow speed. The high pressure gas is introduced into a converging-diverging nozzle, where it

is firstly accellerated to supersonic speed and then it expands. The gas cools as it expands in the spray nozzle and, consequently, its temperature at the exit of the spray gun is usually below ambient temperature. The powder particles are introduced into the high-pressure side of the nozzle and accelerated to high speed, ranging from 30 to 1200 m/s. More recently, a downstream injection has been also employed [27].

Both gas and particles temperatures are much lower than those achieved in other thermal spraying processes. As a consequence, some detrimental effects, such as high temperature particle oxidation and evaporation are rather minimized, as well as the amount of the residual stresses in the as-sprayed coatings.

Cold spraying is a technology developed for particular applications and mainly for spraying of high purity materials, such as pure metals, cermets and composites. Cold sprayed coatings show properties strongly dependent on feedstock properties and commonly possess low ductility.

1.4.5 Other Techniques for Coatings Deposition

Electron Beam Physical Vapour Deposition (EB-PVD) has been used starting from 1980s. It is particularly suitable for deposition of TBCs on rotating components of aircraft engines as high pressure turbine blades. The coating surface is smooth and has not to be polished before its use, unlike plasma sprayed coatings. EB-PVD TBCs show a columnar structure with high strain tolerance, thermal shock resistance and high lifetime under thermal cycling [28].

In EB-PVD process, a ceramic source ingot is melted and evaporated in a vacuum chamber at pressure in the range from 13.33 to 1.33 $x10^{-6}$ Pa, by a high energy electron beam, as illustrated in Figure 1.10. The ingot is bottom-fed into the crucible to ensure continuous growth of the coating. The metal substrates are pre-heated and positioned in the vapour cloud. The evaporated atoms undergo an essentially collisionless line-of-sight transport prior to

condensing on the surface of the substrate. The rates of evaporation and deposition are influenced by vapour pressure of the starting material and the ambient pressure.

EB-PVD process shows any shortcomings in comparison with Plasma Spraying. Firstly, lower deposition rate yields to much smaller coating thickness. Especially for very thick coatings, the operating times can be much higher than in Plasma Spraying and, subsequentely, the cost of manufacturing may become very high. In addition, some large components with complicated shape and geometry, such as blades and vanes of stationary turbines, can not be coated due to the limited dimension of the vacuum chamber. Deep holes and bores can not easily be coated. The current researches are focused to optimize the processing and to outweight the actual and technical limitations. Plasma Spraying is a more reliable and cost-effective technique for a lot of industrial applications. Recently, other alternative processes have been proposed, such as Chemical Vapour Deposition and Slurry-Coating.

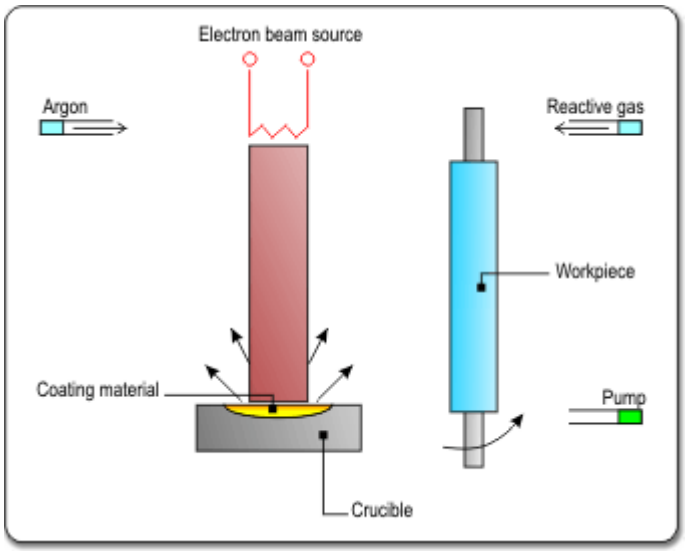

Figure 1.10 – EB-PVD process.

Chemical Vapour Deposition (CVD) is a high temperature process (1000 °C) used to deposit coatings with high density, uniformity and high bonding strength, since the bonding is guaranteed by the diffusion of coating material to the substrate and the interfacial stresses are

very low. Inside a vacuum chamber a gaseous precursor is thermally decomposed and its reaction at the substrate surface forms a coating. The high temperature implies any limitations regarding the substrate material. Complicated geometries can be coated, because the process is omni-directional.

Otherwise, Plasma Enhanced Chemical Vapour Deposition (PECVD) uses a plasma which decomposes the gas at low temperature.

Finally, Chemical Formed Processes (CFP) allow the deposition of coatings up to 100 μm. The substrate is covered by precursor material before heating to temperature between 350 °C and 600 °C, at which the desired chemical reaction takes place and thus a thin coating is formed. The coatings are chemically bonded to the substrate and, as they are fully dense, are particularly suitable for anti-corrosion applications.

1.5 Plasma Spraying Processing and Coatings Microstructure

As previously explained, in Plasma Spraying, the powder particles are heated up above their melting point and melted by a plasma jet. The resulting molten droplets are accelerated toward the substrate in a hot gas stream. They impact the substrate with high temperature and kinetic energy. On impact their flattening produces the formation of splats which adhere to the substrate and rapidly solidify at room temperature, promoting the build-up of a uniform coating characterized by lamellar structure with thin layers or lamellae parallel to the coating-substrate interface. The high solidification rates often promote the retention of high-temperature non equilibrium phases at room temperature, such as amorphous or metastable phases, resulting in anisotropic structures, as schematized in Figure 11. Thermally sprayed coatings show a unique microstructure and typical microstructural defects, such as pores with different shape and size, interlamellar or horizontal microcracks and vertical microcracks. Porosity can originate from entrapped unmelted or partially melted particles, voids not filled by the spreading particles, poor wetting onto adjacent splats, as well as by intrinsic porosity, size and morphology of the feedstock particles. Indeed, the molten splats, when impact the substrate, are flattened and spread over and fill the underlying interstices. The anisotropic features are also related to the degree of melting, determined by the temperature distribution in the plasma jet. The melting degree influences the cohesive strength, the porosity fraction and all the coating properties.

Indeed, the temperature typically decreases from the centre to the periphery of the plasma jet. In a few millimeters a gradient of several thousands of degrees may be appreciated and may affect both gas velocity and viscosity values.

As general remark, the powder particles injected at the inner side of the plasma jet are heated at higher temperature and totally melted, whereas the powder particles injected at the periphery are only partially melted or sometimes remain unmelted, thus generating large pores

in the coating or remaining trapped as unmelted particles. Moreover, some particles could be superheated and other molten particles could resolidified during their flight before impacting the substrate, thus reducing the cohesive strenght between the deposited splats.

Interlamellar cracks, perpendicular to the spraying direction, are produced by rapid cooling and thus affect the cohesive strenght between the lamellae. Vertical microcracks are formed due to solidification, thermal stresses and relaxation of tensile quenching stresses.

The rapid solidification generates residual stresses and their progressive accumulation can promote a spontaneous coating debonding during cooling to room temperature. This phenomenon is more probable when a very thick coating is deposited on metal substrate and can be ascribed to the different thermal expansion coefficients between the same coating and the substrate.

Increased porosity is recommended in coatings for high-temperature applications, because it provides higher strain tolerance, higher thermal shock and thermal cycling resistance. Porosity is also desired for medical implant prostheses, because it allows bone tissue to grow into the coating, accelerating patients healing and reducing their recovery time. On the other hand, denser coatings are more appropriate for enhanced wear and corrosion resistance.

During spraying of metal particles, the interaction between the outer particle surface and the oxygen in atmosphere can promote increased oxidation. High temperature and long dwell times are able to enhance this effect. As a consequence, metal oxides can clearly appear as elongated dark stringers within the coating microstructure, as schematized in Figure 1.11. These phases reveal to be very hard and also very brittle, so they can influence the cohesive strenght and anti-wear properties of the coating. The degree of oxidation depends on the spraying parameters and on the spraying environment. Indeed, it is generally increased in Atmospheric Plasma Spraying and more contained in Vacuum Plasma Spraying and High Velocity Oxy Fuel Spraying. In HVOF spraying process the powder particles are

characterized by lower temperature and higher speed than those experienced in Air Plasma Spraying. However, by optimizing the spraying parameters and, in particular, the plasma gas mixture and the total gas flow rate, results comparable to those obtained by VPS or HVOF may be achieved. Oxidation can be controlled by reducing the temperature of the sprayed particles, by increasing their speed, by using a shroud gas, by reducing stand-off distance, by using feedstocks composed by coarse particles or by reducing the temperature at the interface between substrate and coating.

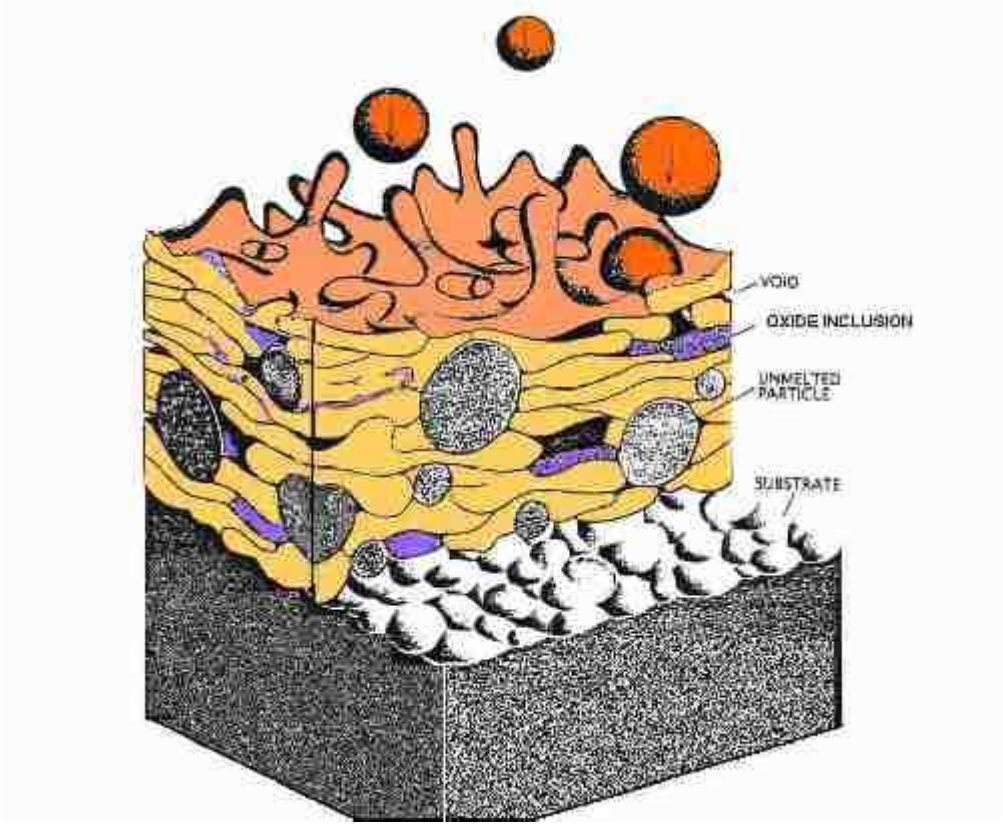

Figure 1.11 – Microstructure of plasma sprayed coating.

Therefore, the most significant spraying parameters can be adjusted to obtain a well-known microstructure and to guarantee the reproducibility of coatings properties. This last is a basic requirement in the purpose to transfer the most promising results of experimental researches to the real applications. To this aim, ceramic coatings require a statistical approach in the

evaluation of the experimental data, because their anisotropic features can determine a large scatter in their thermo-mechanical properties.

Plasma Spraying parameters include torch type and diameter nozzle, arc current intensity, plasma power, process gas or gas mixture, process gas flow rate, carrier gas flow rate, standoff distance between torch and substrate, powder injector diameter, powder feed rate and traverse speed.

These parameters can determine the coating properties as follows.

As arc current increases as plasma power increases and correspondingly the temperature and the velocity of the sprayed particles, promoting better bonding between the deposited splats, as well as lower porosity volume. Oxidation is favoured by high plasma temperature and enthalpy. An increase in total gas flow rate yields to an increase in accelleration of powder particles and in their kinetic energy. At the same time the temperature of the particles slightly decreases. High gas flow rate may be used to increase the momentum of the sprayed particles and to protect their surface from oxidation. Argon is usually used as pure process gas or in mixture with Hydrogen and/or Helium. Pure Argon generates a relatively low-energy plasma. Hydrogen provides high energy and enthalpy, increasing the temperature of the sprayed particles. Helium increases the thermal conductivity of the plasma stream at temperature over 10000 °C, increasing plasma heating capability.

Helium is able to better entrain particles core, especially for metal and carbide particles characterized by intrinsic porosity, reducing the entry of oxygen and the effect of oxidation within the plasma core. However, pure Helium possesses small mass flow and, thus, imparts lower momentum to the sprayed particles. Therefore, it is commonly used as secondary gas, in conjunction with Argon.

As spray distance increases as the interaction between the droplets and the surrounding atmosphere increases. The particles impact the substrate at lower temperature and speed, generally producing lower bonding and higher porosity.

Injector diameter and carrier gas flow rate influence the powder feed rate which has to be set in order to provide a good melting of the sprayed particles and control the final microstructure (thickness and uniformity).

Also the substrate temperature should be monitored and controlled to avoid substrate degradation and other problems associated to possible coating debonding. If necessary, the substrates may be cooled by using air cooling jets.

The process parameters affect deposition efficiency (DE), which measures the percentage of particles injected in the plasma jet that are deposited on the substrate. The process parameters have to be choosen to provide high deposition efficiency, because low efficiency increases the operating times and accordingly the cost of manufacturing.

Feedstock properties can also play an important role on the final microstructure. They include particles size, defined by the upper and lower limits of the powder size distribution, their shape and morphology (angular, rounded, elliptical, equiaxed, hollow spherical), their size distribution in terms of average and skew, their method of manufacturing and, finally, their intrinsic porosity, which influences their interaction with the plasma gas stream. The spherical particles commonly show higher flowability and are affected by lower in-flight oxidation due to their lower surface area to volume ratio.

In order to fabricate high quality coatings, several steps have to be observed.

The substrates have to be properly prepared, cleaned to remove any contaminants and degreased. Then, they are grit blasted to give them a rough surface for mechanical interlocking with the coating. Dry alumina abrasive angular particles are commonly used for steel and Ni-superalloys. These particles are propelled toward the substrate at high velocity,

where they induce a plastic deformation of the surface, producing visible asperities. This deformation is a function of the angularity, size and hardness of the particles.

Ultrasonic cleaning is then performed in order to eliminate further contaminants, as residual entrapped grit after grit blasting in confined or hidden areas. All these last steps have to be carefully followed to provide better adhesion between the substrate and the sprayed particles, *i.e.* better metallurgical interaction, increased surface area for contact, better mechanical interlocking and lower in-plane stresses by inducing folds in the coating.

Preheating can be carried out to heat substrate surface and, consequently, to allow its pre-expanding so that it shrinks with the coating, reducing the residual stresses generated during fast cooling. However, preheating can determine the formation of an oxide film on metal substrates which can degrade at relatively low temperature.

The application of a bond coat is recommended before TBC deposition. This metal coating is often self-bonding. It adheres to the surface by reacting with the substrate to form microscopic alloy layers. This adhesion differs from mechanical interlocking promoted by grit blasting. However, it may be enhanced by a finely grit blasting or a preheating. At higher temperatures, a solid state diffusion may also occur.

It should be noted that Plasma Spray coated components are usually ground and polished to remove surface roughness before they are put into service.

1.6 Thermal Barrier Coatings

In section 1.3.1, some details have been reported about typical industrial applications of thermally sprayed coatings as thermal barrier coatings in hot components of gas turbine and diesel engines. Now, the attention will be focused on the study of advanced materials, as well as on the processing, characterization and testing of thermal barrier coatings. Firstly, it is useful to make some considerations about the failure mechanism of a TBC during service. These consideration are fundamental for the development of high-performance TBCs and the development of useful prediction models.

1.6.1 Failure Mechanism of Thermal Barrier Coatings

The failure of a TBC is produced by cracking and delamination, as it has been deduced by analyzing the components removed from the engines. Small cracks extend and coalesce along the delamination planes located either within the TBC or at the interface between the thermally grown oxide (TGO) and the bond coat, producing the spallation of small or large coating fractions. This mechanism is associated to the high-temperature development and evolution of residual stresses in the tri-layered system composed by ceramic top coat, metal bond coat and substrate. The interaction between substrate, bond coat and top coat has to be carefully investigated. Indeed, these layers are notoriously characterized by different thermal expansion coefficients. In order to develop reliable prediction models, it is fundamental to study the complex damaging mechanism of TBCs during their service and under a wide variety of operating conditions. According to Clarke *et al.* [29] a prevailing failure mechanism is characterized by buckling nucleated from the edge of the sample, followed by spallation. This failure mode is associated to the presence of compressive stresses arisen from different CTEs of coating and substrate. To this purpose, they describe the effect based on the interfacial cracking. The failure of a TBC usually depends on several factors, such as phase

stability, microstructural changes induced by high-temperature sintering, bond coat oxidation, evolution of the residual stresses and strain accumulation by cycling and hot corrosion.

All these aspects have to be carefully considered and investigated in order to manufacture TBCs with high performance and, thus, to transfer the achieved knowledge to the industrial field.

Actually, the full potential of TBCs is not well-known and further researches are addressed to the development of new advanced materials, synthesis techniques and new designs. The future researches have to be addressed to develop reliable models for lifetime prediction, innovative techniques for monitoring during service and validation of experimental results under various operating conditions. Indeed, TBCs have not often considered as integrated parts of hot components, but appear as potential solutions to reduce their surface temperature and to improve their durability. The demand for high performance implies a change in current opinion and new concepts regarding the potentiality of thermal barrier coatings.

The influence of the process parameters on the microstructural and thermo-mechanical properties of plsma sprayed coatings should be properly analyzed , in order to promote a significant enhancement in the reliability, lifetime and performance of thermally sprayed TBCs and to overcome the current limitations [30].

Phase transformations, occurring at high temperature, can generate significant stresses within the coating, the growth and propagation of cracks. As an example, plasma sprayed YSZ coatings are mainly composed of metastable t’ zirconia phase, due to the high cooling rate of molten splats during deposition. It has been found that during coatings annealing at temperature higher than 1200 °C, the metastable t’ phase decomposes into tetragonal t and cubic c phases. Then, on slow cooling to room temperature, the low-yttria tetragonal phase may transform to the monoclinic phase, whereas the high-yttria cubic phase may be retained or it may transform to tetragonal phase. Monoclinic transformation is notoriously

accompanied by a volume change which promotes the appearance of crack networks. The amount of these microstructural defects can influence the high-temperature lifetime of the coating.

Moreover, high-temperature sintering produces of the porous coating produces significant changes in microstructure and mechanical properties, *i.e.* the closure of fine pores and microcracks with a consequent partial densification of the porous structure. The crack morphology changes and between adjacent crack edges sintering necks are formed, thus partially or completely closing pores and microcracks. This yields to the reduction of the porosity volume and to an increase of the elastic modulus, reducing the strain tolerance and increasing the amount of the stresses in the coatings [31]. Therefore, the sintering behaviour affects the durability of TBCs during thermal cycling. Different powder morphologies can produce different microstructures with different thermo-mechanical behaviour and different sintering rate during long-term exposures. Moreover, the sintering rate is strongly related to the operating temperature and is affected by the TBC design. A significant difference has been found between annealed free-standing ceramic coatings and multilayered TBCs, constituted by substrate, bond coat and top coat, due to the different stress state within the coatings [32]. For the entire TBC system, the sintering of the ceramic coating increases the residual stress level and the driving force for debonding at the interface with the metal bond coat and thus promotes the spallation. The presence of the metallic substrate can reduce the stiffening rate of the ceramic layer and the sintering rate. The higher CTE of the substrate generates tensile stresses in the coating during high-temperature exposure and acts as a barrier for the healing of pores and finer microcracks [32].

During processing, and more probably during high-temperature service exposures, a thin thermally grown oxide (TGO) layer is produced by surface oxidation at the interface between bond coat and top coat. Most ceramic materials for TBCs are transparent to the oxygen, as

well as stabilized zirconia. Indeed, these materials show a high amount of oxygen ion vacancies which allow oxygen transport and propagation through coating thickness. At high temperature, O^{2-} ions diffuse in the coating through its open pores and are transported through the pores and cracks of the ceramic layer, promoting the oxidation of the bond coat surface and the formation of the TGO.

A TGO composed of pure Al_2O_3 thin layer might improve the in-service duration of a TBC by improving the thermal insulation between upper ceramic top coat and metal bond coat. This enhancement may be related to the chemical compatibility between the TGO and bond coat materials. Unfortunately, the TGO thickness evolves during long-term exposure at high temperature and increases up to a critical value, producing significant compressive stresses at the interface. These last ones, together to the residual stresses generated by different CTE values, are responsible for the strain energy release rate, *i.e.* global driving force. When this last becomes higher than the fracture energy at the interface, a spontaneous debonding of the ceramic layer occurs, followed by the final spallation [33]. Therefore, spallation is affected by the changes in the stress state and by the reduction of toughness at the interface.

TGO thickness has to be related to operating temperatures and times, in order to investigate the adhesion degree and to predict the spallation and the failure of the TBC. The formation and the evolution of the TGO should be taken in great account to chose TBC material, focusing the attention on materials thermodynamically compatible with alumina. However, as above discussed, the failure of a TBC can not be only attributed to the formation and the evolution of TGO, because it depends on many intrinsic factors [29].

In addition, extended creep occurs in the bond coat at temperature of about 600 °C. The creep reduces tensile stress within the coating during heating and generates compressive stress during cooling.

The surface of the ceramic coating is also subjected to the action of hot gases, which can produce a gradual delamination of the coating, thus increasing the temperature on the metal substrate. During service, gas turbines are periodically started and stopped. The temperature gradients promote a redistribution of the internal stresses and induce thermo-mechanical fatigue and crack growth. In particular, the presence of tensile stresses can reduce the interfacial adhesion. The evolution of cracks (formation or closure) promotes significant change in elastic modulus values.

In addition, hot-corrosion usually characterizes land-based turbines, where low quality fuels are commonly used. The salts combine with fuel contaminants and impurities, such as Vanadium and Sulphur, producing mixtures of sodium sulfates and, mainly, vanadates with low melting points ($3SO_3$ and V_2O_5). It is known that these deposits react with Y_2O_3 contained in yttria partially stabilized zirconia. Some chemical reactions take place, promoting a significant reduction of yttria stabilizer content and destabilizing the tetragonal t' zirconia phase in monoclinic:

$$Y_2O_3 + 3SO_3 - Y_2 (SO_4)_3 \quad (1.1)$$

$$Y_2O_3 + V_2O_5 - 2YVO_4 \quad (1.2)$$

It has been found that ceria-yttria co-stabilized zirconia (CYSZ) coatings show better resistance to hot-corrosion. Also scandia (Sc_2O_3) stabilized zirconia coatings exhibit high resistance to hot corrosion from salts. Above the condensation point of salts (950 °C) the hot corrosion could not affect the hot surfaces. However, it could destabilize colder surfaces. In addition, other extrinsic factors, such as the erosion induced by impact of foreign particles or objects and the damage induced by penetration of deposits of calcium-magnesium-

aluminosilicates formed from the entrainment into the engine of sand and dust which are in atmosphere [34,35,36,37].

1.6.2 Current and New Materials for TBCs

The coating material is designed according to given in-service conditions and taking in a great account the expected life of the component.

1.6.2.1 Yttria Partially Stabilized Zirconia (YSZ) Coatings

Plasma sprayed yttria-stabilized zirconia coatings have been commonly used for protection of gas turbine engine components from many years. Their good thermo-physical and mechanical properties have been measured and can be here reported as follows: CTE = 10-11 10^{-6} K^{-1}; thermal conductivity <=2 $W*m^{-1*}K^{-1}$, fracture toughness 2 $MPa*m^{1/2}$.

However, YSZ coatings seem to be limited to “clean fuel” engines, because yttria stabilizer reacts with the contaminants contained in low-grade fuels which are commonly used in industrial turbine or diesel engines, as previously described. In this case, zirconia phase transformation may occur at relatively low temperatures, *i.e.* 700-900 °C. Indeed, the yttria stabilizer reacts with molten salts, which were penetrated through coating thickness, and the depletion of the stabilizer can promote the monoclinic transition and a significant cracking. The thermal shocks also produce the spallation of large fractions from coating surface up to final delamination.

As above reported, during exposure at high temperatures, significant microstructural changes may occur within the TBC. These modifications lead significant changes in the mechanical properties. Sintering causes an increase of the elastic modulus and, as a consequence, a lower strain tolerance [38]. YSZ thermal barrier coatings are characterized by insufficient phase stability and accelerated sintering during long-term exposures at temperatures higher than

1200 °C. Thereby, alternative materials or alternative stabilizers for zirconia have to be studied, in order to improve the durability of the TBCs and to develop TBCs with outstanding properties for advanced turbines of next generation.

Several ceramic materials showing interesting properties have been studied and proposed as alternatives to YSZ for TBCs development and manufacturing. They have typically one or two properties better than YSZ. However, some of these data are often referred to bulk materials and not to plasma sprayed coatings. To this purpose, it should be noted that YSZ has been studied and used for about 30 years. Both material composition and processing have been optimized. The corresponding properties have been investigated and the coatings have been tested at in-service conditions. However, further investigations are required in order to have a better knowledge of the YSZ TBCs performance at high temperature.

1.6.2.2 Ceria-Yttria co-Stabilized Zirconia (CYSZ) Coatings

Rare earth oxides can be used as stabilizers (CeO_2, Gd_2O_3, Sc_2O_3, Ta_2O_5) for tetragonal or cubic zirconia [39,40,41,42]. Rare earth oxides have lower thermal conductivity and higher CTE than yttria partially stabilized zirconia coatings. However, the experiments about these materials are rare. It should be noted that most pure rare earth oxides are unstable at high temperature, due to their polymorphism, and this would be detrimental for their thermo-mechanical behaviour.

Cerium oxide (CeO_2) represents an interesting alternative as stabilizer for tetragonal zirconia. Ceria and yttria co-stabilized zirconia coatings are more suitable when severe in-service conditions are expected, since they seem to show lower thermal conductivity at room temperature than YSZ [43]. CYSZ deposits show higher phase stability, higher resistance to thermal cycling and higher lifetime during long-term exposures than YSZ ones [38]. A comparison between YSZ and CYSZ has been performed by Moon *et al.* [44] in their

experimental studies. Free-standing coatings were heated at high temperature for 100 h and then cooled to room temperature using different cooling rates. The monoclinic transformation was retarded or prevented for CYSZ TBCs with respect to YSZ TBCs.

Moreover, CYSZ shows higher resistance to hot-corrosion than YSZ in terms of much improved phase stability and reduced damage induced by the molten salts [45]. Ceria is a more acidic stabilizer and it is more resistant to chemical attacks by molten salts, since it possesses lower solubility than yttria. So, CYSZ is recommended when low quality fuels are used. Indeed, the condensation of sulfates and vanadates and their fused salts are extremely corrosive. The monoclinic transformation and the expansion of the damaged area are much retarded. The stabilizer depletion behaviours of YSZ and CYSZ are quite different [45]. The structural defects, such as pores and microcracks, generate a path for penetration of molten salts. The reduction of the porosity might be useful to act as a barrier. However, a more dense TBC would have higher thermal conductivity and lower strain tolerance. Further researches about high-temperature behaviour of CYSZ TBCs are needed.

1.6.2.3 Alumina Coatings

Alumina (Al_2O_3) has been firstly used as TBC material, due to its interesting physical and mechanical properties. However, alumina shows higher thermal conductivity than YSZ and lower CTE. In addition, plasma spraying of alumina powder produces some unstable phases, such as γ-Al_2O_3 and δ-Al_2O_3, which during thermal cycling transform into α-Al_2O_3. This transition is accompanied by a volume change of about 15 %, resulting in the formation and propagation of cracks in the coating microstructure [46]. Alumina can be added to YSZ to enhance its hardness and thermal cycling lifetime [47]. Moreover, alumina may be partially stabilized in α-phase by addition of TiO_2, in order to improve its toughness. Anyway, plasma

sprayed pure alumina and alumina-titania coatings are more suitable for anti-wear coatings, due to their enhanced hardness and wear resistance.

1.6.2.4 Mullite Coatings

Plasma sprayed mullite ($3Al_2O_3$-$2SiO_2$) coatings typically show a part of amorphous structure. They exhibit high thermal stability, low thermal conductivity, but higher than YSZ, and interesting thermo-mechanical properties. They are not oxygen transparent and are suitable to be used in diesel engines, where there are lower temperatures than those experienced in gas turbines [48]. Indeed, at about 980 °C amorphous mullite crystallizes with a volume contraction which can promote the formation and the propagation of cracks. The amount and distribution of the microcracks can influence the lifetime of plasma sprayed mullite coatings during their service. At higher temperatures, their thermal shock resistance is less than YSZ [49]. Mullite coatings show a low CTE, very close to that of SiC-based composites. Thereby, they are particularly promising for protection of these composite materials as EBCs [50].

1.6.2.5 Lanthanum Zirconate (LZ) Coatings

Rare earth zirconates $M_2Zr_2O_7$ (M=La, Gd, Nd, Sm) have been recently proposed as materials for TBCs. Among these materials, lanthanum zirconate ($La_2Zr_2O_7$) is the most known. This is very significant, because a few works have been performed on these new materials. Lanthanum zirconate shows a cubic pyrochlore structure and promising thermal and physical properties. It shows no phase transitions up to the melting point (2300 °C). Previous studies have marked the thermal stability of plasma sprayed lanthanum zirconate coatings during long-term exposures at 1400 °C [51].

Moreover, lanthanum zirconate possesses lower thermal conductivity than YSZ (1.56 $W*m^{-1*}K^{-1}$ versus 2.1-2.2 $W*m^{-1*}K^{-1}$, bulk materials). For sintered materials the elastic modulus of LZ is lower than that of YSZ and so the fracture toughness [52]. Lanthanum zirconates has low ionic conductivity ($9.2 \pm 0.3 \times 10^{-4}\ \Omega^{-1}\ cm^{-1}$ at 1000 °C in air) and it is more oxygen resistant than YSZ which has higher ionic conductivity ($0.1\ \Omega^{-1}\ cm^{-1}$ at 1000 °C in air). Therefore, a better insulation against oxygen is expected, since the oxygen diffuses from the coating surface to the substrate through the pores and cracks and the crystal lattice of the coating material. However, the CTE measured for LZ coatings is lower than that reported for YSZ ones ($9.1\text{-}9.7*10^{-6}\ K^{-1}$ against $10.5\text{-}11.5*10^{-6}\ K^{-1}$), resulting in higher stresses in the TBC system. Lower lifetime has been found in comparison with YSZ coatings during thermal cycling at 1250 °C [51]. Some dopants, as cerium oxide, could be used with the purpose to increase the CTE value. Alternatively, lanthanum zirconate coatings can be used for protection of zirconia coatings at extreme temperatures, realizing a double ceramic coating, as discussed in the next sections. Indeed, lanthanum zirconate seems particularly suitable for extreme temperature applications. It is a candidate material for TBCs and EBCs for gas turbine ceramic matrix composite (CMC) combustor applications, due to its low thermal conductivity and high temperature capability. Looking at other not well-known zirconates, Maloney reports a thermal conductivity of about 1.3 $W*m^{-1}*K^{-1}$ (at 700 °C) for bulk $Gd_2Zr_2O_7$ and a temperature-indipendent thermal conductivity of about 1.0 $W*m^{-}1*K^{-1}$ for porous EB-PVD $Gd_2Zr_2O_7$ TBC.[53] Other results are reported in recent patents [54,55]. Further experimental studies are expected in the next years in order to better know the properties of these materials and to investigate their potentiality as thermal barrier coatings.

1.6.2.6 Other Ceramic Materials for Thermal Barrier Coatings

Looking at some recent preliminary studies, some materials seem to be promising for TBC manufacturing, even if there is a lack in the knowledge of their thermo-mechanical properties and then further investigations have to be performed. Among these materials Yttrium-Aluminium Garnet (YAG), having the chemical composition $Y_3Al_2(AlO_4)_3$, should be mentioned. It has been found that garnets show enhanced thermo-mechanical properties, high phase stability and low thermal conductivity. In addition, they are more resistant to oxygen and thus could be retard the TGO formation. However, they show lower thermal expansion coefficient (~$9*10^{-6}\,K^{-1}$) than YSZ [56,57].

Hexaaluminates could be other candidates for TBC applications. They possess a magnetoplumbite structure. Lanthanum aluminate ($LaMgAl_{11}O_{19}$) coatings has been recently studied. They show a large amount of amorphous phase associated to the thermal effects of plasma spraying, low thermal conductivity (in the range from 1.2 to 2.6 $Wm^{-1}K^{-1}$), high phase stability up to melting point (> 2000 °C) and lower CTE than YSZ (~$9*10^{-6}\,K^{-1}$) [57,58].

Some typologies of silicates, as $ZrSiO_4$, could be also included in the list of TBC materials. They are more resistant to the oxygen and other acidic contaminants and thus could be used as intermediate layer between metal bond coat and ceramic top coat, to prevent the formation and the rapid evolution of the TGO. Unfortunately, their CTE is much lower than those of bond coat and top coat materials. In addition, their thermal conductivity is higher than that of YSZ. During spraying, zircon decomposes at 1676 °C and the coatings are composed of a mixture of crystalline zirconia and amorphous silica.

Other compositions include NZP materials ($Ba_{1.25}Zr_4P_{5.5}Si_{0.5}O_{24}$), Spinell ($MgAl_2O_4$), Perovskites ($BaZrO_3$) and Metal-Glass composites. Among them, despite their low sintering rate, perovskite coatings show lower CTE and shorter lifetime than YSZ ones, as well as partial dissolution in HCl [52,57]. Finally, Metal-Glass composites can be fabricated by a co-

deposition of metal and glass raw materials. They seem to show higher thermal conductivity and higher CTE than YSZ ones, as well as higher thermal cycling lifetime and higher resistance to oxidation and corrosion [57]. It should be noted that the results concerning the above mentioned materials are partial and not conclusive. A few reports have been published about them and further experimental studies are then required. In addition, many of these materials are not commercially available as thermal spray powders. Powders with these chemical compositions are often produced in little quantity in research laboratories and then they can differ about their morphology and other intrinsic properties.

1.7 Characterization and Testing

Thermal sprayed barrier coatings have to be characterized about their phase composition, microstructure, mechanical properties, hardness and high temperature behaviour.

1.7.1 Phase Analysis

XRD analysis may be performed on the as-sprayed samples without any preparation, in order to determine the phase composition, since the thermal effects related to plasma processing may involve some modifications in phase composition of the powder feedstock. Thereby, it is fundamental to make a comparison between starting powders and final coatings. As an example, thermally sprayed metallic or cermet powders suffer oxidation and decarburization, respectively, especially when plasma spraying is performed in air atmosphere. Therefore, several oxides and secondary phases, crystalline or amorphous, which were absent in the original feedstock, can be detected in as-sprayed coating. The phase composition of as-sprayed coatings may be a powerful tool to predict the durability of thermal barrier coatings during service. During high-temperature exposures, a high phase stability is required, since phase transformations may be detrimental for TBC lifetime.

During deposition of yttria-stabilized zirconia coatings, the high cooling rate of quenched molten particles can avoid the monoclinic transformation, producing a metastable tetragonal t' phase [5,59]. The same result has been found for EB-PVD YSZ coatings [60]. During high-temperature annealing, the metastable t' zirconia phase decomposes into tetragonal t and cubic c zirconia phases. Then, on slow cooling to room temperature, the low-yttria tetragonal phase may transform to the monoclinic phase, whereas the high-yttria cubic phase may be retained or it may transform to a high-yttria tetragonal t' phase. This behaviour has been found for YSZ coatings annealed at different temperatures (between 1200 °C and 1600 °C) and for different times [61]. A high cooling rate (> 50 $°C*s^{-1}$) avoids the monoclinic

transformation which is accompanied by high stresses and volume expansion. This volume change may provide the formation or the propagation of cracks, leading to the failure of the TBC. The macroscopic stress state may also influence the phase transformation. Azzopardi *et al.* [62] have found that in EB-PVD YSZ coatings annealed at temperature in the range from 1100 °C and 1500 °C, the t' phase decomposes in a low-yttria tetragonal phase, a high-yttria tetragonal phase and a high-yttria cubic phase.

The yttria concentration of the tetragonal phase is an indicator of the destabilization degree of the tetragonal phase and, consequentely, of TBC state [63]. Coated components should be inspected during service for routine control of phase stability.

1.7.2 Microstructural Characterization

The analysis of the morphological and microstructural features of both feedstock and coatings is typically performed by using optical and Scanning Electron Microscopy (SEM), in the purpose to detect some microstructural features, such as pores, microcracks and splat boundaries.

Fractured surface can be analyzed in as-sprayed state to study the splat morphology. Fracture cross section are obtained by mechanical breaking or cutting. Polished cross sections are more suitable for the investigation of the typical microstructural features of plasma sprayed coatings. In SEM observations scattered and back-scattered electrons (SE and BSE) are usually used to study morphological and microstructural features, respectively. When different phases are within the coating, different grey levels can be appreciated, corresponding to different atomic weight. Generally, brighter areas denote heavier elements and compounds, whereas darker areas mark lighter elements or compounds. To this purpose, Electron Dispersive Spectroscopy (EDS) may be used to perform an elemental analysis.

It should be noted that long-term exposure of porous ceramic coatings at high temperature involves significant changes in their microstructure, *i.e*. a sintering effect that, by the gradual annihilation of finer pores and microcracks, can reduce the porosity volume of the coatings and thus increases their thermal conductivity, elastic modulus and hardness [38]. SEM micrographs are useful tools to appreciate the sintering effects.

The preparation of plasma sprayed coatings for methallography may be very difficult. Cross sections are obtained by sectioning the as-sprayed coatings. They were usually cold-mounted in vacuum in a two-part epoxy resin. Grinding and polishing of coating cross section are commonly performed before SEM observations.

1.7.3 Image Analysis (IA)

In the last years, image analysis (IA) has been largely used to investigate the complex microstructure of porous plasma sprayed coatings. These last ones differ from bulk materials due to their anisotropy and typical microstructural features, such as pores and microcracks, which surely affect their functional properties, such as elastic modulus, hardness, thermal conductivity, thermal cycling resistance and corrosion resistance. Image analysis is a powerful investigation tool because, starting from optical or SEM grey-scale micrographs of coating cross section, allows a quantitative and qualitative analysis of the microstructure. So, using IA, the evolution of the microstructure during service may be easily analyzed. Other techniques, such as computer microtomography (CMT) and small-angle neutron scattering (SANS) have been used to this purpose. Image analysis possesses many advantages, due to its reliability and low cost. Friis *et al.* [64] have developed IA techniques for the investigation of the microstructural features of thermally sprayed coatings. By using Image Analysis, Deshpande *et al.* [65] have studied the microstructural properties of thermally sprayed YSZ and alumina coatings, produced by different feedstocks and thermal spraying processes. Also,

Finally, Kulkarni *et al.* [66,67] have developed IA techniques to estimate coating porosity and thermal conductivity and for property modeling of thermally sprayed coatings.

IA measures both open and closed porosity, due to the high degree of contrast between the dark pores and the more highly reflective material, pore size distribution and pore morphology.

1.7.4 Mechanical properties

Hardness and elastic modulus are the most common mechanical properties to be investigated in plasma sprayed coatings. Hardness may be measured on both as-sprayed surfaces and polished cross-section by using indentation techniques. A great number of measurements is generally performed to obtain an average hardness value for porous coatings. The microhardness average is not enough to characterize thermal sprayed coatings, due to their anysotropy and microstructural defects, such as pores showing different shape and size, microcracks and splat boundaries. Moreover, the indentations can take place on many splats characterized by different morphological features. Nanoindentation (NI) is more suitable to study the local properties of plasma sprayed coatings, due to very small indentation loads and size. The hardness measured by NI becomes similar to that of bulk material with the same composition. However, it is generally lower, due to the presence of finer voids and microcracks along coating thickness.

High indentation loads can promote the formation and propagation of cracks, and, therefore, can be applied in order to compute the fracture toughness of plasma sprayed coatings. To this aim, several models are available in literature, depending on the shape of the imprint and the dimension of the crack induced by indenter. Anyway, it is not easy to obtain reliable results on porous coatings, due to the complex cracking mechanism.

Young's modulus measurement is a fundamental step for quality evaluation and lifetime prediction of a TBC, as well as the study of its high-temperature evolution. Indeed, the mechanism of brittle failure is strongly related to the in-plane coating elastic properties. To this purpose, the evolution of Young's modulus of a TBC is often investigated during isothermal heat treatments or thermal cycling. The first step consists in the measurement of the elastic modulus of as-sprayed coating at room temperature. Indeed, the Young's modulus affects the thermal stress distribution in the TBC and the thermal fatigue behaviour accordingly. A low modulus may play an important role on the thermo-mechanical behaviour of the coating. Young's modulus of plasma sprayed coatings has been measured using different methods, including static, quasi-static and dynamic methods. Static methods include three or four points Bending Tests (BT) which measure the apparent elastic modulus, representative of the macro-elastic coating properties and much lower than the same value obtained for bulk material, due to the presence of pores and cracks along coating thickness. As an example, the value of the elastic modulus for dense YSZ is about 200 GPa, whereas some investigators have measured an elastic modulus of about 25 GPa by using four-point bending test [68,69] However, a broad range of values is reported in literature and these differences may be attributed to the anisotropic microstructural features of thermally sprayed coatings as well as to their different microstructures and testing parameters [70,71] Sintering of porous microstructure of plasma-sprayed YSZ coatings, induced by isothermal post-treatment, can produce the increase of Young's modulus and the corresponding reduction of the strain tolerance [32,72]. Ahrens *et al.* [73] have evaluated the mechanical properties of plasma sprayed TBCs with different microstructures using three-points bending test at room temperature. After annealing at 1200 °C for 100 h they have found an increase by a factor of more than two.

On the other hand, in thermally cycled free-standing plasma sprayed YSZ coatings it has been observed that as thermal cycles increase as elastic modulus decreases. In this experiment three-points bending test was used for the measurement of the elastic modulus on YSZ coatings treated at 1120 °C [74]. During thermal cycling the thermal strains induce the formation and the propagation of cracks within the ceramic coating and reduce the cohesive strength between the lamellae, thus decreasing the Young's modulus.

Indentation techniques allow to measure both the stiffness and the hardness by load-displacement curves by using Vickers or Rockwell indenters. A mean value is not adequate to completely characterize the mechanical properties of plasma sprayed coatings due to their anisotropic microstructural properties. The presence of pores with different sizes, interlamellar and intralamellar microcracks may be responsible of large scatter in the mechanical properties and may cause a broad distribution of the experimental data. So, their distribution is currently analyzed by Weibull statistics. The Young's modulus of plasma sprayed coatings is much lower than that measured on bulk materials with the same chemical composition and, therefore, involves higher strain tolerance. Indentation techniques lead to higher values of the elastic properties in comparison with the macroscopic techniques. The elastic modulus decreases with increasing the indentation load [71]. Higher loads provide an increase of deformation areas, because the number and the weight of pores and cracks and their influence on the measurements increase. However, higher loads are preferable to provide more reliable results, because larger pores would be taken in account. Marshall *et al.* [75] have also used Knoop indentation to determine the Young's modulus of plasma sprayed coatings.

However, NI can be considered as a powerful tool for the evaluation of the local coating properties and their variations by high-temperature sintering, *i.e.* the closure of fine pores and microcracks and the following partial densification of the microstructure. The values are

much higher than the global values and slightly lower than that of fully dense material due to the presence of fine porosities. The NI measures can be also considered as a baseline for the determination of the elastic properties of plasma sprayed coatings by using theoretical micromechanical methods, such as Spriggs' method, Hashin-Hasselmann method and Zhao method. These theoretical methods have been developed to relate the microstructural and mechanical properties of porous structures, whose pore volume has been previously measured. Spriggs' model hypothizes a uniform distribution of spherical pores and allows to calculate the elastic modulus starting from coating porosity and elastic modulus of bulk material having the same composition, through an exponential relationship [76]. Also, Hashin-Hasselmann method takes into consideration the weight of pores, cracks and splat boundaries [77,78]. Finally, Zhao model takes into consideration the anysotropic microstructure and, assuming the same aspect ratio for all the elliptical pores, provides two equations to calculate elastic modulus in both longitudinal and transverse directions [79]. However, it should be noted that these methods do not consider pores with different aspect ratio and, therefore, they often provide values lower than those measured by macromechanical methods, such as BT or resonant techniques [80]. The scatter can be ascribed to the morphology and size distribution of pores and cracks, since the porosity value can be estimated with accuracy using various techniques, such as image analysis, mercury porosimetry and Archimedes' method.

More recently, dynamic resonance techniques have been applied to measure the elastic properties of porous TBCs. The first investigation has been made by Chiu *et al.* [81] which have measured the elastic modulus of coating-substrate composites. Impulse Excitation Technique (IET) has been recently developed and optimized in order to evaluate the elastic modulus and Poisson ratio responses of a by-layer (substrate and coating). The system employed and the results will be discussed in detail in this work. IET is a very promising test

for on-line monitoring of plasma sprayed coatings, because it provides reproducible results about the global mechanical properties of plasma sprayed coatings. In addition, IET involves a very low cost and produces no distortion, without destroying the sample during the test.

1.7.5 Thermal Aging Tests

Thermo-mechanical tests can be arranged in a very easy way. In order to study high-temperature evolution of microstructural and mechanical properties, the as-sprayed coatings can be addressed to heat treatments at well-known temperatures and for different times. Thermal cycling tests are simple and reliable methods which better simulate the operating conditions in turbine engines. In the past, due of a lack of reliable testing methodologies, many technical studies have not been transferred to real applications. A burner rig is the most appropriate equipment for TBC testing, since only the outer surface of the same TBC is directly exposed to high temperature, whereas the temperature on the substrate is maintained much lower. The substrates are commonly cooled by pressurized air.

Isothermal tests are easier to be performed and are much useful to analyze the thermo-mechanical behaviour of thermal barrier coatings. Isothermal tests can be devoted to the study of the sintering kinetics in ceramic coatings as well as to the study of high-temperature oxidation. The properties of treated coatings have to be compared with those of as-sprayed coatings.

Obviously, the substrate should be preferably coated on each side, due to the different thermal expansion coefficients of substrate and coating. This difference usually reflects in much different high-temperature shrinkages, which reduce the interfacial adhesion and favour the debonding. If the coatings were applied on each side, only the external surface of the TBC would experience the highest temperature. However, it is not easy to coat each side of the substrate.

Then, it may be necessary to test free-standing coatings, even if the thermo-mechanical behaviour of a free-standing ceramic layer differs from that of a layered TBC. The coatings are heated to high temperature, hold to this temperature for different times and cooled down to room temperature. The heating rate, the maximum temperature and the cooling rate may influence the thermo-mechanical performance and the durability of a TBC.

Finally, thermal shock tests consist of rapid heating and cooling cycles. The specimens are commonly cooled down in air or quenched to room temperature in a water bath. The cycles are repeated more times. The thermal shock test produces severe thermal stresses which lead to the growth of visible crack networks. The propagation of these cracks or pre-existing cracks within the coating leads to the detachment of large coating fractions from the surface up to the final delamination.

1.8 Future and Perspectives

The current and future researches are focused on searching for new materials with optimized chemical and phase composition, low thermal conductivity at high temperature, low sintering rate and high resistance to oxidation and hot corrosion. The goal is to realize interesting solutions, for a wide variety of operating conditions, temperatures and environments. The development of lifetime prediction models is a basic requirement for these applications, as well as the development of new advanced materials. Other promising TBC systems should be studied, developed and realized, as well as improved methodologies for non-destructive testing and analysis of in-service behaviour of TBCs. About TBC materials, some guidelines have been indicated in previous sections, as the search of better stabilizers for zirconia and the use of nanostructured materials.

Functional graded materials (FMG) and multi-layered thermal barrier coatings represent further and interesting technological solutions.

There are a few investigations on FMG coatings, even if they were developed in the early 1970s and are currently used to protect some turbine components and burner nozzles, and they could be also promising for advanced fuel cells, batteries and biomedical applications. FMG coatings could be manufactured with a graded chemical composition through the thickness (from the bond coat to the top coat), in order to minimize the thermal expansion mismatch between these adjacent layers and the substrate, especially for very high thicknesses. As the number of layers with the same thickness increases as the bond strength of FMG coating is improved. This leads to a significant reduction of thermal and mechanical stresses during service [82]. The properties of metal and ceramic materials are combined to manufacture coatings with enhanced and unique properties in terms of thermal conductivity and oxidation resistance. All the microstructural, thermal and mechanical properties change gradually along the thickness. In the conventional coatings during cooling the significant residual stresses near

the interface can promote cracking and spallation between bond coat and top coat. The application of a thicker coating surely allows an increase of the operating temperature, by an increase of the TBC capability. However, the stresses may be much higher within a thicker coating and this can influence its thermal cycling lifetime. For fabrication of FMG coatings, powders with different chemical compositions can be co-sprayed using two injectors at the same time, gradually varying their rates during co-deposition. Alternatively, the feedstocks can be mixed before spraying. Obviously, the powders have to possess similar particles size, melting point and deposition efficiency. Therefore, their processing can result not easy.

In alternative, multi-layered TBCs, composed of two or more ceramic layers, might be developed to better accommodate the stress state in the entire TBC system [83]. This design has been recently proposed, taking into consideration that no single material seems to satisfy all the requirements for a TBC. The concept of multilayered TBCs is effective for the enhancement of their thermo-mechanical properties of TBCs [84,85]. Both FMG and multi-layered TBCs, and especially this last ones, have shown higher lifetime than YSZ coatings in burner rig at temperatures higher than 1300 °C [83,84]. However, a few experiments have been performed and further investigations are needed in order to confirm these preliminary results..

References

[1] J. R. Davis, Handbook of Thermal Spray Technology, ASM International 2004, Materials Park, OH, USA, 2004, pp. 1-338.

[2] M. McLean, Nickel-base superalloys: Current status and potential, Phil. Trans. R. Soc. Lond. A 351 (1995) 419-433.

[3] D. Stoever and C. Funke, Directions of the development of the thermal barrier coatings in energy applications, J. Mater. Proc. Technol. 92-93 (1999) 195-202.

[4] R. Ruh, K. S. Mazdigasni, P. G. Valentine and H. O. Bielstein, Phase relations in the system ZrO_2-Y_2O_3 at low Y_2O_3 contents, J. Am. Ceram. Soc. 67(9) (1984) 190-192.

[5] H.G. Scott, Phase relationship in the zirconia-yttria system, J. Mater. Sci. 10 (1975) 1527-1535.

[6] S. R. Levine, R. A. Miller and P. E. Hodge, Thermal barrier coatings for heat engine components: Sampe Quarterly 12 (1980) 20-26.

[7] A. Rabiei and A. G. Evans, Failure mechanisms associated with the thermally grown oxide in plasma-sprayed thermal barrier coatings, Acta Mater. 48 (2000) 3963-3976.

[8] A. G. Evans, M. Y. He and J. W. Hutchinson, Mechanics-based scaling laws for the durability of thermal barrier coatings, Prog. Mater. Sci. 46 (2001) 249-271.

[9] A. G. Evans, D. R. Mumm and J. W.Hutchinson, Mechanisms controlling the durability of thermal barrier coatings, Prog. Mater. Sci. 46 (2001) 505-553.

[10] G. Di Girolamo, L. Pilloni, G. Pulci and F. Marra, Tribological characterization of WC-Co plasma sprayed coatings, J. Am. Ceram. Soc. 92(5) (2009) 1118-1124.

[11] D. Zhu, N. P. Bansal and R. A. Miller, Thermal conductivity and stability of HfO_2-Y_2O_3 and $La_2Zr_2O_7$ evaluated for 1650 °C thermal/environmental barrier coating applications, NASA/TM-2003-212544. ARL-TR-3093.

[12] K. N. Lee, Current Status of environmental barrier coatings for Si-based ceramics, Surf. Coat. Technol. 133-134 (2000) 1-7.

[13] H. Liao, B. Normand and C. Coddet, Influence of coating microstructure on the abrasive wear resistance of WC/Co cermet coatings, Surf. Coat. Technol. 124 (2000) 235-242.

[14] Y. Qiao, Y. R. Liu and T. E. Fischer, Sliding and abrasive wear resistance of thermal-sprayed WC-Co coatings, J. Therm. Spray Technol. 10(1) (2001) 118-125.

[15] H. Chen and I. M. Hutchings, Abrasive wear resistance of plasma-sprayed tungsten carbide-cobalt coatings, Surf. Coat. Technol. 107 (1998) 106-114.

[16] R. S. Lima and B. R. Marple, Thermal spray coatings engineered from nanostructured ceramic agglomerated powders for structural, thermal barrier and biomedical applications: A review, J. Therm. Spray Technol. 16(1) (2007) 40-63.

[17] R. Soltani, E. Garcia, T. W. Coyle, J. Mostaghimi, R. S. Lima, B. R. Marple and C. Moreau, Thermomechanical behavior of nanostructured plasma sprayed zirconia coatings, J. Therm. Spray Technol. 15(4) (2006) 657-662.

[18] B. Liang and C. Ding, Thermal shock resistance of nanostructured and conventional zirconia coatings deposited by atmospheric plasma spraying, Surf. Coat. Technol. 197 (2005) 185-192.

[19] W. Q. Wang, C. K. Sha, D. Q. Sun and X. Y. Gu, Microstructural feature, thermal shock resistance and isothermal oxidation resistance of nanostructured zirconia coating, Mater. Sci. Eng. A 424 (2006) 1-5.

[20] R. S. Lima, A. Kucuk and C. C. Berndt, Bimodal distribution of mechanical properties on plasma sprayed nanostructured partially stabilized zirconia, Mater. Sci. Eng. A 327 (2002) 224-232.

[21] R. S. Lima and B. R. Marple, Nanostructured YSZ thermal barrier coatings engineered to counteract sintering effects, Mater. Sci. Eng. A 485 (2008) 182-193.

[22] Y. C. Zhu, K. Yukimura, C. X. Ding and P. Y. Zhang, Tribological properties of nanostructured and conventional WC-Co coatings deposited by plasma spraying, Thin Solid Films 388 (2001) 277-282.

[23] P. H. Shipway, D. G. McChartney and T. Sudaprasert, Sliding wear behaviour of conventional and nanostructured HVOF sprayed WC-Co coatings, Wear 259 (2005) 820-827.

[24] A. P. Alkimov, V. F. Kosarev and A. N. Papyrin, A method of cold gas-dynamic deposition, Sov. Phys. Dokl. 35 (12) (1990) 1047-1049.

[25] A. P. Alkimov, A. N. Papyrin, V. F. Kosarev, N. I. Nesterovich and M. M. Shuchpanov, Gas dynamic spraying method for applying a coating, U. S. Patent No. 5,302,4141, 12 Apr 1994, Re-examination Certificate, 25 Feb 1997.

[26] A. P. Alkimov, A. N. Papyrin, V. F. Kosarev, N. I. Nesterovich and M. M. Shuchpanov, Method and device for coating, European Patent No. 0484533, 25 Jan 1995.

[27] A. I. Kashirin, O. F. Klyuev and T. V. Buzdygar, Apparatus for gas-dynamic coating, U. S. Patent No. 6,402,050, 11 June 2002.

[28] M. F. Trubelja, D. M. Nissley, N. S. Bornstein and J. T. Marcin, Thermal barrier coatings development in advanced turbine systems, Proceedings of the Annual Program Review Meeting 1997, DOE/FETC-98/1057, DE98002004,CONF-971053 (Rept. No. 5.9). Pratt & Whitney, E. Hartford, CT.

[29] D. R. Clarke and C. G. Levi, Materials design for the next generation thermal barrier coatings, Annu. Rev. Mater. Res. 33 (2003) 383-417.

[30] T. Troczinsky, S. Cockcroft and H. Wong, Thermal barrier coatings for heat engines, Key Eng. Mats. 122-124 (1996) 451-462.

[31] B. Siebert, C. Funke, R.Vassen and D. Stoever, Changes in porosity and Young's modulus due to sintering of plasma sprayed thermal barrier coatings, J. Mater. Proc. Technol. 92-93 (1999) 217-223.

[32] J. A. Thompson and T. W. Clyne, The effect of heat treatment on the stiffness of zirconia top coats in plasma sprayed TBCs, Acta Mater. 49 (2001) 1565-1575.

[33] R. Vassen, G. Kerkhoff and D. Stover, Development of a micromechanical life prediction model for plasma sprayed thermal barrier coatings, Mater. Sci. Eng. A 303 (2001) 100-109.

[34] X. Chen, R. Wang, N. Yao, A. G. Evans, J. W. Hutchinson and R. W. Bruce, Foreign object damage in a thermal barrier system: Mechanisms and simulations, Mater. Sci. Eng. A 352 (2003) 221-231.

[35] J. R. Nicholls, M. J. Deakin and D. S. Rickerby, A comparison between the erosion behavior of thermal spray and electron-beam physical vapour deposition thermal barrier coatings", Wear 233-235 (1999) 352-361.

[36] M. P. Borom, C. A. Johnson and L. A. Peluso, Role of environmental deposits and operating surface temperature in spallation of air plasma sprayed thermal barrier coatings, Surf. Coat. Technol. 86-87 (1996) 116-126.

[37] C. Mercer, S. Faulhaber, A. G. Evans and R. Darolia, A delamination mechanism for thermal barrier coatings subject to calcium-magnesium-alumino-silicate (CMAS) infiltration, Acta Mater. 53 (2005) 1029-1039.

[38] P. Langjahr, R. Oberacker and M. J. Hoffmann, Long-term behavior and application limits of plasma-sprayed zirconia thermal barrier coatings, J. Am. Ceram. Soc. 84(6) (2001) 1301-1308.

[39] J. Wilden and A. Wank, Application study on ceria based thermal barrier coatings, Mater. Sci. Eng. Technol. 32(8) (2001) 654-659.

[40] R. L. Jones and D. Mess, Improved tetragonal phase stability at 1400 °C with scandia, yttria-stabilized zirconia, Surf. Coat. Technol. 86-87 (1996), 94-101.

[41] S. Raghavan, H. Wang, W. D. Porter, R. B. Dinwiddie and M. J. Mayo, Thermal properties of zirconia co-doped with trivalent and pentavalent oxides, Acta Mater. 49 (2001) 169-179.

[42] R. A. Miller, Thermal barrier coatings of aircraft engines: History and directions, J. Therm. Spray Technol. 6(1) (1997) 35-42.

[43] S. Sodeoka, M. Suzuki, K. Ueno, H. Sakuramoto, T. Shibata and M. Ando, Thermal and mechanical properties of ZrO_2-CeO_2 plasma-sprayed coatings, J. Therm. Spray Technol. 6 (1997) 361-367.

[44] J. Moon, H. Choi, H. Kim and C. Lee, The effects of heat treatment on the phase transformation behavior of plasma-sprayed stabilized ZrO_2 coatings, Surf. Coat. Technol 155 (2002) 1-10.

[45] C S. Y. Park, J. H. Kim, M. C. Kim, H. S. Song and C. G. Park, Microscopic observation of degradation behavior in yttria and ceria stabilized zirconia thermal barrier coatings under hot corrosion, Surf. Coat. Technol. 190 (2005) 357-365.

[46] J. Ilavsky, C. C.Berndt, H. Herman, P. Chraska and J. Dubsky, Alumina-base plasma sprayed materials. Part II: Phase transformations in alumina, J. Therm. Spray Technol. 6(4) (1997) 439-444.

[47] H. Xu, H. Guo, F. Liu and S. Gong, Development of gradient thermal barrier coatings and their hot-fatigue behaviour, Surf. Coat. Technol. 130(1) (2000) 133-139.

[48] T. M. Yonushonis, Overview of thermal barrier coatings for diesel engines, J. Therm. Spray Technol. 6(1) (1997) 50-56.

[49] P. Ramaswamy, S. Seetharamu, K. B. R. Varma and K. J. Rao, Thermal shock characteristics of plasma sprayed mullite coatings, J. Therm. Spray Technol. 7(4) (1999) 497-504.

[50] K. N. Lee, R. A. Miller and N. S. Jacobson, New generation of plasma sprayed mullite coatings on silicon carbide, J. Am. Ceram. Soc. 78(3) (1995) 705-710.

[51] X. Cao, R. Vassen, F. Tietz, W. Jungen and D. Stoever, Thermal stability of lanthanum zirconate plasma-sprayed coating, J. Am. Ceram. Soc. 84(9) (2001) 2086-2090.

[52] R. Vassen, X. Cao, F. Tietz, D. Basu and D. Stover, Zirconates as new materials for thermal barrier coatings, J. Am. Ceram. Soc. 83(8) (2000) 2023-2028.

[53] M. J. Maloney, Thermal barrier coatings systems and materials", U.S. Patent No. 6,284,323 (2001).

[54] R. Subramanian, Thermal barrier coatings having high phase stability, U.S. Patent No. 6,258,467 (2001).

[55] M. J. Maloney, Thermal barrier coatings systems and materials, U.S. Patent No. 6,117,560 (2000).

[56] C. J. Friedrich, R. Gadow and M. H. Lischka, Lanthanum hexaaluminate thermal barrier coatings, Ceram. Eng. Sci. Proc. 22(4) (2001) 375-382.

[57] X. Q. Cao, R. Vassen and D. Stoever, Ceramic materials for thermal barrier coatings, J. Eur. Ceram. Soc. 24 (2004) 1-10.

[58] R. Gadow and G. W. Schafer, Thermal insulating materials and method for producing SAME, German Patent No. WO 99/42630,1999.

[59] R. A. Miller, J. L. Smialek and R. G. Garlick, in A. H. Heuer and L. W. Hobbs (eds.), Science and Technology of Zirconia, Advances in Ceramics, Vol. 3, The American Ceramic Society, Westerville, OH, 1981, 241-253.

[60] U. Schulz, Phase transformation in EB-PVD yttria partially stabilized zirconia thermal barrier coatings during annealing, J. Am. Ceram. Soc. 83(4) (2000) 904-910.

[61] J. R. Brandon and R.Taylor, Phase stability of zirconia-based thermal barrer coatings. Part I. Zirconia-yttria alloys, Surf. Coat.Technol. 46 (1991) 75-90.

[62] A. Azzopardi, R. Mévrel, B. Saint-Ramond, E. Olson and K. Stiller, Influence of aging on structure and thermal conductivity of Y-PSZ and Y-FSZ EB-PVD coatings, Surf. Coat. Technol. 177-178 (2004) 131-139.

[63] J. Ilavsky, J. K. Stalick and J. Wallace, Thermal spray yttria-stabilized zirconia phase changes during annealing, J. Therm. Spray Technol. 10(3) (2001) 497-501.

[64] M. Friis, C. Persson and J. Wigren, Influence of particle in-flight characteristics on the microstructure of atmospheric plasma sprayed yttria stabilized zirconia, Surf. Coat. Technol. 141 (2001) 115-127.

[65] S. Deshpande, A. Kulkarni, S. Sampath and H. Herman, Application of image analysis for characterization of porosity in thermal spray coatings and correlation with small angle neutron scattering, Surf. Coat. Technol. 187 (2004) 6-16.

[66] A. Kulkarni, Z. Wang, T. Nakamura, S. Sampath, A. Goland, H. Herman, J. Allen, J.Ilavsky, G. Long, J. Frahm *et al*, Comprehensive microstructural characterization and predictive property modeling of plasma-sprayed zirconia coatings, Acta Mater. 51 (2003) 2457-2475.

[67] Y. Tan, J. P. Longtin and S. Sampath, Modeling thermal conductivity of thermal spray coatings: Comparing predictions to experiments, J. Therm. Spray Technol. 15(4) (2006) 545-552.

[68] J. F. Shackelford and W. Alexander, editors. CRC Materials Science and Engineering Handbook. New York (NY): CRC Press; 2001, 766

[69] D. Schwingel, R. Taylor, T. Haubold, J. Wigren and C. Gualco, Mechanical and thermo-physical properties of thick PYSZ thermal barrier coatings: Correlation with microstructure and spraying parameters, Surf. Coat. Technol. 108-109 (1998) 99-106.

[70] S. R. Choi, D.M. Zhu and R. A. Miller, Deformation and strenght behavior of plasma-sprayed ZrO_2-8 wt.%Y_2O_3 thermal barrier coatings in biaxial flexure and trans-thickness tension, Ceram. Eng. Sci. Proc. 21(4) (2000) 653-661.

[71] D. Basu, C. Funke and R. W. Steinbrech, Effect of heat treatment on elastic properties of separated TBCs, J. Mater. Res. 14(12) (1999) 4643-4650.

[72] F. Cernuschi, L. Lorenzoni, S. Ahmaniemi, P. Vuoristo, T. Mantyla, "Study of the sintering kinetics of thick thermal barrier coatings by thermal diffusivity measurements, J. Eur. Ceram. Soc. 25 (2005) 393-400.

[73] M. Ahrens, S. Lampenscherf, R. Vassen and D. Stover, Sintering and creep processes in plasma-sprayed thermal barrier coatings, J. Therm. Spray Technol. 13(3) (2004) 432-442.

[74] F. Tang and J. M. Schoenung, Evolution of Young's modulus of air plasma sprayed yttria-stabilized zirconia in thermally cycled thermal barrier coatings, Scri. Mater. 54 (2006) 1587-1592.

[75] D. B. Marshall, T. Noma and A. G. Evans, A simple method for determining elastic-modulus-to-hardness ratios using Knoop indentation measurements, J. Am. Ceram. Soc. 65 (1982) C175-C176.

[76] R. M. Spriggs, Expression for effect of porosity on elastic modulus of polycrystalline refractory materials, particularly aluminium oxide, J. Am. Ceram. Soc. 44(12) (1961) 628-629.

[77] Z. Hashin, The elastic moduli of heterogeneous materials, J. Appl. Mech.-T. ASME 29(3) (1962) 143-150.

[78] D. P. Hasselmann, On the porosity dependence of the elastic moduli of polycrystalline refractory materials, J. Am. Ceram. Soc. 45 (1962) 452-453.

[79] Y. H. Zhao and G. J. Weng, Effective elastic moduli of ribbon-reinforced composites, J. Appl. Mech.-T. ASME 57 (1990) 158-167.

[80] F. Azarmi, T. Coyle and J. Mostaghimi, Young's modulus measurement and study of the relationship between mechanical properties and microstructure of air plasma sprayed alloy 625, Surf. Coat. Technol. 203 (2009) 1045-1054.

[81] C. C. Chiu and E. D. Case, Elastic modulus determination of coating layers as applied to layered ceramic composites, Mater. Sci. Eng. 132 (1991) 39-47.

[82] K. A. Khor and Y. W. Gu, Effects of residual stress on the performance of plasma sprayed functionally graded ZrO_2/NiCoCrAlY coatings", Mater. Sci. Eng. A 277 (2000) 64-76.

[83] D. Stoever, G. Pracht, H. Lehmann, M. Dietrich, J. E. Doring and R. Vassen, New material concepts for the next generation of plasma-sprayed thermal barrier coatings, J. Therm. Spray Technol. 13(1) (2004) 76-83.

[84] X. Q. Cao, R. Vassen, F. Tietz and D. Stoever, New double-ceramic-layer thermal barrier coatings based on zirconia-rare earth composite oxides, J. Eur. Ceram. Soc. 26 (2006) 247-251.

[85] M. Tamura, M. Takahashi, J. Ishii, K. Suzuki, M. Sato and K. Shimomura, Multilayered thermal barrier coating for land-based gas turbines, J. Therm. Spray Technol. 8(1) (1999) 68-72.

2. Experimental Procedure

2.1 Introduction

This Chapter describes the experimental procedures followed for fabrication, testing and characterization of metallic and ceramic plasma sprayed coatings, focusing the attention on the apparatus and the techniques employed, as well as on the properties of the raw materials and the conditions at which the coatings were produced, tested and characterized.

Four different raw materials were processed to form coatings, *i.e.* a metallic CoNiCrAlY powder feedstock and three ceramic powder feedstocks (two microstructured powders, CYSZ and YSZ, and a nanostructured powder, YSZ).

So, Air Plasma Spraying was employed to fabricate CoNiCrAlY coatings with reduced porosity and low degree of oxidation. The microstructural and the mechanical properties of overlay CoNiCrAlY coatings were investigated in as-sprayed conditions and after early-stage high-temperature oxidation. As an example, both static and dynamic techniques were employed for the determination of the elastic properties of plasma sprayed coatings; a resonant method, known as the Impulse Excitation Technique (IET), was used to measure the Young's modulus in conjunction with a bi-layer specimen configuration (substrate and as-sprayed coating).

Partially yttria stabilized zirconia (YSZ) was studied as reference material for ceramic TBCs, in addition to the above mentioned CYSZ and nanostructured YSZ. The most significant microstructural, thermal and mechanical properties which affect coatings in-service performance, such as porosity, elastic modulus, hardness, thermal expansion coefficient and heat capacity, were determined.

Both YSZ and CYSZ coatings were thermally aged at temperature higher than 1300 °C for different times, in order to study the evolution of their microstructural and mechanical properties and the main mechanisms that influence coating degradation during service. To this

purpose, high-temperature phase changes and sintering phenomena are known as the main factors which affect phase stability, strain tolerance, delamination and thermal transport properties.

Due to the increasing interest in nanostructured materials for the development of advanced TBCs, some preliminary studies about nanostructured zirconia coatings have been also performed in order to study their feasibility, as well as their basic microstructural and mechanical features.

2.2 APS (Air Plasma Spray) Equipment

An APS (Air Plasma Spray) Multicoat equipment, installed at ENEA Brindisi Research Centre, was employed for the fabrication of metal and ceramic coatings. This system is able to deposit coatings with thickness approximately in the range from tens of microns to any millimetres.

The system is equipped with a F4-MB plasma torch with a 6 mm internal diameter nozzle (Sulzer Metco, Wolhen, Switzerland). As shown in Figure 2.1, the plasma gun is moved by an industrial robot (model IRB 2400 M98A, ABB Ltd, Zurich, Switzerland) with six external axes, while the samples to be coated are fixed on a turntable with two external axes. The combination of these two motions allows to coat substrates with complex geometry and different sizes. The motions of the plasma torch and of the turntable are controlled by the operator.

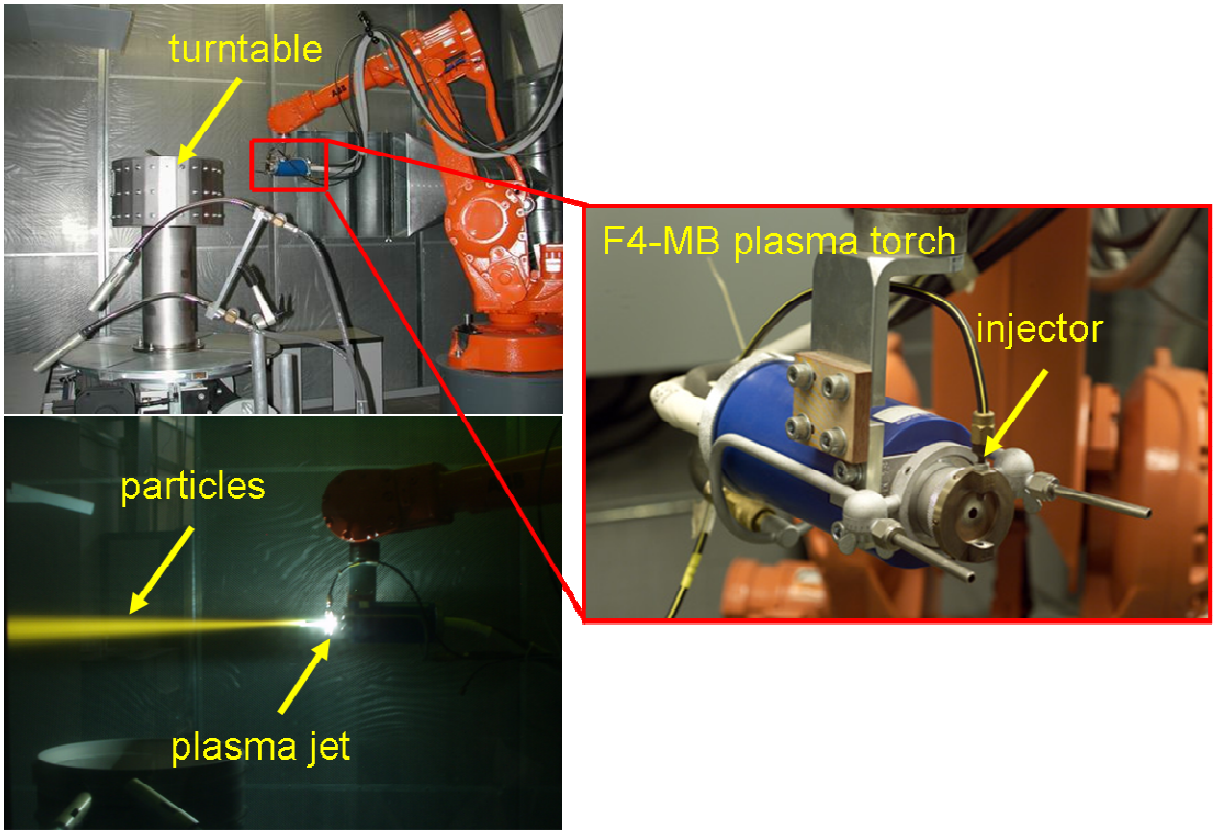

Figure 2.1 – APS system installed at ENEA Brindisi Research Centre.

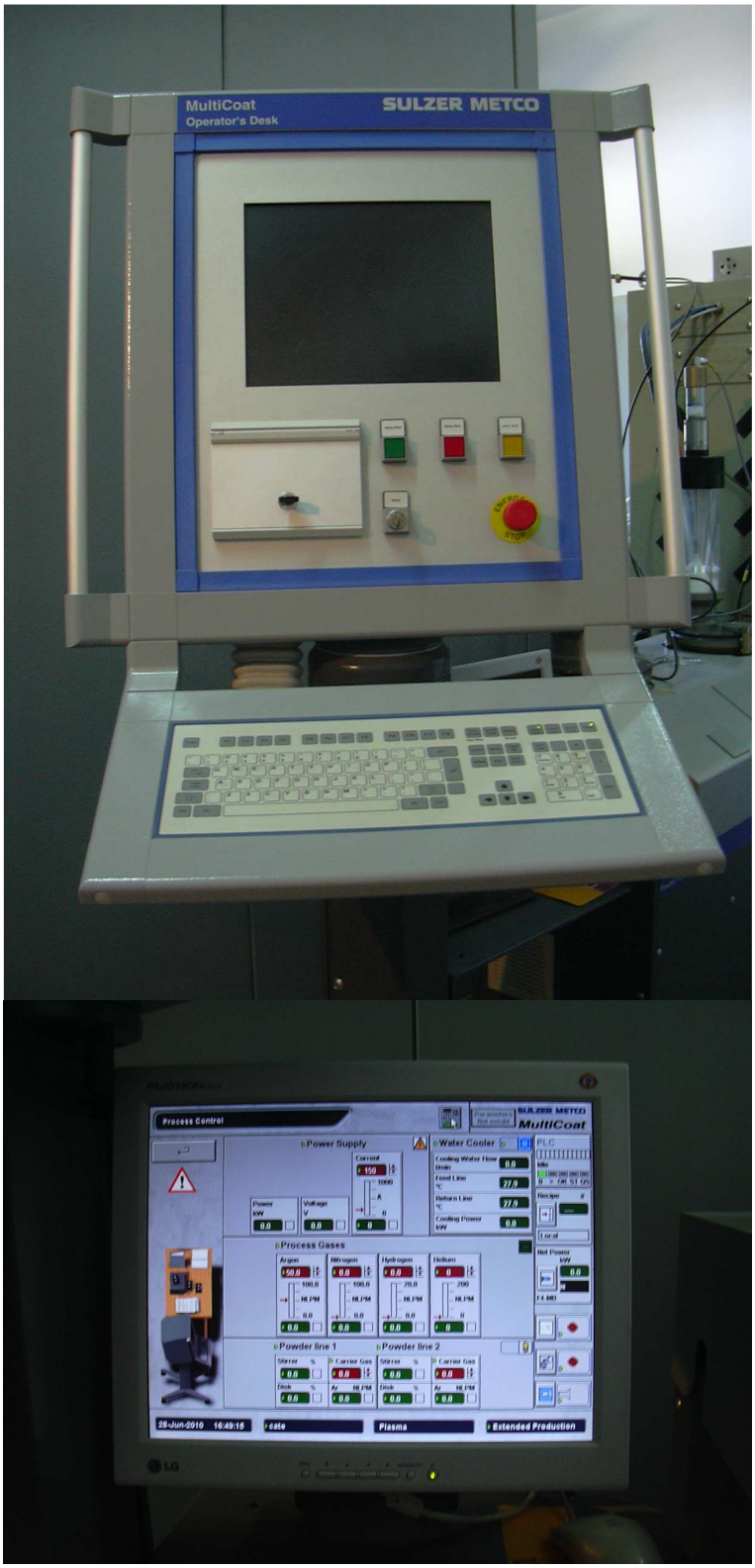

Figure 2.2 – Operator's desk.

An operator's desk (see Fig. 2.2) allows the operator to set the process parameters, to save the recipes for each material to be processed and to visualize all the steps of the deposition

process. A process control center (PCC) controls and monitors the entire plasma spraying process.

The system is equipped with a PT-820E power source (800 A, 100 V). The electric components of the APS system include a direct current (dc) power supply, a high frequency RF spark ignition source and the electric controls for arc current and voltage. The plasma gun includes two electrodes: a cathode, made of copper with a point of a special tungsten alloy, and an anode nozzle which is made of copper with a tungsten insert and is water-cooled. Plasma forming gas flows around the cathode and through the anode which is shaped as a constricting nozzle. The plasma is started by a high-voltage discharge which produces a localized ionization and a conductive path for a DC arc to form between the electrodes. The resistance heating from the arc causes the gas to reach high temperature, dissociate and ionize to form a high-energy plasma.

The plasma exits the anode nozzle as a free or neutral plasma frame. When the plasma parameters are established and the system is ready for spraying, the electric arc extends down the nozzle instead of shorting out to the nearest edge of the anode nozzle. This stretching of the arc is due to a thermal pinch effect. Cold gas around the surface of the water-cooled anode nozzle being electrically non-conductive constricts the plasma arc, raising its temperature and velocity. Figure 2.3 shows any components of the plasma torch, such as the electrodes and the powder injectors.

Gas management center controls the flow of the process gases, mixes the same gases in accordance with the parameters set by the operator and routes the mixture to the Jam-Box. The current, the process gas and the cooling water are joined in the Jam-Box: from there the operating media are routed to the gun. The Jam-Box measures and monitors the parameters of the cooling water circuit (water temperature, water flow and water conductivity). Gas supply, gas flow controls, hoses and regulators are used to control the flow rate of plasma gas mixture

and powder carrier gas. Indeed, proper gas mixtures are used to generate and to stabilize high-temperature plasma, depending on the intrinsic characteristics of powder feedstocks (morphology, chemical composition and melting point). They are usually composed of a primary inert gas (argon) and a secondary gas (hydrogen or helium).

Figure 2.3 – A view of some plasma torch components.

The plasma is always started up using a pure argon flow. Argon is a noble gas and is completely inert to all the sprayable materials. Argon is less aggressive toward electrode and nozzle hardware than other gases. However, the use of pure argon gas mixture typically generates a relatively low-energy plasma. So, other secondary gases are commonly added to argon to form a proper process gas mixture, in order to increase both plasma energy and temperature and to properly process high-melting point materials such as ceramic powder particles. The addition of hydrogen affects heat transfer properties and modifies plasma characteristics, since it increases both plasma temperature and enthalpy and, consequently, the temperature and the melting degree of the sprayed particles. Hydrogen is used as one control for setting plasma voltage and energy. Helium is completely inert to all the sprayable materials and is used with argon when hydrogen is known to produce deleterious effects on the spraying of well-determined typologies of materials. Indeed, oxidation and

decarburization phenomena can take place during atmospheric plasma spraying of metal and cermet powder particles, respectively. Helium imparts good heat transfer properties and gives high sensitivity for the control of plasma energy. It is commonly used together to argon to increase plasma velocity and particles speed and to reduce the interaction between the surface of the sprayed particles and the surrounding environment. As an example, helium can be added to argon or a mixture of argon and hydrogen, thus forming a proper gas mixture in order to fabricate high-quality cermet coatings. Argon-helium mixtures are able to reduce the air entrainment in the plasma jet core. They better entrain cermet particles, giving them faster velocity and reducing their residence time into the flame, and thus the degree of decarburization.

The starting material is typically composed of micron-sized or nano-sized powder particles which have to be heated and partially or totally melted to form a coating. A part from their chemical composition, plasma spray powder feedstocks can be characterized in terms of their size distribution, shape and morphology as well as in terms of the corresponding manufacturing process (produced by sintering and crushing, spray drying, etx.). Their size is defined by the upper and lower limits of the size distribution. The particles can be angular, blocky, spherical or quasi spherical, dense or porous. Spherical particles show higher flowability and are preferred in order to avoid significant drawbacks associated to their transport and melting. Porous particles with an intrinsic porosity involve low heat transfer and are more prone to be well-melted. Denser particles are less prone to oxidize in high-temperature plasma environment, due to their lower surface-to-volume ratio. However, they are usually only partially melted, reducing the bonding strength of the final coating.

The powder particles are placed in a powder feeder (mod. Twin-120-A, see Fig. 2.4) and herein they are stirred by a stirrer vibrator, so that they may precipitate on the upper surface of a rotating disk where they are collected by an inert gas (argon) and carried through a carrier

tube up to the injector which is placed near the anode nozzle exit (the distance between the centre of the injector and the exit of anode nozzle is equal to 5 mm).

Figure 2.4 – Plasma spray powder feeder.

They are then injected into high-temperature plasma flame, where they are superheated, partially or totally melted, then accelerated at high temperature and kinetic energy and propelled toward a cold substrate where they impact, so that they are flattened and are rapidly cooled down to room temperature (quenching), thus promoting the deposition of irregular thin lamellae named splats. The deposition of overlapping splats during successive torch passes on the substrate or previously deposited material produces the gradual build-up of a thick coating

with a splat-like microstructure characterized by networks of pores and microcracks. This unique porous microstructure typically implies both low thermal conductivity and stiffness in comparison with bulk materials having the same chemical composition.

2.3 Processing

Before deposition, the substrates were properly prepared in order to increase the surface roughness and to achieve a proper adhesion between each coating and the corresponding substrate. The conditions for better metallurgical interaction can be obtained by an increased contact surface area, a better mechanical interlocking and lower in-plane stresses by inducing folds in the coating. To this purpose, metal substrates were grit-blasted by using an industrial blasting machine (mod. S8011, Norblast, Bologna, Italy) and an alumina abrasive powder (Metcolite F, Sulzer Metco, Westbury, NY, U.S.),

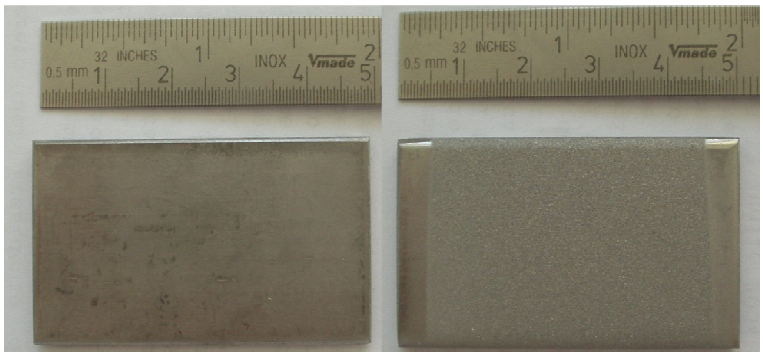

Figure 2.5 – Substrate surface before and after grit-blasting.

Dry abrasive angular particles were propelled at high speed toward substrate surface, where they impact and induce a plastic deformation, producing visible asperities. Grit blasting was carried out at a pressure of 4.5 bar for a dwell time of 15 s, with an angle of impact approximately equal to 45° and at a distance of about 100 mm from substrate surface. These parameters have been set on the basis of previous experiments in order to guarantee a surface

roughness higher than 2 µm. Figure 2.5 shows the surface of a stainless steel substrate before and after grit-blasting, respectively.

Feedstock	Supplier	Chemical composition	Morphology and granulometry
Amdry 995C (CoNiCrAlY)	Sulzer Metco, Westbury, NY, U.S.	38Co-32Ni-21Cr-8Al-0.5Y	Gas atomized 45-75 µm
Metco 204 NS (YSZ)	Sulzer Metco, Westbury, NY, U.S.	ZrO_2-8 wt. % Y_2O_3	HOSP 11-125 µm
Metco 205 NS (CYSZ)	Sulzer Metco, Westbury, NY, U.S.	ZrO_2-25 wt. % CeO_2-2.5 wt. %Y_2O_3	HOSP 10-110 µm
Nanox S4007 (NYSZ)	Inframat Advanced Materials LLC, Manchester, CT, U.S.	ZrO_2-7 wt. % Y_2O_3	Agglomerated 15-150 µm

Table 2.1 – Powder feedstocks used for plasma spray deposition.

The substrates were then ultrasonically cleaned in ethanol for 10 min to remove the residual entrapped within surface asperities after grit-blasting, dried in a oven at 100 °C and finally mechanically fixed to the turntable in front of the plasma torch which, in turn, traversed vertically.

Elements	wt. %
Al	7.84
C	0.01
Co	38.05
Cr	21.20
Ni	32.28
Y	0.5
T.A.O	< 0.1
H_2	< 0.005
O_2	0.017
N_2	0.005

Table 2.2 – Chemical composition of CoNiCrAlY powder.

The area scanned by the plasma torch was adjusted by software in order to uniformly coat the substrate surface.

Elements	wt. %
Al_2O_3	< 0.01
Fe_2O_3	0.02
HfO_2	1.59
MgO	0.02
SiO_2	0.08
TiO_2	0.11
Y_2O_3	7.52
ZrO_2	92.08
CaO	0.01
T.A.O	0.14
U & Th	< 0.01
Moisture	0.02

Table 2.3 – Chemical composition of YSZ powder.

For fabrication of metal and ceramic coatings commercially available feedstocks were used. Their chemical compositions, morphologies and particle distributions are summarized in Table 2.1, while the detailed chemical compositions of the same powders are reported in Tables 2.2, 2.3, 2.4 and 2.5, respectively.

Elements	wt. %
Al_2O_3	< 0.01
Fe_2O_3	0.01
HfO_2	1.2
MgO	< 0.01
SiO_2	0.04
TiO_2	0.1
Y_2O_3	2.4
ZrO_2	70.84
CaO	0.03
T.A.O	0.0
U & Th	0.01
CeO_2	25.28

Table 2.4 – Chemical composition of CYSZ powder.

Elements	wt. %
ZrO_2	93.0
Y_2O_3	7.0

Table 2.5 – Chemical composition of NYSZ powder.

As specified by the manufacturer, Amdry 995C feedstock was produced by gas atomization, while YSZ and CYSZ powders possess an HOSP morphology (hollow oven spherical particles). Spherical hollow particles typically guarantee good flowability and good deposition efficiency. Indeed, they experience a more uniform melting when injected in the plasma plume and are particularly suitable to fabricate porous ceramic thermal barrier coatings, due to their lower density with respect to similar particles produced by other manufacturing methods (sintering and crushing).

Plasma spray parameters typically include arc current intensity, voltage, process gas flow rates, powder feed rate, gun speed, turntable speed and stand-off distance.

Arc voltage is an output value automatically provided by plasma power supply, so that plasma energy and enthalpy mainly depend on the value of the arc current intensity set by the operator. Higher current intensity involves higher temperature and velocity of the sprayed particles and generally leads to coatings with lower porosity and higher bonding strength. Indeed, the melting degree of the sprayed particles depends on the plasma energy and temperature.

Plasma gas flow rate has to be high enough to guarantee a good deposition efficiency, *i.e.* to transport a sufficient amount of molten or semimolten particles from the plasma core to the substrate. On the contrary, a great part of sprayed particles would be dispersed into the atmosphere and not deposited, thus implying low process efficiency and not sustainable costs. It is generally accepted that an increase in plasma gas flow rate increases the velocity of the sprayed particles and slightly decreases their temperature.

Carrier gas flow rate, injector diameter, powder feeder stirrer vibrator and disk speeds were adjusted before deposition in order to guarantee both good flowability of powder particles and good powder feed rate. Powder feed rate was measured as the powder weight injected in the

plasma plume per minute, by using a digital balance with a resolution of 0.01 g (model Europe 1700, Gibertini, Milan, Italy).

Gun velocity and turntable speed were set to well-determined values in the range imposed by the process controller.

Stand-off distance was also adjusted in a well-determined range, in order to guarantee a good powder flow rate and to avoid such detrimental effects on the metal substrates, such as high-temperature surface oxidation, metallurgical changes and distortions. An increase of the spray distance reduces both temperature and velocity of the sprayed particles which impact on the substrate.

An air cooling system was arranged during the deposition process, in order to increase the quenching rate of the molten droplets and to avoid some detrimental phase changes which can occur during slow cooling to room temperature (tetragonal-to-monoclinic transformation for YSZ). Indeed, it is an important key issue to preserve at room temperature the same crystalline phases formed at high temperature. Forced air cooling allows to reduce the substrate temperature and it was performed by two air jets attached to the plasma gun and two additional air jets positioned near the turntable. The pressure of the cooling air was equal to 5 bar.

Plasma sprayed YSZ and CYSZ coatings were deposited on stainless steel (Aisi 310S, 25x25x4 mm^3) and Ni-superalloys substrates (IN738, Φ = 25 mm, thickness = 5 mm) with a final thickness of 450 µm. An intermediate layer (bond coat) with a thickness of approximately 160 µm was previously applied on the substrate, using metal powder feedstock mentioned above (Amdry 995C). The adhesion of the bond coat is favoured by the chemical reactions which take place at the interface and form microscopic alloy layers. At higher temperature, a solid state diffusion may occur. Some substrates were only coated with 160 µm thick CoNiCrAlY coating, in order to investigate the microstructural and thermo-mechanical

properties of this metal coating. Figure 2.6 shows some plasma sprayed CoNiCrAlY coatings deposited on IN738 superalloy substrates. In turn, Figure 2.7 and 2.8 show some examples of YSZ and CYSZ coatings deposited on stainless steel substrates, respectively. Finally, Figure 2.9 shows some examples of nanostructured zirconia coatings.

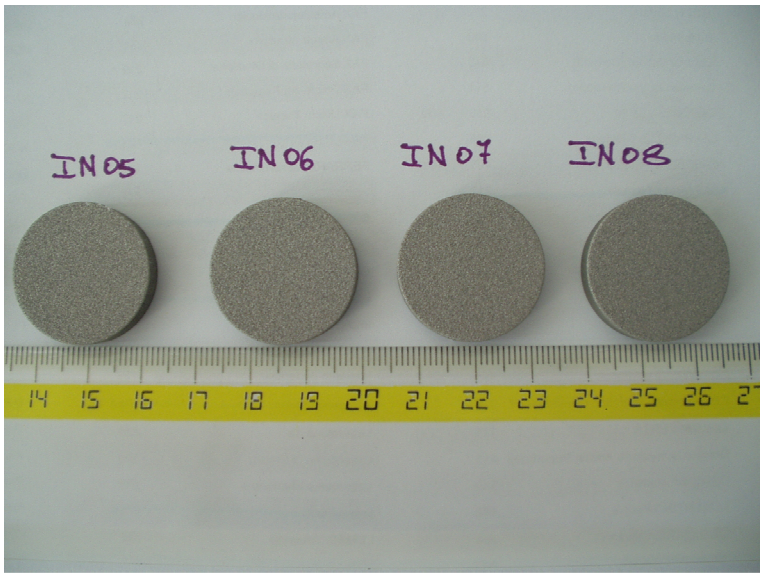

Figure 2.6 – Plasma sprayed CoNiCrAlY coatings on IN738 substrates.

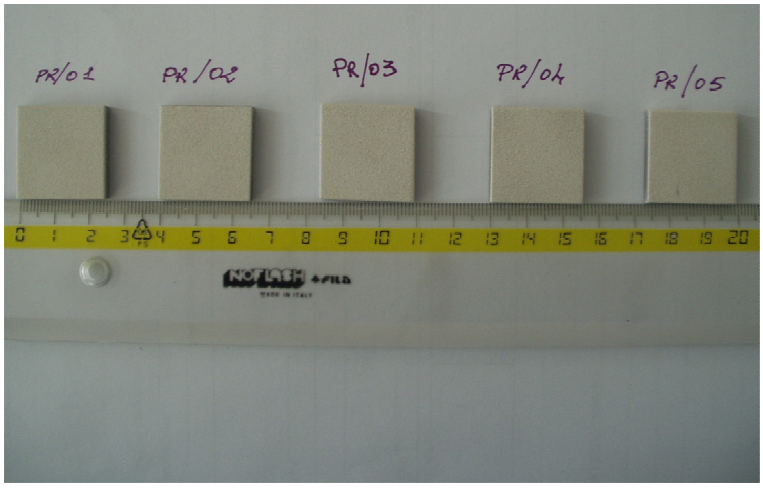

Figure 2.7 – Plasma sprayed YSZ coatings on stainless steel substrates.

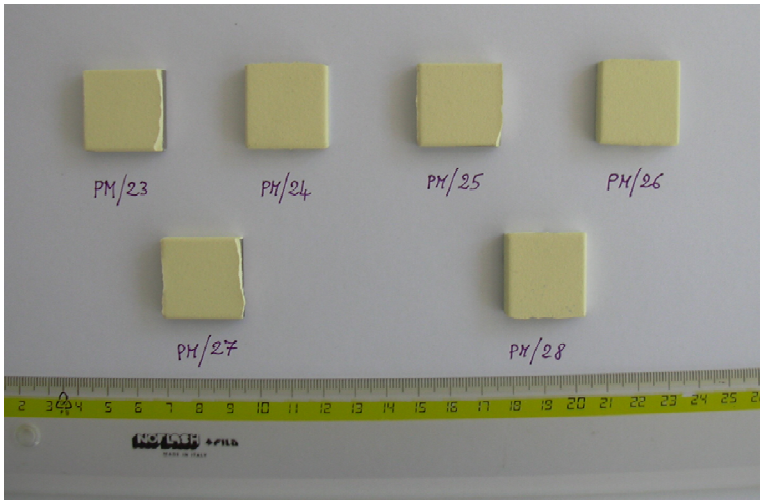

Figure 2.8 – Plasma sprayed CYSZ coatings on stainless steel substrates.

Figure 2.9 – Plasma sprayed NYSZ coatings on stainless steel substrates.

For thermo-physical characterizations, YSZ and CYSZ coatings were deposited with a final thickness of about 2 mm, because lower thicknesses were not enough to provide reliable and accurate data. Obviously, it should be noted that thick thermal barrier coatings are more suitable for thermal protection of metal combustion chamber components in turbine and diesel engines rather than for thermal insulation of turbine blades and vanes. The mechanism of degradation of a thick coating can be different with respect to a thin coating (up to 400-450 µm). We have previously discussed about the phase changes and high-temperature sintering phenomena, which occur at operating conditions. In addition, the failure of a thin coating is

also affected by high-temperature oxidation which leads to the formation of the TGO at the interface between the top coat and the bond coat. On the contrary, the mismatch between the thermal expansion coefficients of coating and substrate affects the duration of a thick coating at higher extent, together to hot corrosion and mechanical loads. A thick coating is able to tolerate higher thermal gradients through the thickness, but higher stresses are expected during high-temperature exposure. The evolution of thermal stresses within the TBC influences the service life and it is strongly related to high-temperature phase changes, grain growth and sintering of the porous microstructure. It is important to highlight these details, even if they are outside the objectives of the present work, because they can be only studied during very long-term thermal exposures in real engines (for months or years).

For mechanical characterization (by Impulse Excitation Technique) the deposited thicknesses were 300 µm for CYSZ and YSZ coatings and 350 µm for CoNiCrAlY coatings. Fe360 plates (100x25x3 mm^3) were coated. These values have been chosen on the basis of previous numerical calculations. Figure 2.10 shows some examples of plasma sprayed CYSZ coatings deposited on steel plates.

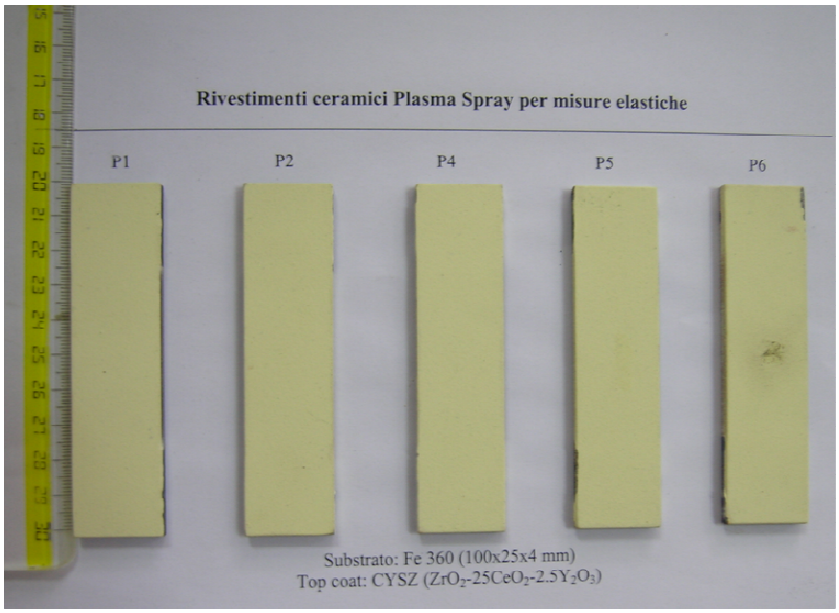

Figure 2.10 – CYSZ coatings on Fe 360 steel substrates for mechanical characterization.

Plasma Spraying parameters for CoNiCrAlY coatings were chosen following an empirical method based on previous experiments performed in our laboratories or elsewhere, as well as for YSZ and CYSZ coatings. Plasma spraying parameters used in this work are summarized in Table 2.6. We also took into consideration the recommendations provided by powders manufacturer.

For CoNiCrAlY coatings deposition, the carrier gas flow rate, the rotation speed of powder feeder stirrer and disk and the injector diameter have been set with the purpose to achieve a powder feed rate of about 50 g/min and to deposit an average thickness per torch pass of about 18 µm.

Parameter	CoNiCrAlY	YSZ	CYSZ	NYSZ
Arc current [A]	600	600	600	600
Voltage [V]	71.4	64.3	70	68.8
Turntable velocity [rpm]*	50	100	100	150
Substrate tangential speed [mm/s]	1041	2083	2083	3124
Gun velocity [mm/s]	4	4	4	4
Primary gas Ar flow rate [slpm]**	55	33	38	40
Secondary gas H_2 flow rate [slpm]**	11	10	11	12
Stand-off distance [mm]	120	100	120	100
Carrier gas Ar flow rate [slpm]**	3	2.6	2.6	2.8
Powder feed rate [g/min]	49.7	42.6	44	28.5
Injector diameter [mm]	1.8	1.8	1.8	1.8
Injector angle [°]	90	90	90	90
Distance torch-injector [mm]	6	6	6	5

Table 2.6 – Plasma spraying parameters used in this work for fabrication of metal and ceramic coatings. *rpm: rotations per minute. **slpm: standard litres per minute.

For YSZ and CYSZ, the same parameters were set with the purpose to achieve a powder feed rate of about 40-50 g/min and to deposit an average thickness per torch pass higher than 12 µm. YSZ coatings were produced at high and low substrate temperature, respectively, to study the effect of the cooling rate on the phase composition and the evolution of zirconia phases during re-heating. Two air jets attached to the plasma gun were used for forced air cooling. In this case, the tangential speed was three times higher than that used for slowly cooled coatings

(300 and 100 rpm, respectively). Substrate tangential speed was calculated from the turntable velocity and the turntable radius (199 mm), taking into consideration the thickness of the substrate. For plasma spraying of YSZ and CYSZ feedstocks we chose plasma spraying parameters in order to fabricate coatings with a porosity volume close to 10 %, which is the value usually recommended by turbine manufacturers in their technical specifications for real TBC applications.

For each material the deposition efficiency was calculated from the ratio between the coating mass and the total feedstock mass delivered to the plasma torch, which was determined from the powder feed rate and the spraying time on the substrate. The deposition rate of CoNiCrAlY powder, *i.e.* the average thickness per torch pass, was measured by a digital micrometer with a resolution of 1 µm (Digitrix II, Nsk, Osaka, Japan) and was equal to 18.1 µm (standard deviation = 1.7 µm), while the average deposition efficiency was equal to 80.1 % (standard deviation = 6.3 %).

For slowly cooled YSZ coatings, produced at 100 rotation/min, the deposition rate was equal to 14.4 µm with a standard deviation of 0.2 µm. In turn, the deposition efficiency was equal to 53.5 %, with a standard deviation of 0.8 %. At constant coatings thickness, with increasing the substrate rotation up to 300 rpm, the deposition rate decreased to 12.7 µm (standard deviation = 0.1 µm), while the deposition efficiency decreased to 47.1 % (standard deviation = 0.4 %). The deposition rate for CYSZ was 12.9 µm (standard deviation = 1.0 µm), while the deposition efficiency was 47.5 % (standard deviation = 3.78 %).

For nanostructured coatings the deposition rate was 9.64 µm (standard deviation = 0.21 µm), while the deposition efficiency was 47.2 % (standard deviation = 1.04 %).

After deposition the coated samples were ultrasonically cleaned in ethanol for 10 min and dried at 100 °C in oven. Their weight was measured by using an analytical balance with a resolution of 0.02 mg (mod. AA200DS, Denver Instrument, Arvada, CO, U.S.) and their

thickness was measured by using a digital multimeter with a resolution of 1 µm (Digitrix II, NSK, Osaka, Japan). Standard and optimized metallographic procedures were performed for characterization purposes.

2.4 Microstructural Characterization

2.4.1 Phase Analysis

Phase composition of powder feedstocks, as-sprayed and heat-treated metallic and ceramic coatings was investigated by using an X-ray Powder Diffractometer (PW1880, Philips, Almelo, Netherlands) operating with CuKα radiation (λ = 0.154186 nm) produced at 40 kV and 40 mA. The analyzed range of the diffraction angle 2θ was between 20° and 90° with a step width of 0.02° and a time per step equal to 5 s. XRD analysis was performed on the surface of metal and ceramic coatings without any surface preparation. The phase composition of all the plasma sprayed coatings was qualitatively investigated and compared to that of the starting powder feedstocks, to analyze the thermal effects associated to high-temperature plasma spraying process.

Quantitative structural analysis was carried out on as-sprayed and annealed YSZ and CYSZ coatings, by using the Rietveld technique and the free-domain Maud software (Material Analysis Using Diffraction, version 2.074, Luca Lutterotti, University of Trento, Italy, 2009), in order to study high-temperature evolution of zirconia phases after thermal aging. Due to the coexistence of several zirconia phases whose peaks are partially or totally overlapped, the Rietveld refinement can result very difficult and tedious, so that the best solution was to analyze the coating structure in well-determined 2θ ranges, where the various zirconia phases were well observable and their contents were quantifiable with precision. The (200) and (400) reflections were the most suitable peaks for quantitative analysis of zirconia phases. To this purpose, the (400) crystalline peaks were deconvoluted and analyzed in the range 72-75°. This range was considered for the calculation of the relative proportions of tetragonal and cubic zirconia phases in as-sprayed and annealed coatings. The range 27-32° and the (100) crystalline peaks were in turn considered to calculate the percentage monoclinic phase.

The peak shape was fitted with a pseudo-Voigt function convoluted with an asymmetric function, whereas the background was adjusted by a five-parameter polynomial function. The instrumental parameters, including three Caglioti parameters for Full Width at Half-Maximum (FWHM), two asymmetry factors and two parameters for Gaussian content of peak profiles, were fixed to the values obtained for standard material used for the determination of the instrumental broadening.

The lattice parameters, the crystallite size and the r.m.s. microstrains were refined for both tetragonal and cubic zirconia phases, as well as the fractional z coordinate of the O^{2-} anion in the tetragonal asymmetric unit. The R_p parameter, representative of fitting goodness, was calculated after removing the background contribution. It should be noted that surface roughness may generate a microabsorption effect, *i.e.* a reduction of the peak intensity, especially at low angles. B-factors (isotropic temperature factors) were fixed for each chemical element to standard values, without modifying the quality of the fit.

The lattice parameters of zirconia phases depend on the content of the stabilizer. In particular, for a standard YSZ system, a metastable t' phase can be distinguished from a stable t phase due to its smaller c/a lattice parameter ratio, *i.e.* higher stabilizer content.

The yttria content in both tetragonal zirconia phases was quantified by using the formula reported by Ilavsky [1]:

$$Y_2O_3 \text{ (mol. \%)} = \frac{\left(1.0225 - \frac{c}{a\sqrt{2}}\right)}{0.0016} \qquad (2.1)$$

where a [Å] and c [Å] are the lattice parameters for each tetragonal phase.

In turn, the yttria content of the cubic phase was calculated from [2]:

$$Y_2O_3 \text{ (mol. \%)} = \frac{(a - 5.1159)}{0.001547} \qquad (2.2)$$

where a [Å] is the lattice parameter of the cubic phase.

2.4.2 Morphology and Microstructure of Plasma Sprayed Coatings

The metallographic preparation of plasma sprayed coatings is an important step which can strongly affect their final properties. Coating surface may be generally observed without any preparation, as well as the fractured cross section which may be obtained by mechanical breaking or cutting. However, in order to better analyze all the microstructural features of plasma sprayed coatings, such as pores, splat boundaries and microcracks, coating cross section has to be properly prepared. Grinding and polishing steps are needed to produce a cross section suitable for SEM observation at both low and high magnifications.

In this work, the cross sections were obtained by sectioning the coatings by low-speed precision saw (Isomet, Buelher Ltd, Lake Bluff, Illinois, U.S.), equipped with diamond wafering blades recommended for precise and accurate sectioning of thermally sprayed coatings (see Fig. 2.11).

Then they were cleaned and cold-mounted in vacuum in a two-part epoxy polymer, composed of resin and hardener, respectively. The specimens were evacuated in a vacuum dessiccator (Vacuum Impregnation Pump, Buelher, Lake Bluff, Illinois, U.S.), as well as the mounting material which might penetrate and fill the open pores and the microcracks. The filling is recommended in order to preserve the starting size and the shape of the pores and to minimize the pull-out effect which may occur during grinding and polishing steps. Moreover, it allows a high definition of all the microstructural features during SEM observations.

The cross sections were ground by using a grinder-polisher machine (Motopol 2000, Buelher Ltd, Lake Bluff, Illinois, U.S.) and SiC abrasive papers with grain size of 35 and 26 μm, and special diamond discs (20 and 10 μm). Running water was used as lubricant in order to remove and to flush the abrasion debris from the abrasion track.

Figure 2.11 - Low speed saw used for coating sectioning.

Figure 2.12 – Consumables for grinding and polishing procedures.

After each step the specimens were ultrasonically cleaned in demineralized water. Then, they were polished in order to remove the damages produced during the previous steps. Texmet cloths were used in conjunction with diamond abrasive pastes and suspensions (6 µm, 3 µm and 1 µm, respectively). Finally, they were finished up to 0.25 µm by using an alumina suspension. A suspension composed of ethanol and oil was used for cooling and surface

lubrication during polishing. The contact pressure and the rotation speed were set on the basis of the recommendations provided by Buehler manual for thermally sprayed coatings, in order to reduce coating damaging. It is well known that a typical pull-out effect can occur during polishing, thus modifying the final microstructure. Unmelted or partially melted hard ceramic particles can be pull-out from the coating cross section, producing large pores that lead to an overestimation of the porosity volume. Figure 2.12 shows some grinding papers and Texmet cloths used for grinding and polishing as well as diamond coated blades used for coating sectioning.

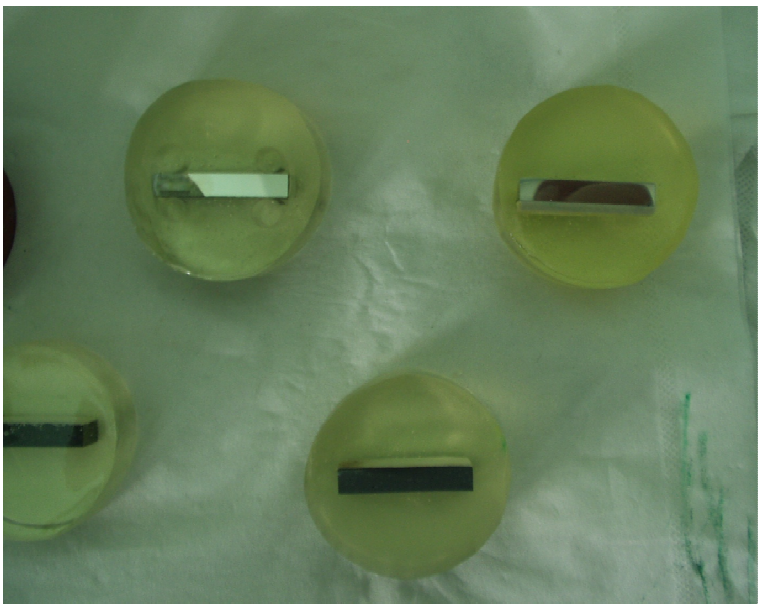

Figure 2.13 – Polished coatings cross sections.

The polished cross sections were ultrasonically cleaned in ethanol and dried at 100 °C in oven (Ghibli Plus, Carlo Erba Reagenti, Milano). Figure 2.13 shows some polished coating cross sections (metal substrate is observable), while Figure 2.14 shows polished cross sections of free-standing CYSZ coatings after aging tests at 1315 °C for different times.

Preliminary observations were performed by using an optical microscopy (Olympus Vanox AHMT3, Olympus Europe GmbH, Hamburg, Germany). A very thin gold film (thickness ~

20 nm) was sputter-deposited on each polished cross section to prevent surface charging during SEM observations. The feedstock morphology and the microstructure of plasma sprayed coatings were analyzed by using Scanning Electron Microscopy (SEM) equipped with energy-dispersive spectroscopy (EDS) for analysis of elements and compounds. The following microscopes have been used: SEM XL40, Philips, Eindhoven, Netherlands; SEM Evo 40, Carl Zeiss, Oberkochen, Germany. Both SE and BSE detectors were employed to investigate the morphology and the microstructure of coating cross section, respectively.

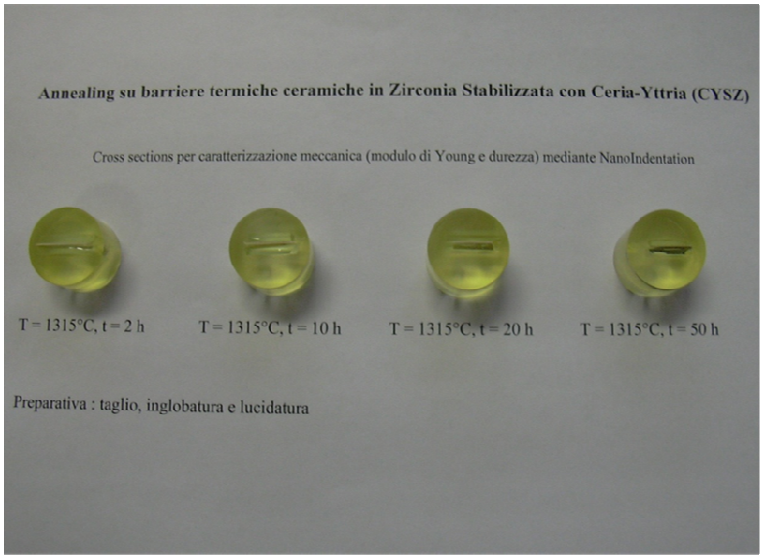

Figure 2.14 – Polished cross sections of annealed free-standing CYSZ coatings.

Several micrographs at various magnifications (400x, 700x, 900x, 1000x, 1200x, 2000x, 3000x) were acquired in order to cover large areas of coating cross-section and to better appreciate all the microstructural features. In some cases fractured surfaces and cross sections of as-sprayed and annealed coatings were also analyzed.

2.4.3 Image Analysis

In this work, image analysis (IA) was used for quantitative and qualitative analysis of coating microstructure, to study both morphology and size of microstructural defects and to calculate the porosity volume. Grey-scale SEM images at various magnifications were processed by using a free image analysis software (Image J, National Institutes of Health, Bethesda, MD, U.S.). Image Analysis measures both open and closed porosity, due to the high degree of contrast between the dark pores and the highly reflective material. A numerical value, ranging from 0 to 255 for 8-bit images, was automatically assigned by the software to each pixel depending on the brightness.

The software associated a grey-scale histogram to each area selected by the operator, computing the number of pixels for each grey level. The images were automatically thresholded and transformed in binary-images (black and white), taking into account the significant light scattering. So, the microstructure was considered as a two-phase composite material, composed of ceramic and air. The cumulative number of dark pixels versus total pixels (bright and dark) provided the porosity volume.

Simple binary operations were performed on grey-scale images in order to highlight and to distinguish all the typical microstructural features of plasma sprayed coatings, such as globular pores, interlamellar and intralamellar microcracks. The globular pores can be more or less homogeneously distributed. They include coarse pores with spherical shape and finer pores, produced by incomplete filling between the deposited splats. Microcracks include finer interlamellar pores resulting from the incomplete contact between the overlapping lamellae during coating formation (when a splat is deposited, the previously deposited material is just solidified) and vertical microcracks, resulting from relaxation of thermal stresses within each deposited splat during rapid cooling to room temperature. Obviously, the final microstructure

of the as-sprayed coatings is strongly related to processing parameters and to the thermal history of the sprayed particles, *i.e.* their temperature and velocity.

To this purpose, an opening operation was performed on each starting binary image, so that a layer of pixels was removed from the periphery of each object (pore or microcrack) and then a layer of pixels was added to the perimeter of each remaining object. Therefore, the thinnest objects were deleted, whereas the objects showing larger area-perimeter ratio were retained. By subtracting this last image to the starting binary image, a picture for only microcracks was obtained. These cracks were classified as horizontal or vertical, depending on their angle with coating-substrate interface.

Otherwise, as discussed in detail in the next sections, metal coatings were denser than ceramic ones and their microstructure was mainly composed by globular pores and oxides produced by high-temperature in-flight oxidation of the exposed surface of the molten sprayed particles during deposition. These oxides appeared as dark veins that run approximately parallel to the coating-substrate interface. So, they could be distinguished from the globular spherical pores due to their elongated shape (different aspect ratio). Thereby, their amount was quantified. It should be noted that tens of SEM images at different magnifications have been considered for an accurate estimation of the porosity volume for all the coatings.

2.5 Mechanical properties

2.5.1 Impulse Excitation Technique

The knowledge of Young's modulus is of concern because it has a significant effect on the strain tolerance and the stress level and, hence, on the durability of plasma sprayed coatings. The knowledge of the stiffness enables the determination of additional mechanical properties, such as fracture toughness, using the barb shear test, or it can be adopted, in conjunction with the porosity level, to predict the residual stress distribution using micromechanical models and/or object-oriented finite element method. Limited informations can be found in literature concerning some mechanical properties of plasma sprayed coatings. The data published in literature about Young's modulus are mainly referred to YSZ coatings and they have been obtained by mainly resorting to instrumented indentation [3,4] or standard static bending techniques [5,6,7]. Indentation techniques provide local values of Young's modulus and, as a consequence, these last ones can be significantly different from those provided by bending tests which, on the contrary, are macroscopic values, *i.e.* averaged over the sample volume [8]. Bending tests provide the in-plane elastic modulus as the tangent of the stress-strain curve corresponding to the coating. However, it has been demonstrated that bending tests could be problematic for APS coatings, their inherent porosity leading to material crushing near loading pins during testing [8]. Owing to splat boundary sliding and propagation of cracks, inelastic deformations occur during testing. As an alternative, vibration-based iterative procedures have been recently proposed for the elastic characterization of APS YSZ coatings [9,10,11]. The common thread is the application of inverse finite element routines to estimate the elastic properties (and the damping factor) of the coatings from the measured experimental frequencies of vibration. In [9,10] the damping and the Young's modulus of APS YSZ coatings have been investigated as a function of strain amplitude using coated cantilever-

beam specimens, whereas in [11] beam-shaped samples with free boundary conditions have been employed for elastic properties calculation.

These dynamic techniques have the advantage of being simple, fast and accurate. Moreover, they require an inexpensive experimental equipment and can be used for rapid production process monitoring. In addition, dynamic techniques allow to determine the elastic modulus subjecting the specimen to lower strains, so that they are measured nearly at the origin of the stress-strain curve, thus preventing fracture and non-linear material response.

In this study, a macroscopic value of Young's modulus for CoNiCrAlY and CYSZ coatings was measured using a resonant method known as the impulse excitation technique (IET) [12,13,14], in conjunction with a bi-layer specimen configuration. The IET is a resonant-based method for measuring the elastic properties of a solid. It can be applied if a proper frequency equation, relating the stiffness to the natural frequencies, the mass and the geometrical properties of the specimens, is given. In this work, the specimens adopted for stiffness measurements were beam-shaped steel (Fe360) substrates (100 x 25 x 3 mm^2) coated with a nominal 300 µm thick CYSZ coating. Indeed, in order to simplify the calculation procedure, the bond coat was not applied. Moreover, the macroscopic elastic modulus of CoNiCrAlY coatings was also measured, taking into consideration the same substrates, but coated with a 350 µm thick CoNiCrAlY coating. First experimental trails were performed to study the feasibility and to optimize the experimental procedure. In both cases, each layer is considered to be homogeneous, isotropic and with a linear elastic behaviour. In addition, a perfect bonding at the interface between the coating and the substrate was assumed. For such a composite beam, a proper frequency equation may be expressed, neglecting shear and rotary inertia, as follows [15]:

$$f = \frac{k_n{}^2}{2\pi L^2}\sqrt{\frac{B(E_c I_c + E_s I_s)}{m}} \qquad (2.3)$$

where k_n, in the case of flexural vibration and free edge conditions, are the solutions to the characteristic equation $1 + \cos(k_n)\cosh(k_n) = 0$; I is the moment of inertia about the centroidal axis of the beam; m is the mass per unit length of the coated sample; L is specimen length; B is specimen width; f is the fundamental flexural frequency of free vibration; E is Young's modulus; finally, the subscripts c and s denote the coating and the substrate, respectively. The detailed procedure followed for the determination of the frequency equation is reported in Appendix I.

It is worth noting that in Eq. (2.3) all the laminate constituent materials were assumed to be homogeneous and dense. This implies that coating porosity is taken in account indirectly by reducing the elastic properties.

Young's modulus of the substrates was determined before coating deposition, resorting to the standard procedures and the recommendations of ASTM standards for the elastic characterization of isotropic materials [16]. In particular, E_s was determined using the following equation:

$$E_s = 0.9465 \frac{m_s f_s^2}{B} \frac{L^3}{h_s^3} \left[1 + 6.585 \left(\frac{h_s}{L} \right)^2 \right] \tag{2.4}$$

where, m_s is the mass of the test beam, f_s the fundamental natural frequency of vibration and h_s represents the substrate thickness. Therefore, the elastic modulus of the coating was obtained inverting Eq. (2.3) for E_c if the corresponding experimental variables were properly measured.

In particular, for the system examined herein, a sensitivity analysis showed that the experimental variables which greatly contribute to measurement uncertainty were substrate thickness (h_s) as well as frequency (f) measurements. A digital micrometer (± 0.001 mm) and

a digital calliper (± 0.01 mm) were employed to measure the thickness and the in-plane dimensions, respectively. Mass measurement was carried out using a precision digital balance (± 0.01g).

Finally, frequency measurements were carried out in a non-contact way out using a previously developed *ad hoc* apparatus [13,14] which allows resolutions up to 0.1 Hz to be obtained. A schematic depiction of the experimental set-up is reported in Fig. 2.15.

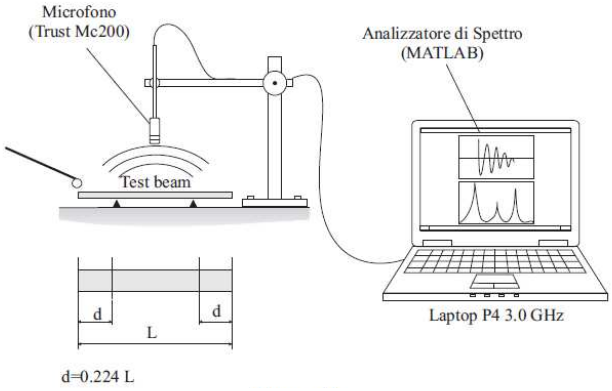

Figure 2.15 – Experimental set-up employed for IET measurements.

In order to accommodate the free boundary condition described by Eq. (2.3), each sample was supported on direct contact supports made of soft material, *i.e.* soft sponge, showing a minimal contact area with the specimen. The supports were placed in location (nodal lines) which allowed the beam to oscillate resembling free boundary conditions, *i.e.* 0.224 L from specimen edges. In fact, specimens suspension is of critical concern in order to achieve good quality frequency measurement. The procedure adopted herein required specimens with all the edges free in order to accommodate free boundary conditions.

Impact excitation was imparted lightly hitting the beam and the resulting vibration was then picked up using a microphone (Trust MC200, frequency bandwidth from 50 Hz to 14000 Hz) placed near the surface of the sample. The acoustic signal was then analyzed and post-processed by a suitable program written in MATLAB^{TM} environment (MATLAB, The

Mathworks Inc., 1994-2007), in order to extract the fundamental flexural frequency of vibration (f). It transformed the sampled time functions into a frequency spectrum by a Fast Fourier Transform (FFT) algorithm allowing the identification of the fundamental natural frequency. The resolution of the measurement system depended on the time length (t_a) of the signal acquired. In this work, each measurement was carried out using an acquisition time equal to 10 s. The tests were carried out using a sample frequency of 44100 Hz. A resolution up to $\Delta f = 1/\Delta t = 0.1$ Hz was achieved. The advantage of using free boundary conditions is usually represented by a higher reproducibility. Indeed, no significant deviation was observed among the values of repeated measurements. In addition, the average signal obtained by impacting the specimen three times was considered in order to mitigate the environmental noise and to better illustrate the peaks of the frequency spectrum.

It should be noted that the presence of pores and cracks in plasma sprayed coatings has a severe impact on the mechanical properties as it can induce an anisotropic behaviour. In particular, inter-lamellar cracks and pores affect the in-plane stiffness, while the out-of-plane stiffness is affected by the intra-lamellar cracks. As a consequence, it is necessary to consider the measurement direction in determining the elastic modulus of the deposit or comparing the results provided by different techniques.

The results obtained have been then discussed and a cross-check on their consistency was carried out by resorting to a micromechanical model, as described in the next sections.

Since Nanoindentation (NI) was also used for mechanical characterization of plasma sprayed coatings, it should be noted that Impulse Excitation Technique and NI provide different results, because they typically measure the mechanical properties of the same coatings at different scales. NI probes the microstructure at splat level, then the corresponding values of Young's modulus should be regarded as a local material property. On the other hand, IET works at the macroscopic level, *i.e.* it provides material properties averaged over sample

volume. As a consequence, a direct comparison cannot be made. However, the local values of Young's modulus as well as the porosity level can be adopted as inputs in a micromechanical model in order to get a rough estimation of coating global stiffness (E*). Such values can be compared with the values provided by the IET, thus providing a cross-check on the consistency among the various results obtained. From this standpoint, various theoretical models have been proposed in the literature: the Hashin-Hasselman model [17,18] is widely employed. Young's modulus is given as follows:

$$E^* = E_0 \cdot \left[1 + \frac{A \cdot p}{1 - (A+1)p} \right] \qquad (2.5)$$

where A = -33.4 [19], p is the volume fraction of all the pores, cracks and interfaces, and E_0 is the elastic modulus of the dense material. The Poisson's ratio (ν = 0.22) reported in [20] was considered for calculations.

2.5.2 Microhardness

The mechanical characterization of plasma sprayed coatings is commonly performed by using indentation tests. In this work, microhardness measurements were carried out on the polished cross sections of as-sprayed and heat-treated CYSZ coatings. These tests are destructive, but several indentations can be performed on very small samples.

To this purpose, a Vickers microindenter (Matsuzawa, Seiki MHT-1) was employed. The measurements were performed at room temperature in air using a load of 300 gf and a dwell time of 15 s. The Vickers microhardness was calculated using the following equation [21]:

$$HV = \frac{2P\sin\left(\frac{\theta}{2}\right)}{d^2} = 1.854 \cdot \frac{P}{d^2} \quad (2.6)$$

where P is the applied load, θ the angle between the opposite faces of the pyramidal indenter (136°) and d the mean diagonal of the indentation. For each sample, the average was measured from the mean of at least 15 indentations and the spacing between each of them was kept at least thrice the diagonal to avoid further stresses induced by mutual influence of consecutive indentations.

For as-sprayed CoNiCrAlY coatings a load of 200 gf was used, while for as-sprayed nanostructured YSZ coatings a load of 100 gf was used, because higher indentation loads typically induced significant cracks in these coatings.

To this purpose, it is worth noting that plasma sprayed porous coatings are commonly characterized by several microstructural defects, such as pores with different size and shape, vertical microcracks and splat boundaries. These features are responsible of a large scatter in the distribution of hardness values. So, a Gaussian distribution can be less useful to analyze the mechanical properties. On the contrary, Weibull statistical analysis is more suitable for this purpose and, therefore, the experimental data obtained during the mechanical tests were presented by means of Weibull statistical analysis.

2.5.3 Nanoindentation

Nanoindentation is increasingly employed for measuring the mechanical properties of thermally sprayed coatings, because it offers some significant advantages in comparison with other techniques. Indeed, it allows to perform multiple tests on a single specimen and to obtain reliable data about some basic mechanical properties, such as Young's modulus and hardness

In this work, depth-sensing nanoindentation tests were performed to calculate both local elastic properties and hardness of as-sprayed and heat-treated CYSZ and CoNiCrAlY coatings, in order to study the evolution of these mechanical properties as a function of the aging time. Single-cycle NI tests were carried out on coating cross sections using a Nano-Test Platform 2 (Micromaterials Ltd, Wrexham, UK) employing a Berkovich tip (radius < 100 nm). For such a test, the selected samples were prepared by using the same procedure as that adopted for SEM observations. A microscope allowed the user to select the indentation location on coating cross section. The hardness and the reduced Young's modulus were determined from the analysis of the data corresponding to the unloading segment of the load-penetration (P-h) curves, following the procedures outlined by Oliver and Pharr [3,22]. A typical P-h curve is presented in Fig. 2.16. Figure 2.17 illustrates some characteristic parameters which come into play in the determination of the mechanical properties and which are introduced in what follows.

In particular, the hardness of the coatings can be expressed as the ratio of the maximum applied load P_{max} to the projected indentation area, A_c, as follows:

$$H = \frac{P_{\max}}{A_C} \tag{2.7}$$

where

$$A_C = 24.5 \cdot h_c^2 \tag{2.8}$$

in the ideal case. In our case, the diamond area function of the Berkovich indenter was calibrated by indentations to different depth into a calibration standard of fused quartz (load range: 0.5-20 mN) and was found to be $A_c = 25.2\,h_c^2 + 5779.2\,h_c$.

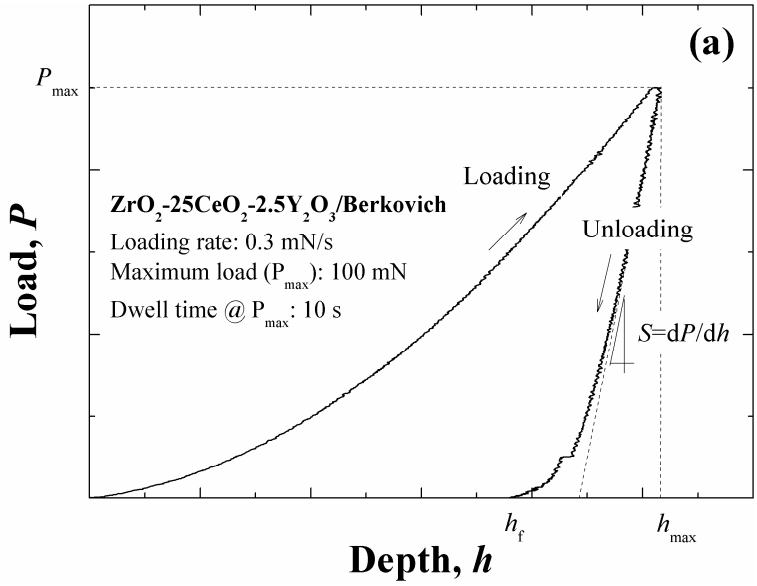

Figure 2.16 – Typical load-penetration (P-h) curve obtained from a Nanoindentation test on as-sprayed CYSZ coating.

The plastic or contact depth h_c before unloading can be estimated from the P-h curve using the following equation:

$$h_C = h_{max} - \varepsilon \frac{P_{max}}{S} \qquad (2.9)$$

where $\varepsilon = 0.72$ is a constant depending on the geometry of the indenter and $S = dP/dh$ is the slope of the unloading curve.

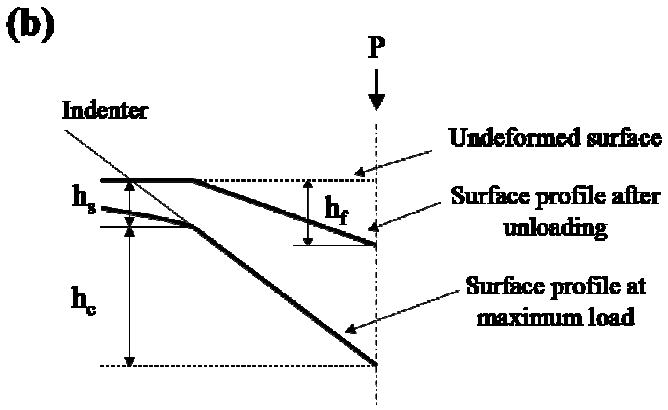

Figure 2.17 – Geometrical parameters related to key experimental quantities.

Assuming that the contact area remains constant during initial unloading, the reduced Young's modulus E_r can be expressed as follows:

$$E_r = \frac{1}{2\beta h_c}\sqrt{\frac{\pi}{A_c}}\left(\frac{dP}{dh}\right) \tag{2.10}$$

with

$$\frac{1}{E_r} = \frac{1-\nu^2}{E} + \frac{1-\nu_i^2}{E_i} \tag{2.11}$$

where E_i = 1141 GPa and ν_i = 0.07 are Young's modulus and Poisson's ratio of the diamond indenter, E is the Young's modulus of the coating and β is dimensionless parameter which varies with indenter shape (1.012 < β < 1.034). The later value has been adopted for instrumented indentation testing with Berkovich indenter in [22]. In order to assess the influence of the loading rate on the hardness and the Young's modulus, the first tests were carried out at 0.3, 3 and 10 mN s^{-1}, respectively. Holding time and the maximum load through

the tests were set to 10 s and 100 mN, respectively. Then, the loading rate was set equal to 0.3 mN/s for CYSZ coatings and 3.0 mN/s for CoNiCrAlY coatings.

The dwell time for CoNiCrAlY coatings was selected to account for creep issues during the experiments. In particular, for a constant load hold period, the indentation depth may increase with time. It follows that creep effects can lead to a net increase of indentation depth during the early stages of unloading thereby affecting the elastic modulus determined using Eq. (2.10). An extensive study on this subject was carried out in [23], it was shown that the maximum load should held constant for a time interval in the range 10-60 s to make creep effects negligible. In the present work a holding time of 60 s was then selected. An array of 5 x 10 indents was made for each condition and the results were presented using Weibull statistics.

A total number of almost twenty indentations was carried out for each sample to obtain an average value; the distance between the indentations was equal to 40 μm to avoid a mutual influence of consecutive responses.

2.6 Thermal Properties

As mentioned in the previous sections, for thermo-physical characterization the thickness of the ceramic TBCs was of about 2 mm, because lower thicknesses were not suitable for a reliable and an accurate determination of the thermal properties. Indeed, it is rather difficult to measure thermal properties of thin coatings.

Various measurement techniques were employed for the determination of the thermo-physical properties of as-sprayed and annealed YSZ and CYSZ coatings. For the measurement of the thermal expansion, the samples were analyzed with a Netzsch dilatometer (Model TMA 402, Netzsch-Gerätebau GmbH, Selb, Germany). The system here employed is mounted vertically and consists of a linear variable displacement transducer (LVDT) with thermo-stated housing. Changes in length of a sample caused by expansion or shrinkage move the quartz pushrod on the ferrite core of LVDT and cause an electrical signal in its coil. This electrical signal is amplified and recorded as a change in length. The temperature of the sample was measured and recorded by a thermocouple. Thermal expansion measurements were carried out in static air on free-standing samples 8 mm long and 2 mm thick, at 10 °C/min heating rate and up to 900 °C. Three consecutive scans were collected for each sample and both in-plane and out-of-plane thermal expansions were measured. To check the accuracy of the push-rod dilatometer three measurements in the same conditions were carried out on a synthetic sapphire (NS SRM 732) from room temperature to 900°C. The calculated mean linear expansion coefficient was compared with the mean value of the standard material reported in literature (9.2×10^{-6} K^{-1}). The accuracy was equal to 3 %.

For the determination of specific heat capacity and for DSC analysis of YSZ and CYSZ samples, the Simultaneous Thermal Analyzer (Model STA 429, Netzsch-Gerätebau GmbH, Selb, Germany) equipped with a sample holder for differential scanning calorimetry (type *S*

sensor) was used. Eq. (2.12) constitutes the ratio method and was used to determine the specific heat of the ceramic coating directly from the STA data [24]:

$$Cp_s = Cp_{std}\,(m_{std}/m_s)(\Delta T_s/\Delta T_{std}) \qquad (2.12)$$

The subscript *std* indicates the sapphire standard, *s* indicates the sample, ΔT are the ordinate deflections from the sample, standard and baseline, and *m* indicates the mass. DSC samples were approximately cut to 3x3x2 mm^3. The sample weight used for Cp and DSC measurements was approximately 120 mg, and the measurements were done in static air using Pt crucibles with lids, at 10 °C/min heating rate. The measurements were performed from room temperature up to 1250 °C. As standard reference material a synthetic sapphire disc was used (Cp of sapphire at 20 °C: 0.775 J/g*K – NBS literature value). Three consecutive measurements cycles were performed for each sample. The evolution of the above mentioned thermal properties was investigated for YSZ and CYSZ thermal barrier coatings during thermal aging, in order to study their high-temperature sintering behaviour.

2.7 High-temperature Aging Tests

Plasma sprayed metal and ceramic coatings have to be carefully characterized and tested in order to predict their behaviour at in-service conditions.

It can be rather difficult to reproduce in laboratory the same operating conditions experienced during service. However, isothermal tests can be arranged. Indeed, in order to study the evolution of the microstructural and mechanical properties at high temperature and in oxidizing atmosphere, the coatings can be exposed at high temperatures and for different times.

2.7.1 Early-Stage Oxidation Behaviour of CoNiCrAlY Coatings

CoNiCrAY coatings were isothermally heat treated in air furnace at 1030 °C and 1110 °C for 2 and 24 h at heating rate of 6 °C/min, in order to study the effects of first-stage oxidation on the phase composition, the microstructural and the mechanical properties. Fig. 2.18 shows some examples of as-sprayed and oxidized CoNiCrAlY coatings. It should be noted that the coated components are commonly exposed for much longer times in real environments, but the oxidation rate is higher in the first 10-20 hours of thermal exposure and it has a strong effect on the oxidation rate of the following steady-state oxidation stage. Instead, the study of medium and long-term oxidation resistance is out of the objectives of this work.

After isothermal oxidation tests, the coatings were addressed to XRD analysis, SEM observations and NI measurements, using the experimental procedures previously described. Phase analysis and oxide scale characterization were performed by using X-Ray Diffraction (XRD). The study of high-temperature phase changes is an important key issue. Indeed, as known, a ceramic top coat can be also applied on the surface of CoNiCrAlY coating to guarantee a further thermal protection. During in-service high-temperature exposure, a thermally grown oxide (TGO) layer typically grows on the top-surface of CoNiCrAlY

coating. An uniform and dense TGO, composed of pure Al_2O_3 and with a slow growth rate, may provide further protection against oxygen and increase the component lifetime [25,26].

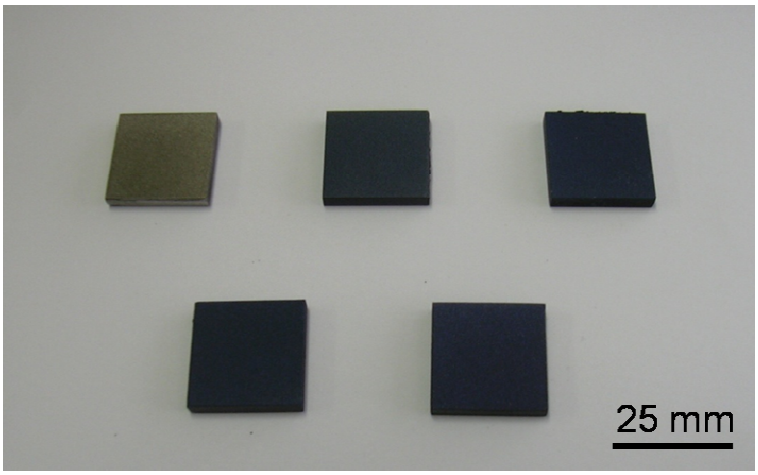

Figure 2.18 – As-sprayed and oxidized CoNiCrAlY coatings.

On the contrary, a rapid oxide growth rate induces localized stress concentrations at the interface, accelerating cracking and leading to TBC spallation.

2.7.2 Aging Tests on Micron-Sized Zirconia-Based TBCs: Study of Phase Stability and Sintering Behaviour

Isothermal tests can be also performed in order to study the sintering behaviour of ceramic coatings during high-temperature exposure. The properties of heat-treated coatings were compared to those of as-sprayed ones, in order to study the phase stability and high-temperature sintering kinetics of the porous microstructure, *i.e.* the evolution of the microstructural properties (porosity), mechanical properties (hardness and Young's modulus) and thermal properties (CTE and heat capacity).

Before heat treatment, YSZ and CYSZ coatings were cut to the desired dimensions and stripped off from their substrates by chemical etching, by using a 50/50 (vol. %) HCl-H_2O

solution. The acid attacked the interface between the bond coat and the top coat. Then, the detached ceramic coatings were cleaned by rinsing and infiltration of water, acetone and ethanol to remove acid residue and other contaminants. Free-standing coatings were then isothermally annealed at 1315 °C in an air furnace for 2, 10, 20 and 50 h, at heating rate of 6 °C/min and then slowly furnace cooled down to room temperature (mod. B.E. 35, Bicasa, Milano, Italy). In fact, the overall effects of thermal aging on the microstructure are emphasized within the first 25-50 hours of heat treatment and then they slow down as the coating is partially sintered.

The specimens were studied in free-standing state because the temperature chosen for the tests was above the capability of the metal substrate. This choice was also made to avoid high-temperature diffusion of elements at the interface between bond coat and top coat. Moreover, it has been reported that the thermal stresses generated by the mismatch in thermal expansion coefficients between coating and substrate can hinder and retard sintering effects [27]. For this reason, comparative analyses are often performed considering free-standing specimens [27,28,29]. Thermal residual stresses can also affect indentation responses and, as a consequence, hardness and Young's modulus determination [30,31,32,33].

In particular, since the sintering behaviour of YSZ thermal barrier coatings have been reported in previously published works, the attention was mainly focused on CYSZ coatings. The evolution of the phase composition has been studied by means of X-ray Diffraction, whereas Scanning Electron Microscopy was employed to study the evolution of the microstructure with increasing the aging time. The porosity was evaluated on SEM pictures by using Image Analysis. High-temperature evolution of the mechanical properties was investigated by performing NI measurements.

Appendix I

The frequency equation can be generally obtained by integration of the equation of motion in accordance with the prescribed boundary conditions. For example, an exact solution of the three-dimensional form of the differential equation of motion was obtained for the axial and the torsional vibration of an infinite length isotropic circular bar with free edge conditions [34]. For finite length isotropic bars (circular or rectangular cross sections) and other simple geometries, such as circular thick plates, only approximate numerical solutions exist [35,36,37,38,39] and these approximate numerical solutions are recommended in ASTM standards for the elastic characterization of isotropic materials [16,40]. Nevertheless, different geometries could be also used if the corresponding frequency equations are known. For example, a procedure that extends resonant method to isotropic samples in the form of thin rectangular plates was proposed in [12] and then it was applied to a free-standing diamond coating in [13,14]. However, the methodologies mentioned above are not suited for coated samples, *i.e.* coating-substrate systems. Therefore, it is necessary to develop a proper frequency equation. To this aim, let consider a composite beam consisting of two homogeneous, isotropic, linear elastic layers with constant cross section. Neglecting shear and rotary inertia effect and assuming a perfect bonding at the interface, the transverse, i.e. flexural, vibration is described by the following well-known Bernoulli-Euler equation:

$$-\left(E_c I_c + E_s I_s\right)\frac{\partial^4 w}{\partial x^4} = \left(\rho_c A_c + \rho_s A_s\right)\frac{\partial^2 w}{\partial t^2} \qquad (2.13)$$

where I is the moment of inertia about the centroidal axis of the beam, w (x,t) is the transverse displacement, A is the cross sectional area, ρ is the mass density, E is the modulus of elasticity while the subscripts c and s denote the coating and the substrate, respectively. A schematic depiction of the resulting composite beam is reported in Fig. 2.19.

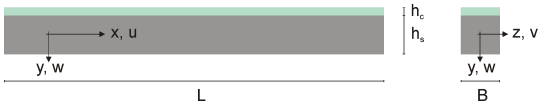

Figure 2.19 – Schematic representation of a bi-material beam.

In order to solve Eq. (2.13), one can resort to the method of separation of variables. Therefore, considering harmonic free vibrations, the transverse displacements can be written as:

$$w(x,t) = W(x)\, e^{i\omega t} \tag{2.14}$$

where ω is the frequency of vibration and W (x) is a mode shape function. Substituting this solution in Eq. (2.13) and rearranging yields the following:

$$\frac{d^4 W(x)}{dx^4} - k^4\, W(x) = 0 \tag{2.15}$$

where

$$k = \left[\frac{\rho_c A_c + \rho_s A_s}{E_c I_c + E_s I_s} \omega^2 \right]^{1/4} \tag{2.16}$$

A suitable shape function for solving Eq. (2.15) has the following form:

$$\begin{aligned} W(x) &= C_1 \sin(kx) + C_2 \cos(kx) + \\ &+ C_3 \sinh(kx) + C_4 \cosh(kx) \end{aligned} \tag{2.17}$$

where the C_i are integer constants which depend on the boundary conditions. From the experimentalist point of view it is advisable to choose free ends condition, because it is easier

to reproduce and affects less the frequency measurements if compared, for instance, with clamped configuration. As a consequence, for a free-free beam, since the bending moments and the shear forces are zero at both free ends, the boundary conditions of the transverse vibration are given by $W_{,xx} = 0$, $W_{,xxx} = 0$ at both x = 0 and x =L. Imposing the boundary conditions it is possible to obtain $C_1 = C_3$ and $C_2 = C_4$. The remaining equations give rise to system which solved for nontrivial solutions of C_1 and C_2 leads to the eigenvalue equation for the undamped free flexural vibration of a composite beam with free ends:

$$\cos(k\,L)\cdot\cosh(k\,L)-1=0 \tag{2.18}$$

It has an infinite number of solutions k_nL, where the subscript n refers to the mode number. The eigenvalues corresponding to the first four modes of vibration are easily found using the software package Mathematica (Stephen Wolfram, the Mathematica Book, 4th ed., Wolfram Media-Cambridge University Press, 2006) [41]. In particular, $k_1L = 4.73004$, $k_2L = 7.8532$, $k_3L = 10.9956$ and $k_4L = 14.1372$. Substituting the eigenvalues in the definition of k, *i.e.* Eq. (2.16), and using the relationship $\omega = 2\pi f$, it is possible to obtain the frequency equation:

$$f_n=\frac{(k_n L)^2}{2\pi L^2}\left(\frac{E_c I_c+E_s I_s}{\rho_c A_c+\rho_s A_s}\right)^{1/2} \tag{2.19}$$

The in-plane elastic modulus of the coating can be thus be obtained.

References

[1] J. Ilavsky and J. K. Stalick, Phase composition and its changes during annealing of plasma-sprayed YSZ, Surf. Coat. Technol. 127(2-3) (2000) 120-129.

[2] J. Ilavsky, J. K. Stalick and J. Wallace, Thermal spray yttria-stabilized zirconia phase changes during annealing, J. Therm. Spray Technol. 10(3) (2001) 497-501.

[3] W. C. Oliver and G. M. Pharr, An improved technique for determining hardness and elastic modulus using load and displacement sensing indentation experiments, J. Mater. Res. 7 (1992) 1564-1583.

[4] O. Racek and C. C. Berndt, Mechanical property variations within thermal barrier coatings, Surf. Coat. Technol. 202 (2007) 362-369.

[5] F. Tang and J. M. Schoenung, Evolution of Young's modulus of air plasma sprayed yttria-stabilized zirconia in thermally cycled thermal barrier coatings, Scripta Mater. 54 (2006) 1587-1592.

[6] F. Cernuschi, P. G. Bison, S. Marinetti and P. Scardi, Thermophysical, mechanical and microstructural characterization of aged free-standing plasma-sprayed zirconia coatings, Acta Mater. 56 (2008) 4477-4488.

[7] M. Beghini, G. Benamati, L. Bertini and F. Frendo, Measurement of coatings' elastic properties by mechanical methods: Part 2. Application to thermal barrier coatings, Exp. Mech. 41 (2001) 305-311.

[8] H. J. Kim and Y. G. Keown, Elastic modulus of plasma-sprayed coatings determined by indentation and bend tests, Thin Solid Films 342 (1999) 201-206.

[9] S. Patsias, N. Tassini and K. Lambrinou, Ceramic coatings: effect of deposition method on damping and modulus of elasticity for yttria-stabilized zirconia, Mater. Sci. Eng. A 442 (2006) 504-508.

[10] N. Tassini, K. Lambrinou, I. Mircea, M. Bartsch, S. Patsias and O. Van der Biest, Study of the amplitude-dependent mechanical behaviour of yttria-stabilized zirconia thermal barrier coatings, J. Eur. Ceram. Soc. 27 (2007) 1487-1491.

[11] T. Lauwagie, K. Lambrinou, S. Patsias, W. Heylen and J. Vleugels, Resonant-based identification of the elastic properties of layered materials: application to air-plasma sprayed thermal barrier coatings, NDT & E Int. 41 (2008) 88-97.

[12] M. Alfano and L. Pagnotta, Determining the elastic properties of isotropic materials by modal vibration testing of rectangular thin plates, J. Sound Vibration 293 (2006) 426-439.

[13] M. Alfano and L. Pagnotta, Measurement of the dynamic elastic properties of a thin coating, Rev. Scient. Instr. 77 (2006) art. No. 056107.

[14] M. Alfano and L. Pagnotta, A non destructive technique for the elastic characterization of thin isotropic plates, NDT & Int. 40 (2007) 112-120.

[15] C. C. Chiu and E. D. Case, Elastic modulus determination of coating layers as applied to layered ceramic composites, Mater. Sci. Eng. A 132 (1991) 39-47.

[16] American Society for Testing Materials, Standard test method for dynamic Young's modulus, shear modulus and Poisson's ratio by impulse excitation of vibration, ASTM E1876-01; American Society for Testing Materials, Philadelphia, PA, 2001.

[17] Z. Hashin and S. Shtrikman, A variational approach to the theory of the elastic behaviour of multi-phase materials, J. Mech. Phys. Sol. 11(2) (1962) 452-453.

[18] D. P. H. Hasselman, On the porosity dependence of the elastic moduli of polycrystalline refractory materials, J. Am. Ceram. Soc. 45 (1962) 452-453.

[19] X. Q. Cao, R. Vassen and D. Stoever, Ceramic materials for thermal barrier coatings, J. Eur. Ceram. Soc. 24 (2004) 1-10.

[20] R. M. Spriggs, Expression for effect of porosity on elastic modulus of polycrystalline refractory materials, particularly aluminum oxide, J. Am. Ceram. Soc. 44 (1961) 628-629.

[21] A. C. Fisher-Cripps, Nanoindentation. Springer-Verlag Mechanical Engineering Series, Springer-Verlag, New York, 2002.

[22] W. C. Oliver and G. M. Pharr, Measurement of hardness and elastic modulus by instrumented indentation: advances in understanding and refinements to methodology, J. Mater. Res. 19(1) (2004) 3-20.

[23] T. Chudoba and F. Richter, Investigation of creep behaviour under load during indentation experiments and its influence on hardness and modulus results, Surf. Coat. Technol. 148(2-3) (2001) 191-198.

[24] J. B. Henderson, W. D. Emmerich and E. Wassmer, Measurement of the specific heat and heat of decomposition of a polymer composite to high temperatures, J. Therm. Anal. 33(4) (1988) 1067-1077.

[25] W. R. Chen, X. Wu, B. R. Marple and P. C. Patnaik, The growth and influence of thermally grown oxide in a thermal barrier coating, Surf. Coat. Technol. 201 (2006) 1074-1079.

[26] P. K. Wright and A. G. Evans, Mechanisms governing the performance of thermal barrier coatings, Current Opinion in Solid State and Materials Science 4 (1999) 255-265.

[27] J. A. Thompson and T. W. Clyne, The effect of heat treatment on the stiffness of zirconia top coats in plasma sprayed TBCs, Acta Mater. 49 (2001) 1565-1575.

[28] S. Paul, A. Cipitria, S. A Tsipas and T. W. Clyne, Sintering characteristics of plasma sprayed zirconia coatings containing different stabilizers, Surf. Coat. Technol. 203 (2009) 1069-1074.

[29] D. Basu, C. Funke and R. W. Steinbrech, Effect of heat treatment on elastic properties of separated thermal barrier coatings, J. Mater. Res. 14(12) (1999) 4643-4650.

[30] T. Y. Tsui, W. C. Oliver and G. M. Pharr, Influences of stress on the measurement of mechanical properties using nanoindentation. 1. Experimental studies in an aluminum alloy, J. Mater. Res. 11 (1996) 752-759.

[31] A. Bolshakov, W. C. Oliver and G. M. Pharr, Influences of stress on the measurement of mechanical properties using nanoindentation: Part. II. Finite element simulations, J. Mater. Res. 11(3) (1996) 760-768.

[32] S. Suresh and A. E. Giannakopoulos, A new method for estimating residual stresses by instrumented sharp indentation, Acta Mater. 46(16) (1998) 5755-5767.

[33] X. Zhao and P. Xiao, Residual stresses in thermal barrier coatings measured by photoluminescence piezospectroscopy and indentation technique, Surf. Coat. Technol. 201 (2006) 1124-1131.

[34] R. M. Davies, The frequencies of longitudinal and torsional vibration of unloadedand loaded bars, Philosophic Magazine 25 (1938) 364-370.

[35] G. Pickett, Equation for computing elastic constants from flexural and torsional resonant frequencies of vibration of prisms and cylinders, in Proceedings of the American Society for Testing and Materials, ASTM, 45 (1975) 846-865.

[36] S. Spinner and W. E. Tefft, A method for determining mechanical resonance frequencies and for calculating elastic moduli from these frequencies, in Proceedings of the American Society for Testing and Materials, ASTM, 61 (1961) 1221-1238.

[37] F. J. Nieves, L. Gascòn and A. Bayòn, Precise and direct determination of the elastic constants of a cylinder with a length equal to its diameter, Rev. Sci. Instr. 71 (200) 2433-2439.

[38] G. Martincek, The determination of Poisson's ratio and the dynamic modulus of elasticity from the frequencies of natural vibration in thick circular plates, J. Sound Vibration 2 (1965) 116-127.

[39] J. C. Glandus, PhD dissertation, University of Limoges, 1981.

[40] American Society for Testing Materials, Standard test method for dynamic Young's modulus, shear modulus and Poisson's ratio by sonic resonance, ASTM E1875-00e1; American Society for Testing Materials, Philadelphia, PA, 2003.

[41] S. Wolfram, The Mathematica Book, 4th ed., Wolfram Media/Cambridge, University Press, 1999.

3. Results and Discussion

3.1 Plasma sprayed CoNiCrAlY coatings

3.1.1 Phase composition of as-sprayed and oxidized coatings

Fig. 3.1 shows the phase composition of CoNiCrAlY powder and as-sprayed coating, while Fig. 3.2 shows the phase composition of CoNiCrAlY coatings oxidized at 1110 °C for 2 and 24 h, respectively.

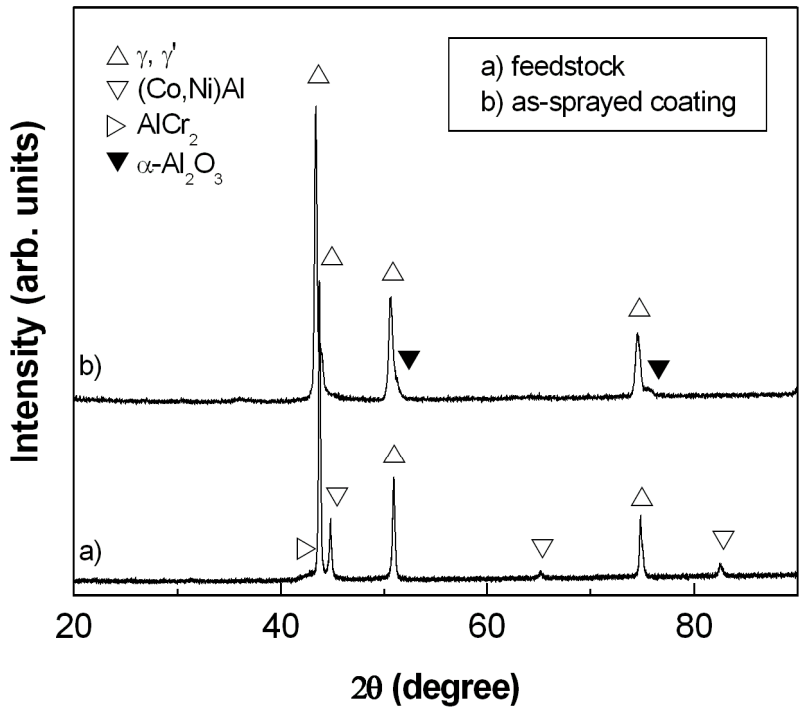

Figure 3.3 - XRD patterns of (a) CoNiCrAlY powder feedstock and (b) CoNiCrAlY as-sprayed coating.

As shown in Fig. 3.1, CoNiCrAlY alloy feedstock is composed of a mixture of γ-(Ni,Co,Cr) and γ'-$(Ni,Co,Cr)_3Al$ phases, with smaller contents of β-(Ni,Co)Al and $AlCr_2$ phases. The as-sprayed coating is mainly composed of γ-(Ni,Co,Cr) and γ'-$(Ni,Co,Cr)_3Al$ phases. The intensity of β-(Ni,Co)Al decreases, suggesting a corresponding reduction in the content of this crystalline phase. Very small peaks for α-Al_2O_3 phase are detectable. Alumina-type oxides are

formed during plasma spray deposition, since Al has higher affinity for oxygen than the other feedstock constituents, but the degree of oxidation seems to be rather low. It is worth noting that an increased oxidation would be able to assist the formation of undesired spinel-type oxides during plasma spraying; this feature has been already reported by other investigators for as-produced HVOF (High Velocity Oxygen Fuel) and APS (Air Plasma Spray) coatings [1,2]. The experimental results herein discussed are in good agreement with those obtained for similar coatings fabricated by VPS (Vacuum Plasma Spray) or HVOF processes [3,4].

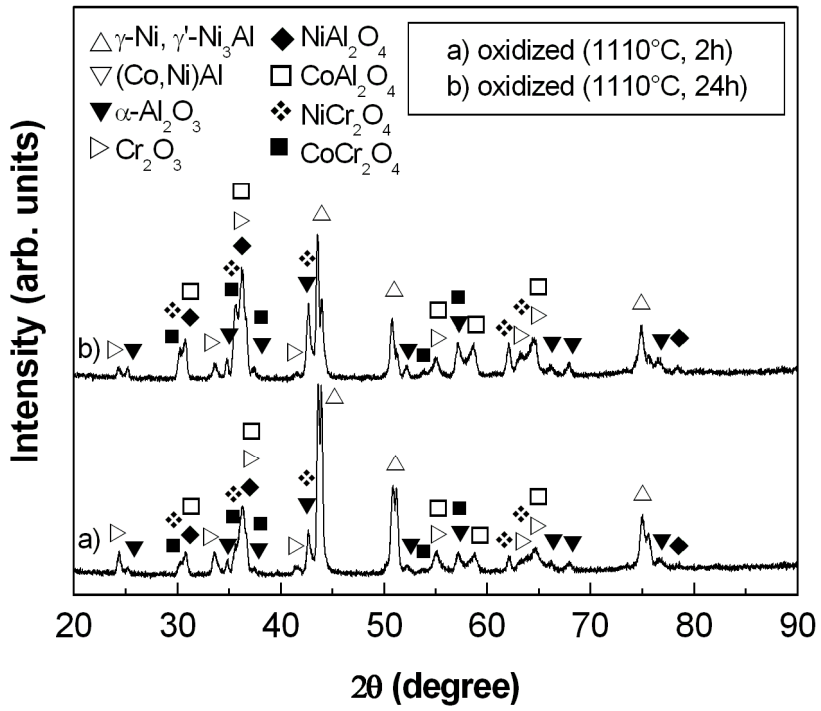

Figure 3.2 – XRD patterns of CoNiCrAlY coatings oxidized at 1110 °C for 2 and 24 h, respectively.

As shown in Fig. 3.2, with increasing the aging time the peak intensity for γ-(Ni,Co,Cr) and γ'-$(Ni,Co,Cr)_3Al$ phases significantly decreases, whereas the appearance of new peaks suggests the formation of other crystalline phases. According to Joint Committee on Powder Diffraction Standards (JCPDS), available at International Centre for Diffraction Data (ICDD), high-temperature oxidation produces the formation of several oxides, such as α-Al_2O_3, Cr_2O_3

and spinels ($NiAl_2O_4$, $CoAl_2O_4$, $NiCr_2O_4$ and $CoCr_2O_4$). These last can be addressed to chemical reactions or diffusion phenomena occurring in the coating. Indeed, Al depletion occurs near the coating surface, while the diffusion of Ni and Cr through the alumina layer and their reaction with the same Al_2O_3 lead to the formation of spinel-type phases. In addition, the formation of Cr_2O_3 phase occurs at the interface between oxide and metal phases [5].

It should be noted that the peak intensity of both alumina and spinel phases increases with increasing the aging time, suggesting a gradual increase in their content on the coating surface. In particular, the amount of spinel-type phases increases more rapidly than that of other oxides, due to higher growth rate.

The results are in good agreement with those reported for CoNiCrAlY and NiCrAlY coatings deposited by APS, VPS and HVOF and oxidized at 1000 °C and 1100 °C [6,7].

Otherwise, Richer *et al.* [2] have found a significant content of NiO within the oxide scale in addition to spinels after 5 h of isothermal oxidation at 1000 °C, which implies a low oxidation resistance. An enhanced oxidation has been also observed by Brandl *et al.* [1] for HVOF CoNiCrAlY coatings treated at 950 °C for 50 and 100 h. The low oxidation resistance of these coatings can be explained in terms of higher degree of oxidation during processing. Indeed, the degree of oxidation of as-sprayed coatings may be considered as a baseline in order to predict their performance during high-temperature exposure [1,2]. In order to compare the various results reported in literature, it should be noted that the oxidation behaviour of CoNiCrAlY coatings, *i.e.* the oxide scale composition and the corresponding growth rate, can be affected by the deposition technique employed, as well as by the parameters used in the oxidation tests (temperature and time).

3.1.2 Microstructure

Figure 3.3 shows the morphology of gas atomized CoNiCrAlY powder, composed of spherical particles with uniform size distribution (from 15 to 45 µm).

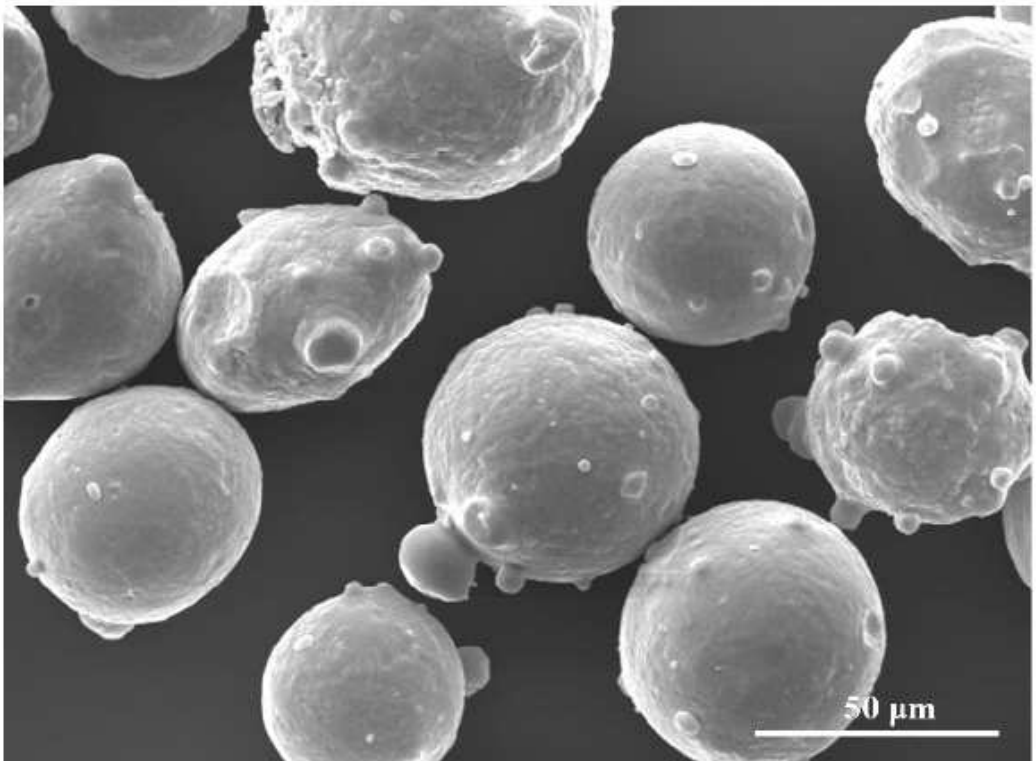

Figure 3.3 - SEM image showing the spherical morphology of gas atomized CoNiCrAlY particles (SE).

The cross section of the APS CoNiCrAlY coating, reported in Fig. 3.4, shows a typical lamellar microstructure rich of globular pores and oxide stringers (α-Al_2O_3). The oxide stringers are typically located at splat boundaries and appear as dark grey segmented streaks running approximately parallel to the coating-substrate interface. Indeed, the high plasma temperature and the oxidizing environment promote the oxidation of the exposed surface of the molten particles in the plasma jet, whereas their core does not suffer oxidation. The oxidation of metal particles starts in the plasma core and continues during their flight prior to their impact on the substrate. It is worth noting that the large particle size and the high gas

mixture flow rate employed herein allowed us to achieve a relatively low degree of oxidation. Within the coating microstructure, areas characterized by two different grey contrasts can be observed; they are associated to different Al contents.

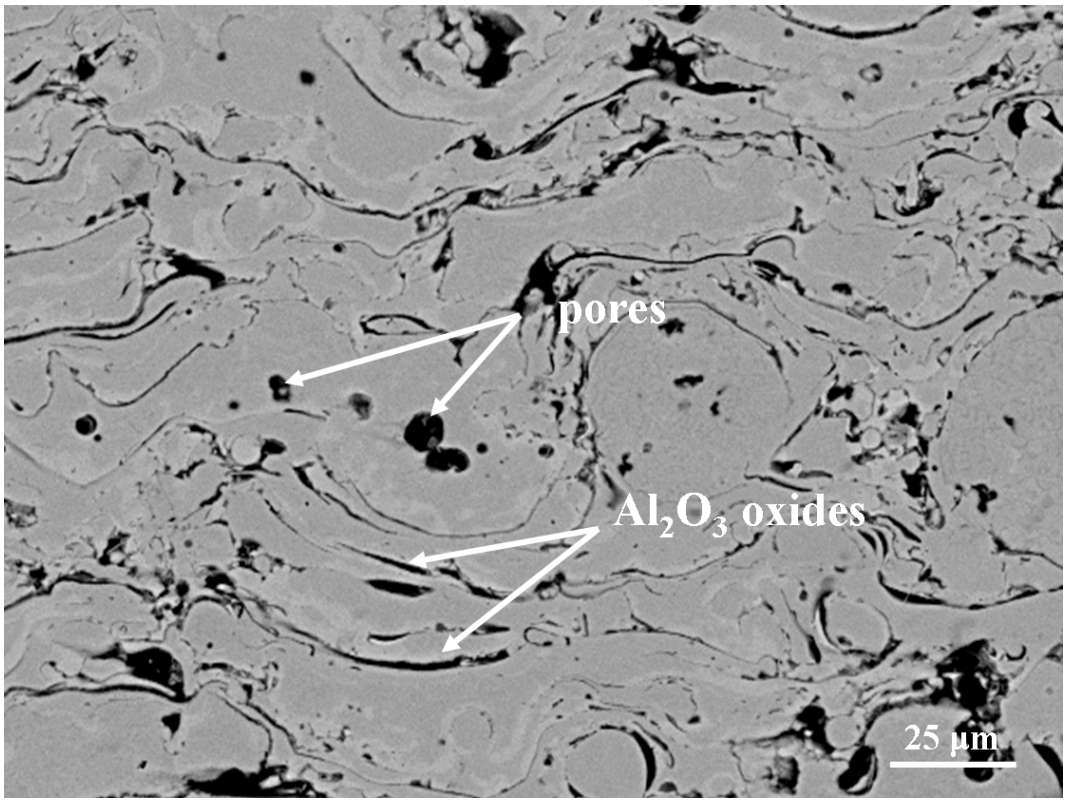

Figure 3.4 - Microstructure of as-sprayed CoNiCrAlY coating cross section showing pores and oxide stringers (BSE).

Some unmelted particles which resemble the feedstock morphology are also observable, as shown in Fig. 3.5. In this case, the dark grey regions which are well-detectable within the light grey matrix are composed of retained (Co,Ni)Al precipitates.

Several SEM pictures at various magnifications have been processed and transformed in binary images by software. The globular pores and the long-shaped oxides have been classified by their aspect ratio, so that their corresponding fractions could be calculated.

Figure 3.6 illustrates the procedure followed to distinguish the microstructural defects such as pores and oxides. The image shows the microstructure of as-sprayed CoNiCrAlY coating cross section near the top-surface. Small pores with surface area lower than 9 μm^2 are

homogeneously distributed in the coating microstructure; these pores originate from gas entrapped in the molten droplets.

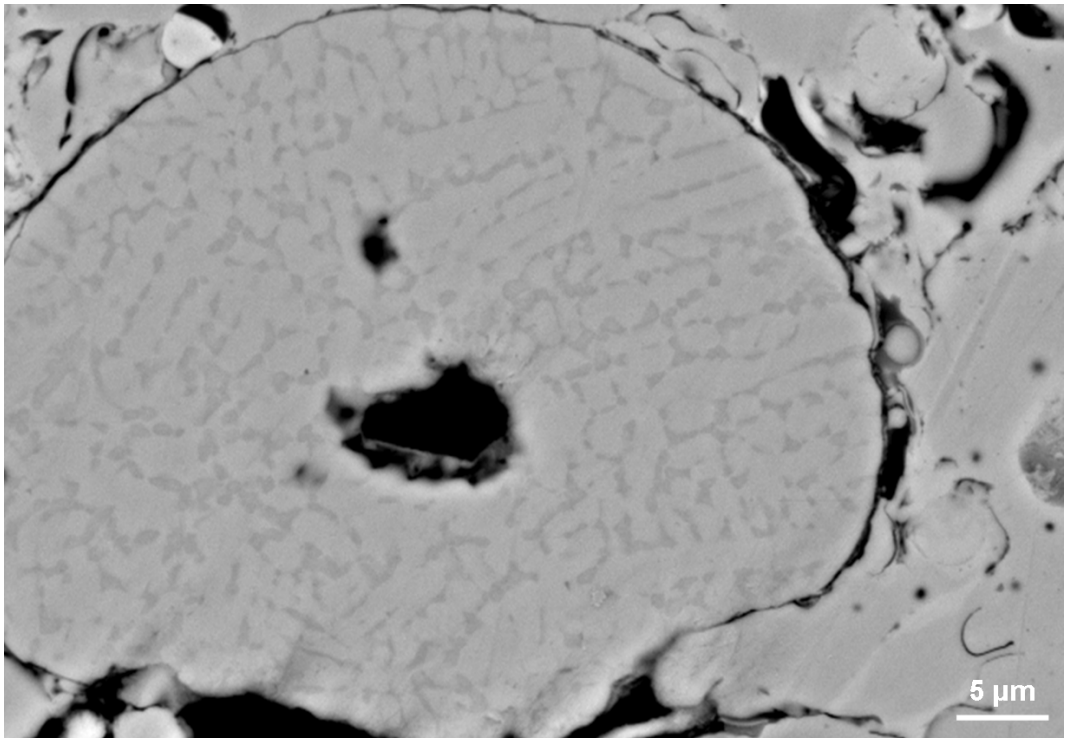

Figure 3.5 - SEM cross section of an unmelted CoNiCrAlY particle embedded in coating microstructure (BSE).

On the other hand, circular and elliptical pores with surface area higher than 9 μm^2 derive from pull-out of unmelted or partially melted particles during grinding and polishing steps, as well observable in Fig. 3.4.

The average porosity volume is about 3.3 % (standard deviation = 1.2 %), whereas the percentage of alumina oxides in the coating microstructure is approximately 4.5 % (standard deviation = 1.7 %). Interestingly, these values are slightly lower than those measured on similar CoNiCrAlY coatings deposited by Plasma Spraying and HVOF [2,8]. For a better comprehension, a comparison between the present coatings and other coatings studied in literature is shown in Table 3.1. It is worth noting that the coatings herein produced show very interesting properties (relatively low porosity), even if denser coatings have been also

obtained by using HVOF and HFPD methods [10,11]. It should be noted that the coating porosity could be overestimated, due to the pull-out of unmelted particles during grinding and polishing procedures.

Sample	Average porosity [%]	Processing
This work	3.3 ± 1.2	APS
Ref. [2]	5.3 ± 0.5	APS
Ref. [8]	5.1 ± 0.7	APS
Ref. [8]	4.6 ± 1.5	HVOF
Ref. [9]	~ 6.5	APS
Ref. [9]	~ 5	LPPS*
Ref. [10]	~ 1	HVOF
Ref. [11]	0.8 ± 0.2	HFPD

Table 3.1 – Porosity of as-sprayed CoNiCrAlY coatings.*LPPS. Low Pressure Plasma Spray.

The SEM micrographs in Fig. 3.7 illustrate the evolution of the oxide scale on the coating top-surface after 2 h and 24 h of isothermal exposure at 1110 °C, respectively. A duplex oxide scale is observed and it is composed of an inner and dense layer of α-Al_2O_3 (darker layer) and an upper layer composed of spinels and Cr_2O_3 (brighter layer). The upper layer is generally not uniform and has low density; moreover, it exhibits irregular protrusions.

The total thickness of surface oxide layer is generally lower than 2 µm after 2 h of isothermal exposure at 1110 °C, whereas it increases up to 3-4 µm after 24 h (the oxide scale tends to become continuous). Therefore, a first transient oxidation stage is followed by steady-state oxidation, characterized by lower rate of oxide growth.

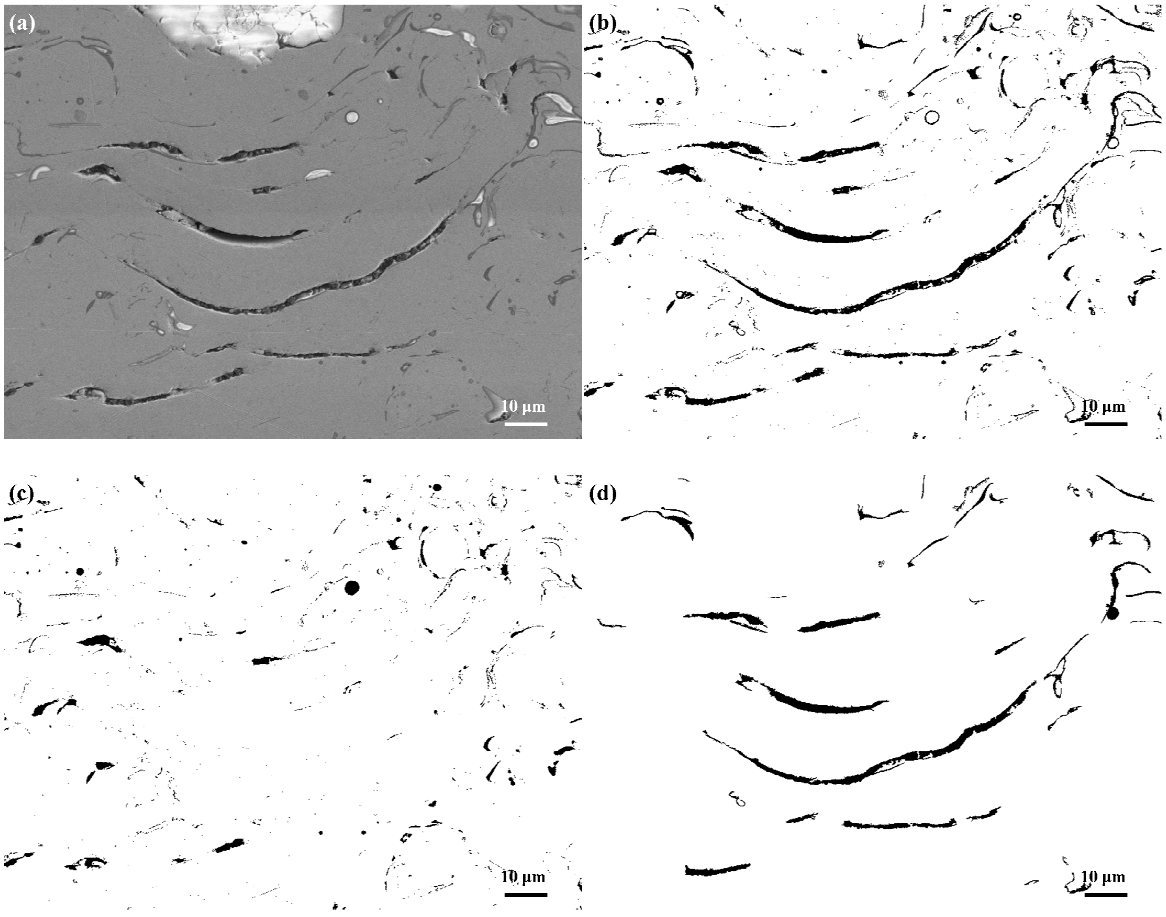

Figure 3.6 - Image analysis procedure for separating coating microstructural defects: (a) starting SEM micrograph of as-sprayed coating cross section, (b) binary image, (c) pores and (d) oxide stringers.

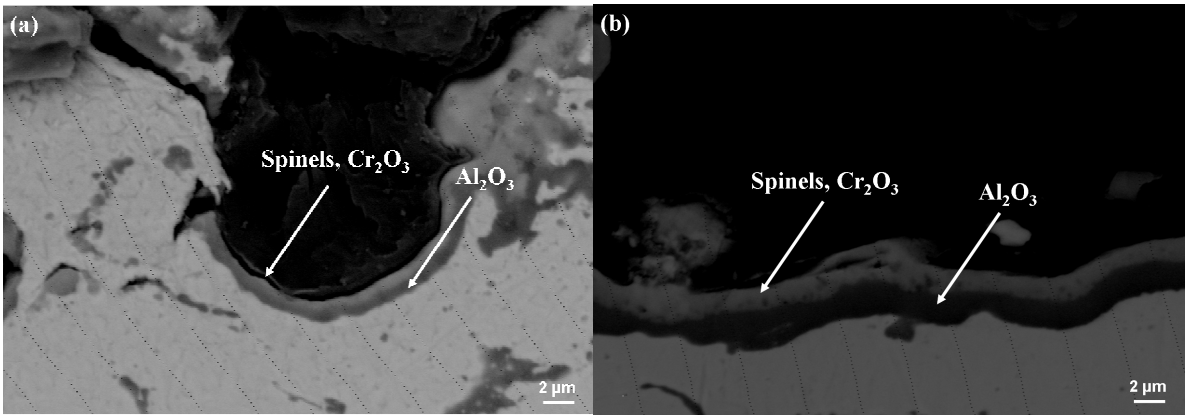

Figure 3.7 - SEM images showing the top-surface of oxidized CoNiCrAlY coatings: (a) coating oxidized at 1110 °C for 2 h and (b) coating oxidized at 1110 °C for 24 h. A duplex oxide scale gradually grows with increasing the aging time (BSE).

SEM observations demonstrate that the formation of the upper spinel layer follows the formation of the alumina layer but does not prevent the gradual growth of the same alumina

layer by Al diffusion from the CoNiCrAlY coating. The formation of a continuous alumina layer is beneficial for the oxidation resistance of plasma sprayed CoNiCrAlY coating, because it is able to reduce and retard oxygen penetration as well as the diffusion of any elements and the subsequent growth of spinel-type oxides on the coating top-surface, which are typically characterized by faster growth rate [6].

It is interesting to compare the results herein discussed with those reported in literature for similar coatings fabricated by various deposition techniques. Tang *et al.* [4] reported a different oxide scale kinetics for HVOF sprayed nanostructured CoNiCrAlY coatings oxidized at 1000 °C for 24 h. Indeed, the authors found that the formation of the subscale alumina layer occurred only after the formation of the upper spinel oxide layer which rapidly grew after 1 h of isothermal exposure [4,9]. In their work, a dual oxide layer was observed after 24 h. A dual oxide layer has been also detected by Saeidi *et al.* [6] on the surface of CoNiCrAlY coatings deposited by VPS and HVOF after 1 h of thermal exposure at 1100 °C. The same authors have also found a significant improvement of the oxidation resistance for coatings previously heat treated in vacuum for 3 h at 1100 °C. It was pointed out that a short heat treatment in vacuum induces the formation of a stable thin alumina layer which in turn acts as a barrier during the subsequent oxidation tests. In addition, the heat treatment promotes the densification of the coating microstructure and improves the adhesion to the substrate by means of interdiffusion phenomena. Moreover, it has been already reported that for High-Frequency Pulse Detonation CoNiCrAlY coatings the first 6-8 hours of oxidation at 1000 °C provide a significant internal oxidation, due to the diffusion of oxygen through the pores near coating surface; however, for increasing aging time, the oxidation rate stabilized to lower values owing to the formation of a uniform alumina layer [11]. However, the formation of this alumina layer did not circumvent the rapid growth of an upper spinel-type oxide layer

[11]. The same behaviour has been detected for HVOF coatings oxidized at 950 °C for 50-100 h as well as for APS coatings oxidized at 1000 °C [1,2].

Sample	Average porosity [%]	Standard deviation [%]
As-sprayed	3.3	1.2
Oxidized (1110 °C, 2 h)	2.4	0.2
Oxidized (1110 °C, 24 h)	2.1	0.2

Table 3.2 – Porosity average and standard deviation of as-sprayed and oxidized CoNiCrAlY coatings.

To this purpose, it should be noted that the oxidation behaviour is also affected by the coating porosity, since open pores may act as paths for oxygen propagation.

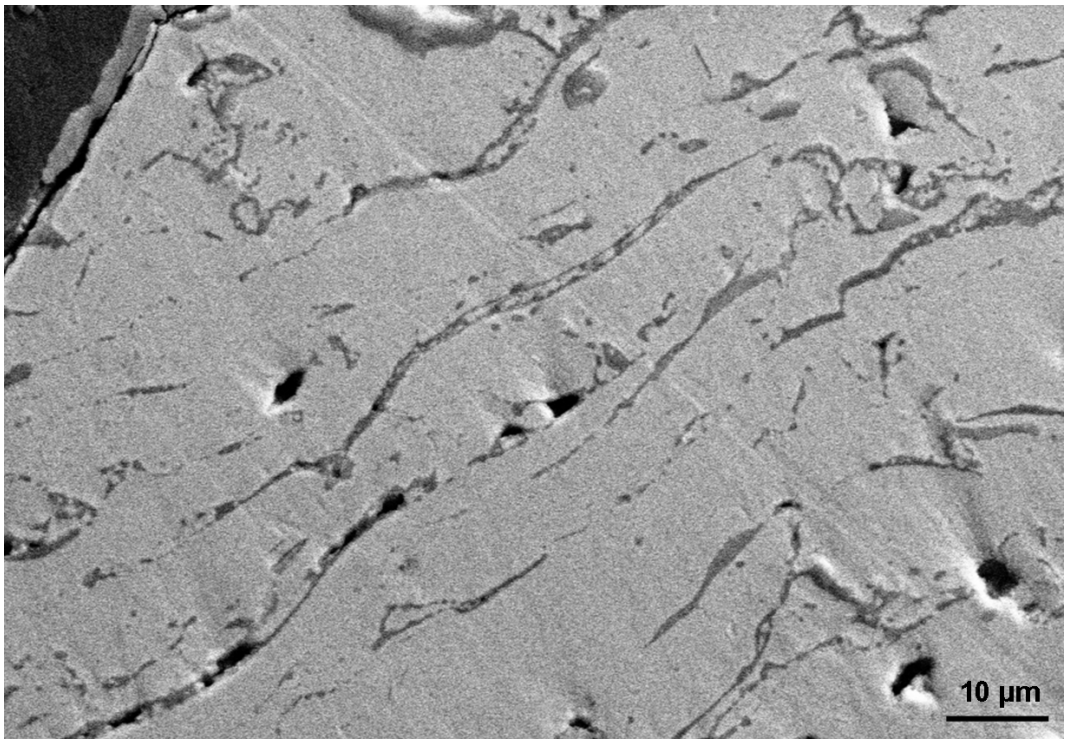

Figure 3.8 – SEM cross sectional microstructure of CoNiCrAlY coating oxidized for 24 h, showing a partial densification of the same microstructure (BSE).

However, in this work the heat treatment did not produce significant internal oxidation. To this purpose, Fig. 3.8 shows an example of the cross sectional microstructure of a CoNiCrAlY coating oxidized at 1110 °C for 24 h. It can be seen that after thermal exposure some thin interfaces and fine pores tend to disappear, promoting a partial densification of the microstructure and leading to a decrease of the total porosity, as shown in Table 3.2. This partial densification occurs after a very short exposure time (2 h) and allows to reduce the effective surface area subjected to the next oxidation stage.

3.1.3 Determination of elastic properties by IET

As discussed in section 2.5.1 (Chapter 2), the elastic modulus of as-sprayed CoNiCrAlY coatings has been measured by IET, using a bi-layer configuration (substrate and coating). Fe 360 plates (100 x 25 x 3 mm^3) were used as substrates. With the exception of coating type, the specimens were similar to those shown in Fig. 2.10 in section 2.3.

The mass and dimensional properties of the specimens are summarized in Table 3.3. The table contains, for each experimental variable, the mean value of *n* measurements. In particular, the sample thickness was measured in two steps. In the first step the thickness of the uncoated substrates was measured, and in the second step the thickness of the coated plates was measured. It was observed a difference among the so obtained coating thickness and the nominal value. On the average, the thickness of the CoNiCrAlY coating was 348 ± 8 μm. The elastic modulus of the steel substrates was equal to 190 GPa (standard deviation = 0.4 %).

The fundamental frequency of vibration of coated samples and the corresponding values of E_c are reported in Table 3.4. The mean value is equal to 66.5 GPa and the associated experimental uncertainty is found to be 10 % [12]. The mean value obtained herein is somewhat higher with respect to those reported in other works for an APS bond-coat of similar composition and obtained using vibration-based iterative procedures [13,14,15].

However, it is worth to point out that the porosity level for the coatings reported in these works was almost three-four times higher with respect to that of the present coating [13,14,15].

Specimen	*n*	S1	S2	S3	S4	S5
length, *L* [mm]	4	100.05	99.86	99.67	98.57	98.97
width, *B* [mm]	6	25.06	25.01	25.01	25.00	25.03
substrate thickness, t_s [mm]	9	2.986	2.986	2.998	2.978	2.990
coating thickness, t_c [mm]	9	0.359	0.344	0.342	0.352	0.341
sample mass, *m* [g]	3	63.028	62.519	62.685	61.823	62.049

Table 3.3 – Dimensional and mass properties of the specimens.

Specimen no.	S1	S2	S3	S4	S5
Fundamental frequency, *f* [Hz]	1558.4	1569.4	1573.2	1604.5	1607.5
Coating elastic modulus, E_c [GPa]	62.8	67.4	62.5	66.7	73.1

Table 3.4 - Fundamental frequencies of coated samples and corresponding Young's modulus of CoNiCrAlY coatings.

3.1.4 Microhardness of as-sprayed and oxidized coatings

Vickers microindentation was carried out on the cross section of as-sprayed CoNiCrAlY coatings to measure their microhardness. Hardness measurement is often a difficult task due to the heterogeneous microstructure of the coating, which is characterized by the presence of microcracks, pores, splat boundaries and unmelted particles.

Accurate Vickers microhardness measurements rely on visual resolution of the residual indentation; however, the diagonal of the indentation, *d*, can be difficult to resolve, indeed the load should be low enough to avoid cracking, which otherwise occurs within the indentation site [16]. Then an accurate choice of the applied load must be done. So, some preliminary tests were carried out and indicated that a load of 200 gf avoids cracking and retains the resolution of the residual indentation.

As the heterogeneous microstructure of an APS coating can lead to scattered data, a minimum of 20 indentations was performed on each coating cross section.

The results have been in turn presented by means of Weibull statistics, because a Gaussian distribution is generally not adequate to describe the variation of mechanical data for plasma sprayed coatings, due to their microstructural defects, such as pores with different size, splat boundaries and microcracks. Indeed, during microhardness tests the indentations can take place on many splats characterized by different morphological and structural properties.

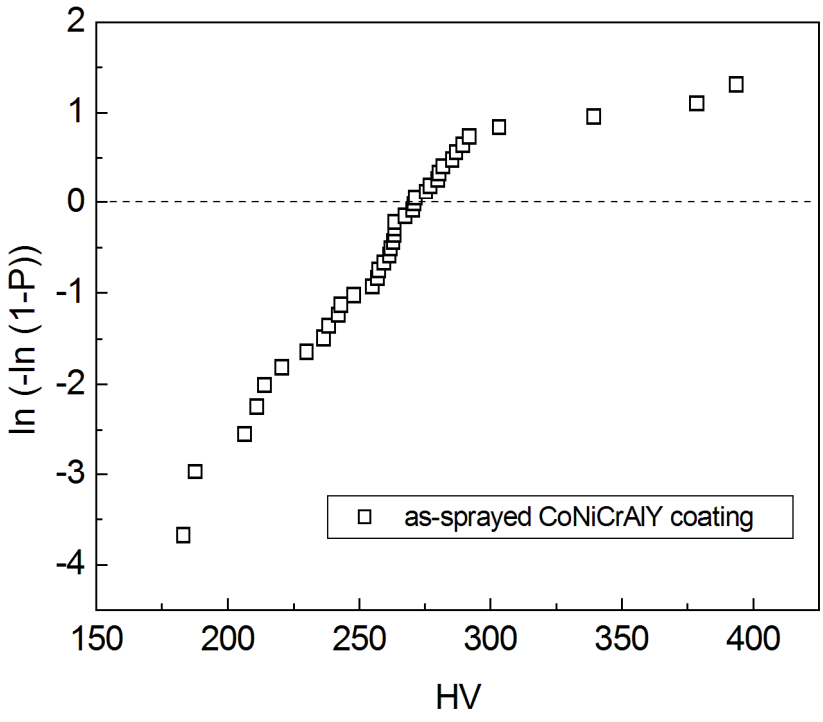

Figure 3.9 – Weibull distribution of microhardness data for as-sprayed CoNiCrAlY coatings.

In particular, the experimental data have been sorted in ascending order and the cumulative density function of probability, defined as P = (*i*-0.5)/N, was assigned to each hardness and elastic modulus data.

The Weibull plots corresponding to the microhardness data are reported in Fig. 3.9 (we report the hardness values in HV for a better comprehension).

The mean value of the hardness is represented by the intersection of x-axis (y = 0) and the Weibull plot. On the other hand, information related to the experimental scatter are provided by the Weibull modulus, *m*, *i.e.* the slope of the line in the plot; in particular, a higher modulus represents low experimental scatter. The average microhardness of as-sprayed CoNiCrAlY coating is 267.9 HV (standard deviation = 47.3 HV). The Weibull modulus of microhardness data is 7.06.

Microhardness measurements were then carried out on as-sprayed and oxidized samples at different indentation loads (100 gf and 300 gf) and for a dwell time of 20 s. Twenty indentations were performed for each sample.

Sample	Load [gf]	HV	SD	m_H
As-sprayed	100	307	49	7.05
As-sprayed	300	285	40	7.72
Oxidized (1110 °C, 2 h)	100	425	74	6.95
Oxidized (1110 °C, 2 h)	300	423	40	11.9
Oxidized (1110 °C, 24 h)	100	461	93	5.1
Oxidized (1110 °C, 24 h)	300	316	42	8.5

Table 3.5 - Weibull parameters for microhardness data of as-sprayed and oxidized CoNiCrAlY coatings.

The data were processed by using Weibull statistics. The results are summarized in Table 3.5. It should be noted that the values obtained at 100 gf are more scattered than those obtained at 300 gf: their higher Weibull modulus is higher. The hardness tends to decrease with increasing the indentation load and with increasing the aging time. However, lower values have been observed at 300 gf for the coating oxidized at 1110 °C for 24 h. To this purpose, the imprints have been observed by 3D optical profilometer: significant pile-up has been detected only on this sample and can explain this behaviour. The corresponding penetration depth-distance curves are not herein reported for the sake of brevity.

3.1.5 Nanoindentation

A typical set of nanoindentation load–depth curves is presented in Fig. 3.10. It can be observed that the maximum penetration depth decreases with increasing aging time; on the other hand, the slope of the curves tends to increase. This behaviour can be attributed to the partial densification of the coating microstructure, which occurs after a few hours of heat treatment.

Note that the distance between the indentations was kept equal to 30 μm to avoid a mutual influence of consecutive responses. Moreover, NI data related to indentations performed near visible pores have been not considered in the analyses. Figures 3.11 and 3.12 show the Weibull plots corresponding to hardness and Young's modulus data for as-sprayed and heat treated CoNiCrAlY coatings, respectively. The most meaningful data provided by the plots are the mean values of H and E_r as well as the Weibull parameter, *i.e.* the slope m_W (Weibull modulus).

The latter is directly related to the measurement scatter; in particular, steeper lines mean reduced experimental scatter.

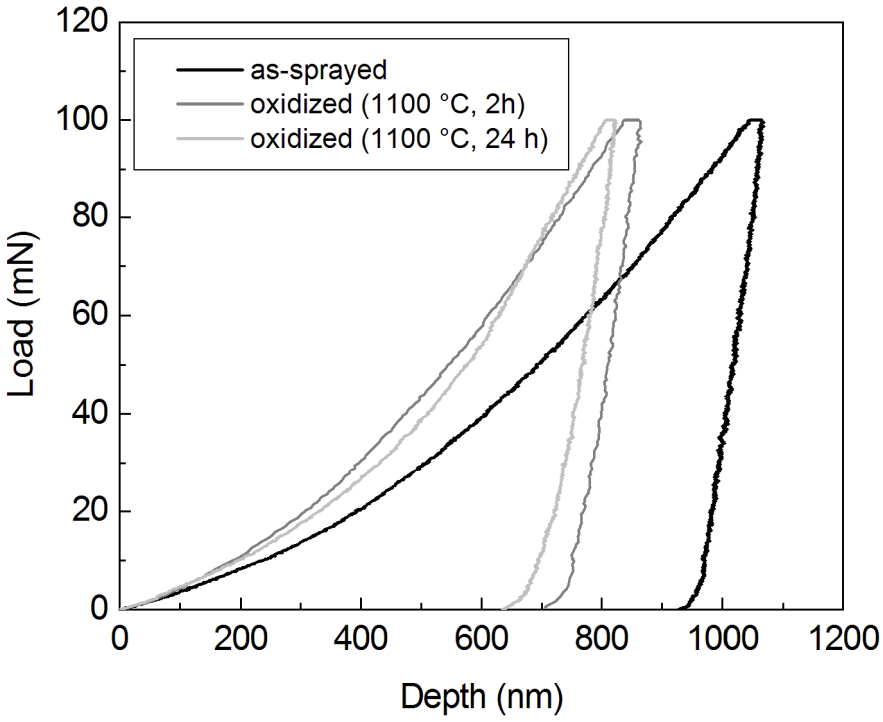

Figure 3.10 – Typical load-displacement (P-h) curves obtained during Nanoindentation tests for as-sprayed and annealed plasma sprayed CoNiCrAlY coatings.

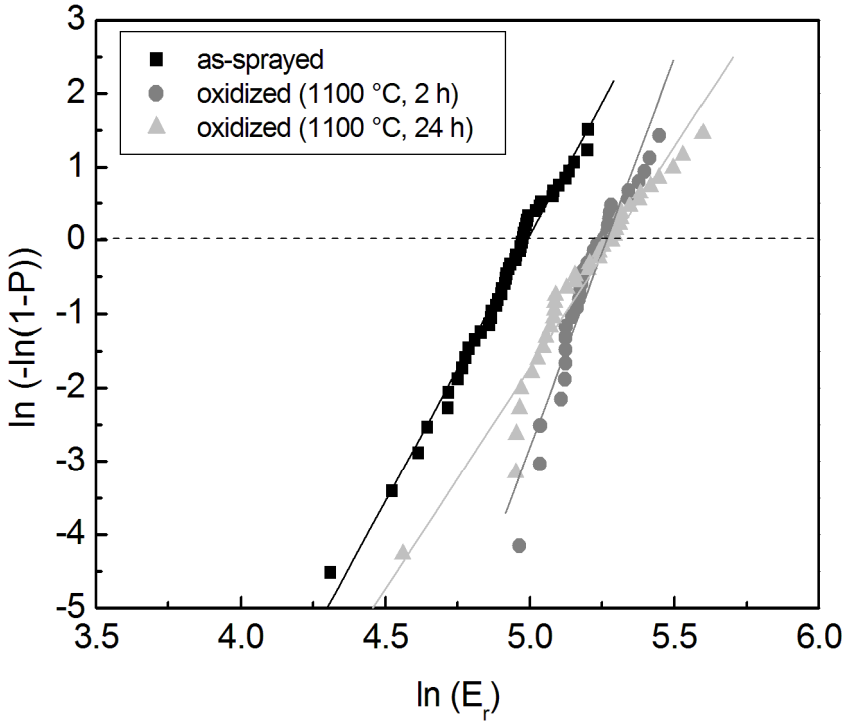

Figure 3.11 - Weibull plots for Young's modulus data of as-sprayed and oxidized CoNiCrAlY coatings. The Weibull curves shift toward higher Young's modulus values with increasing the aging time.

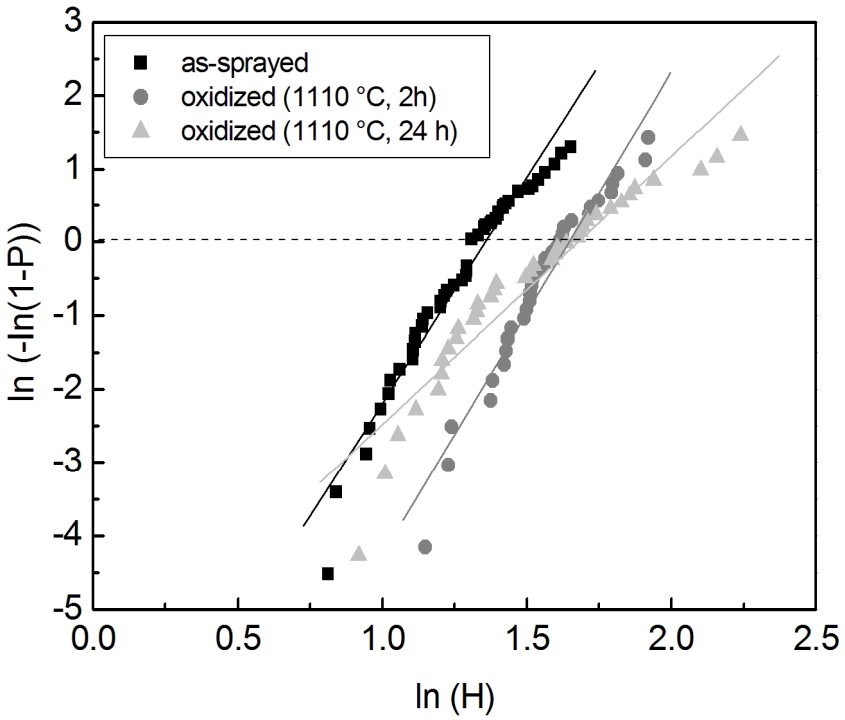

Figure 3.12 - Weibull plots for hardness data of as-sprayed and oxidized CoNiCrAlY coatings. The Weibull curves shift toward higher hardness values with increasing the aging time.

The scatter in the mechanical properties is related to the presence of fine pores embedded in the coating microstructure, as well as to the presence of interphase boundaries near the indent. With increasing the annealing time both hardness and elastic modulus increase, due to the partial healing of coating porosity[1] and the partial disappearance of splat boundaries, which provide a better insulation from the diffusion of oxygen and of corrosive agents from the coating surface to the substrate. The precipitation of intermetallic phases within the microstructure also increases the coating hardness. As shown in Figs. 3.11 and 3.12, the Weibull curves shift towards higher values of hardness and Young's modulus. The corresponding Weibull parameters (mean value and modulus) are reported in Table 3.6.

The lowest Weibull modulus is found for CoNiCrAlY coatings treated for 24 h; apparently, the denser microstructure provided reduced scatter for hardness and Young's modulus, since

[1] this point can be addressed to diffusion phenomena occurring during the heat treatment.

the effect of finer pores and splat boundaries is considerably reduced, while the large pores and the retained internal oxide stringers still influence the global mechanical properties. The mean value of the reduced elastic modulus is 147.8 GPa for as-sprayed CoNiCrAlY coating and increases with increasing the aging time up to 200.8 GPa after 24 h at 1110 °C. In turn, the average hardness for as-sprayed coating is 3.95 GPa and increases up to 5.69 GPa after 24 h at 1110 °C.

Sample	H [GPa]	m_H	E_r [GPa]	m_{Er}
As-sprayed	3.95	6.2	147.8	7.2
Oxidized (1110 °C, 2 h)	5.24	6.6	197.1	10.6
Oxidized (1110 °C, 24 h)	5.69	3.66	200.8	6.0

Table 3.6 - Weibull parameters for hardness and elastic modulus data of as-sprayed and oxidized CoNiCrAlY coatings.

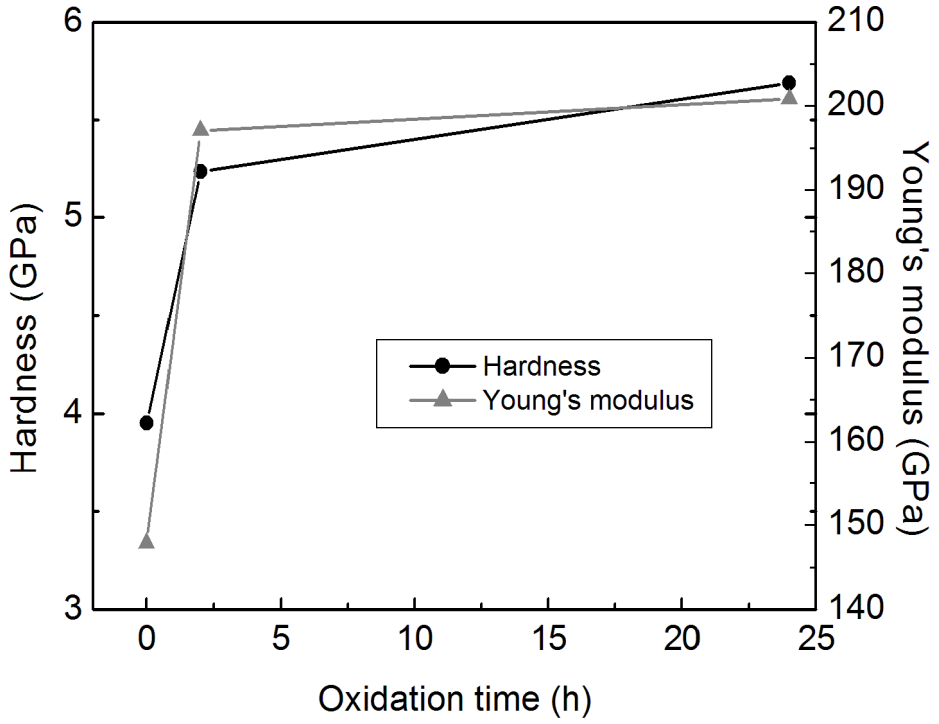

Figure 3.13 - The graph shows the average Young's modulus and the average hardness of CoNiCrAlY coatings as functions of the aging time. The oxidation rate is higher in the first hours of heat treatment and then significantly decreases.

The increase in Young's modulus and hardness are rather sharp; indeed, after 2 h at 1110 °C the increase in Young's modulus is of about 33 %, while it achieves 36 % after 24 h. In turn, the increase in hardness is around 33 % after 2 h of isothermal exposure and achieves 44 % after 24 h of thermal aging. So, it is worth noting that a strong correlation exists between the changes occurring in microstructure and the mechanical properties during early-stage high-temperature oxidation.

In Fig. 3.13, both the Young's modulus and the hardness of plasma sprayed CoNiCrAlY coatings are reported as a function of the oxidation time. The oxidation mechanism affects the mechanical properties in two stages, characterized by different oxidation rates. Indeed, in the first hours of isothermal exposure the main microstructural modifications described in the previous section induce significant variations of the mechanical properties, *i.e.* a rapid increase of both hardness and elastic modulus. The rate of oxidation then decreases with increasing the aging time. The average elastic modulus of as-sprayed CoNiCrAlY coating is much higher than that reported by Kwon *et al.* [17] for similar coatings deposited by air plasma spraying (90 GPa) and very close to that found for the same coatings fabricated by HVOF (155 GPa). In both cases the hardness has been measured by the Nanoindentation technique.

The average values of hardness reported by the same authors were 3.2 GPa and 5.0 GPa for coatings produced by APS and HVOF, respectively. The improved mechanical properties of our air plasma sprayed CoNiCrAlY coatings can be likely related to their denser microstructure and lower degree of oxidation. Unfortunately, in the above mentioned studies,

the effect of high-temperature oxidation on the mechanical properties was not investigated and therefore a comparison is not feasible.

It is worth noting that Zotov *et al.* [18] have reported an average elastic modulus of 166 GPa and an average nanohardness of 5.5 GPa for CoNiCrAlY coatings deposited by Electron Beam Physical Vapour Deposition (EB-PVD). Obviously, the different microstructures of plasma sprayed and EB-PVD coatings can easily explain the differences in their mechanical properties. After annealing at 1000 °C the Young's modulus of EB-PVD coatings increased up to 100 h and then decreased, whereas their hardness increased up to 50 h and then decreased. At constant oxidation time the coatings produced in the present work exhibit higher Young's modulus and the same hardness than the corresponding values reported by Zotov *et al.* [18] for EB-PVD coatings. However, it should be noted that the aging tests herein discussed have been performed at higher temperature (1110 °C against 1000 °C) and the number of nanoindentation measurements performed on each coating cross section was 5-8 times higher than that performed on EB-PVD coatings.

The local values of Young's modulus measured on as-sprayed CoNiCrAlY coatings, as determined using NI, in conjunction with porosity level have then been adopted as inputs into a micromechanical model in order to get a rough estimate on the global stiffness of the coating (E^*). Such value can be compared to the value provided by the IET, thus providing a cross-check on the consistency among the various results obtained. This approach has been used only for as-sprayed coatings, because the substrates used for IET measurements were not suitable to be exposed at 1110 °C. The Hashin-Hasselman model has been adopted to the purpose [19,20].

In particular, Young's modulus is given as follows:

$$E^* = E_0 \cdot \left[1 + \frac{A \cdot p}{1 - (A+1)p} \right] \tag{3.1}$$

where A = -33.4, p is the volume fraction of all pores, cracks and interfaces, and E_0 is the elastic modulus of the dense material [21].

Given inputs for as-sprayed CoNiCrAlY coating such as the estimated porosity fraction (3.3 %), the mean value of the reduced Young's modulus determined using NI and Poisson's ratio provided in literature (ν = 0.30), Eq. 3.1 estimates an average Young's modulus of about 65.43 GPa [22]. So, the theoretical prediction of Young's modulus are very close to the global value measured using the IET.

Multistep indentations were also performed to assess the variation of elastic modulus and hardness with the indentation load. The indentation load was varied in the range between 100 and 500 mN, by step of 100 mN.

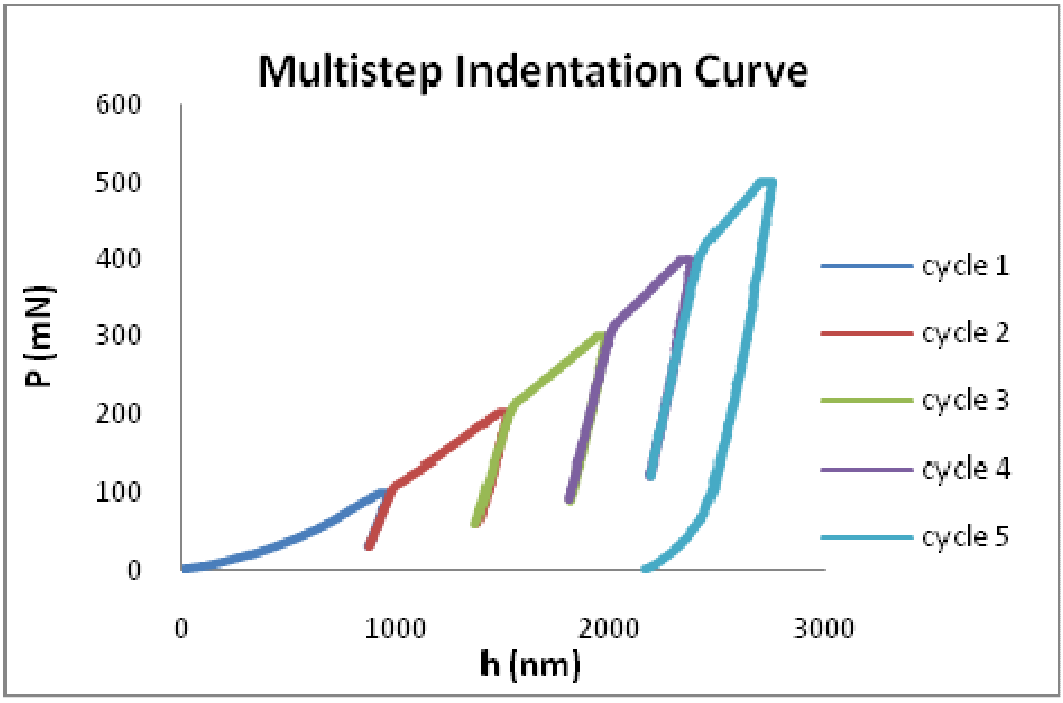

Figure 3.14 – Typical multistep indentation curves on CoNiCrAlY coating.

The typical multistep indentation curves are reported in Fig. 3.14. It can be seen that for each cycle the unloading stage reaches 30 % of the maximum load associated with the same cycle.

The results obtained are reported in Figs. 3.15 and 3.16. Both elastic modulus and hardness decrease with increasing the maximum load. It is possible to conclude that they are dependent on the applied load at relatively low loads. However, for increasing load this effect becomes smaller and it is usually accepted to consider the corresponding materials properties as representative of the mechanical behaviour.

This behaviour may be related to the accuracy achieved in the determination of the contact area at low loads. Indeed, at lower load the contact area is usually underestimated. Moreover, problems associated with the "pile-up" or "sink-in" of the material on the edges of the indent during the indentation process could affect the measured values.

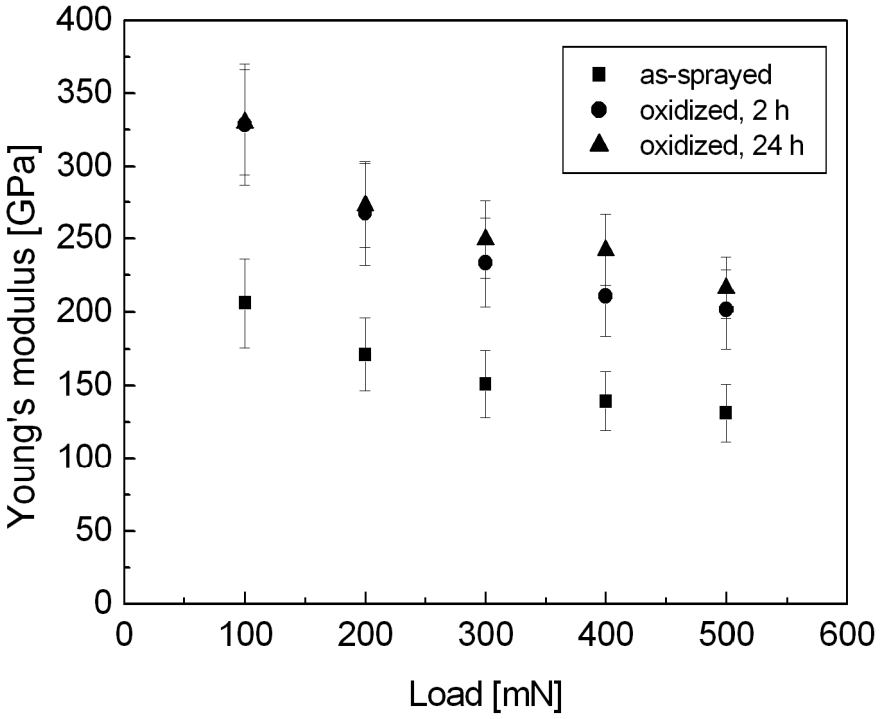

Figure 3.14 – Evolution of Young's modulus as a function of the maximum indentation load.

To this purpose, as shown in Fig. 3.17, no significant pile-up or sink-in is observed. Moreover, Figs. 3.15 and 3.16 confirm that Young's modulus and nanohardness increase with increasing the aging time. A sharp increase is noticed during the first hours of high-

temperature exposure and then it tends to stabilize. The mean value of reduced Young's modulus, measured at 500 mN, is 131.4 GPa for as-sprayed coating and increases up to 216.3 GPa after 24 h at 1110 °C. In turn, the average hardness is 3.53 GPa for as-sprayed coating and increases with increasing the aging time up to 5.34 GPa after 24 h at 1110 °C.

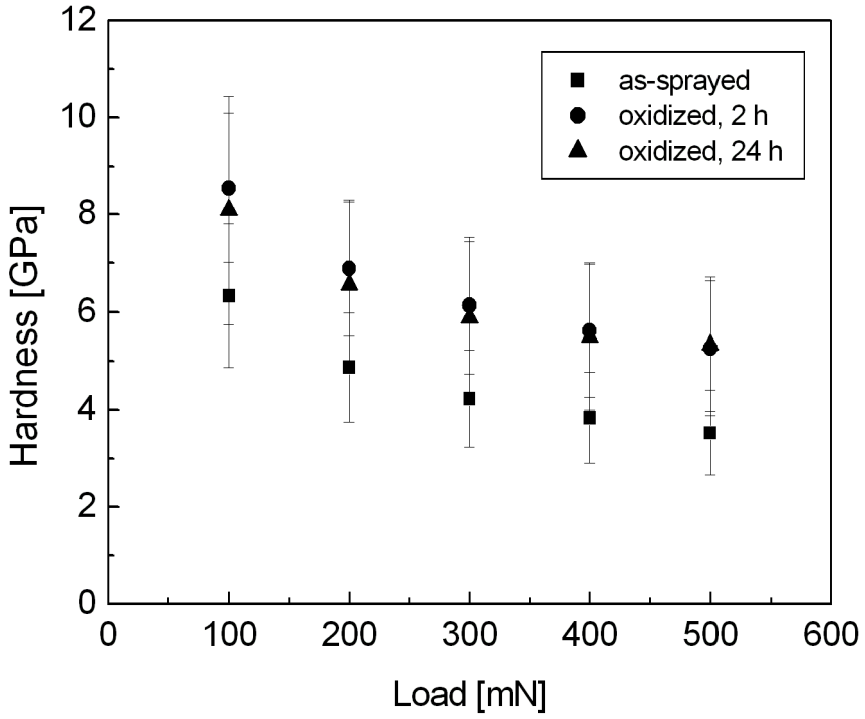

Figure 3.15 - Evolution of nanohardness as a function of the maximum indentation load.

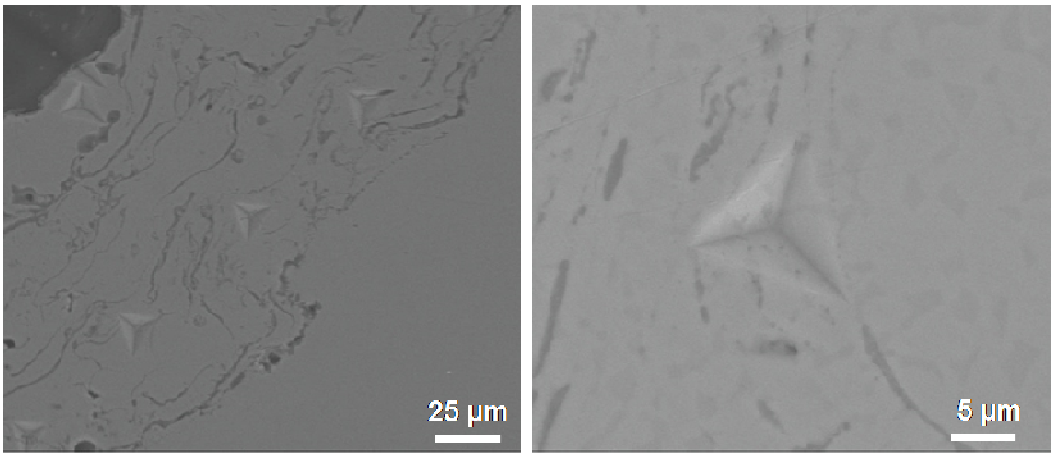

Figure 3.16 – SEM images showing indents within coating microstructure.

3.2 Plasma sprayed CYSZ coatings

3.2.1 Phase composition and high-temperature phase stability

X-ray diffraction patterns of CYSZ powder and as-sprayed coatings are shown in Fig. 3.18. It can be seen that the phase composition is quite complex. The feedstock is mainly composed of tetragonal t' and cubic c ZrO_2 phases, according to Joint Committee on Powder Diffraction Standards (JCPDS) for tetragonal t-ZrO_2 (JCPDS 81-1544) and cubic c-ZrO_2 (JCPDS 49-1642), available at International Centre for Diffraction Data (ICDD). Other lower peaks were also detected, as representative of small amounts of monoclinic m ZrO_2 and cubic c CeO_2 stabilizer, according to m-ZrO_2 (JCPDS 37-1484) and cubic c-CeO_2 (JCPDS 81-0792).

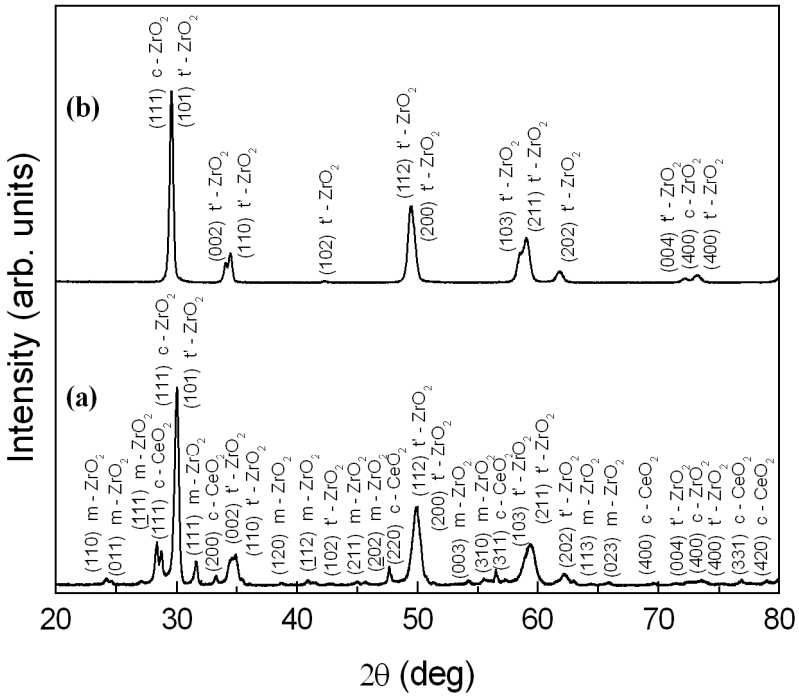

Figure 3.18 – X-ray diffraction patterns of (a) CYSZ powder and (b) CYSZ as-sprayed coating.

The as-sprayed coating shows a polycrystalline structure composed of non-equilibrium t'-ZrO_2 and cubic c-ZrO_2 phases. The peaks for cubic c-ZrO_2 are not clearly detectable due to

the overlapping between the diffraction peaks of the same cubic c and the tetragonal t' zirconia phases. Therefore, the (111) c-ZrO_2 and (400) c-ZrO_2 have been only localized in the pattern. The Miller indices (hkl) denote the crystalline planes of zirconia. As an example, a profile fit of the (400) type reflections in the region 2θ = 72-75° is plotted in Fig. 3.19, where both tetragonal t' and cubic c zirconia phases are detectable. After plasma spraying, m-ZrO_2 disappeared, because it was transferred to the non-transformable t'-ZrO_2 phase. A weight loss of CeO_2 also occurs, since this last one is partially evaporated in the plasma plume, thereby leading to a stoichiometric variation with respect to the starting phase composition.

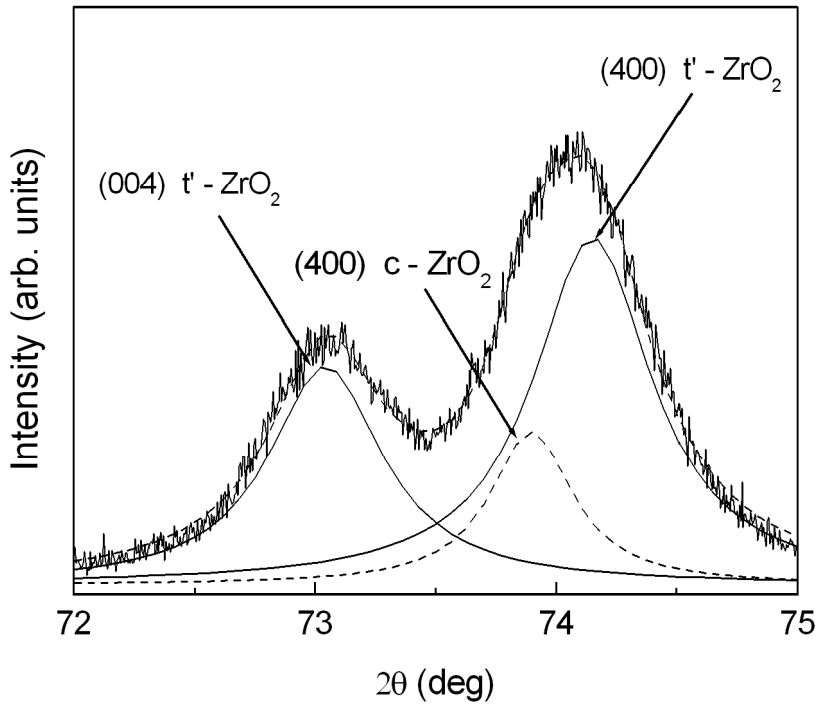

Figure 3.19 - XRD pattern of CYSZ coating in the range 72-75°.

The tetragonal t' phase arose from high quenching rate of molten droplets upon impact on the substrate. During plasma spraying, part of high-temperature cubic phase is transferred to metastable tetragonal t' phase by a fast diffusionless transformation, without any composition

change. The remaining part of high-temperature cubic c zirconia phase is retained at room temperature.

It should be noted that some chemical reactions take place during deposition of CYSZ coatings. High temperature processes commonly promote changes in valence state, i.e. the reduction of Ce^{4+} ions to Ce^{3+} ions. However, during spraying a partial re-oxidation of Ce^{3+} ions to Ce^{4+} ions occurs at the coating surface and it results in the decrease of oxygen vacancies and cubic phase content. After plasma spraying, the light-gray colour of the feedstock changes in yellow, which is the typical colour of a ZrO_2-CeO_2-Y_2O_3 solution. Ce^{3+} cation and the resulting oxygen vacancies play an important role in the stabilization of the cubic phase, whereas Ce^{4+} ions are able to stabilize zirconia in the tetragonal form, as described by Choi *et al.* in a previous work [23,24].

The addition of CeO_2 stabilizer to zirconia produces a distortion effect and an increase in lattice parameters for both tetragonal and cubic phases. Indeed, the peak positions shift towards small angles in comparison with standard tetragonal and cubic zirconia phases. Indeed, the lattice parameters of CYSZ are located between the correspondent values of YSZ and pure CeO_2 (a = 5.4113 Å).

The whole XRD spectra in the range between 20° and 80° of as-sprayed and annealed coatings are shown in Fig. 3.20.

Figure 3.21 shows the low-angle 27-32° range of XRD patterns, whereas Fig. 3.22 shows the high-angle 71-75° range, where the (004) and (400) peaks for tetragonal t' zirconia and the (400) peak for cubic zirconia are detectable.

It should be noted that the (400) peaks for cubic and tetragonal zirconia are partially overlapped and their separation was automatically performed by software. As mentioned above, as-sprayed coatings are composed of a mixture of tetragonal t' and cubic c zirconia phases.

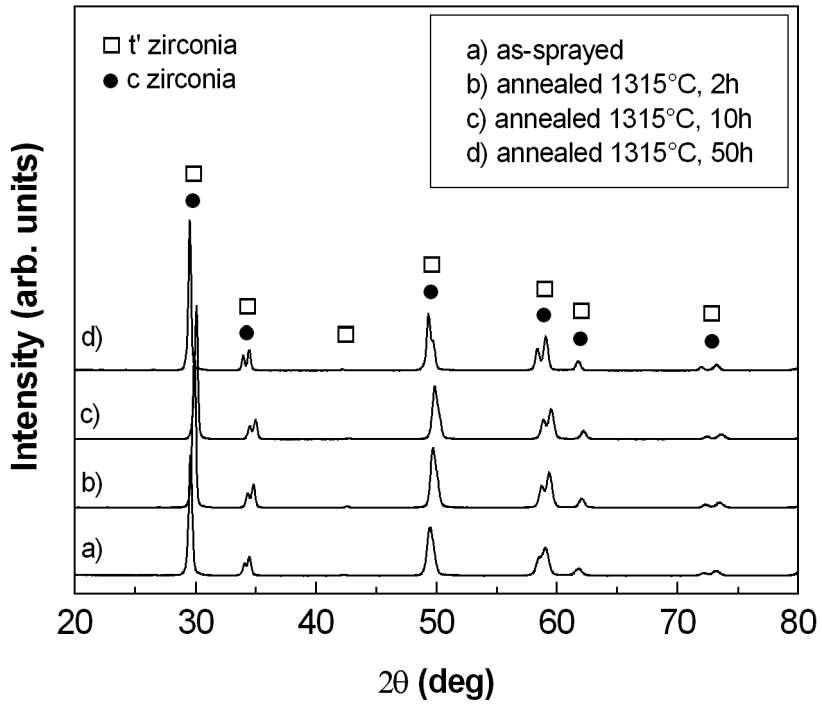

Figure 3.20 - XRD spectra in the range between 20° and 80° of as-sprayed and annealed CYSZ coatings.

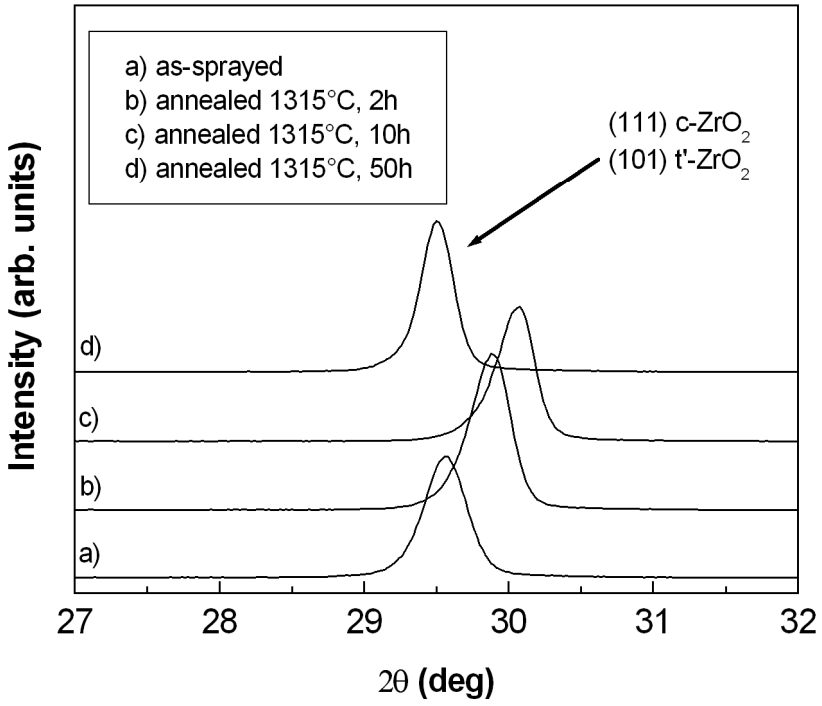

Figure 3.21 - Low-angle region of XRD patterns.

The overlapping between the tetragonal and cubic zirconia peaks may make rather difficult their deconvolution and their separation is automatically performed by software.

Therefore, the (400) reflections in the range between 71° and 75° have been considered for quantitative analysis. The volume fractions for cubic c and tetragonal t' zirconia phases, calculated by Rietveld analysis, are 16 % and 84 %, respectively (c+t' = 100 %).

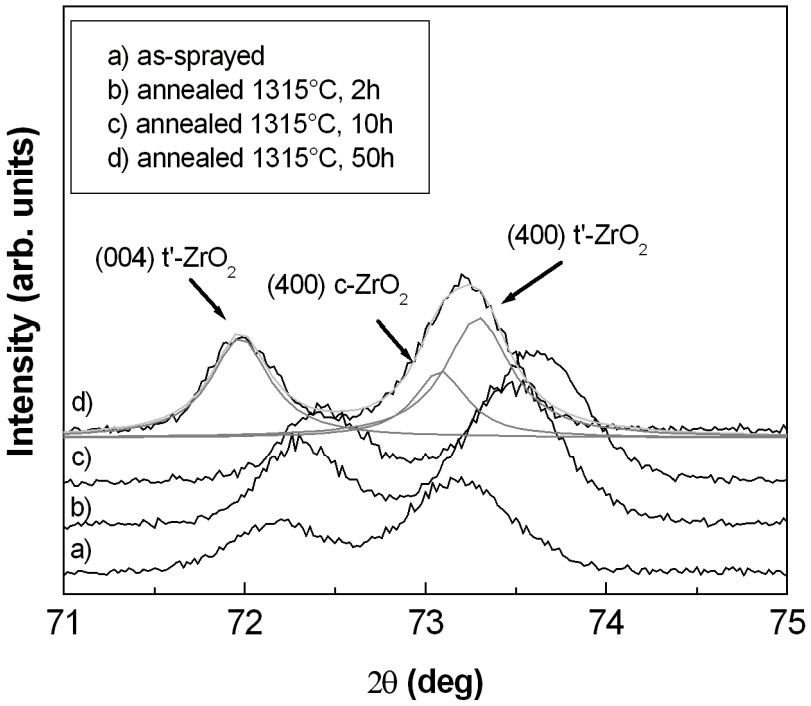

Figure 3.22 - High-angle region of XRD patterns.

Sample	c-ZrO_2	c	t'-ZrO_2	a	c	R_P
	[%]	[Å]	[%]	[Å]	[Å]	
As-sprayed	16	5.1912	84	3.6549	5.2355	9.13
Annealed 1315 °C, 2 h	14	5.1717	86	3.6427	5.2253	9.01
Annealed 1315 °C, 10 h	14	5.1656	86	3.6373	5.2186	8.38
Annealed 1315 °C, 50 h	8	5.1923	92	3.6553	5.2466	9.21

Table 3.7 - Lattice parameters and volume fraction for tetragonal and cubic zirconia phases in as-sprayed and annealed coatings.

Table 3.7 shows the lattice parameters and the corresponding volume fractions for both tetragonal t' and cubic c zirconia phases, as obtained from Rietveld analysis.

XRD results show no phase decomposition after isothermal annealing. Indeed, looking at the 27-32° range, no monoclinic phase is detectable. The tetragonal to monoclinic transformation is notoriously promoted by crystallite growth and only occurs when the grain size becomes higher than a critical value [25].

Slight changes can be observed in the 71-75° range, as consequence of crystallite size growth and microstrains' evolution. Part of the cubic fraction is transferred to tetragonal t' phase. The volume fraction of cubic zirconia decreases with increasing the annealing time, due to a diffusionless of cubic *c* to tetragonal *t*' zirconia, and it is equal to 8 % after 50 h of thermal aging (t' phase = 92 %). This transformation is strongly related to the local microstructure of each coating, *i.e.* the content of stabilizer oxides (ceria and yttria).

Figure 3.23 illustrates the r.m.s (root mean square) microstrains versus annealing time for tetragonal and cubic phases. The fluctuation of the lattice parameters from grain to grain, associated to the presence of a distribution of stabilizer content inside the crystallites, produces the microstrains. These microstrains are larger in as-sprayed conditions, due to higher lattice distortion, and then they are partially released during thermal aging, due to lattice stress relaxation. In many works, an increase in microstrain for t' phase has been noticed in annealed YSZ coatings, as a consequence of the diffusion of the yttria stabilizer, the reduction of the tetragonal t' zirconia phase and the increase of other phases, such as cubic phase and low-yttria tetragonal phase. It has been also reported that the microstrain level in cubic YSZ phase decreases. For CYSZ coatings, the mechanism seems to be different, at least in the first 50 h of thermal exposure, due to the reduction of the cubic phase. These values of microstrains are not high enough to allow crack formation and propagation.

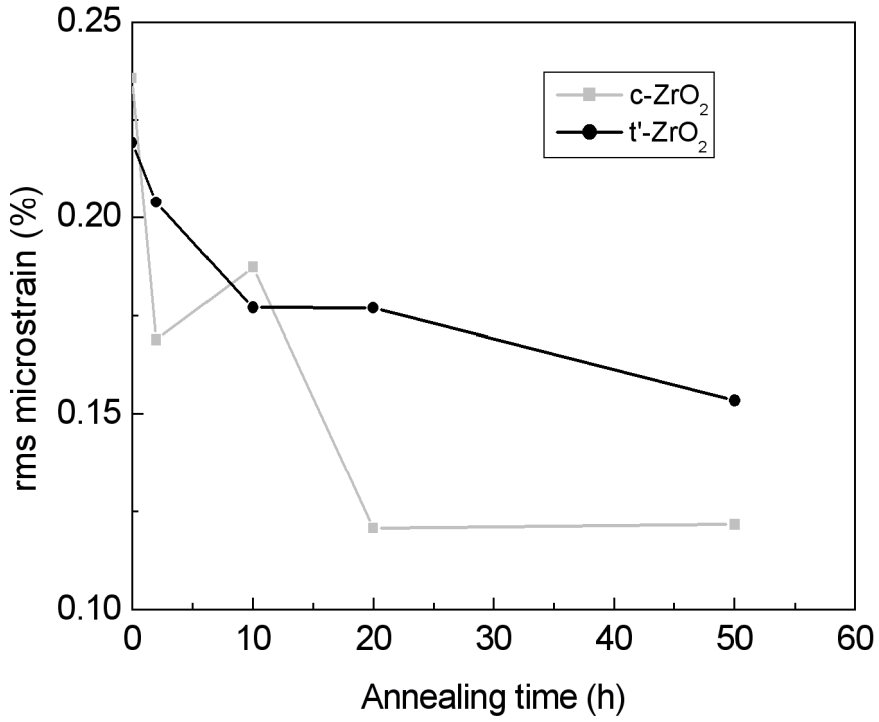

Figure 3.23 - Microstrains versus annealing time for tetragonal and cubic zirconia phases.

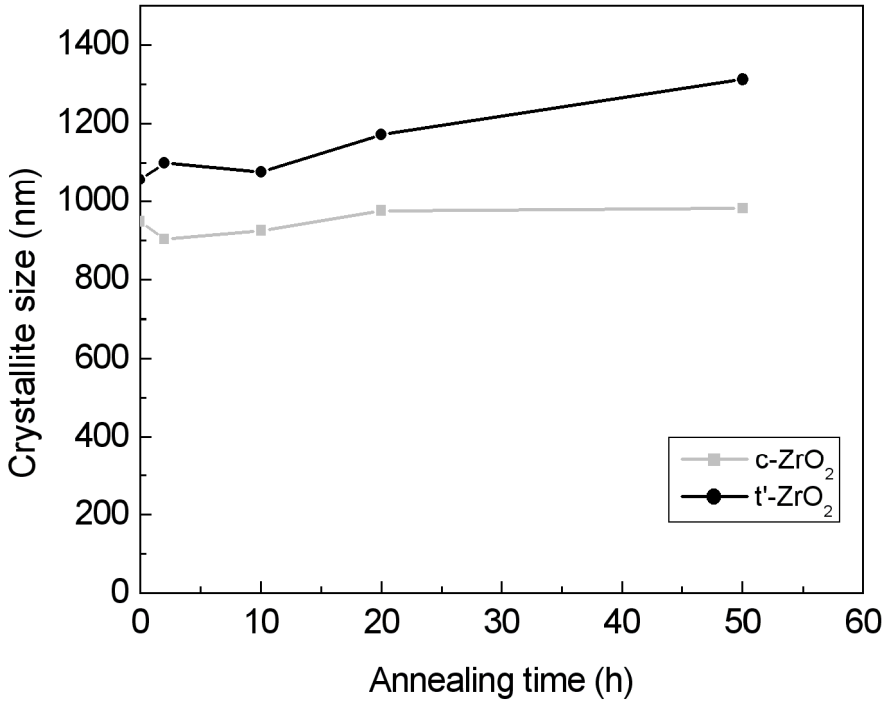

Figure 3.24 - Crystallite size versus annealing time for tetragonal and cubic zirconia phases.

Figure 3.24 shows the relationship between crystallite size and annealing time for both zirconia phases. The grain size increases with annealing time due to the thermal aging, even if this increase is not particularly large. It should be noted that the crystallites are much smaller than columnar grains, typically observed within the lamellae. Structural changes can be also related to sintering and crystal lattice scale.

3.2.2 Microstructure

As shown in Fig. 3.25, the powder particles are spherical. Their size is in the range between 10 and 110 μm. As shown in Fig. 3.26, within the agglomerates some particles are nanosized, even if the powder herein employed can be considered as micronsized..

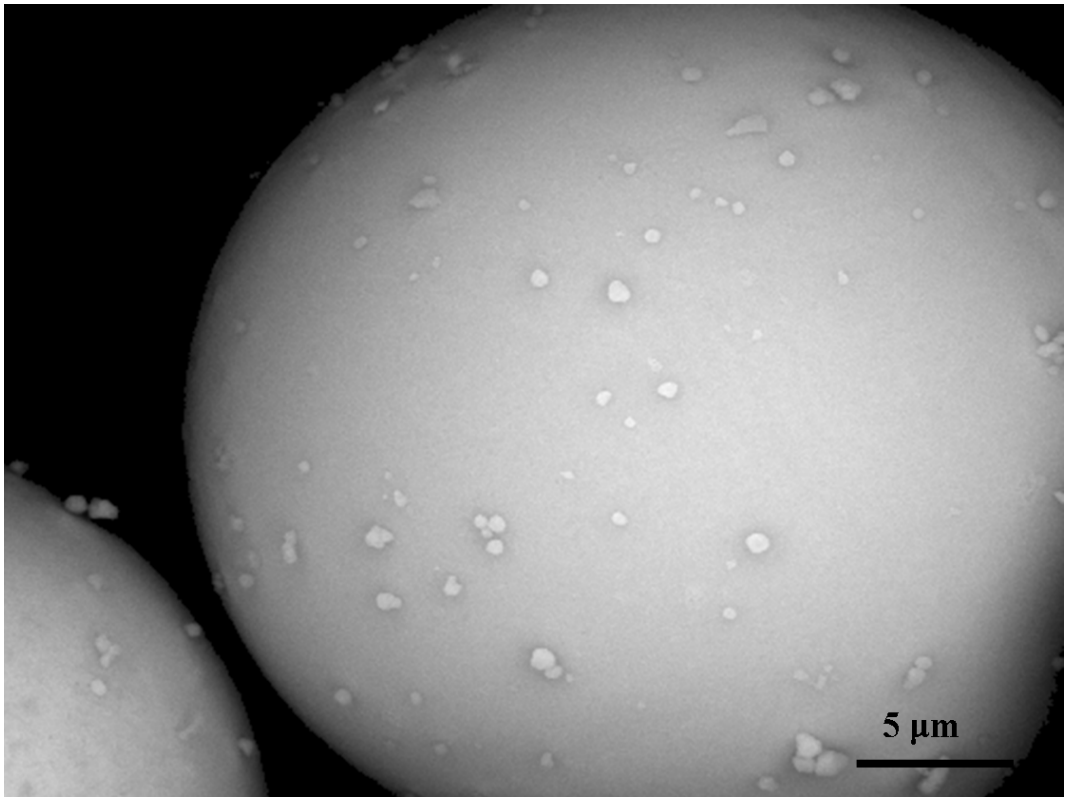

Figure 3.25 – External surface of spherical CYSZ particle (SE).

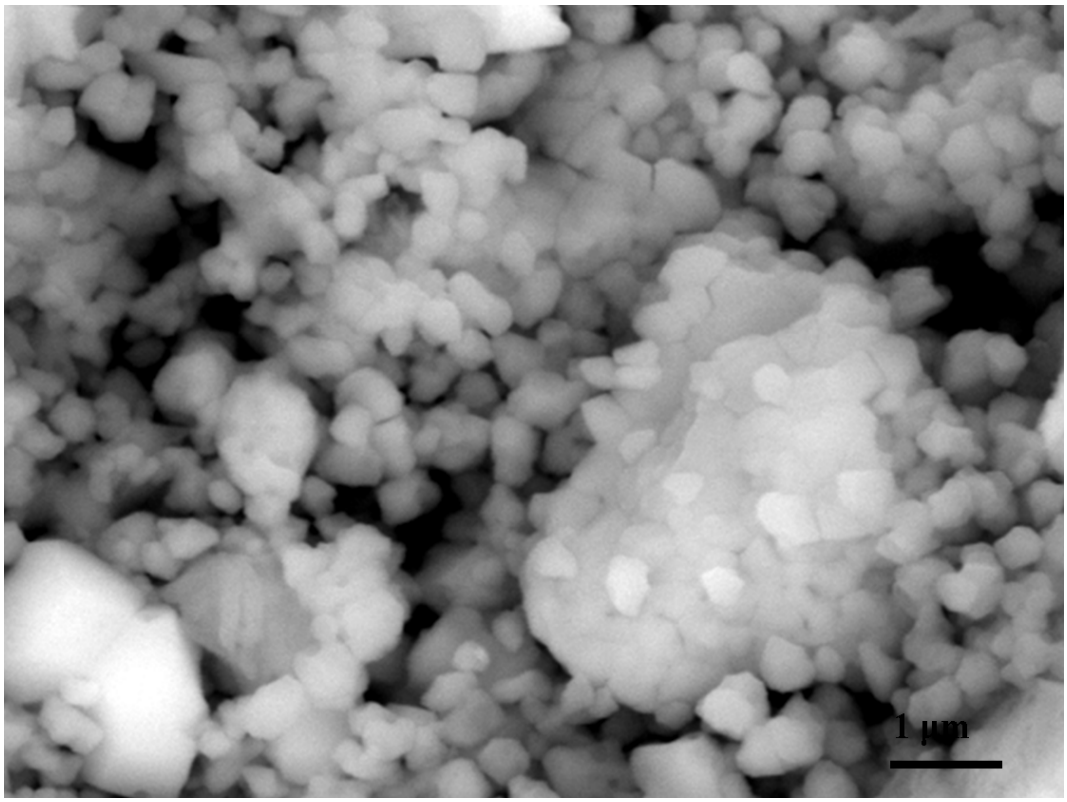

Figure 3.26 – Nanosized particles inside CYSZ micronsized particle (SE).

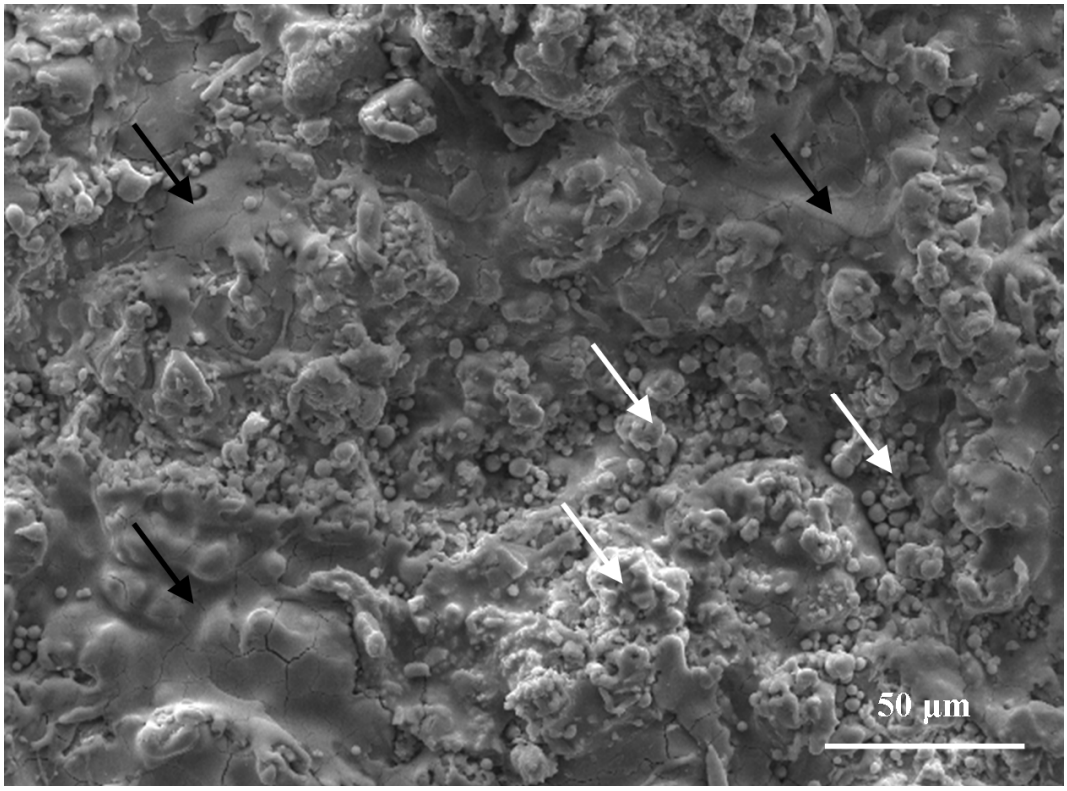

Figure 3.27 - Surface morphology of as-sprayed CYSZ coating (SE).

Plasma sprayed CYSZ coatings show a complex microstructure composed of splats (or lamellae) generated by the rapid solidification of well-melted and/or partially-melted feedstock particles. A SEM image of CYSZ fractured coating surface is shown in Fig. 3.27. Surface morphology shows different areas which are associated with partially melted (white arrows) and well-melted (black arrows) zones. Surface microcracks are also observed.

Figure 3.28 shows a SEM micrograph of the entire TBC, composed of metal substrate, bond coat and thick CYSZ top coat. A SEM image of TBC cross section is reported in Fig. 3.29. As clearly shown, the stacking sequence (from the bottom) is as follows: Ni-based superalloy substrate, CoNiCrAlY bond coat and CYSZ top coat. Inclusions and/or un-bonded area are not observed at top-coat/bond-coat and bond-coat/substrate interfaces, denoting the achievement of a good interfacial adhesion.

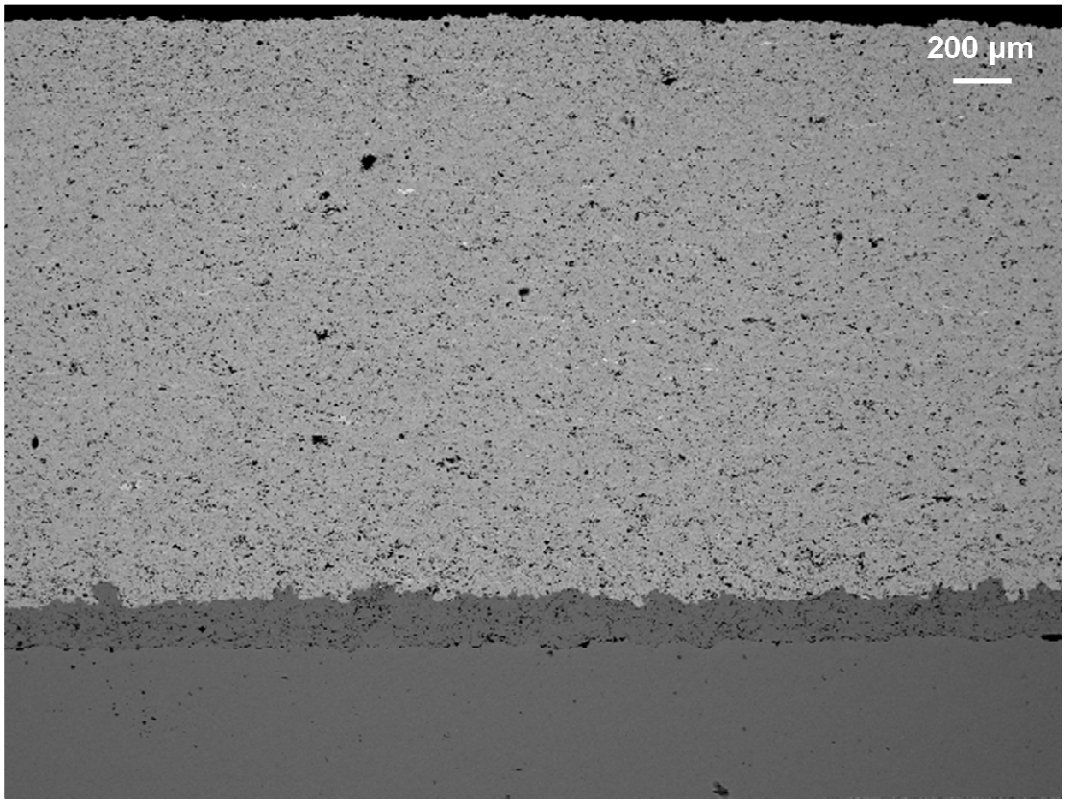

Figure 3.28 - Microstructure of thick CYSZ thermal barrier coating (BSE).

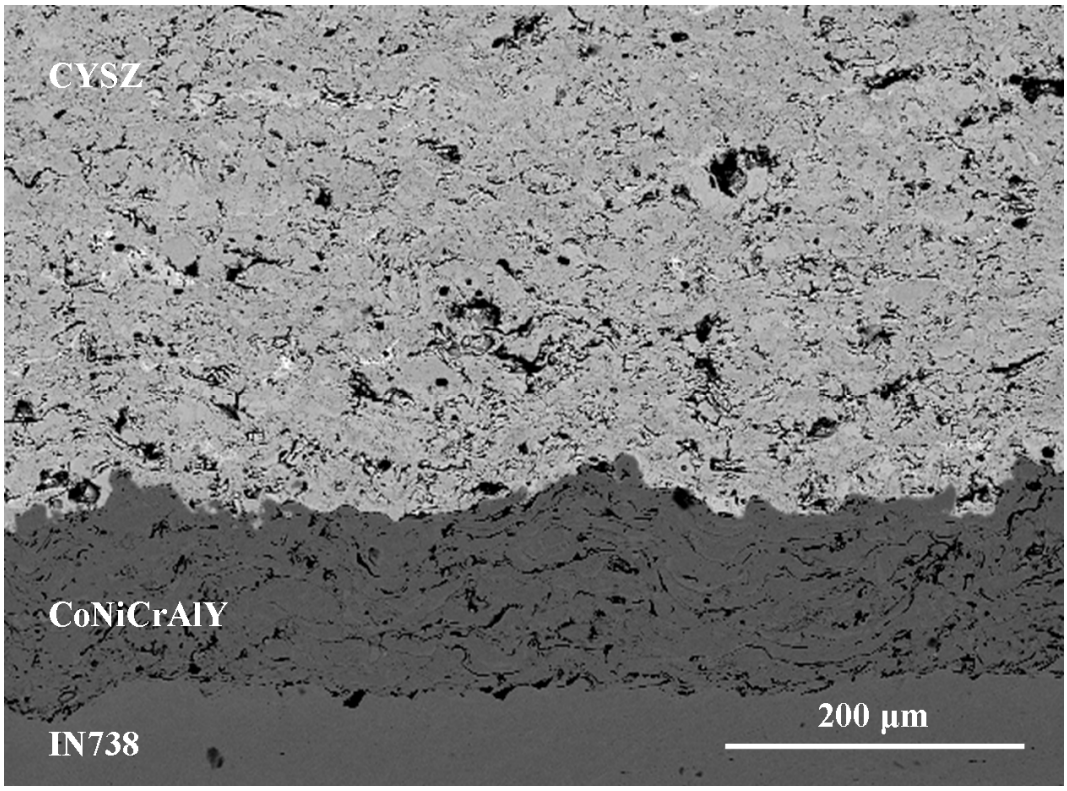

Figure 3.29 - SEM image of TBC cross section (BSE).

The typical microstructural features of CYSZ coating are shown in Fig. 3.30. The overlapping of rapidly quenched splats leads to the formation of a heterogeneous and lamellar porous microstructure, consisting of irregular thin lamellae parallel to the coating-substrate interface and embedded in a network of microcracks and voids. These lamellae are thicker at their center and thinner at their periphery and their thickness is approximately from 0.5 to 4.5 µm.

Moreover, both inter-splat microcracks and intra-splat microcracks can be noticed. Inter-splat cracks originate during deposition process from weak horizontal splat boundaries and they are typical in plasma sprayed coatings. Intra-splat cracks initiate from the splat boundaries as a consequence of stress relaxation during cooling to room temperature.

The former cause a reduction in the cohesive strength between the lamellae. The latter contribute to a reduction in thermal conductivity and to an increased thermal shock resistance.

However, intra-splat cracks can also allow corrosive agents to penetrate inside the coating, promoting a premature failure [26,27].

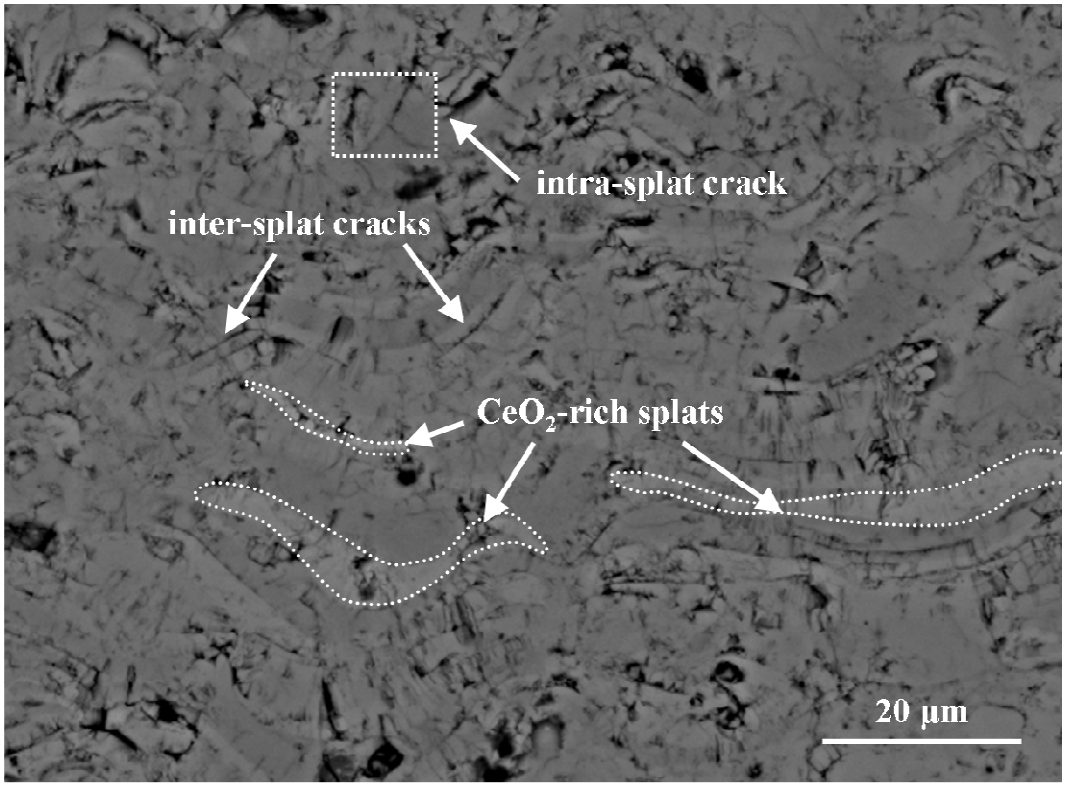

Figure 3.26 - SEM image of CYSZ coating cross section showing inter-lamellar and intra-lamellar cracks (BSE).

Different areas characterized by different grey contrasts can be observed in the coating, denoting elements and compounds with different atomic weight. In particular, due to the higher scattering intensity of heavier atoms, darker regions correspond to elements and compounds with lower atomic weight whereas brighter regions correspond to elements characterized by higher atomic weight. Energy Dispersive Spectroscopy (EDS) analysis showed these brighter areas to be more CeO_2 stabilizer-rich; however, it does not allow us to gain a quantitative and accurate estimation of the content of each element in the coating.

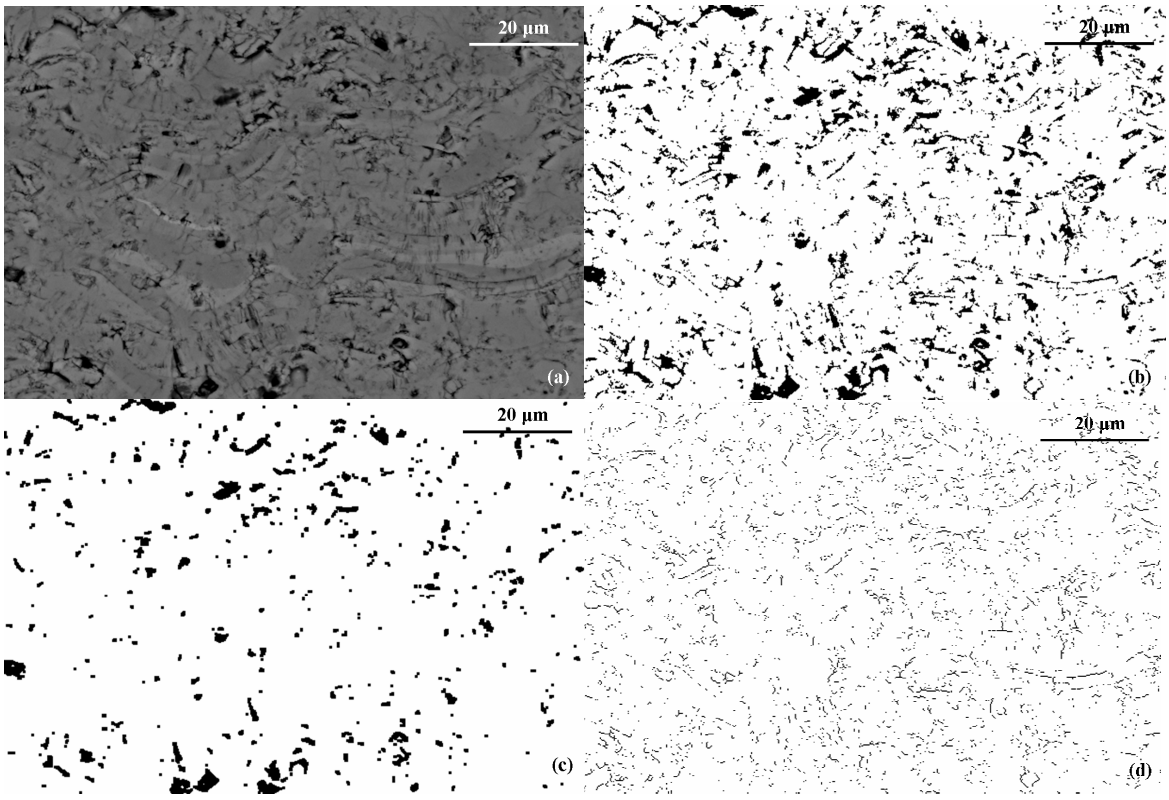

Figure 3.31 - Image analysis procedure for separating microstructural defects, (a) original greyscale image, (b) binary image showing total porosity, (c) image with globular porosity, (d) inter-lamellar and intra-lamellar cracks.

In order to study the topology and the volume of the typical porosities detected within as-sprayed CYSZ coating, several SEM micrographs (618 x 420 pixels, 103 x 70 µm) were processed using Image Analysis (IA). Each greyscale image is thresholded depending on the different contrast between the dense material and the pores, so that within each binary image all the microstructural defects, *i.e.* pores and microcracks, may be identified and classified about their size and shape. To this purpose, each binary image was processed by means of binary operations. As an example, Fig. 3.31 reports the details related SEM image processing. The sequence illustrates: (a) original grey-scale micrograph, (b) binary image obtained by tresholding, (c) globular porosity and (d) microcracks.

The microstructure contains globular pores, inter-lamellar and intra-lamellar microcracks. Globular porosity includes large circular or elliptical pores (d > 3µm) and more fine pores (d

< 3 μm). The latter are homogeneously distributed. These fine pores derive by gas entrapped under the liquid droplets, while the coarse pores were associated with filling defects in the coating microstructure, caused by unmelted or semi-molten particles. Some irregular large pores, not equally distributed were determined by pull-out of unmelted particles during polishing and were discarded for quantitative measurements, as they may provide an over-estimation of the porosity volume. Moreover, inter-lamellar and intra-lamellar microcracks can be also identified. The former with size from 0.1 to 3 μm derive from an imperfect bonding between the splats during the coating build-up, due to high impact velocity of the molten droplets and the corresponding rapid solidification. The latter have a thickness ranging from 0.01 to 0.5 μm and result from relaxation of stresses generated by high cooling rate. The average of 45 measurements provides a porosity fraction approximately equal to 10.2 % (standard deviation 2.0 %), which is the desired value for TBC industrial applications and much lower than that reported in a previous work, where optical micrographs were processed for porosity calculation [28]. Such value guarantees a good compromise in terms of low elastic modulus, high strain tolerance, low thermal conductivity and satisfactory protection against the entrainment of corrosive agents. Similar values have been obtained by Park *et al.* for their CYSZ coatings sprayed using Detonation Gun [27]. It has been observed that spatial resolution and image contrast have a reduced influence on the results obtained using Image Analysis.

After annealing, a partial sintering of the porous microstructure is observed. A comparison between the microstructures of annealed CYSZ coatings is reported in Fig. 3.32. It is apparent that the size and the distribution of both microcracks and globular pores are affected by thermal aging and a progressive closure of finer pores and microcracks can be observed with the progression of the thermal aging.

In particular, Fig. 3.32(d) shows the microstructure of CYSZ coating annealed at 1315 °C for 50 h at higher magnification. The coating is not fully sintered after heat treatment, indeed pores and inter-splat microcracks (approximately perpendicular to spraying direction) are partially retained. The intra-lamellar microcracks (approximately parallel to spraying direction) are still observable within the coating after the first hours of heat treatment but tend to disappear with increasing the aging time. Moreover, Fig. 3.32(c) shows that the densification which follows the heat treatment affects only to a lesser extent the size and the distribution of the large globular pores.

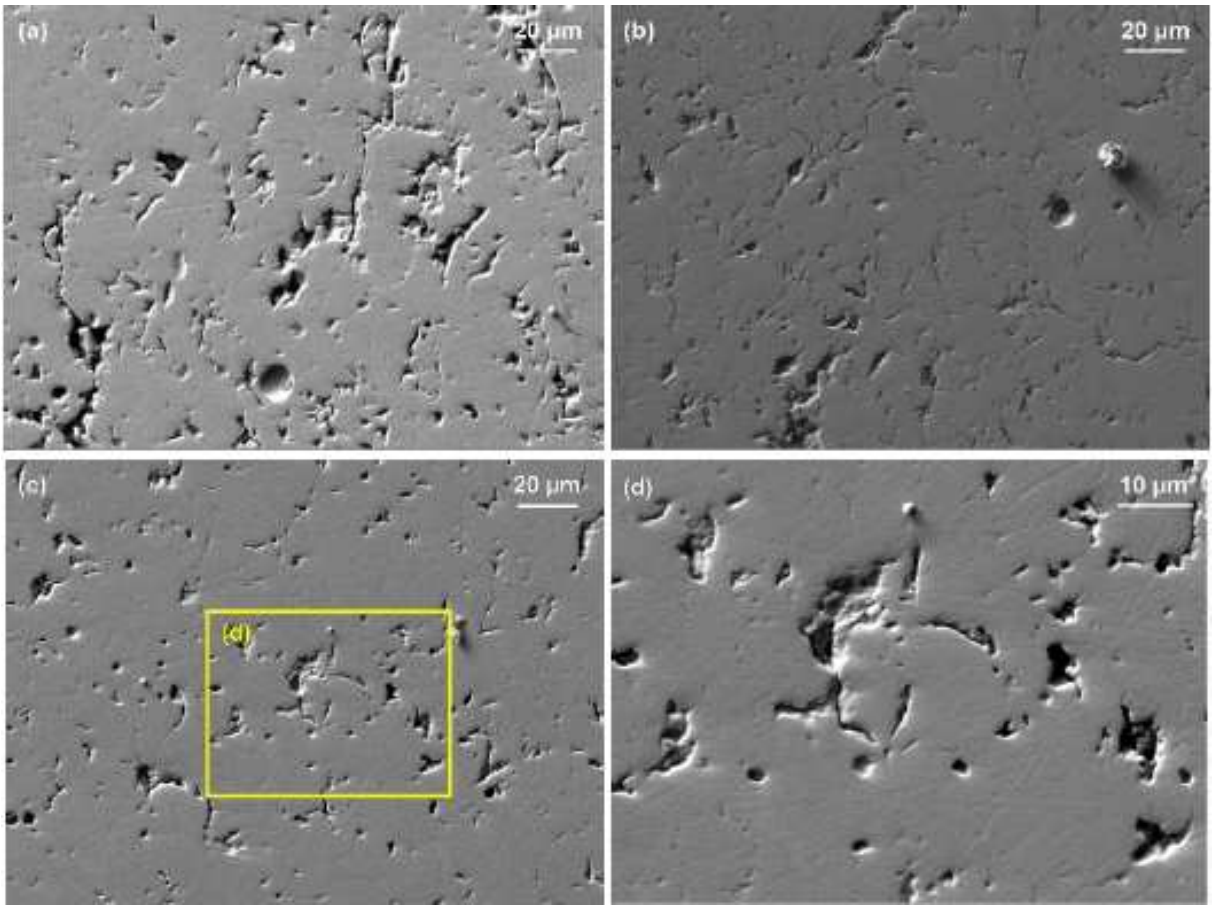

Figure 3.32 – Microstructure of annealed CYSZ coatings after (a) 2 h, (b) 10 h and (c-d) 50 h. (Spraying direction from the top to the bottom).

It is worth noting that the nature of pores and interfaces plays an important role in the sintering behaviour of plasma sprayed coatings. Since the first hours of heat treatment, the

formation of sintering necks between the lamellae reduces the interlamellar porosity. In particular, after heat treatment it is difficult to distinguish the original lamellar microstructure of the as-sprayed coatings. This feature was also observed in a previous study carried out on air plasma sprayed YSZ coatings [29].

SEM secondary electron images reported in Figs. 3.33, 3.34 and 3.35 show the fractured cross sections for as-sprayed and annealed coatings, respectively.

The as-sprayed CYSZ coating shows a lamellar structure composed of lamellae approximately parallel to coating-substrate interface, separated by splat boundaries and embedded in a network of cracks and voids. Within molten splats we can observe columnar grains with size lower than 1 µm (some hundreds of nanometers), oriented from the bottom to the top of each splat.

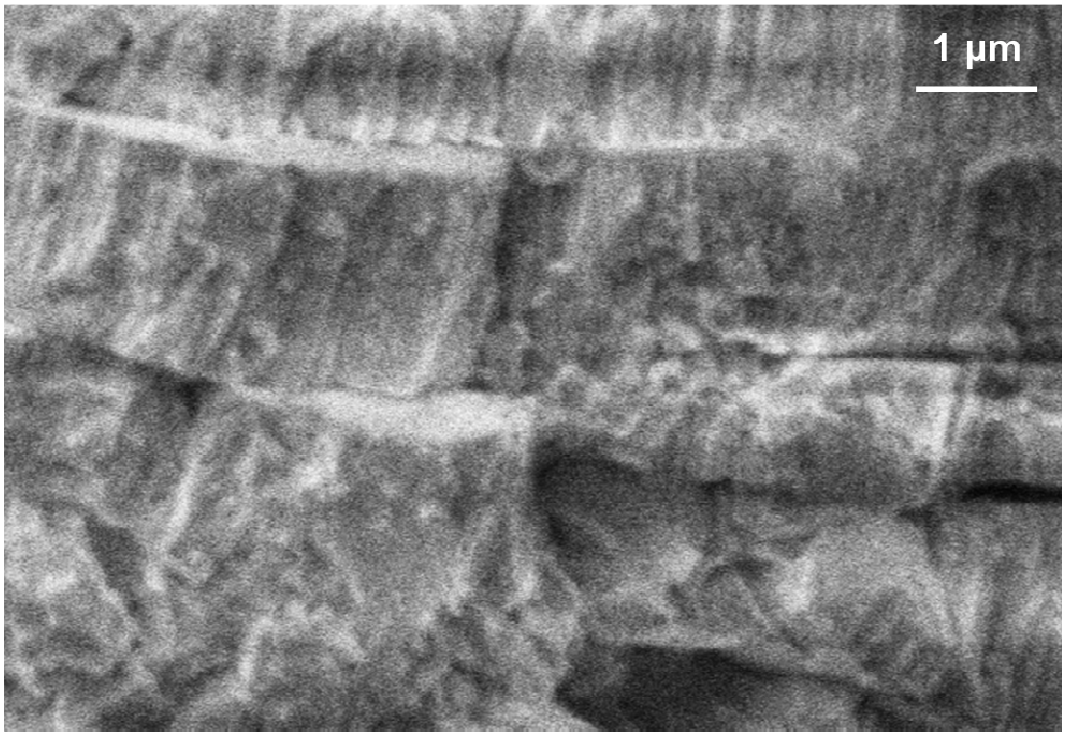

Figure 3.33 - Fractured cross section of as-sprayed CYSZ coating, showing columnar grains within the molten splats (SE).

They possess a preferential direction, since they are oriented from the bottom to the top of the splats. The thickness of each lamella increases with increasing the annealing time, by the gradual growth of these columnar grains across splat boundaries.

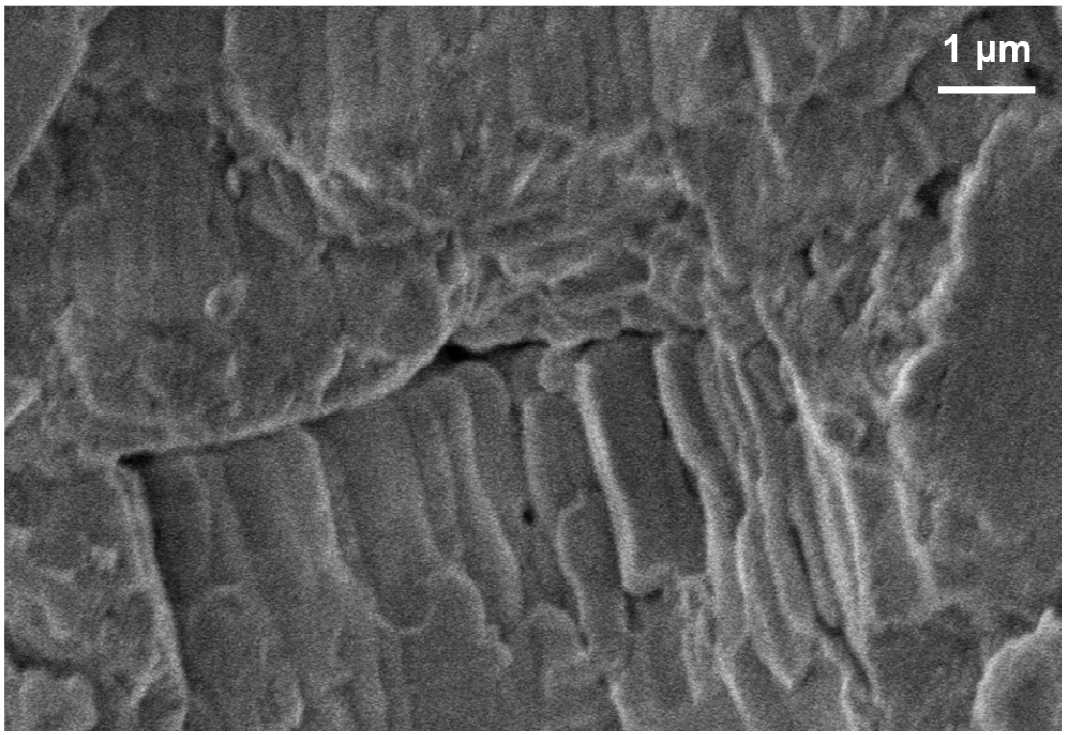

Figure 3.34 - Fractured cross section of CYSZ coating annealed for 10 h at 1315 °C (SE).

After 50 h, grain rotation among neighboring grains occurs, producing a coherent grain-grain interface, the disappearance of grain boundaries and, consequently, grain coalescence. A similar behaviour has been appreciated for plasma sprayed nanostructured YSZ coatings [30]. The grain orientation changes and some equiaxed grains grow and replace the columnar structure that tends to disappear. Moreover, a trans-granular fracture is observed in the CYSZ coatings after high-temperature exposure.

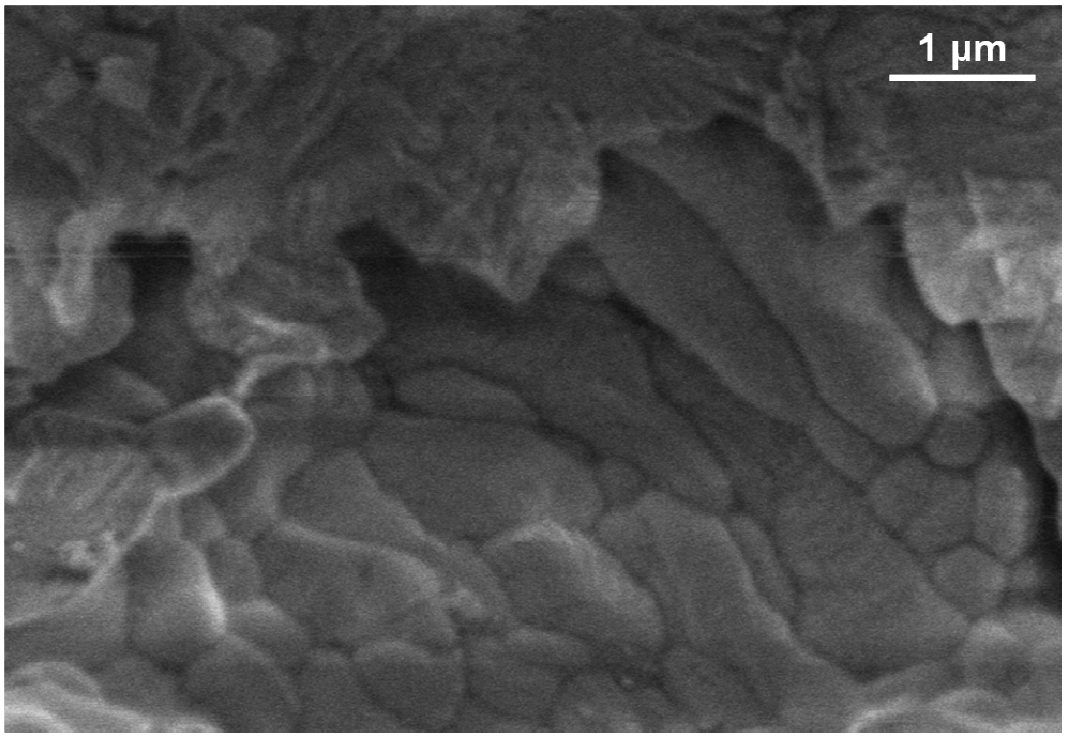

Figure 3.35 - Fractured cross section of CYSZ coating annealed for 50 h at 1315 °C (SE).

3.2.3 Determination of elastic properties by IET

The elastic modulus of CYSZ coating was determined using IET as previously described.

Before plasma spraying, the elastic modulus of each substrate was determined according to the ASTM standard [31].

The so-obtained elastic modulus is equal to 190 GPa (standard deviation = 0.4 %). The results present a reduced scatter and are in agreement with the common values reported for steel. The mass density of the steel substrates has been determined from the plate volume and mass. The value obtained for the substrates is 7.78 g/cm^3. The measured mass density of as-sprayed CYSZ coating is 5.4 g/cm^3.

Firstly, three specimens have been tested. Then, the procedure has been improved, and further five samples with lower thickness (~285 µm against ~360 µm) have been measured. The dimensional and mass properties of the coated samples are shown in Tables 3.8 and 3.9,

respectively, while the corresponding values for fundamental frequency vibration and elastic modulus are reported in Tables 3.10 and 3.11.

So, the results shown in Tables 3.8 and 3.10 have to be considered as preliminary, while the results reported in Tables 3.9 and 3.11 can be considered as the real properties of the samples. Table 3.11 contains, for each experimental variable, the mean value of *n* measurements. Young's modulus of CYSZ coating is determined using Eq. 2.4.

Specimen no.	*N*	P1	P2	P3
length, *L* [mm]	2	100.53	100.55	99.73
width, *B* [mm]	4	25.08	25.09	24.92
substrate thickness, t_s [mm]	5	3.986	4.021	4.027
coating thickness, t_c [mm]	5	0.362	0.357	0.367

Table 3.8 - Dimensional and mass properties of the first set of specimens (preliminary measurements).

Specimen no.	*N*	S1	S2	S3	S4	S5
length, *L* [mm]	4	99.30	99.82	99.78	99.62	100.14
width, *B* [mm]	6	24.97	24.97	24.99	24.99	24.94
substrate thickness, t_s [mm]	9	3.000	3.009	2.985	2.988	3.007
coating thickness, t_c [mm]	9	0.281	0.289	0.283	0.288	0.286
sample mass, *m* [g]	3	61.21	61.11	61.46	61.49	61.99

Table 3.9 - Dimensional and mass properties of the second set of specimens (final measurements).

The mean value of elastic modulus for as-sprayed CYSZ coating is equal to 29.2 GPa and the associated experimental uncertainty was found to be 9 % [12].

Specimen no.	P1	P2	P3
Fundamental frequency, f [Hz]	2092.0	2094.7	2134.1
Coating elastic modulus, E_c [GPa]	25.1	25.5	23.4

Table 3.10 – Fundamental natural frequencies and corresponding Young's modulus of CYSZ coatings (preliminary measurements).

Specimen no.	S1	S2	S3	S4	S5
Fundamental frequency, f [Hz]	1544.2	1534.9	1519.0	1519.4	1516.6
Coating elastic modulus, E_c [GPa]	32.0	26.9	31.4	26.9	29.1

Table 3.11 - Fundamental frequencies of coated samples and corresponding Young's modulus of CYSZ coatings (final measurements).

The mean value obtained herein is somewhat higher (20 %) with respect to those reported in [13,14,15] for APS YSZ coatings obtained using vibration-based iterative procedures. This result could be addressed to the different feedstock morphology and coating microstructure.

On the other hand, by using IET technique both fracture and non linear material response are prevented because the sample is subjected to low strains, nearly at the origin of the stress-strain curve. However, sensitivity issues may arise using IET. A careful choice of coating to substrate thicknesses ratio (t_c/t_s) should be made. A very thin substrate would increase the sensitivity, *i.e.* a larger shift in the fundamental frequency of vibration could be observed after coating deposition. However, the development of thermal residual stresses may lead to sample distortion and, as a consequence, may induce large errors on E_c measurements. This drawback actually restricts the choice of substrate thickness. A series of finite element analyses, not

reported herein for the sake of brevity, was carried out in order to select the ratio t_s/t_c which provides negligible sample curvature after fabrication; the analyses showed that the frequency shift related to the ratio herein employed ($t_s/t_c \approx 10$) provides an error on elastic modulus calculation less than 1 %.

3.2.4 Microhardness

The heat treatment affects the microstructure of CYSZ coating. In order to assess the corresponding influence on hardness, Vickers microindentation was carried out. Hardness measurement is often a difficult task due to the heterogeneous microstructure of the coating, which is characterized by the presence of microcracks, pores, splat boundaries and unmelted particles.

Accurate Vickers microhardness measurements rely on visual resolution of the residual indentation; however, the diagonal of the indentation, *d*, can be difficult to resolve, indeed the load should be low enough to avoid cracking, which otherwise occurs within the indentation site [16]. Preliminary indentation tests indicated that a load of 300 gf avoided cracking and retained the resolution of the residual indentation.

As the heterogeneous microstructure of plasma sprayed coatings can lead to scattered data, a minimum of 20 indentations was performed on each coating cross section. The results have been in turn presented by means of Weibull statistics, as a Gaussian distribution is not adequate to describe the variation of the mechanical data for plasma sprayed porous ceramic coatings.

In particular, the experimental data have been sorted in ascending order and the cumulative density function of probability, defined as $\alpha = (i\text{-}0.5)/N$, was assigned to each hardness data. The Weibull plots corresponding to the microhardness data are reported in Fig. 3.36. The mean value of the hardness is represented by the intersection of x-axis (y = 0) and the Weibull

plot. On the other hand, information related to the experimental scatter are provided by the Weibull modulus, *m*, *i.e.* the slope of the line in the plot; in particular, a higher modulus represents low experimental scatter. Table 3.11 shows the values of the Weibull parameters pertaining to Vickers microhardness data obtained on as-produced and annealed CYSZ samples.

An increase in Vickers microhardness for increasing annealing time is observed, indeed the plots in Fig. 3.36 shift toward higher hardness for increasing the aging time. This effect can be attributed to the partial sintering of the porous microstructure and is in agreement with the microstructural observations (Fig. 3.28). Similar behaviour has also been observed on heat treated YSZ coatings [32]. In particular, the increase in microhardness is found to be 7 % after 2 h, and it reaches 31 % after 50 h of isothermal aging. Besides, there is not a clear trend in the Weibull modulus of microhardness data, as shown in Table 3.12.

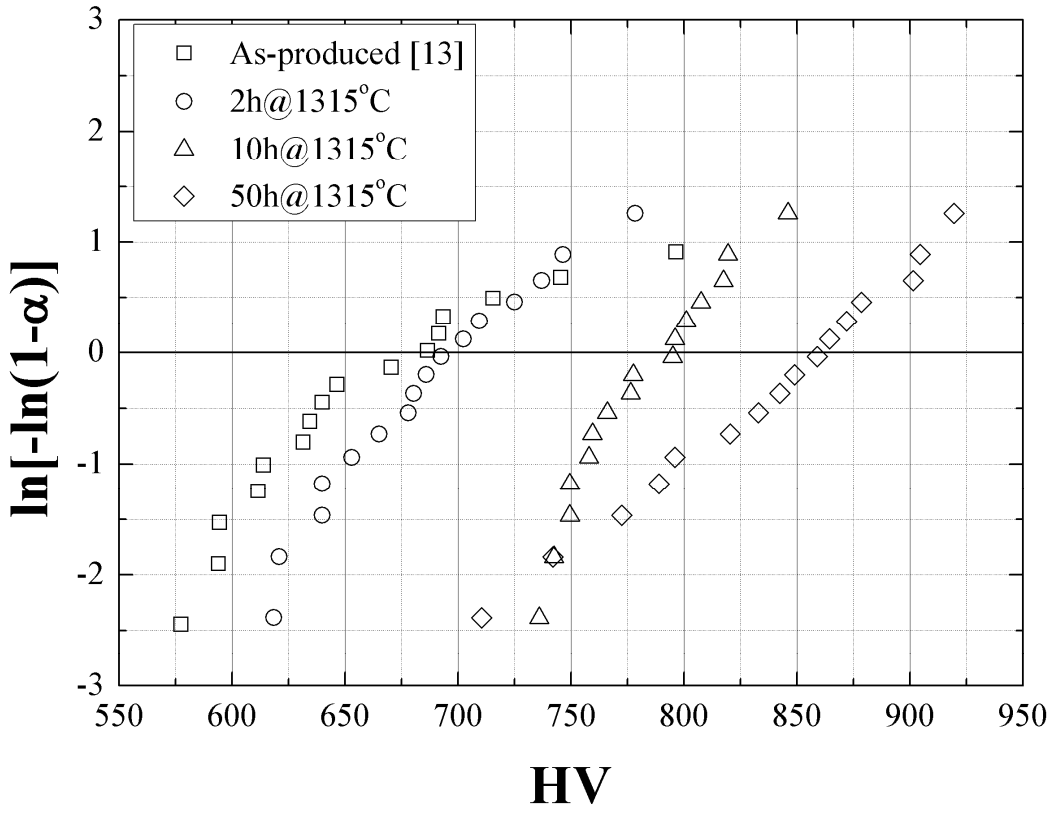

Figure 3.36 - Weibull plots of Vickers microhardness data.

	Hardness [HV]	m
As sprayed	654	19.1
Annealed, 1315°C, 2 h	700	12.4
Annealed, 1315°C, 10 h	793	24.6
Annealed, 1315°C, 50 h	857	14.9

Table 3.12 - Microhardness of annealed CYSZ coatings.

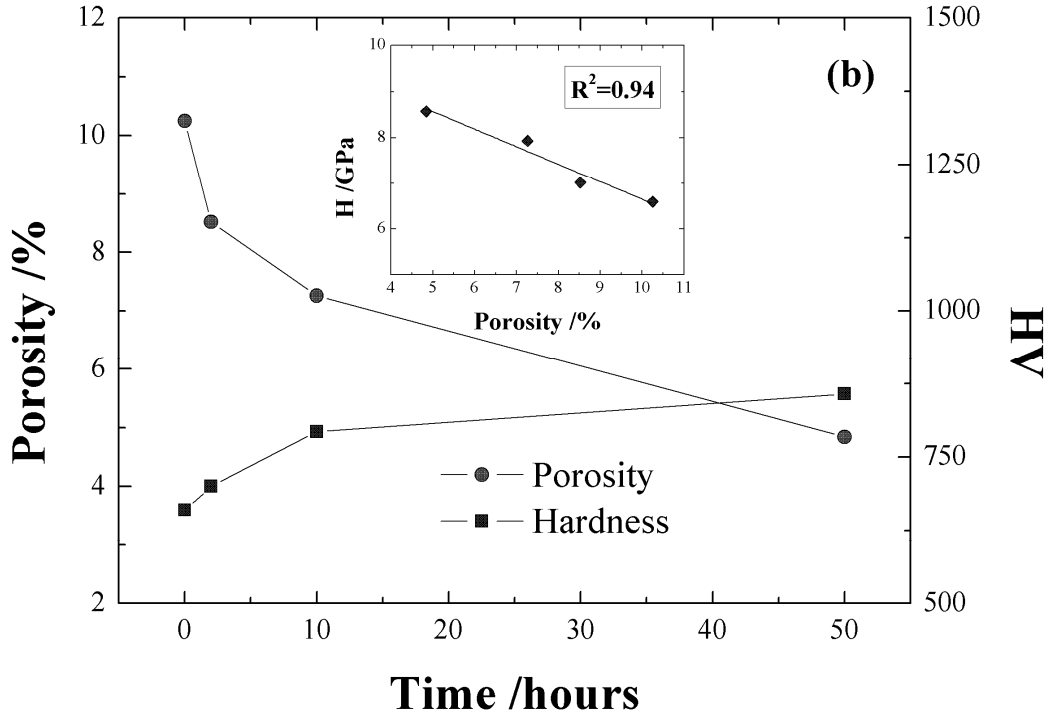

Figure 3.37 – Evolution of porosity level and microhardness as a function of the annealing time.

This feature could be attributed to the presence of globular porosity which has not fully recovered during the heat treatment; during the tests the indenter tip can impinge on these pores by leading to pronounced scatter in the experimental data.

The initial porosity fraction of the coating is about ~10 %. However, as shown in Fig. 3.37, after 50 h at 1315 °C the porosity decreases to ~5 %.

It is worth noting that the total porosity of the coating includes the contribution of globular porosity as well as the porosity derived from microcracks and splat boundaries.

The evolution of microhardness with annealing time is also reported in Fig. 3.37. Microhardness mean values progressively rise with annealing time. As expected, the graph shows a correlation between porosity and microhardness; in particular, in the inset in Fig. 3.33 a linear relationship between microhardness and porosity fraction can be observed.

3.2.5 Nanoindentation

Similarly, consistent hardness measurements can be also obtained with depth-sensing nanoindentation technique using low loads with no evidence of cracking. The first tests have been performed on as-sprayed CYSZ coatings.

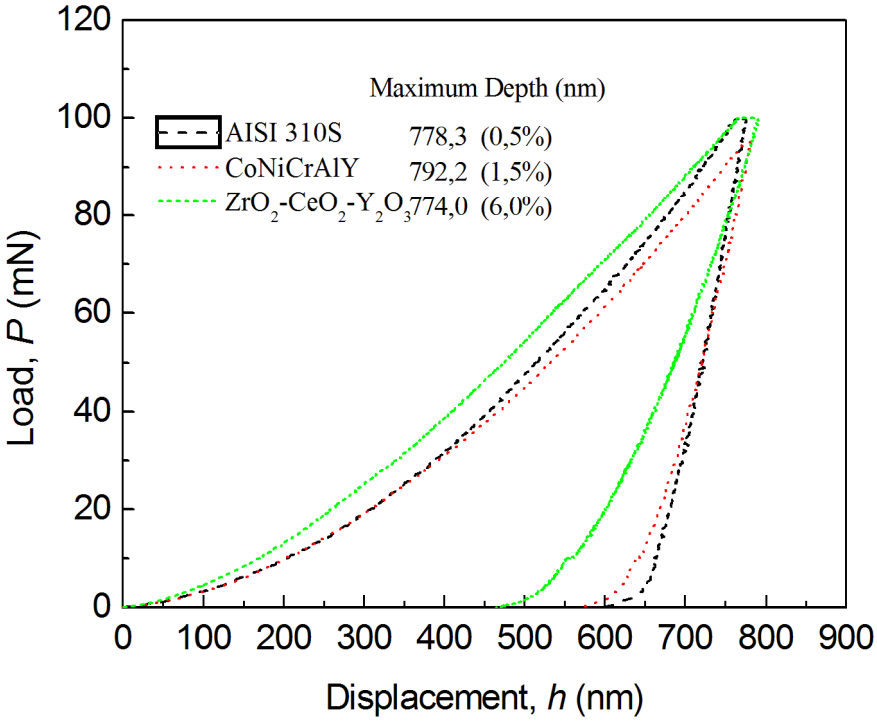

Figure 3.38 - Typical nano-indentation responses for the TBC examined.

The hardness as well as the reduced Young's modulus of CYSZ coatings have been determined. Typical indentation load-displacement curves, obtained on coating polished cross-section, are reported in Fig. 3.38.

A total of N = 20 indentation was carried out for each measurement. The distance between each indentation was equal to 25 µm so that it is possible to avoid a mutual influence of consecutive responses. Three loading rates have been adopted in the tests. The corresponding two-parameters Weibull plots for H and E_r are reported in Fig. 3.39.

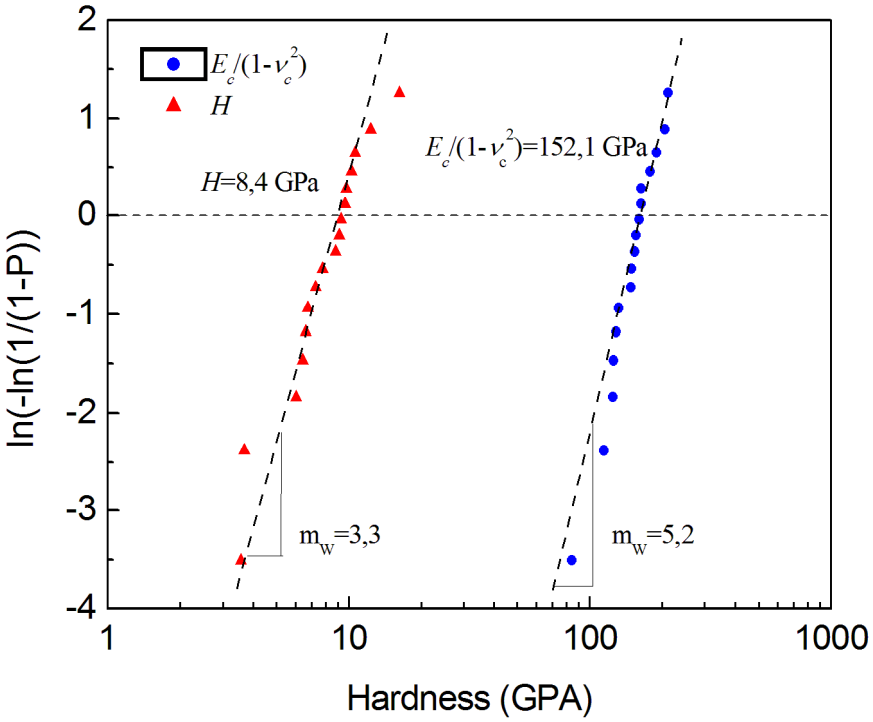

Figure 3.39 - Weibull hardness and Young's modulus plots for CYSZ coating.

In particular, the experimental data have been sorted in ascending order and the corresponding the cumulative density function of probability, defined as P = (i-0.5)/N, was assigned to each hardness and elastic modulus data. The most meaningful data provided by the plot are the mean values of H and E_r as well as the Weibull parameter, *i.e.* the slope m_W. The latter is

directly related to the measurement scatter, in particular steeper lines mean reduced experimental scatter. It is worth mentioning that NI data related to indentations performed near visible microcracks and pores have been not considered for calculation purposes. The results were found to be essentially independent on the loading rate; for this reason, the Weibull parameters reported in Fig. 3.39 are referred to NI tests carried out at 0.3 mN/s.

Young's modulus obtained using NI is much higher than that measured by IET (five time greater). Obviously, the difference in the results can be attributed to the different measurement scale associated with the techniques employed. NI probes the microstructure at splat level, then the corresponding values of Young's modulus should be regarded as a local material property. On the other hand, IET works at the macroscopic level, *i.e.* it provides material properties averaged over sample volume. As a consequence, a direct comparison cannot be made.

However, in order to provide a cross-check on the consistency among the results obtained using NI and IET, a micromechanical method, known as Hashin-Hasselman model [19,20], has been applied. Given inputs for CYSZ coating such as the measured porosity fraction (10.2 %), the reduced Young's modulus determined using NI and Poisson's ratio provided in [22] (ν = 0.22), Eq. 3.1 (see section 3.1.3) estimates a Young's modulus of 33.7 GPa. So, the theoretical prediction of Young's modulus is similar to that provided using the IET. Moreover, the elastic modulus as obtained using IET shows reduced scatter and high reproducibility as opposed to NI. Indeed, NI measurements are very sensitive to local surface conditions and anisotropies. Under the circumstances where indent falls at a pore/solid edge in CYSZ coating, there might be slip of the indenter tip thereby leading to scattered results. Then the Nanoindentation technique has been applied to study high-temperature sintering of the porous microstructure of plasma sprayed CYSZ coatings. To this purpose, in the present

work, the nanoindentation tests were carried out using a maximum load of 100 mN. The reduced Young's modulus (E_r) of the coating was obtained by means of Eq. 2.10.

A total number of 30 indentations was carried out for each sample obtained under different conditions. In particular, three sets of 10 indentations have been made in the through-thickness direction and the distance between each of them was equal to 40 µm so that it is possible to avoid a mutual influence of consecutive indentations. Selected load-depth curves are reported in Fig. 3.40.

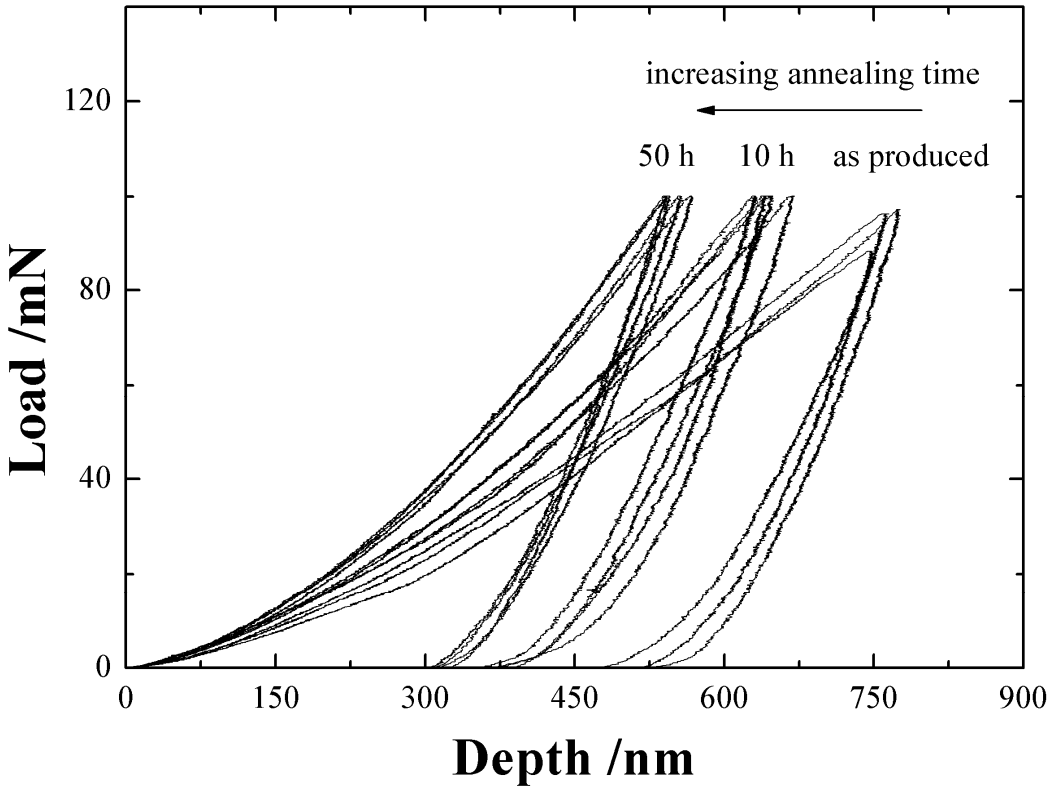

Figure 3.40 – Selected load-depth curves obtained during NI tests carried out on as produced and heat-treated samples.

It can be observed that the maximum penetration depth (h_{max}) decreases with increasing annealing time, whereas the slope of the unloading curve increases. This behaviour can be attributed to the progressive densification of the coating and results in increasing values of H and E_r, and it is clearly shown by the Weibull plots in Figs. 3.41 and 3.42, where the

cumulative density function of probability is marked as α. In particular, a shift of the Weibull curves toward higher values of H and E_r can be observed for increasing aging time.

The corresponding Weibull parameters are reported in Table 3.13. The increase in nanohardness is rather sharp, indeed, Table 3.12 shows that H increases from 7.00 GPa to 9.45 GPa (+ 35 %) after 2 h and steps to 11 GPa (+ 60 %) after 10 h. However, for longer aging time no further increase is observed.

These features are also illustrated in Fig. 3.43, where H and E_r are reported as a function of the aging time. The inset in Fig. 3.43 also shows that a non-linear relationship between the mechanical properties and the porosity seems to hold in this case.

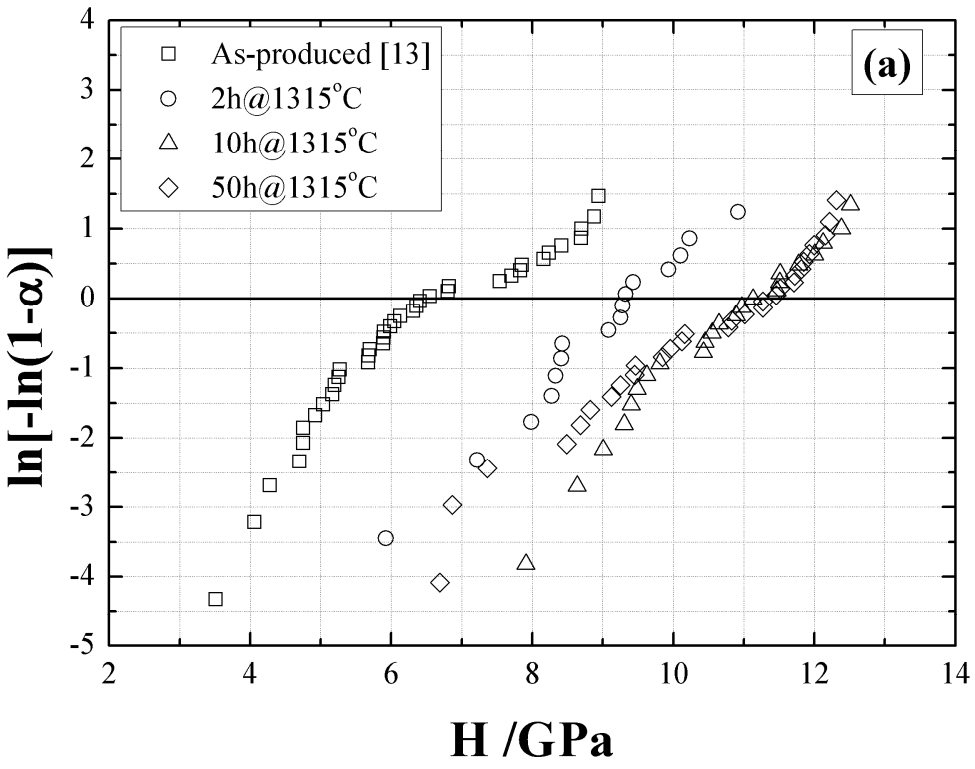

Figure 3.41 - Weibull plots of hardness data, determined by nanoindentation testing with a Berkovich indenter.

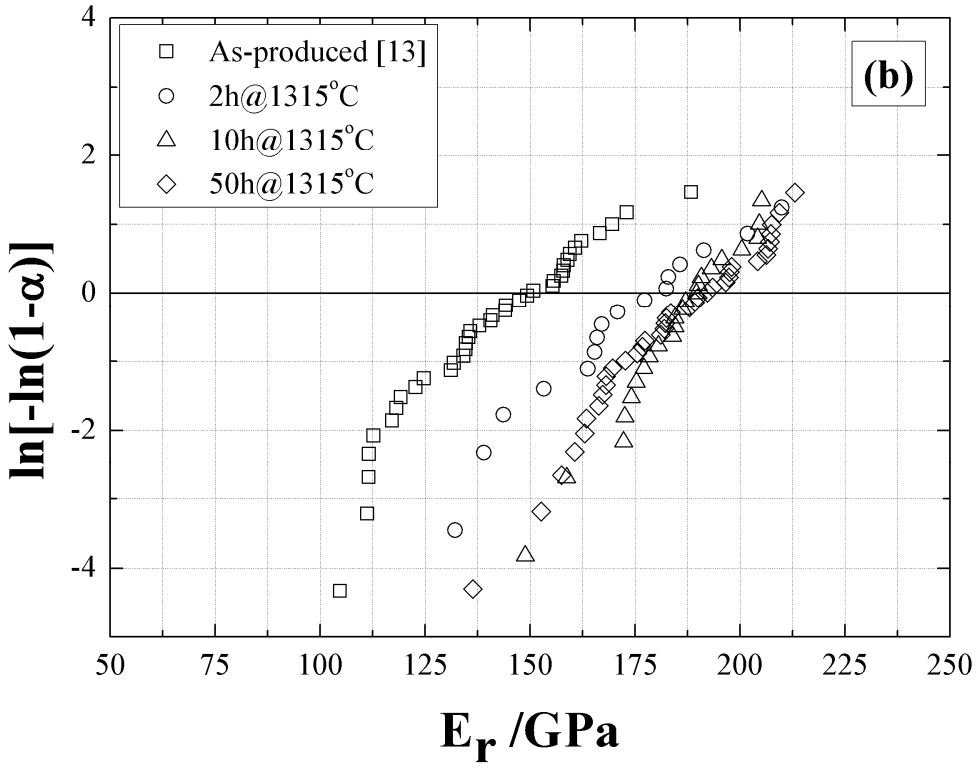

Figure 3.42 – Weibull plots of reduced Young's modulus data, determined by nanoindentation testing with a Berkovich indenter.

	H [GPa]	m_H	E_r [GPa]	m_E
As sprayed	7.0	5.2	152.7	6.9
Annealed, 1315°C, 2 h	9.4	8.2	181.8	9.3
Annealed, 1315°C, 10 h	11.2	10.0	190.7	15.0
Annealed, 1315°C, 50 h	11.0	7.2	192.8	11.8

Table 3.13 – Hardness and reduced Young's modulus of annealed CYSZ coatings.

Regarding the hardness, it is apparent that after 10 h of isothermal aging a plateau in the curve is reached. This point can be explained in terms of variation of the porosity fraction. Although

large globular pores are not fully recovered after thermal aging[2], the fine scale porosity (*e.g.* microcracks and poor inter-splat contact), largely responsible for low stiffness and low conductivity, tends to be partially removed since the first hours of the heat treatment [29,32,33,34].

As the size-scale at which nanoindentations are performed is comparable to the fine porosity observed in the coatings, it follows that NI data are mostly sensitive to these microstructural features, therefore the hardness shows a plateau for greater aging times.

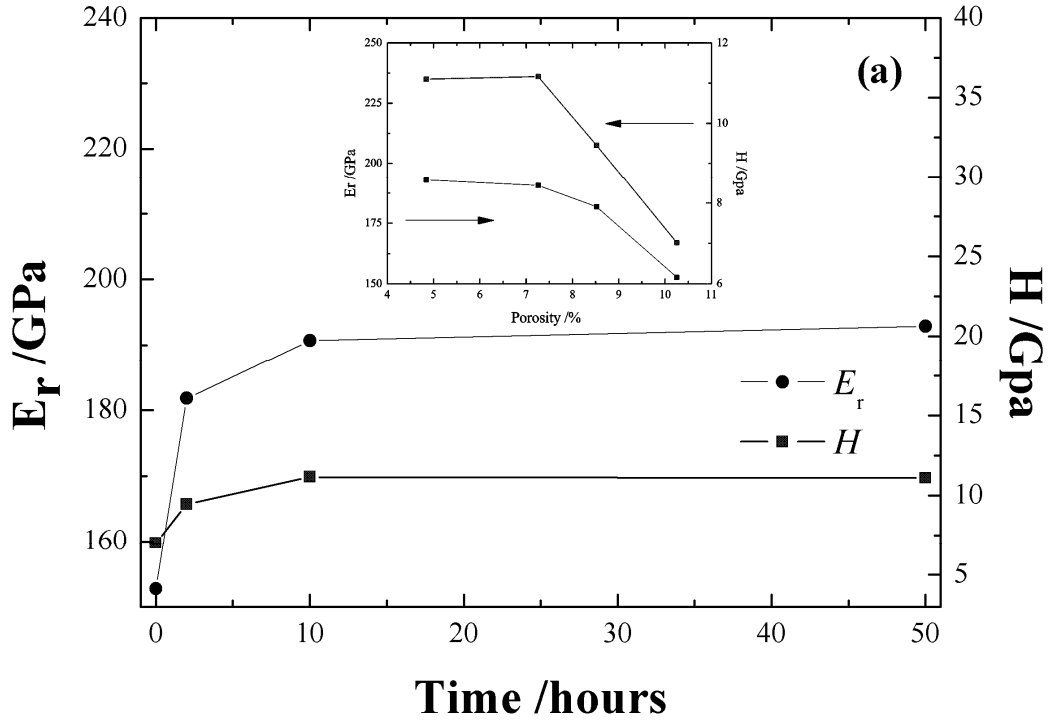

Figure 3.43 – Evolution of E_r and H as a function of annealing time (the inset shows the variation of E_r and H with porosity).

Moreover, it is worth noting that, comparing the results reported in Tables 3.10 and 3.11, a good agreement among nanohardness and microhardness values can be observed.

From Fig. 3.43, it is also possible to appreciate a similar trend for the Young modulus (E_r), however, the increase in E_r after 10 h was lower and equal to 25 %.

[2] Globular porosity is not fully recovered after thermal aging because grain-growth across splats boundaries do require the splats to be in a fairly intimate contact [29].

A similar behaviour has been reported for APS YSZ coatings in [29,33]. In particular, the initial increase in the mechanical properties (and then the high sintering rate) was therein addressed to the improved bonding and coherence across the splat boundaries. The subsequent step was characterized by a lower increase in stiffness and was addressed to the repair of microcracks. However, it is worth mentioning that in [29,33] the stiffness of the coating was determined by means of static bending and a resonant based method. Moreover, the deviation of mechanical properties in the through-thickness direction is not significant, as illustrated in Fig. 3.44. So, the high-temperature sintering of CYSZ coating is uniform along coating thickness.

It is important to underline that E_r and H measured by nanoindentation could be affected by thermal residual stresses in the samples [35].

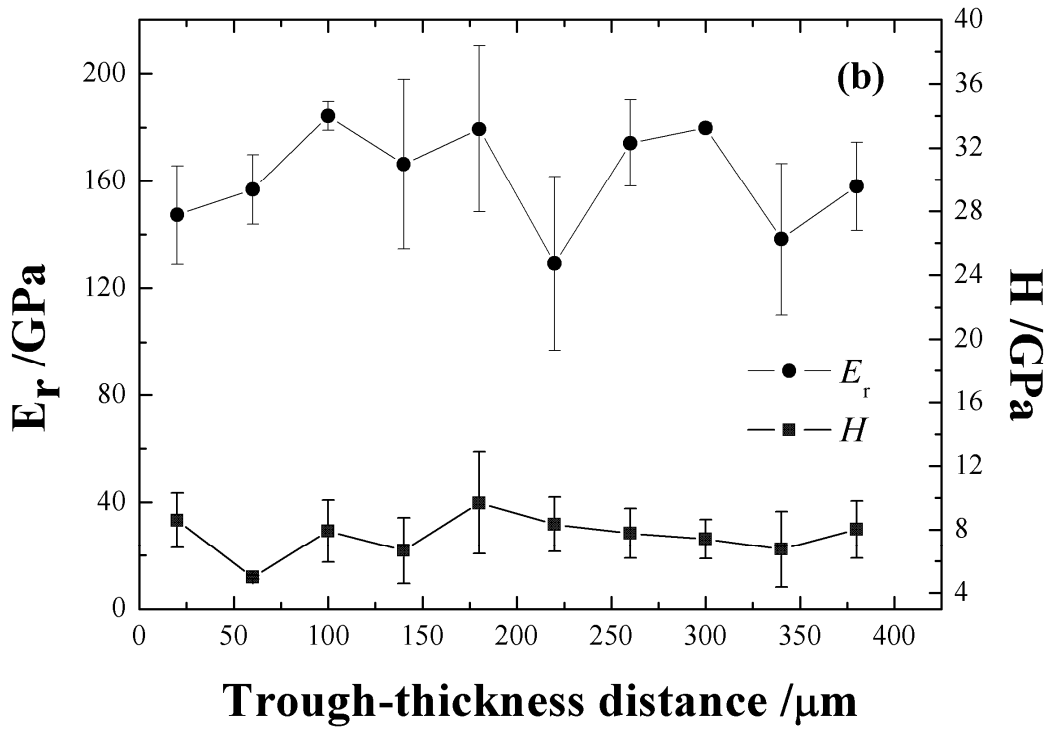

Figure 3.44 –Variation of E_r and H in the through-thickness direction (sample heat-treated for 50h).

It has been demonstrated that this is an artefact caused by indenter-to-sample contact area variation due to the presence of thermal stresses and which is not taken into account for the analysis procedure [36,37]. However, these stresses mainly arise as a consequence of the thermal mismatch between the top-coat (ceramic) and the underlying layers (bond-coat and substrate). Unsupported (free-standing) ceramic top-coats are relatively unstressed and then the load-displacement curves obtained during NI (and in turn the mechanical properties) are unaffected by the standard data analysis procedure [38].

3.2.6 Thermal expansion

The in-plane and through-thickness thermal expansions of as-sprayed, 10 h and 50 h annealed CYSZ coatings are shown in Fig. 3.45 and Fig. 3.46, respectively.

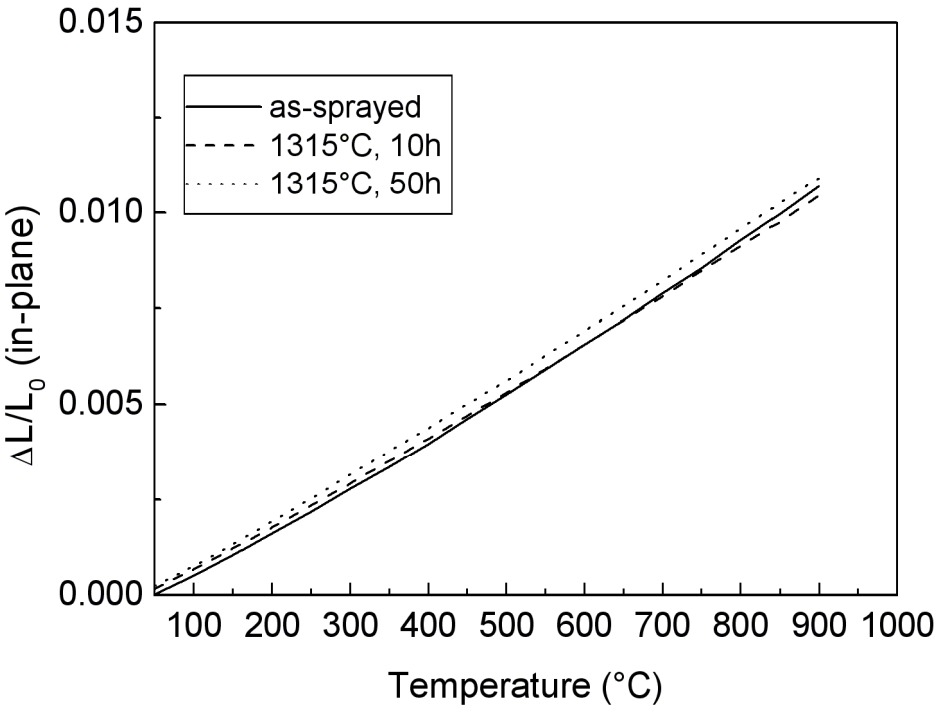

Figure 3.45 - In-plane thermal expansion of as-sprayed and annealed CYSZ coatings.

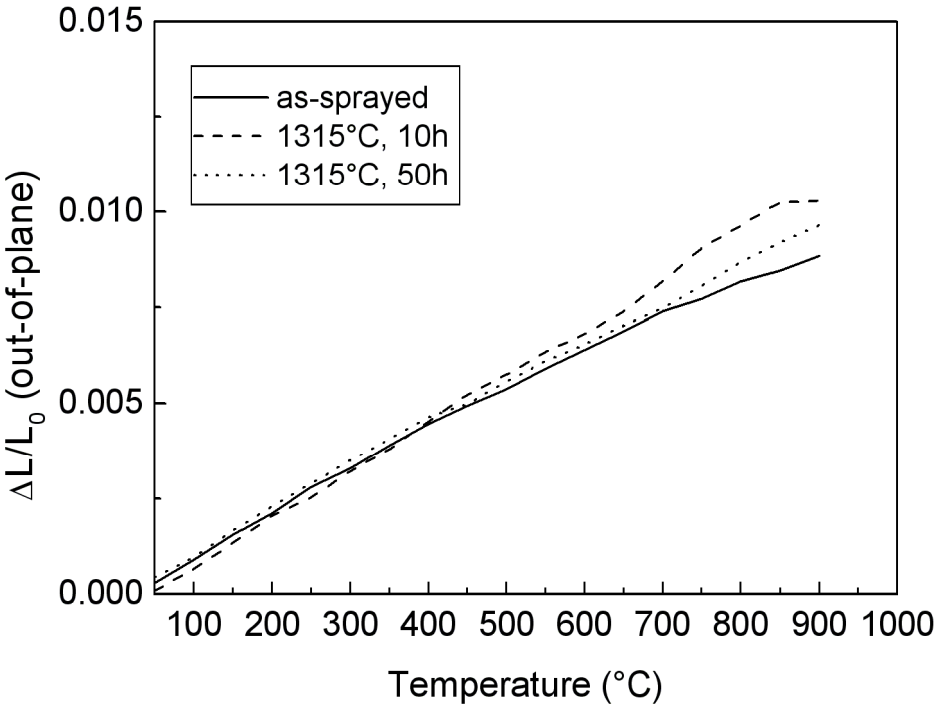

Figure 3.46 - Out-of-plane thermal expansion of as-sprayed and annealed CYSZ coatings.

In-plane and out-of-plane thermal expansions are almost linear between 50 °C and 900 °C for both as-sprayed and annealed coatings. No in-situ sintering occurs up 900 °C. It should be noted that the presence of small impurities in the starting feedstock and then in as-sprayed and heat treated coatings is not observable by XRD analysis, however, it can surely affect the thermal expansion of the samples during heating. The thermal expansion coefficients in 50-900 °C range are summarized in Table 3.14. The thermal expansion coefficient is sensitive to the thermal aging in the out-of-plane direction and varies from 10.1 x 10^{-6} to 12.5 x 10^{-6} K^{-1}. Otherwise, the thermal expansion coefficient is rather constant in plane direction (~ 12-12.6 x 10^{-6} K^{-1}). It should be noted that the out-of-plane CTE is affected by inter-lamellar microcracks which run between coating lamellae, whereas the in-plane CTE is affected by vertical microcracks. High-temperature sintering produces the closure of interlamellar

porosity and mainly affects out-of-plane shrinkage, without providing significant changes in plane direction. Moreover, the distribution of vertical microcracks and pores within the CYSZ coating is rather uniform and yields to similar high-temperature features along orthogonal directions.

Coating	α_X (50-900 °C)	α_Z (50-900 °C)
	$[10^{-6}K^{-1}]$	$[10^{-6}K^{-1}]$
As-sprayed	12.62	10.13
Annealed, 1315°C 10 h	12.14	12.45
Annealed, 1315°C 50 h	12.64	10.69

Table 3.14 - In-plane and out-of-plane thermal expansion coefficients for as-sprayed and annealed coatings.

The in-plane CTE of CYSZ coatings is larger than that of YSZ coatings reported in literature and calculated using the same procedure. This enhancement can be explained in terms of different structure, *i.e*. the presence of cubic structure and higher concentration of oxygen vacancies. Indeed, changes in crystal structure and valence state can influence the thermal expansion, also explaining the slight differences in CTE of as-sprayed and annealed CYSZ coatings. Guo *et al.* [39] have reported a value of 11.2 x 10^{-6} K^{-1} in plane direction for as-sprayed and annealed YSZ coatings between room temperature and 1200 °C, since the thermal expansion coefficient was not affected by coating microstructure in their experiments. However, it should be noted that their coatings were only heat treated at 1200 °C for 10 h.

The same coatings showed high segmentation crack density, even if their porosity was comparable to that found for our coatings. Moreover, the values measured in this work are higher than those reported in literature for CYSZ coatings [40]. As an example, Ahmaniemi *et*

al. [41] have measured a CTE of $10.8x10^{-6}$ K^{-1} in plane direction between 50 and 1000 °C for similar CYSZ coatings.

The results herein discussed are notably promising, since a larger CTE is surely able to reduce the stresses arising from the thermal expansion mismatch between top coat and bond coat, thus increasing the lifetime of TBC during thermal cycling.

3.2.7 Heat capacity

The averages of specific heat capacity measurements on as-sprayed and thermally aged CYSZ coatings are illustrated in Fig. 3.47.

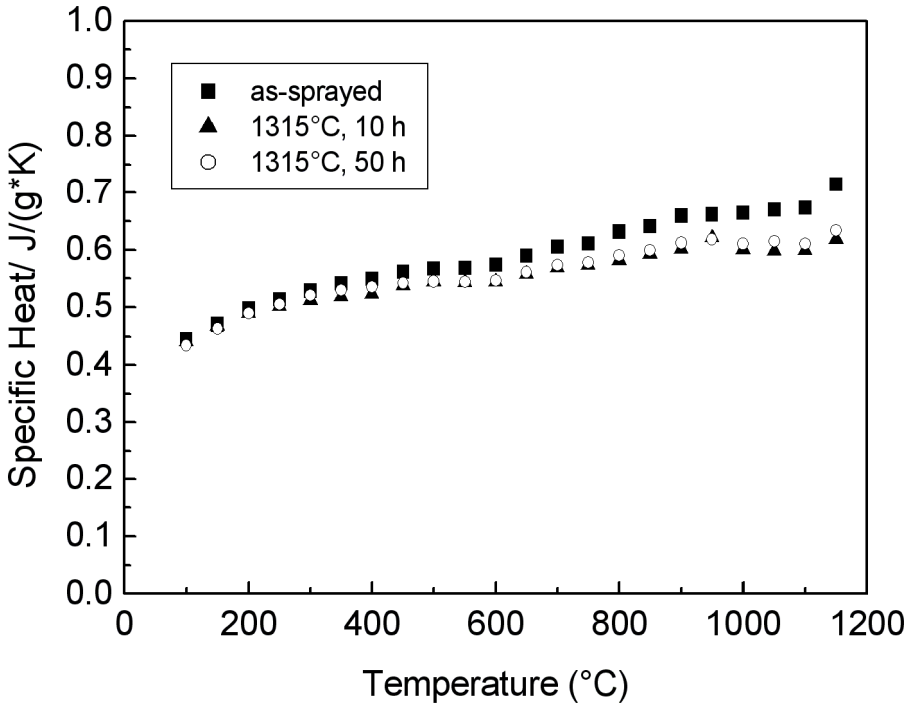

Figure 3.47 - Specific heat capacity of as-sprayed and annealed CYSZ coatings.

$C_p(T)$ curves are calculated as a mean value of three consecutive measurement cycles. It can be seen that the specific heat increases gradually as the temperature increases. At any given

temperature, below 600 °C, there appears to be no distinct difference of specific heat between as-sprayed and thermally aged CYSZ coatings. The specific heat capacity curves up 600 °C clearly show a sensitive variation between as-sprayed and annealed coatings, which may be associated to grain growth, high-temperature sintering and densification of the porous microstructure, since all these effects affect the heat transmission mechanism through the anisotropic microstructure. Until now, it has been reported that C_P is not sensitive to the coating microstructure. For as-sprayed coatings, C_P is around 0.44 $J*K^{-1}*g^{-1}$ at 100 °C and 0.71 $J*K^{-1}*g^{-1}$ at 1150 °C. This values are almost similar to those found for other plasma-sprayed YSZ coatings [42].

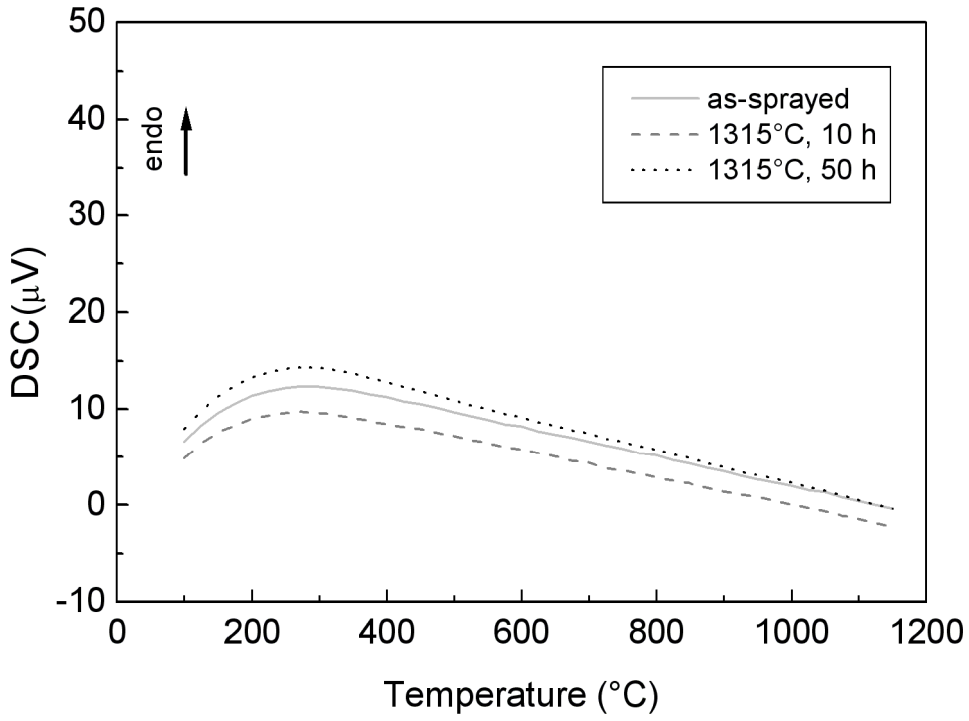

Figure 3.48 - DSC curves of as-sprayed and annealed CYSZ coatings.

However, high-temperature specific heat capacity decreases for heat treated coatings. This variation is in the range between 11 and 13.5 %. The aging time seems not to influence the

heat capacity, suggesting very close microstructural and thermal properties for coatings aged up to 50 h. Thereby, high-temperature aging reduces the heat capacity of CYSZ coatings by sintering of the porous microstructure. The formation of sintering necks between the lamellae and/or the disappearance of splat boundaries result in a decrease of interlamellar porosity and a better contact between the same lamellae, thus influencing the thermal transport properties [43]. In conclusion, the CYSZ coatings show a relatively contained high-temperature sintering. No phase transformations are detectable in DSC curves, as shown in Fig. 3.48.

3.3 Plasma sprayed YSZ coatings

3.3.1 Phase composition and high-temperature phase stability

The whole XRD patterns of YSZ feedstock, as-sprayed and annealed coatings are reported in Fig. 3.49. The as-sprayed coatings are mainly composed of tetragonal t' zirconia phase, with smaller amounts of stable tetragonal t, cubic c and monoclinic m zirconia phases, according to JCPDS (no. 81-1544 for tetragonal, no. 49-1642 for cubic and no. 37-1484 for monoclinic zirconia) available at the International Centre for Diffraction Data (ICDD). Shift in peak positions can be related to microstrains and different yttria contents in each zirconia phase, as discussed later.

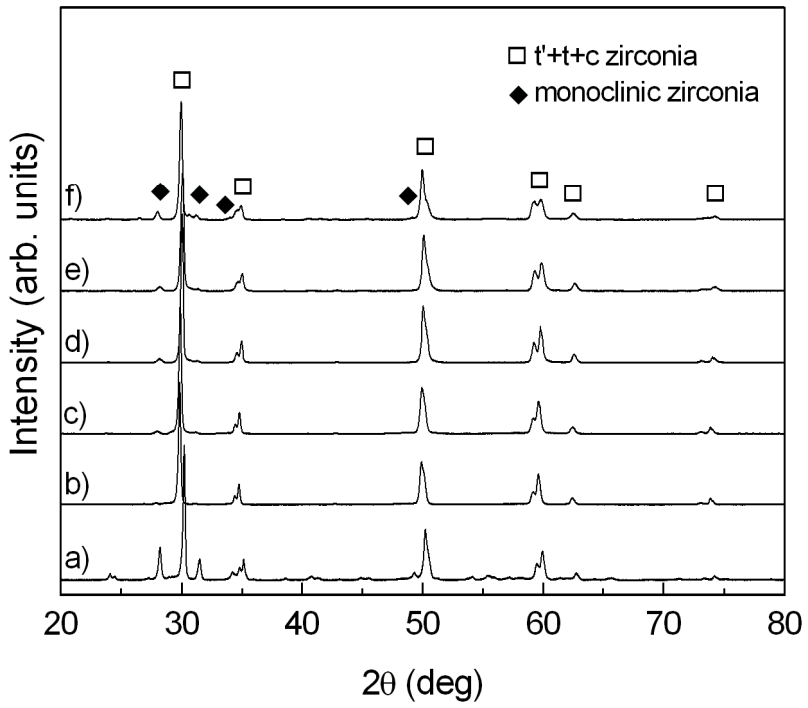

Figure 3.49 - XRD patterns of YSZ feedstock and coatings: a) feedstock; b) as-sprayed - rapidly cooled; c) as-sprayed - slowly cooled; d) annealed for 2 h; e) annealed for 10 h; f) annealed for 50 h.

Figures 3.50 and 3.51 show low-angle (27-32°) and high-angle (72-75°) regions of XRD patterns, respectively.

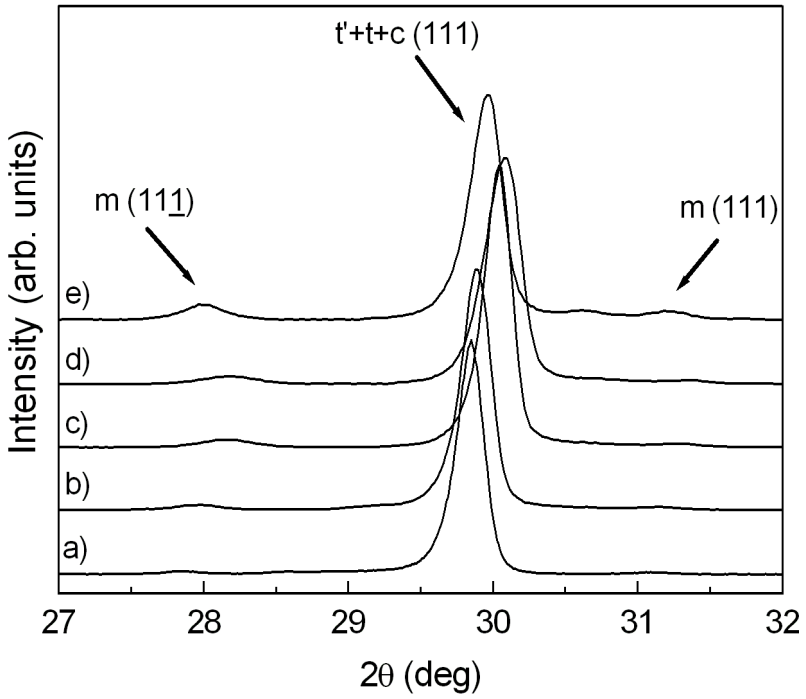

Figure 3.50 – Low-angle range of the diffraction patterns for YSZ coatings: a) as-sprayed – rapidly cooled; b) as-sprayed – slowly cooled; c) annealed for 2 h; d) annealed for 10 h; e) annealed for 50 h.

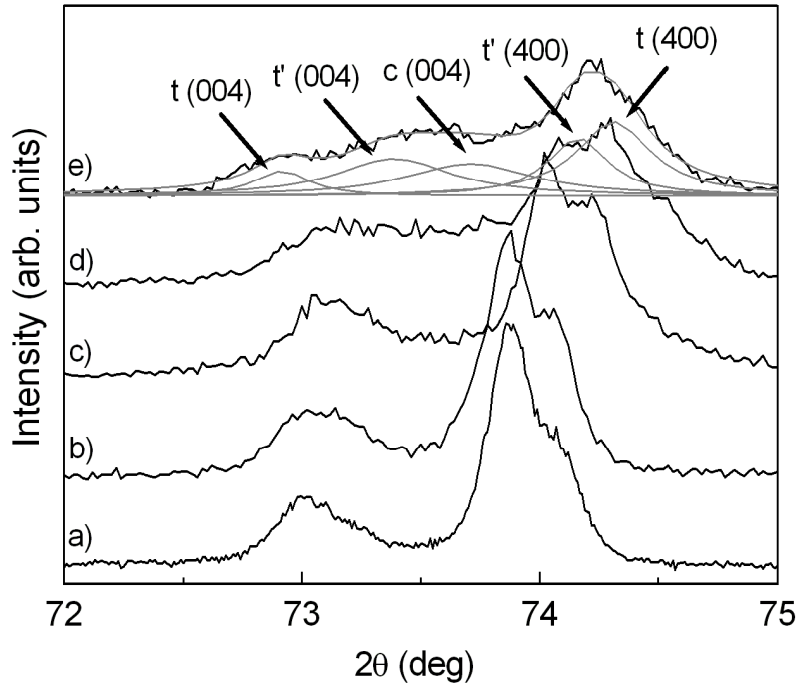

Figure 3.51 - High-angle range of the diffraction patterns for YSZ coatings: a) as-sprayed – rapidly cooled; b) as-sprayed – slowly cooled; c) annealed for 2 h; d) annealed for 10 h; e) annealed for 50 h.

Figure 3.50 shows the (111) peak for (t'+t+c) zirconia and the (11$\underline{1}$) and (111) peaks for monoclinic zirconia. In Fig. 3.51 the (004) and (400) peaks for both t' and t zirconia phases are detectable, as well as the (004) peak for cubic phase. A qualitative example of peak deconvolution is illustrated for YSZ coating aged for 50 h.

Different cooling rates employed during plasma spraying or thermal treatment of YSZ coatings can promote remarkable chemical and physical reactions, such as reduction to lower valence states, stabilizing oxide depletion or enrichment, formation of zirconium and yttrium sub-oxides and impurity segregation phenomena [24].

More precisely, when the samples are forced air cooled during deposition the molten splats are rapidly quenched and, therefore, the high oxygen vacancies formed at high temperature tend to be retained at room temperature, suppressing the tetragonal to monoclinic transformation. The coating is mainly composed of metastable tetragonal t' phase (~ 92.9 %), with small traces of cubic c and monoclinic m phases, while stable tetragonal t phase is absent.

Otherwise, a slow cooling rate reduces the level of oxygen vacancies and can promote the transformation of tetragonal to monoclinic phase, promoting possible compressive stresses in as-produced coatings. However, in our experiments the content of monoclinic phase found in slowly cooled coatings is slightly higher than that found in rapidly cooled ones, *i.e.* 4.2 % and 5 %, respectively. Therefore, it can be supposed that the monoclinic phase is substantially associated to unmelted or partially melted particles embedded in coating microstructure. To this purpose, it should be noted that the feedstock herein employed is characterized by a large amount of monoclinic phase (m = 36.8 % and t' = 63.2 %). Moreover, slowly cooled coatings contain a little amount of stable tetragonal phase, equal to 1.9 %.

As shown in Table 3.15, the content of monoclinic phase tends to gradually increase with increasing the aging time up to 13.8 % after 50 h. The peaks for monoclinic zirconia are rather

broad, suggesting a very low grain size, and then their width slightly decreases with increasing the aging time. The presence of relatively large amount of monoclinic phase at room temperature has been also noticed in YSZ coatings annealed or thermally shocked at 1300 °C (up to 20 %) [44,45].

Sample	c-ZrO_2	c	Yttria content	t'-ZrO_2	a	c	Yttria content	t-ZrO_2	a	c	Yttria content	m-ZrO_2	R_P
	(%)	[Å]	(%)	(%)	[Å]	[Å]	(%)	(%)	[Å]	[Å]	(%)	(%)	
Feedstock	-	-	-	63.2	3.6126	5.1600	7.82	-	-	-	-	36.8	10.3
As-sprayed (rapidly cooled)	2.9	5.1450	18.81	92.9	3.6251	5.1810	7.44	-	-	-	-	4.2	11.8
As-sprayed (slowly cooled)	3.5	5.1430	17.52	89.6	3.6259	5.1785	7.89	1.9	3.6162	5.1922	4.52	5.0	10.6
Annealed 1315 °C, 2 h	6.2	5.1393	15.13	70.4	3.6193	5.1747	7.20	15.8	3.6078	5.1882	3.53	7.6	10.9
Annealed 1315 °C, 10 h	13.5	5.1388	14.80	43.4	3.6168	5.1702	7.31	33.2	3.6045	5.1857	3.25	9.9	10.7
Annealed, 1315 °C, 50 h	16.1	5.1405	15.90	35.5	3.6178	5.1682	7.73	34.6	3.6078	5.1902	3.28	13.8	10.8

Table 3.15 - Relative percentages, lattice parameters and yttria contents for zirconia phases in as-sprayed and annealed YSZ coatings (Rietveld analysis).

It should be noted that the shape of the peak at ~ 30° depends on the relative proportions of cubic and tetragonal phases and the corresponding grain size.

To calculate their relative proportions, the high-angle (72-75°) range has been considered. As shown in Fig. 3.51, the metastable t' phase is unstable during high-temperature exposure and decomposes into low-yttria tetragonal phase and high-yttria cubic phase, due to the gradual diffusion of yttria stabilizer. In particular, the excess of yttria allows the nucleation and growth of cubic zirconia grains. The peak intensities for stable tetragonal t and cubic c phases increase with increasing the aging time, as well as their amounts, while the content of metastable t' phase decreases. During slow cooling to room temperature the cubic phase may be retained or may transform to tetragonal phase, whereas low-yttria tetragonal phase may

transform to monoclinic, depending on the grain growth. The transformation of tetragonal to monoclinic zirconia is noticed prior to the full decomposition of t' phase. Therefore, t', t, c and m zirconia phases coexist in annealed YSZ coatings. The small grain size of the t phase (the corresponding peaks are broader than those corresponding to the t' phase) and the retained amount of yttria in the same phase reduce the extent of the monoclinic transformation.

The calculated percentages of zirconia phases, as well as their unit cell dimensions and the corresponding contents of yttria stabilizer are summarized in Table 3.15. The R_p parameters, representative of the quality of the fit, are also reported. After 50 h of heat treatment, a significant amount of the metastable t' phase (35.5 %) is still present, together to the cubic c phase and the stable tetragonal t phases (16.1 % and 34.6 %, respectively). Therefore, long-term exposures are needed to promote the total decomposition of t' phase. It should be noted that the lattice constants increase with increasing the yttria content. The yttria content in the cubic phase is higher in as-sprayed coatings. With increasing the aging time, it firstly decreases and then increases up to 15.9 %. The yttria content in t' phase is in the range from 7.2 % to 7.9 %, while the yttria content in t phase is between 3.2 % and 4.5 %. The rapid diffusion of yttria generates low and high-yttria regions, so that no zirconia phases with intermediate stabilizer contents are observed. The phase stability can be affected by spraying parameters, as well as by microstructural features, which can locally change due to yttria fluctuations from grain to grain.

It is worth noting that high-temperature phase evolution of plasma sprayed YSZ coatings is substantially different from that found for ceria-yttria co-stabilized zirconia (CYSZ) coatings and, therefore, strongly depends on the nature and the amount of the oxides used as zirconia stabilizers. On the basis of quantitative XRD analysis, CYSZ coatings possess higher high-

temperature phase stability than YSZ coatings treated at the same experimental conditions. Indeed, they showed no monoclinic phase after thermal aging.

3.3.2 Microstructure

Figure 3.52 shows YSZ powder particles: they are spherical and their size distribution is approximately in the range between 11 and 125 µm. The size and the morphology of YSZ particles are similar to those of CYSZ ones: both powder particles show HOSP morphology. As shown in Fig. 3.53, some particles within the agglomerates are nanosized, as also observed in the case of CYSZ particles.

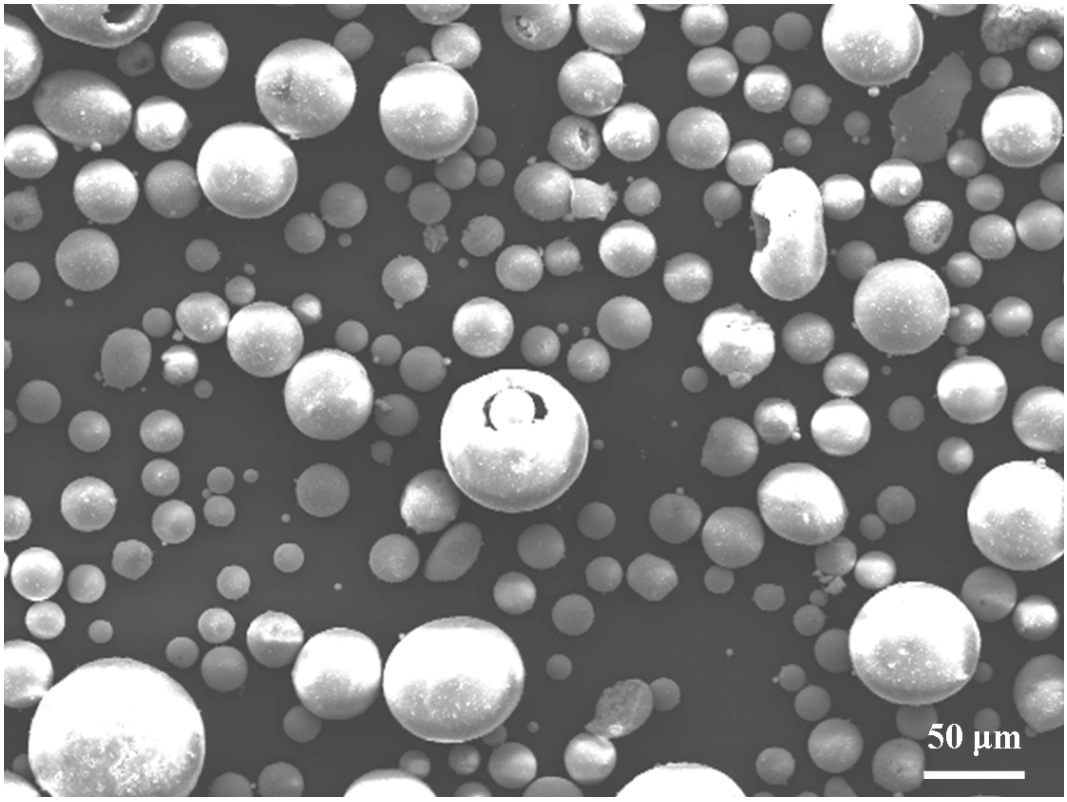

Figure 3.52 – SEM image showing YSZ particles with HOSP morphology (SE).

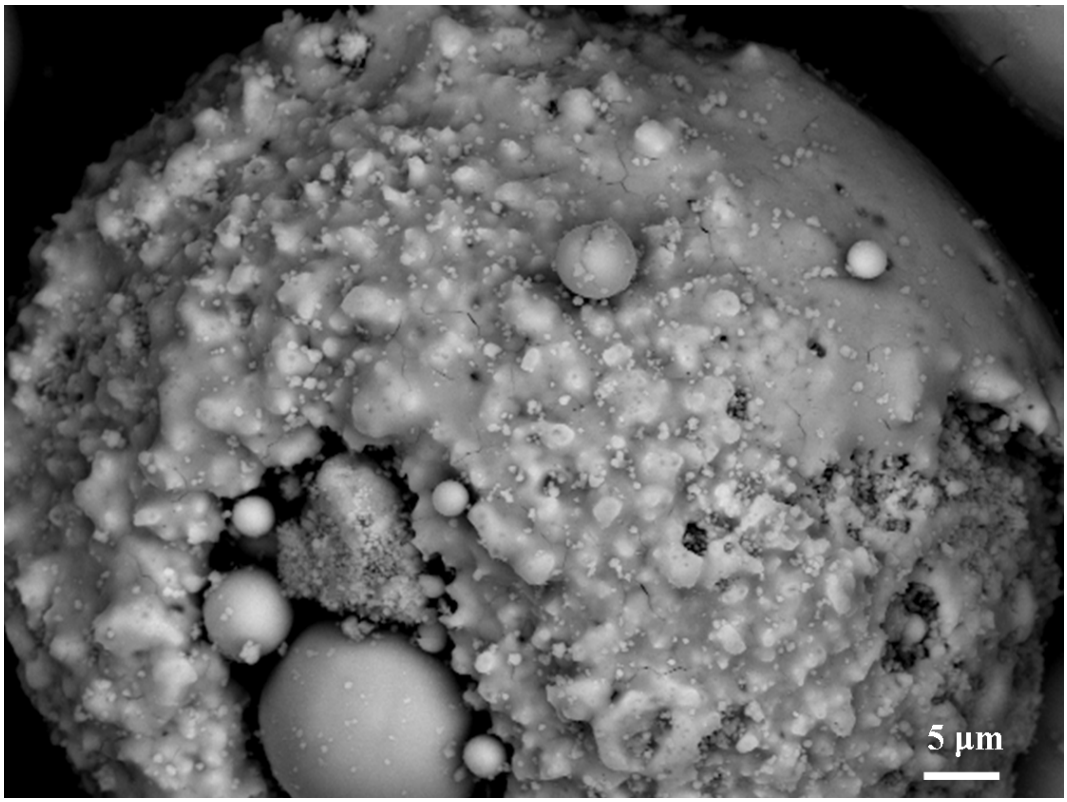

Figure 3.53 – Nanosized particles inside YSZ agglomerates (SE).

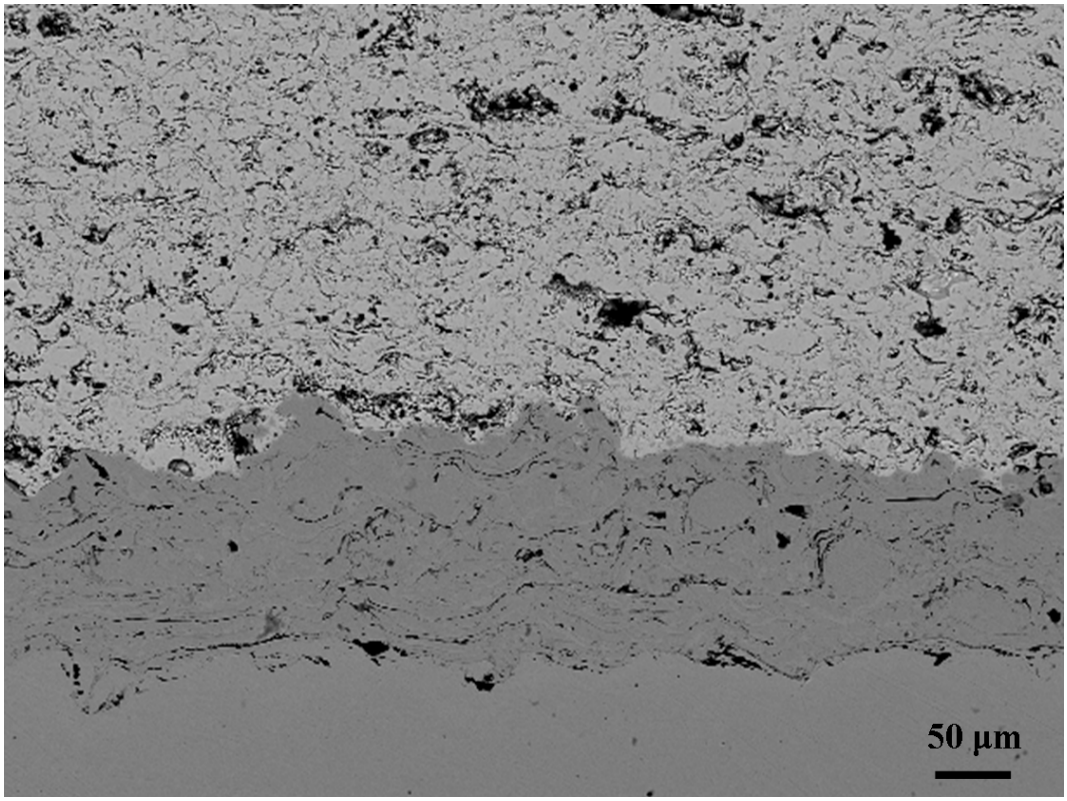

Figure 3.54 – SEM image of TBC cross section (BSE). The TBC is composed of three different layers (substrate, bond coat and top coat).

Figure 3.54 shows the cross sectional microstructure of the entire TBC, composed of Ni-based superalloy substrate, CoNiCrAlY bond coat and YSZ top coat (from the bottom). A good qualitative interface adhesion is observable between substrate and bond coat and between bond coat and top coat. Figure 3.55 shows the cross section of as-sprayed YSZ coating, characterized by porous microstructure with lamellae parallel to the substrate and embedded in a network of globular pores, inter-lamellar and intra-lamellar microcracks. The pore morphology is similar to that observed in CYSZ coatings. The average porosity is 12.2 % with a standard deviation equal to 1.5 %. So, the porosity of YSZ coatings is slightly higher than that measured on CYSZ coatings and lower than that obtained in [28].

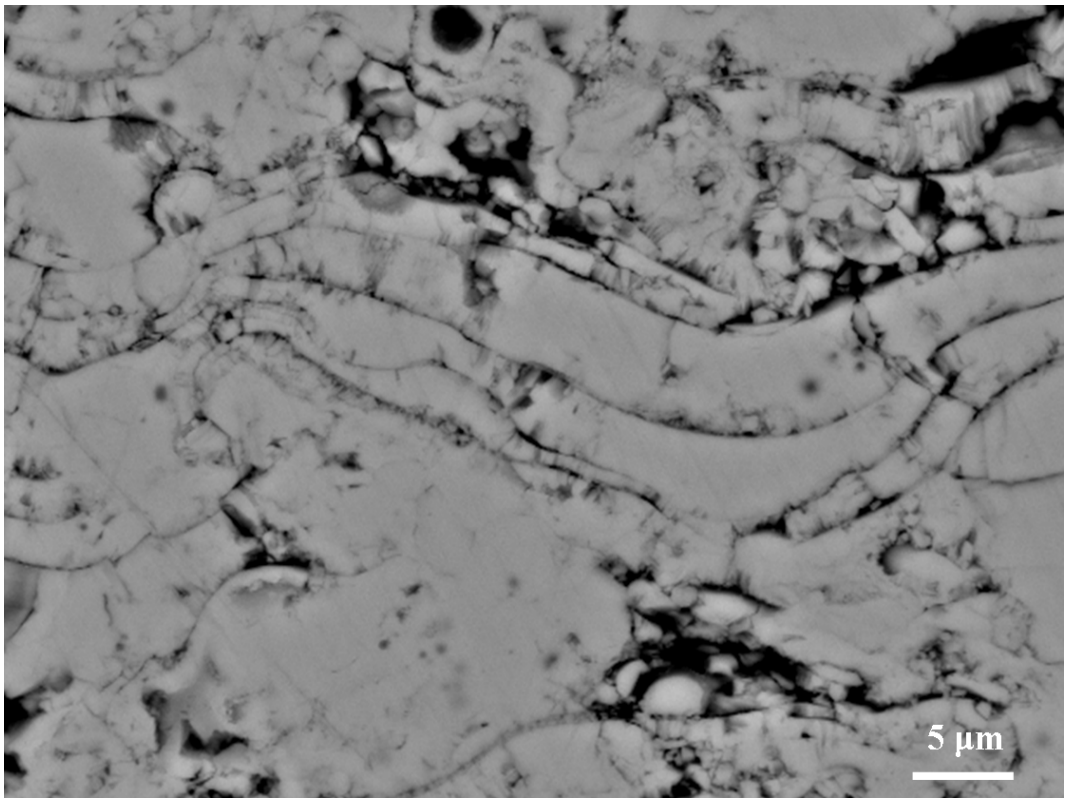

Figure 3.55 – SEM image of as-sprayed YSZ coating showing a lamellar microstructure rich of pores and microcracks (BSE).

After annealing, a partial sintering of the porous microstructure is observed. A comparison between the microstructures of annealed CYSZ coatings is reported in Fig. 3.56. It is apparent

that the size and the distribution of both microcracks and globular pores are affected by thermal aging and a progressive closure of finer pores and microcracks can be observed with the progression of the thermal aging. In particular, Fig. 3.56(d) shows the microstructure of YSZ coating annealed at 1315 °C for 50 h at higher magnification. The coating is not fully sintered after heat treatment, indeed pores and inter-splat microcracks (approximately perpendicular to spraying direction) are partially retained. The intra-lamellar microcracks (approximately parallel to spraying direction) are still observable within the coating after the first hours of heat treatment but tend to disappear with increasing the aging time. Moreover, Fig. 3.526c) shows that the densification which follows the heat treatment affects only to a lesser extent the size and the distribution of the large globular pores.

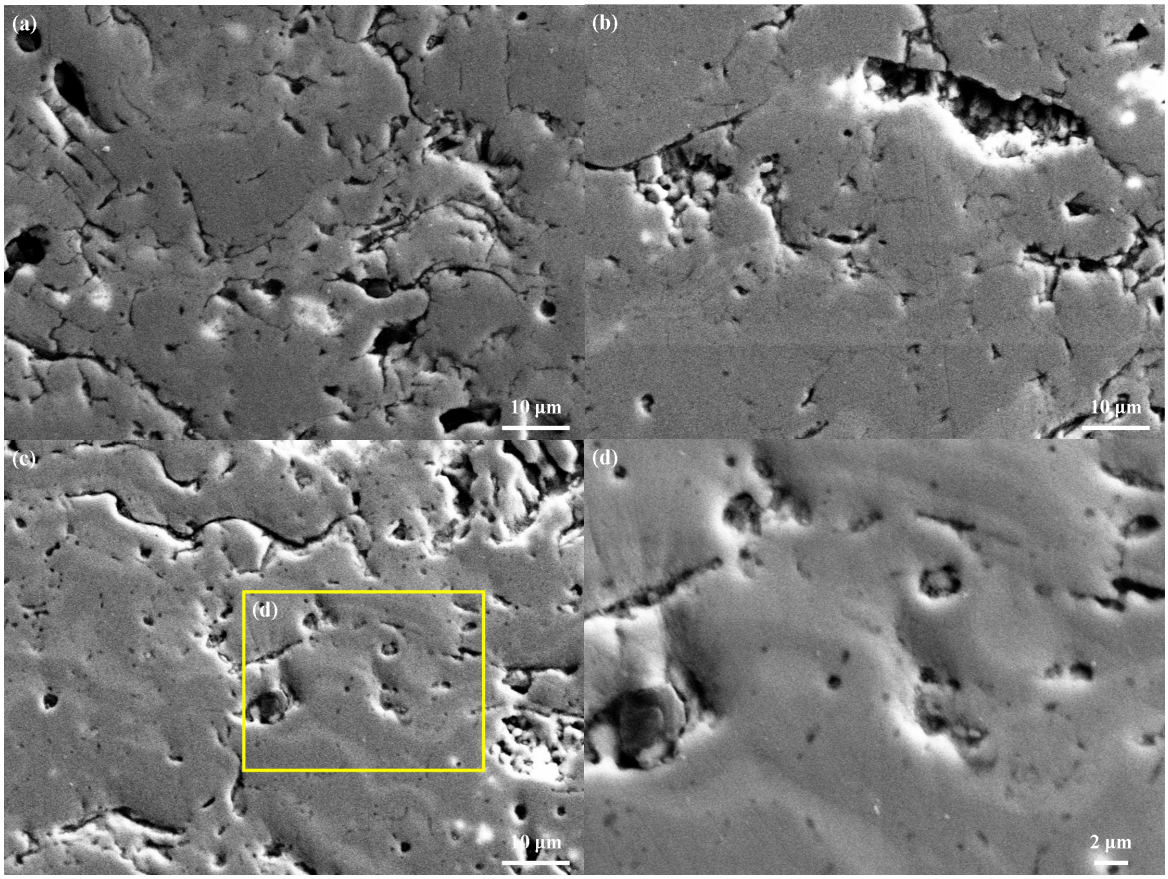

Figure 3.56 –Microstructure of annealed YSZ coatings after (a) 2 h, (b) 10 h, (c-d) 50 h. (Spraying direction from the top to the bottom).

It is worth noting that the nature of pores and interfaces plays an important role in the sintering behaviour of plasma sprayed coatings. Since the first hours of the heat treatment, the formation of sintering necks between the lamellae reduces the inter-lamellar porosity. In particular, after the heat treatment it is difficult to distinguish the original lamellar microstructure of the as-sprayed coatings.

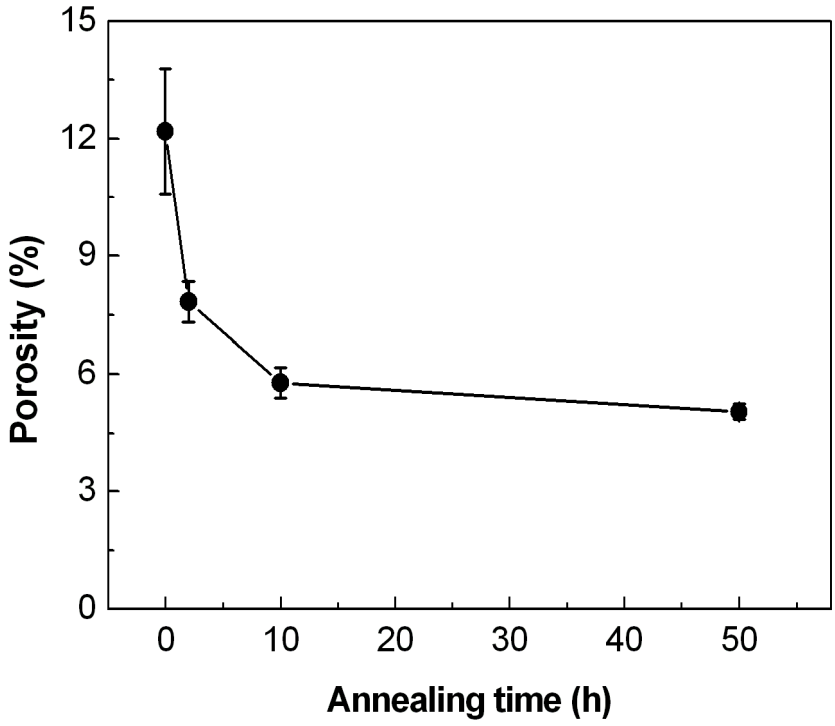

Figure 3.57 – Evolution of porosity level as a function of the annealing time.

The mechanism is similar to that observed for CYSZ coatings, even if the as-sprayed YSZ coatings are slightly more porous than CYSZ ones (~ 12 % against 10 %). Figure 3.57 shows the evolution of coating porosity during thermal aging: the porosity rapidly decreases during the first hours of heat treatment and then tends to stabilize as the coating is partially sintered. After 50 h of isothermal exposure, the coating porosity decreases up to ~ 5 %.

3.3.3 Microhardness of as-sprayed coatings

Microhardness measurements have been performed on as-sprayed YSZ coatings. Accurate Vickers microhardness measurements rely on visual resolution of the residual indentation; however, the diagonal of the indentation, *d*, can be difficult to resolve, indeed the load should be low enough to avoid cracking, which otherwise occurs within the indentation site [16]. Then an accurate choice of the applied load must be done. Preliminary tests carried out by the authors indicated that a load of 300 gf avoids cracking and retains the resolution of the residual indentation.

As the heterogeneous microstructure of an APS coating can lead to scattered data, a minimum of 20 indentations was performed on each coating cross section. The results have been in turn presented by means of Weibull statistics, as a Gaussian distribution is not adequate to describe the variation of mechanical data for plasma sprayed porous ceramic coatings.

In particular, the experimental data have been sorted in ascending order and the cumulative density function of probability, defined as $P = (i\text{-}0.5)/N$, was assigned to each hardness data. The Weibull plots corresponding to the microhardness data are reported in Fig. 3.58 (cumulative density function of probability versus hardness).

The mean value of the hardness is represented by the intersection of x-axis ($y = 0$) and the Weibull plot. On the other hand, information related to the experimental scatter are provided by the Weibull modulus, *m*, *i.e.* the slope of the line in the plot; in particular, a higher modulus represents low experimental scatter. The average microhardness of as-sprayed YSZ coating is 601.45 HV (standard deviation = 80.62 HV). The Weibull modulus of microhardness data is 9.46. It is worth noting that as-sprayed YSZ coatings are less harder than CYSZ coatings, since the average microhardness of these last ones, measured at the same indentation load, is 654 HV.

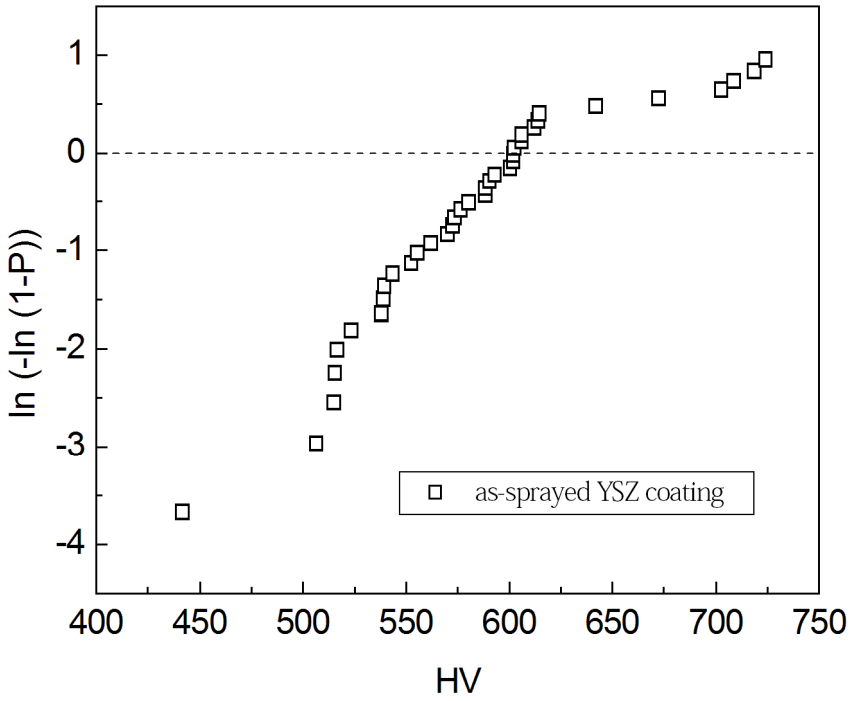

Figure 3.58 – Weibull distribution of microhardness data for as-sprayed YSZ coatings.

3.3.4 Thermal expansion

Thermal expansion curves of as-sprayed and annealed YSZ coatings are plotted in Figs. 3.59 and 3.60. Figure 3.59 shows in-plane thermal expansion of as-sprayed and annealed YSZ samples between 50 °C and 900 °C. It can clearly be seen that thermal expansion increases linearly over the entire temperature range and the shrinkage for as-sprayed and annealed YSZ coatings is approximately 0.93-0.94 %.

The out-of-plane thermal expansion curves of as-sprayed and annealed YSZ coatings are shown in Fig. 3.60. The values of the shrinkage are influenced by the annealing time and are in the range between 0.82 % and 0.94 %. YSZ coatings annealed for 10 h show the highest thermal expansion, while the corresponding values for as-sprayed and 50 h annealed coatings are ~ 13 % smaller.

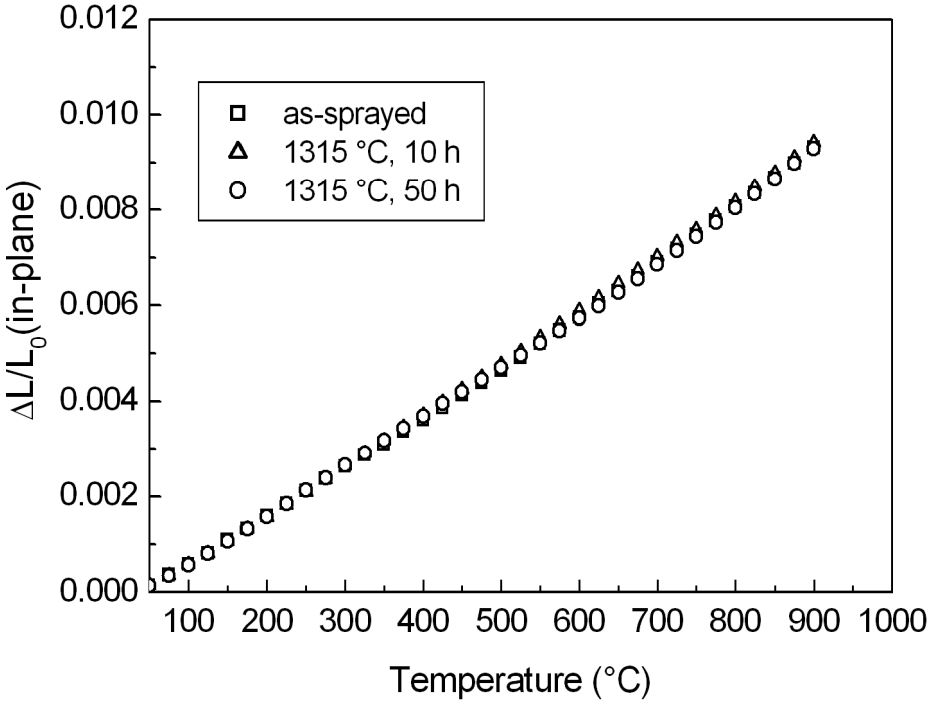

Figure 3.59 - In-plane thermal expansion curves for as-sprayed and annealed YSZ coatings.

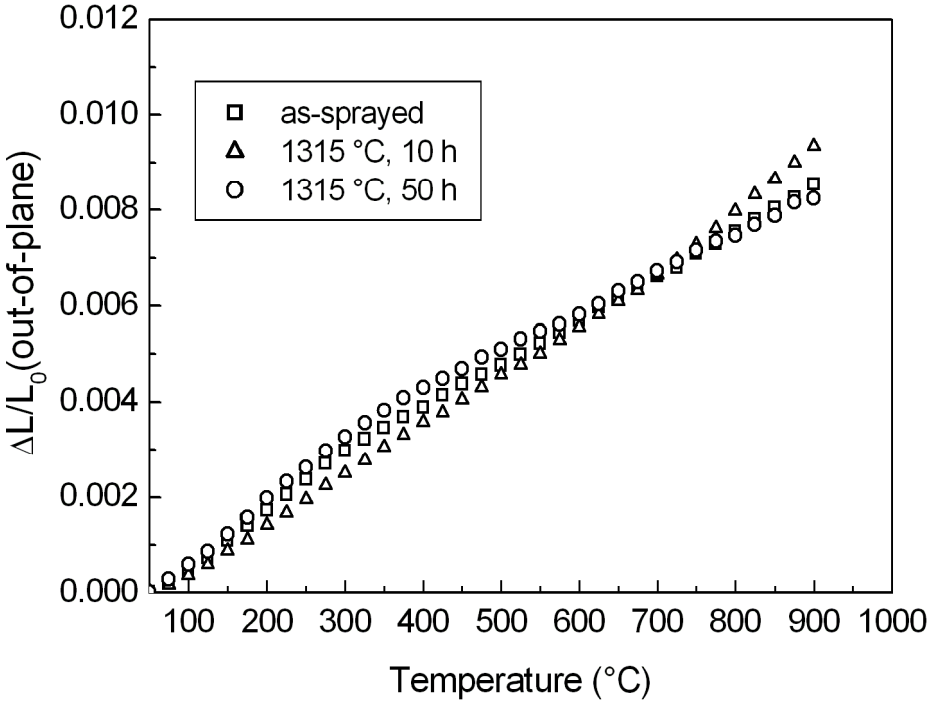

Figure 3.60 – Out-of-plane thermal expansion curves for as-sprayed and annealed YSZ coatings.

Therefore, we can deduce that high-temperature sintering of the porous microstructure is more sensitive to the formation of sintering necks at splat boundaries rather than to the closure of intra-lamellar microcracks which are of lower size, as also observed for plasma sprayed CYSZ coatings.

The mean values of thermal expansion coefficients for as-sprayed and heat-treated YSZ coatings are given in Table 3.16. The in-plane CTE is approximately 10.7 x 10^{-6} K^{-1} for as-sprayed and annealed YSZ coatings between 50 °C and 900 °C. This value is higher than those reported in any previous works [41,46] and more close to the results found by Schwingel *et al*. for plasma sprayed YSZ coatings [47].

Coating	α_x (50-900 °C) [10^{-6} K^{-1}]	α_Z (50-300 °C) [10^{-6} K^{-1}]	α_Z (300-900 °C) [10^{-6} K^{-1}]
As-sprayed	10.73	12.33	9.17
Annealed, 1315 °C, 10 h	10.94	10.25	11.13
Annealed, 1315 °C, 50 h	10.67	13.42	8.16

Table 3.16 - In-plane (α_x) and out-of-plane (α_Z) thermal expansion coefficients for as-sprayed and annealed YSZ coatings.

On the contrary, the out-of-plane CTE is more sensitive to the thermal aging. A single linear fit of the experimental points between 50 °C and 900 °C provides CTE values in the range between 9.49 x 10^{-6} K^{-1} and 10.82 x 10^{-6} K^{-1} (the lowest value is found for the coating aged for 50 h). However, if we carefully observe the thermal expansion curves, we can see that at temperatures higher than 300 °C a change in their slope can be noticed and a corresponding decrease of the thermal expansion coefficient, except for YSZ coatings treated for 10 h. Taking into consideration this behaviour, CTE values vary from 12.3 x 10^{-6} K^{-1} to 13.4 x 10^{-6}

K^{-1} between 50 °C and 300 °C and from 9.2 x 10^{-6} K^{-1} to 8.2 x 10^{-6} K^{-1} between 300 °C and 900 °C.

To this purpose, it should be noted that the CTE is strongly related to the crystal structure of the coating and to some phase transitions which could occur during heating. Indeed, at about 300 °C part of the tetragonal phase may transform to monoclinic, while at temperature higher than 600 °C the monoclinic phase may transform to the tetragonal one. These transformations have been already noticed for annealed or thermally shocked YSZ coatings [45,48].

Moreover, the microstructural properties can locally vary within each coating, as well as the concentration of yttria from grain to grain or within a grain. In addition, the shrinkage and the sintering characteristics can be strongly influenced by the presence of relatively small impurities within the coating. These impurities can enhance the diffusion rates for grain boundaries, lattice and surface diffusion [49,50].

In particular, the possible formation of a glassy phase at grain boundaries plays a significant role on the grain growth and, therefore, on the sintering rate [24]. All these aspects may be responsible for the fluctuations in CTE values. Otherwise, we can surely argue that no sintering occurs during measurements up to 900 °C.

In-plane CTE of YSZ coatings is lower than that of CYSZ ones (~ 12.6 x 10^{-6} K^{-1} for as-produced CYSZ coating), due to the different amount of oxygen vacancies. The CTE generally increases with increasing the oxygen vacancies, even if Hayashi *et al.* [51] have reported that it decreases with increasing the yttria content for sintered YSZ samples.

To the purpose, it is worth noting that, when a ceramic TBC is applied on a metal substrate, the thermal expansion mismatch can promote tensile stresses and then the formation and the propagation of cracks within the same TBC, reducing the sintering effect.

3.3.5 Heat capacity

In Fig. 3.61 the specific heat curves of as-sprayed and thermally aged YSZ coatings are plotted as a function of temperature. $C_p(T)$ curves were calculated as a mean value of three consecutive measurement cycles. For as-produced coatings two different curves are reported. The former corresponds to the first heating cycle, while the latter is the average of three successive measurement cycles. Indeed, it is worth noting that the first heating provides some irreversible changes, such as first-stage sintering and stress relaxation, and a corresponding increase of heat capacity at high temperature, whereas no deviations were observed in the next runs. Changes at crystal lattice scale may also have a significant effect on C_P values, since during heating a decrease of structural defects can occur. The specific heat increases gradually as the temperature increases.

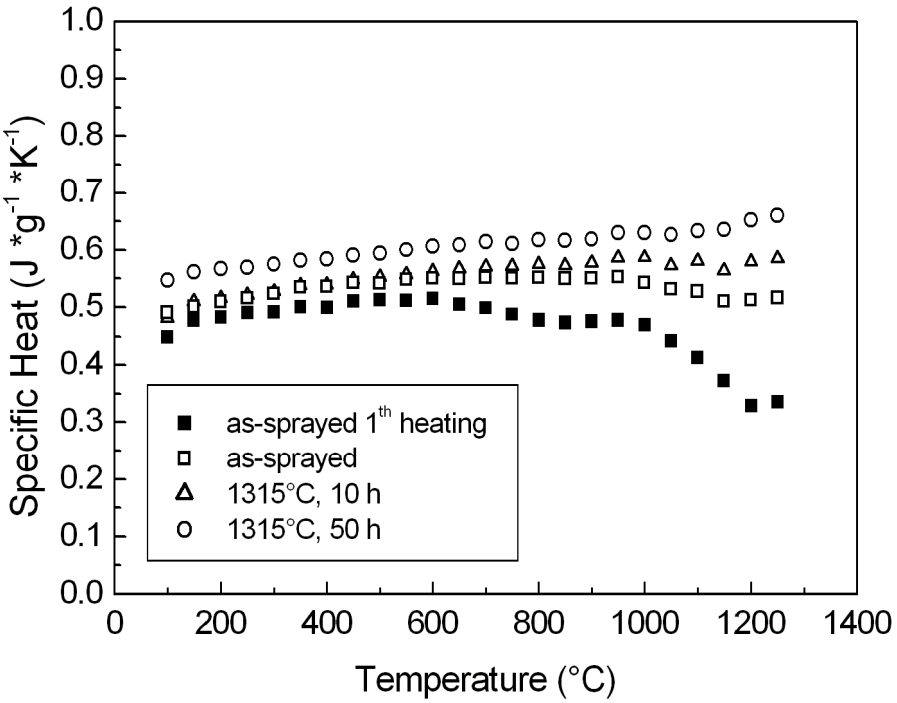

Figure 3.61 - Specific heat capacity of as-sprayed and annealed YSZ coatings as a function of temperature.

For as-sprayed YSZ coating C_P value is found to be 0.49 $J*K^{-1}*g^{-1}$ at 100 °C and 0.52 $J*K^{-1}*g^{-1}$ at 1250 °C. These values are lower than those reported by other authors for YSZ sintered samples and plasma sprayed coatings [42,52]. For coatings exposed for 50 h C_p value is found to be 0.55 $J*K^{-1}*g^{-1}$ at 100 °C and 0.66 $J*K^{-1}*g^{-1}$ at 1250 °C.

Therefore, the specific heat capacity increases with increasing the aging time, due to high-temperature sintering of the porous microstructure, grain growth and decomposition of the metastable t' phase. The healing of vertical microcracks as well as an enhanced bonding at splat boundaries promoted by grain growth and microcracks closure produce a partial densification of the porous microstructure, reducing the porosity volume and correspondingly increasing the elastic modulus [33.50].

Therefore, the TBC becomes less strain tolerant and more heat conductive. As a consequence, the thermal insulation could be notably reduced after long-term high-temperature exposure, even if the main changes typically occur after relatively short times and then the sintering activity tends to stabilize.

In conclusion, thermal annealing of YSZ coatings produces an increase of specific heat capacity, while a slight decrease has been observed for CYSZ coatings treated at the same conditions. The different evolution of thermophysical properties of these zirconia-based TBC systems can be explained in terms of different phase compositions and sintering behaviour. However, the C_P values measured at the highest temperature (1250 °C) are comparable and we can deduce that they have the same influence on the thermal conductivity.

3.4 Plasma sprayed nanostructured YSZ coatings

3.4.1 Phase composition of as-sprayed coatings

X-Ray diffraction patterns of both powder and as-sprayed coating are shown in Fig. 3.62. The feedstock is mainly composed of tetragonal t zirconia, with a smaller amount of cubic c and monoclinic m zirconia phases, which are then transferred to tetragonal t' phase during thermal spraying.

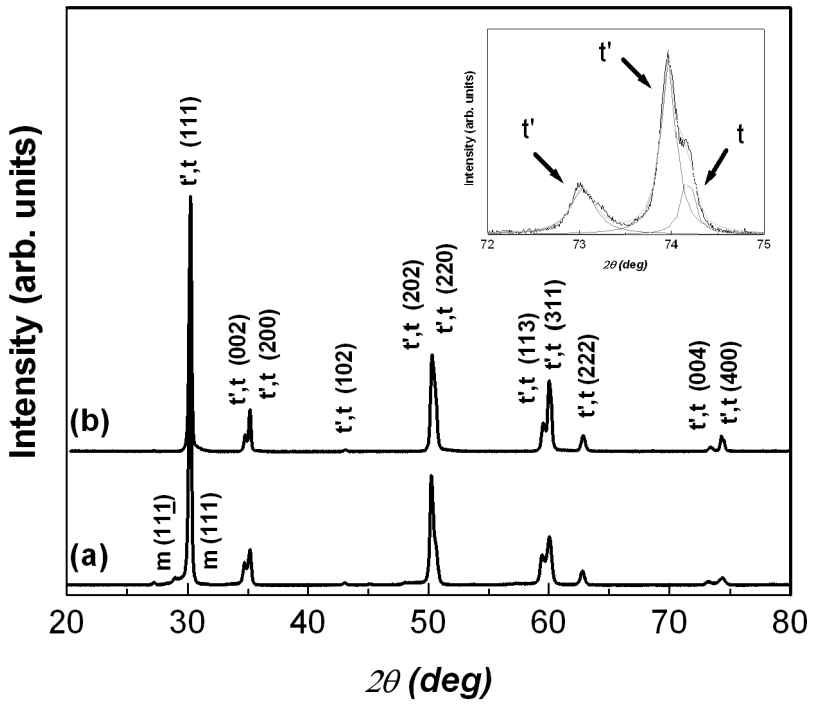

Figure 3.62 – XRD patterns of nanostructured YSZ powder and as-sprayed coatings.

Thereby, the coating is composed of a mixture of non-trasformable tetragonal t' and tetragonal t zirconia phases, as illustrated in the 72-75° range of the diffraction pattern, where an example for the profile fit of the (400) reflections is shown. The metastable tetragonal t' phase arises from the quenching of molten droplets at room temperature, while the tetragonal t phase is associated to retained unmelted particles embedded in coating microstructure. The high

cooling rate (10^6-10^7 K/s) prevents the typical and detrimental transformation to monoclinic m zirconia which is usually accompanied by volume change and crack formation [53]. It is worth noting that the structure of as-sprayed conventional YSZ coatings were mainly composed of t' phase with relatively low amounts of cubic c, tetragonal t and monoclinic phases.

3.4.2 Microstructure

Figure 3.63 shows the morphology of spray-dried agglomerated particles. Their size is between 15 and 150 μm, as reported by the manufacturer. The inset illustrates the morphology of YSZ nanoparticles, whose grain size is in the range between 30 and 200 nm. The agglomeration of the nanoparticles becomes necessary because they do not possess a high flowability and, due to their too low mass, they are unable to be carried in a moving gas stream and deposited on a substrate [54].

The intrinsic porosity formed by the agglomeration of nanoparticles may play an important role on the microstructural properties of the coating. Indeed, during plasma spraying, the hot gas can penetrate inside agglomerated particles and melt their surface. Due to the heating of the gas herein entrapped, the same particles are pressurized and eventually destroyed, blowing up into several smaller ones, prior to impact toward the substrate [55]. Their internal cores remain unmelted, reducing the grain growth and preserving the starting nanostructure. The short residence time of the sprayed particles in the plasma jet, the low heat transfer associated to their intrinsic porosity and their high cooling rate play an important role on this mechanism [56]. As clearly displayed in Fig. 3.64, the coating shows two different kinds of microstructure. The details inserted at the opposite corners of the picture illustrate a poorly consolidated structure and a well-melted splat, respectively.

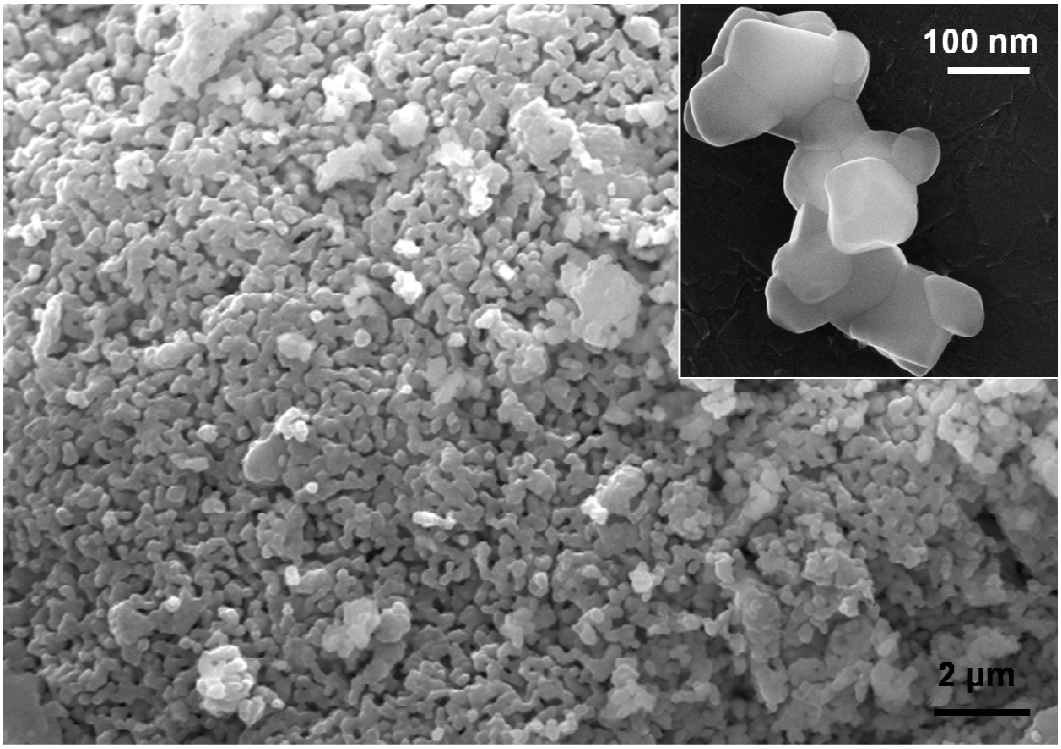

Figure 3.63 – Surface of agglomerated nanoparticles. The inset shows the morphology of YSZ nanoparticles (SE).

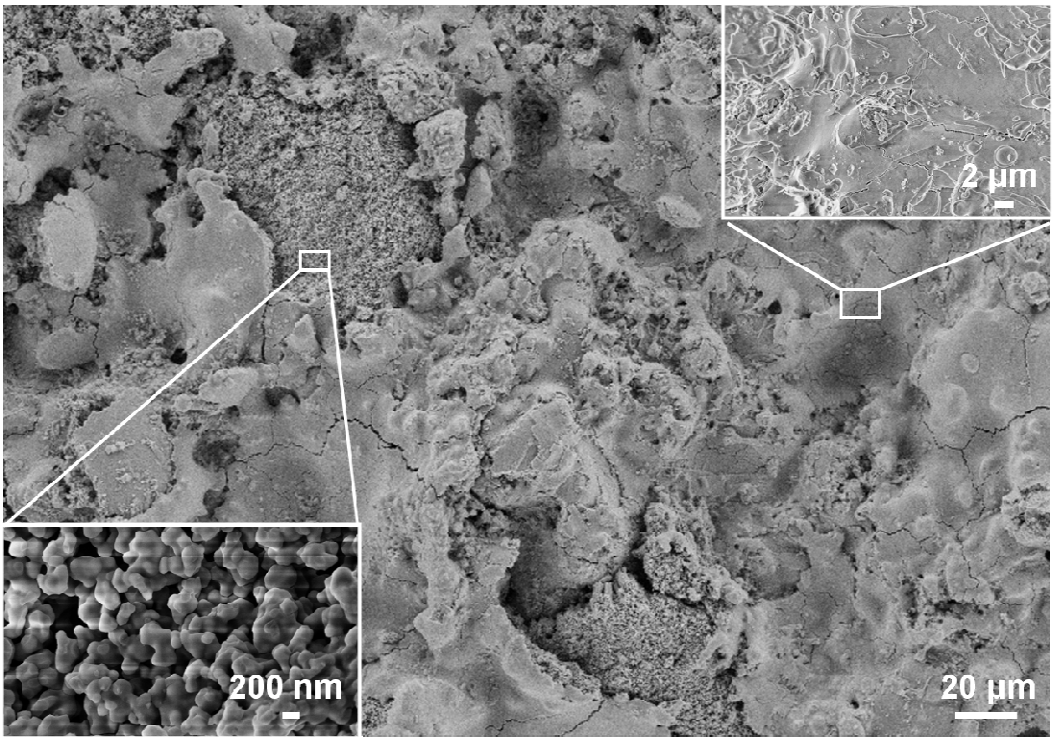

Figure 3.64 – Surface morphology of as-sprayed nanostructured YSZ coatings showing unmelted and totally melted particles (SE).

The former is composed by fine loose particles which resemble the feedstock morphology. In these regions the starting nanostructure can be largely retained, *i.e.* the grain growth is avoided or is not significant. The latter shows a smooth surface and is formed by means of the impact of well-melted particles on the substrate. These particles are heated at lower rate and are more sensible to grain growth. To this purpose, it should be noted that, during plasma spraying, the powder particles are commonly characterized by different thermal history, due to the temperature distribution in the plasma jet. Indeed, the temperature rapidly decreases from the centre to the periphery of the plasma jet, so that the particles injected in the centre typically experience the highest temperature and are generally totally melted, while the particles injected at the periphery of the plasma plume are just partially melted [57].

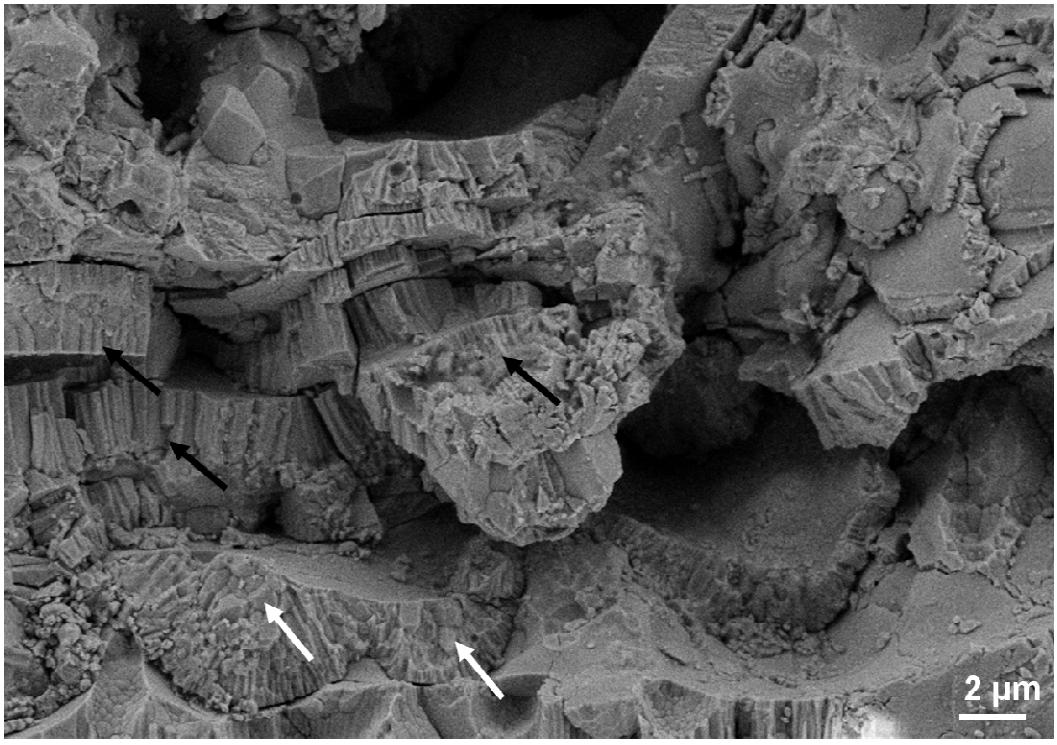

Figure 3.65 – Cross sectional SEM image showing a typical lamellar microstructure containing columnar and equiaxed grains (SE).

Fig. 3.65 shows the cross sectional microstructure of as-sprayed nanostructured coating, composed of thin lamellae with thickness ranging from 0.5 to 4 μm. The gradual solidification

of the deposited splats may provide a thin inter-lamellar porosity, reducing the cohesive strenght between the lamellae. Columnar grains can be observed within the lamellae (black arrows). They are oriented along the direction of grain growth, as also observed for plasma sprayed CYSZ coatings. Their diameter is in the range between 0.04 to 0.5 μm), while their morphology can be related to their heterogeneous nucleation at splat boundary and their growth into the molten splat, promoted by the heat flow rate released by the crystallization of previously deposited material [58,59]. However, if the heat loss promoted by cooling at the substrate interface is higher than the heat released by the crystallization a homogeneous nucleation occurs, leading to the formation of equiaxed grains, denoted in Fig. 3.65 by white arrows.

Fig. 3.66 shows the polished cross section of as-sprayed nanostructured YSZ coating, where unmelted or partially melted areas are cemented by well-melted areas. It should be noted that it is very difficult to resolve the retained nanosized zones and their intrinsic fine porosity by Image Analysis. The measured percentage of retained nanosized areas is equal to 22 % (standard deviation = 1.15). Higher percentage of unmelted particles embedded in coating microstructure probably could involve lower particle adhesion and cohesion and it would be more suitable for the fabrication of a more friable coating (abradable coating).

The coating shows pores of heterogeneous size and several microcracks, which arise from the residual stresses induced by high cooling rate. The total porosity is of about 22 % (standard deviation = 2.5 %), much higher than that found for CYSZ and YSZ coatings (~10 % and 12 %, respectively), due to the contribution of the intrinsic porosity of nanoparticles agglomerates, which are partially melted and are retained in coating microstructure. High porosity can be useful for TBC applications, because it is able to reduce the thermal conductivity and the elastic modulus. However, it can also involve lower hardness and lower resistance to the penetration of oxygen and corrosive agents. Anyway, it should be noted that

the porosity of nanostructured coatings could be overestimated, due to the pull-out of unmelted particles during grinding and polishing steps. This effect could be emphasized by the high content of unmelted particles in coating microstructure.

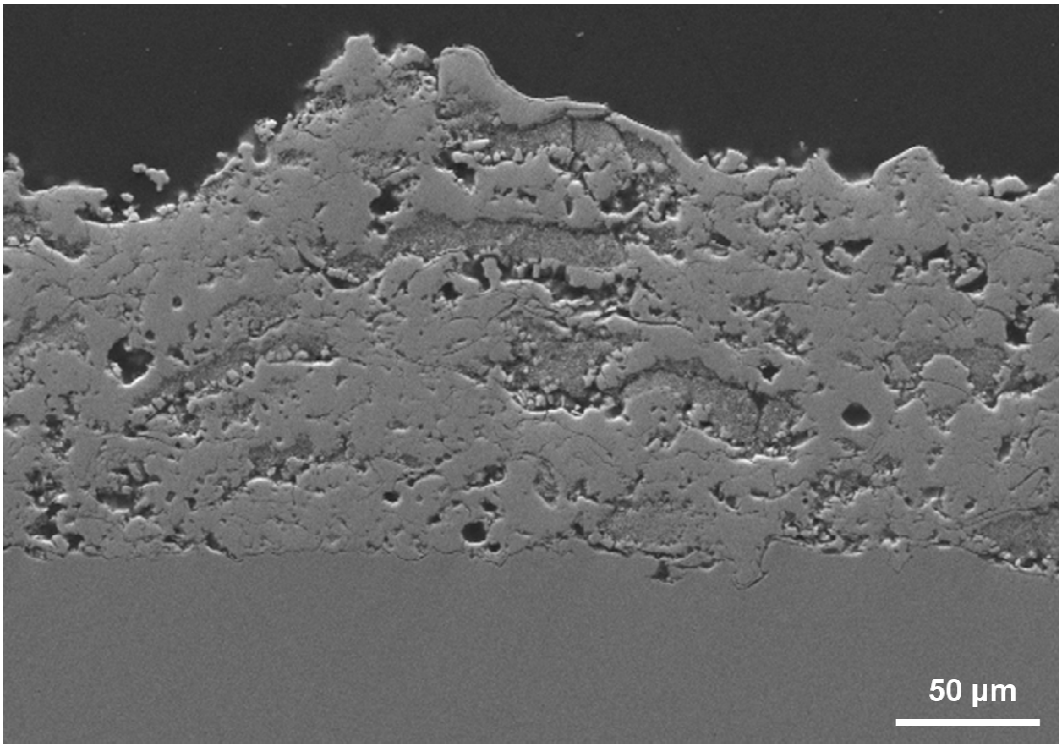

Figure 3.66 – Coating cross section showing well-melted and partially melted regions (SE).

3.4.3 Microhardness of as-sprayed coatings

Accurate Vickers microhardness measurements rely on visual resolution of the residual indentation; however, the diagonal of the indentation, *d*, can be difficult to resolve, indeed the load should be low enough to avoid cracking, which otherwise occurs within the indentation site [16]. Then an accurate choice of the applied load must be done. Preliminary tests carried out by the authors indicated that a load of 100 gf avoids cracking and retains the resolution of the residual indentation.

The average microhardness of as-sprayed nanostructured YSZ coating is 536 HV (standard deviation = 107 HV). It is worth noting that as-sprayed nanostructured YSZ coatings are less harder than conventional ones, due to the presence of unmelted nanoparticles, as well as to higher coatings porosity. These factors also determine a large scatter in data distribution.

The results have been in turn presented by means of Weibull statistics. In particular, the experimental data have been sorted in ascending order and the cumulative density function of probability, defined as P = (*i*-0.5)/N, was assigned to each hardness data. The Weibull plots corresponding to the microhardness data are reported in Fig. 3.67 (cumulative density function of probability versus hardness).

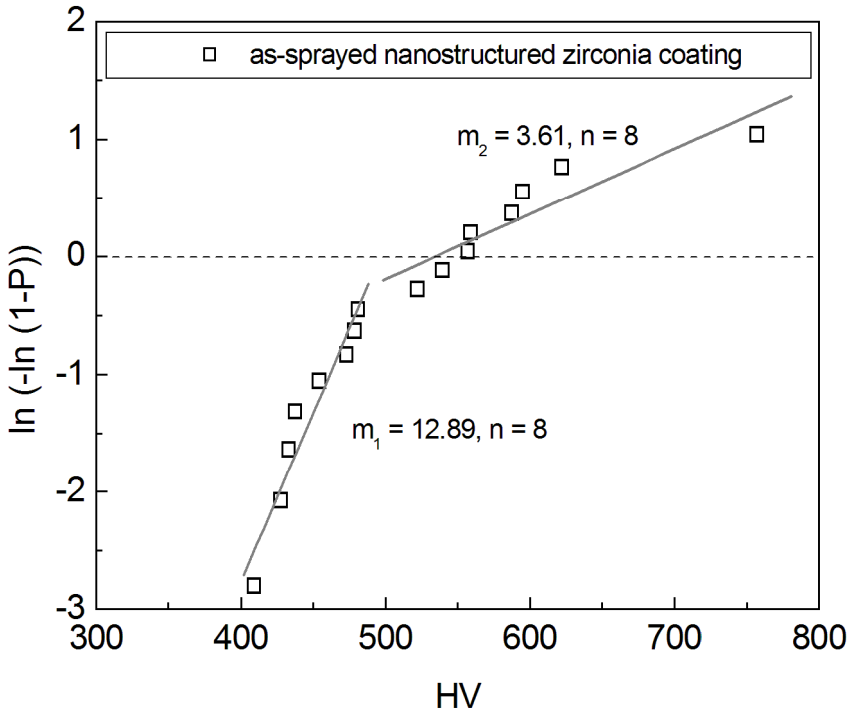

Figure 3.67 – Weibull distribution of microhardness data for as-sprayed nanostructured YSZ coatings.

On the other hand, information related to the experimental scatter are provided by the Weibull modulus, *m*, *i.e.* the slope of the line in the plot; in particular, a higher modulus represents low experimental scatter. It is worth noting that a bimodal distribution of microhardness data can

be appreciated, *i.e.* two different values of Weibull modulus, due to the presence of a bimodal microstructure, composed of well-melted and unmelted particles, respectively. Well-melted regions possess higher hardness, while lower hardness can be associated to partially melted regions. The results about plasma sprayed nanostructured coatings have to be considered as preliminary, due to their unique microstructural and mechanical properties, but make them very interesting for multi-functional applications, such as TBCs, abradable and anti-wear coatings.

References

[1] W. Brandl, G. Marginean, D. Maghet and D. Utu, Effects of specimen treatment and surface preparation on the isothermal oxidation behaviour of the HVOF-sprayed MCrAlY coatings, Surf. Coat. Technol. 188-189 (2004) 20-26.

[2] P. Richer, M. Yandouzi, L. Beauvais and B. Jodoin, Oxidation behaviour of CoNiCrAlY bond coats produced by plasma, HVOF and cold gas dynamic spraying, Surf. Coat. Technol. doi: 10.1016/j.surfcoat.2010.03.043 (2010).

[3] P. Poza and P. S. Grant, Microstructure evolution of vacuum plasma sprayed CoNiCrAlY coatings after heat treatment and isothermal oxidation, Surf. Coat. Technol. 201 (2006) 2887-2896.

[4] F. Tang, L. Ajdelsztajn, G. E. Kim, V. Provenzano and J. M. Schoenung, Effects of surface oxidation during HVOF processing on the primary stage oxidation of a CoNiCrAlY coating, Surf. Coat. Technol. 185 (2004) 228-233.

[5] H. Choi, B. Yoon, H. Kim and C. Lee, Isothermal oxidation of air plasma spray NiCrAlY coatings, Surf. Coat. Technol. 150 (2002) 297-308.

[6] S. Saeidi, K. T. Voisey and D. G. McCartney, The effect of heat treatment on the oxidation behavior of HVOF and VPS CoNiCrAlY coatings, J. Therm. Spray Technol. 18(2) (2009) 209-216.

[7] C. H. Lee, H. K. Kim, H. S. Choi and H. S. Ahn, Phase transformation and bond coat oxidation behavior of plasma-sprayed zirconia thermal barrier coatings, Surf. Coat. Technol. 124 (2000) 1-12.

[8] V. Higuera, F. J. Belzunce and J. Riba, Influence of the thermal-spray procedure on the properties of a CoNiCrAlY coating, Surf. Coat. Technol. 200 (2006) 5550-5556.

[9] H. Waki, K. Ogura, I. Nishikawa and A. Ohmori, Monotonic and cyclic deformation behavior of plasma-sprayed coatings under uni-axial compressive tests, Mater. Sci. Eng. A 374(1-2) (2004) 129-136.

[10] L. Zhao, M. Parco and E. Lugscheider, High velocity oxy-fuel thermal spraying of a NiCoCrAlY alloy, Surf. Coat. Technol. 179 (2004) 272-278.

[11] F. J. Belzunce, V. Higuera and S. Poveda, High temperature oxidation of HFPD thermal-sprayed MCrAlY coatings, Mater. Sci. Eng. A 297 (2001) 162-167.

[12] International organization for standardization, guide to the expression of uncertainty in measurement, Switzerland, 1995, ISBN 92-67-10188-9.

[13] S. Patsias, N. Tassini and K. Lambrinou, Ceramic coatings: effect of deposition method on damping and modulus of elasticity for yttria-stabilized zirconia, Mater. Sci. Eng. A 442 (2006) 504-508.

[14] N. Tassini, K. Lambrinou, I. Mircea, M. Bartsch, S. Patsias and O. Van der Biest, Study of the amplitude-dependent mechanical behavour of yttria-stabilized zirconia thermal barrier coatings, J. Eur. Ceram. Soc. 27 (2007) 1487-1491.

[15] T. Lauwagie, K. Lambrinou, S. Patsias, W. Heylen and J. Vleugels, Resonant-based identification of the elastic properties of layered materials: application to air plasma sprayed thermal barrier coatings, NDT & E Int. 41 (2008) 88-97.

[16] S. Chowdhury, E. de Barra and M. T. Laugier, Hardness Measurement of CVD diamond coatings on SiC substrates, Surf. Coat. Technol. 193 (2005) 200-205.

[17] J. Y. Kwon, J. H. Lee, Y. G. Jung and U. Paik, Effect of bond coat nature and thickness on mechanical characteristic and contact damage of zirconia-based thermal barrier coatings, Surf. Coat. Technol. 201 (2006) 3483-3490.

[18] N. Zotov, M. Bartsch and G. Eggeler, Thermal barrier coating systems – analysis of nanoindentation curves, Surf. Coat. Technol. 203 (2009) 2064-2072.

[19] Z. Hashin and S. Shtrikman, A variational approach to the theory of the elastic behavoiur of multiphase materials, J. Mech. Phys. Sol. 11(2) (1962) 452-453.

[20] D. P. H. Hasselmann, On the porosity dependence of the elastic moduli of polycrystalline refractory materials, J. Am. Ceram. Soc. 45 (1962) 452-453.

[21] R. M. Spriggs, Expression for effect of porosity on elastic modulus of polycrystalline refractory materials, particularly aluminum oxide, J. Am. Ceram. Soc. 44(12) (1961) 628-629.

[22] X. Q. Cao, R. Vassen and D. Stoever, Ceramic materials for thermal barrier coatings, J. Eur. Ceram. Soc. 24 (2004) 1-10.

[23] H. Choi, H. Kim and C. Lee, Phase evolutions of plasma sprayed ceria and yttria stabilized zirconia thermal barrier coating, J. Mater. Sci. Letters 21 (2002) 1359-1361.

[24] G. M. Ingo and T. De Caro, Chemical aspects of plasma spraying of zirconia-based thermal barrier coatings, Acta Mater. 56 (2008) 5177-5187.

[25] D. Chen, M. Gell, E. H. Jordan, E. Cao and X. Ma, Thermal stability of air plasma spray and solution precursor plasma spray thermal barrier coatings, J. Am. Ceram. Soc. 90(10) (2007) 3160-3166.

[26] P. A. Langjahr, R. Oberacker and M. J. Hoffmann, Long-term behaviour and application limits of plasma-sprayed zirconia thermal barrier coatings, J. Eur. Ceram. Soc. 84 (2001) 1301-1308.

[27] S. Y. Park, J. H. Kim, M. C. Kim, H. S. Song and C. G. Park, Microscopic observations of degradation behaviour in yttria and ceria stabilized zirconia thermal barrier coatings under hot corrosion, Surf, Coat. Technol. 190 (2005) 357-365.

[28] S. Ahmaniemi, M. Vippola, P. Vuoristo, T. Mantyla, F. Cernuschi and L. Lutterotti, Modified thick thermal barrier coatings: thermophysical characterization, J. Eur. Ceram. Soc. 24 (2004) 2669-2679.

[29] J. A. Thompson and T. W. Clyne, The effect of heat treatment on the stiffness of zirconia top coats in plasma sprayed TBCs, Acta Mater. 49 (2001) 1565-1575.

[30] N. Wang, C. Zhou, S. Gong and H. Xu, Heat treatment of nanostructured thermal barrier coating, Ceram. Int. 33 (2007) 1075-1081.

[31] ASTM E1876-01 Standard test method for dynamic Young's modulus, shear modulus, and Poisson's ratio by impulse excitation of vibration, Am. Soc. Test. Mater., Philadelphia, 2001.

[32] D. Basu, C. Funke and R. W. Steinbrech, Effect of heat treatment on elastic properties of separated thermal barrier coatings, J. Mater. Res. 14(12) (1999) 4643-4650.

[33] S. Paul, A. Cipitria, S. A. Tsipas and T. W. Clyne, Sintering characteristics of plasma sprayed zirconia containing different stabilizers, Surf. Coat. Technol. 203 (2009) 1069-1074.

[34] S. A. Tsipas, I. O. Golosnoy, R. Damani and T. W. Clyne, The effect of a high thermal gradient on sintering and stiffening in the top coat of a thermal barrier coating system, J. Therm. Spray Technol. 13(3) (2003) 370-376.

[35] T. Y. Tsui, W. C. Oliver and G. M. Pharr, Influences of stress on the measurement of mechanical properties using nanoindentation: Part I. Experimental studies in an aluminum alloy, J. Mater. Res. 11(3) (1996) 752-759.

[36] A. Bolshakov, W. C. Oliver and G. M. Pharr, Influences of stress on the measurement of mechanical properties using nanoindentation: Part II. Finite element simulations, J. Mater. Res., 11(3) (1996) 760-768.

[37] S. Suresh and A. E. Giannakopoulos, A new method for estimating residual stresses by instrumented sharp indentation, Acta Mater. 46(16) (1998) 5755-5767.

[38] X. Zhao and P. Xiao, Residual stresses in thermal barrier coating measured by photoluminescence piezospectroscopy and indentation technique, Surf. Coat. Technol. 201 (2006) 1124-1131.

[39] H. B. Guo, R. Vassen and D. Stover, Thermophysical properties and thermal cycling behavior of plasma sprayed thick thermal barrier coatings, Surf. Coat. Technol. 192 (2005) 48-56.

[40] S. Sodeoka, M. Suzuki, K. Ueno, H. Sakuramoto, T. Shibata and M. Ando, Thermal and mechanical properties of ZrO_2-CeO_2 plasma-sprayed coatings, J. Thermal Spray Technol. 6(3) (1997) 361-367.

[41] S. Ahmaniemi, P. Vuoristo, T. Mantyla, F. Cernuschi and L. Lorenzoni, Modified thick thermal barrier coatings: thermophysical characterization, J. Eur. Ceram. Soc. 24 (2004) 2669-2679.

[42] R. Vassen, X. Cao, F. Tietz, D. Basu and D. Stover, Zirconates as new materials for thermal barrier coatings, J. Am. Ceram. Soc. 83 (8) (2000) 2023-2028.

[43] W. Chi, S. Sampath and H. Wang, Microstructure-thermal conductivity relationship for plasma-sprayed yttria-stabilized zirconia coatings, J. Am. Ceram. Soc. 91(8) (2008) 2636-2645.

[44] U. Schulz, Phase transformation in EB-PVD yttria partially stabilized zirconia thermal barrier coatings during annealing, J. Am. Ceram. Soc. 83(4) (2000) 904-910.

[45] C. H. Lee, H. K. Kim, H. S. Choi and H. S. Ahn, Phase transformation and bond coat oxidation behavior of plasma-sprayed zirconia thermal barrier coatings, Surf. Coat. Technol. 124 (2000) 1-12.

[46] W. Ma, D. E. Mack, R. Vassen and D. Stöver, Perovskite-type strontium zirconate as a new material for thermal barrier coatings, J. Am. Ceram. Soc. 91(8) (2008) 2630-2635.

[47] D. Schwingel, R. Taylor, T. Haubold, J. Wigren and C. Gualco, Mechanical and thermophysical properties of thick PYSZ thermal barrier coatings: correlation with microstructure and spraying parameters, Surf. Coat. Technol. 108-109 (1998) 99-106.

[48] J. R. Brandon and R. Taylor, Phase stability of zirconia-based thermal barrier coatings. Part I. Zirconia-yttria alloys, Surf. Coat. Technol. 46 (1991) 75-90.

[49] R. Vassen, N. Czech, W. Malléner, W. Stamm and D. Stöver, Influence of impurity content and porosity of plasma-sprayed yttria-stabilized zirconia layers on the sintering behaviour, Surf. Coat. Technol. 141 (2001) 135-140.

[50] S. Paul, A. Cipitria, I. O. Golosnoy, L. Xie, M. R. Dorfman and T. W. Clyne, Effects of impurity content on the sintering characteristics of plasma-sprayed zirconia, J. Therm. Spray Technol. 16(5-6) (2007) 798-803.

[51] H. Hayashi, T. Saitou, N. Maruyama, H. Inaba, K. Kawamura and M. Mori, Thermal expansion coefficient of yttria stabilized zirconia for various yttria contents, Solid State Ion. 176 (2005) 613-619.

[52] F. Cernuschi, L. Lorenzoni, S. Ahmaniemi, P. Vuoristo and T. Mantyla, Studies of the sintering kinetics of thick thermal barrier coatings by thermal diffusivity measurements, J. Eur. Ceram. Soc. 25 (2005) 393-400.

[53] R. McPherson, The relationship between the mechanism of formation, microstructure and properties of plasma-sprayed coatings, Thin Solid Films 83 (1981) 297-310.

[54] R. S. Lima, A. Kucuk and C.C. Berndt, Integrity of nanostructured partially stabilized zirconia after plasma spray processing, Mater. Sci. Eng. A 313 (2001) 75-82.

[55] R. S. Lima, A. Kucuk and C.C. Berndt, Evaluation of microhardness and elastic modulus of thermally sprayed nanostructured zirconia coatings, Surf. Coat. Technol. 135 (2001) 166-172.

[56] H. Chen, Y. Zeng and C.X. Ding, Microstructural characterization of plasma-sprayed nanostructured zirconia powders and coatings, J. Eur. Ceram. Soc. 23 (2003) 491-497.

[57] G. Mariaux and A. Vardelle, 3-D Time Dependent Modeling of the Plasma Spray Process, Part 1: Flow Modeling, Int. J. Therm. Sci. 44 (2005) 357-366.

[58] P. Bengtsson and T. Johannesson, Characterization of microstructural defects in plasma-sprayed thermal barrier coatings, J. Therm. Spray Technol. 4 (1995) 245-251.

[59] R. McPherson, On the formation of thermally sprayed alumina coatings, J. Mater. Sci. 15 (1980) 3141-3149.

4. Validation of coatings properties and perspectives

In this work, Air Plasma Spraying (APS) was used to fabricate advanced metallic and ceramic coatings for thermal barrier coatings applications. These coatings are addressed to the protection of metallic hot section components of turbine engines from heat, oxidation and hot corrosion, with the purpose to increase their durability and the turbine efficiency as well as to reduce the emissions into the atmosphere.

The microstructural, thermal and mechanical properties of microstructured plasma sprayed coatings were investigated in as-sprayed conditions and after isothermal exposure at temperatures higher than those commonly experienced in the actual turbines, focusing the attention on the main mechanisms that lead to coating degradation: high-temperature oxidation for metallic coatings, phase transitions and sintering phenomena for ceramic TBCs.

In particular, CoNiCrAlY overlay coatings were successfully deposited by APS. A relatively low porosity (3.3 %) as well as a relatively low degree of oxidation were achieved.

Coating	Average porosity [%]	Processing
This work	3.3 ± 1.2	APS
Ref. [3]	5.3 ± 0.5	APS
Ref. [4]	5.1 ± 0.7	APS
Ref. [4]	4.6 ± 1.5	HVOF
Ref. [5]	~ 6.5	APS
Ref. [5]	~ 5	LPPS
Ref. [6]	~ 1	HVOF
Ref. [7]	0.8 ± 0.2	HFPD

Table 4.1 – Porosity of as-sprayed CoNiCrAlY coatings fabricated using different thermal spraying methods.

The results were comparable to those obtained using HVOF spraying and LPPS (or VPS) methods, which are notoriously less flexible and more expensive processes, respectively [1,2]. Table 4.1 shows a comparison between the results herein reported and some data available in literature for similar coatings fabricated by various thermal spraying processes. It is worth noting that a metallic coating has to possess low porosity, in order to protect the underlying component from the penetration of oxygen and hot gases. HVOF, VPS and Detonation Gun technologies are often used in industry for fabrication of dense coatings with low content of oxides.

In turn, the mechanical properties (hardness and elastic modulus) of plasma sprayed CoNiCrAlY coatings were better than those reported in literature for similar coatings deposited using APS and similar to those obtained using HVOF and EB-PVD. Nanoindentation (NI) was successfully employed to the purpose. Table 4.2 reports a comparison between the mechanical properties of CoNiCrAlY coatings fabricated using different manufacturing processes.

The influence of early-stage high-temperature oxidation at 1110 °C on coating properties was also investigated, since the first stage of oxidation is fundamental to evaluate the coating performance. During thermal exposure, a double oxide layer (alumina + spinels) gradually grew on coating top-surface, while a partial densification of the microstructure occurred, thus leading to a significant increase in both hardness and elastic modulus. The results of phase analyses are in good agreement with those reported for CoNiCrAlY and NiCrAlY coatings deposited by APS, VPS and HVOF and oxidized at 1000 °C and 1100 °C [8,9].

Otherwise, Richer *et al.* [3] have found a significant content of NiO within the oxide scale in addition to spinels after 5 h of isothermal oxidation at 1000 °C, which implies a low oxidation

resistance. An enhanced oxidation has been also observed by Brandl *et al.* [10] for HVOF CoNiCrAlY coatings treated at 950 °C for 50 and 100 h.

The evolution of the mechanical properties of plasma sprayed CoNiCrAlY coatings due to high-temperature oxidation has been studied. It should be noted that the investigations about the mechanical properties of thermally sprayed MCrAlY (M=Ni, Co) coatings are rare in literature.

Coating	Average hardness [GPa]	Average Young's modulus [GPa]	Processing
This work	3.95	147	APS
This work (after 24 h at 1110 °C)	5.69	200.8	APS
Ref. [11]	3.2	90	APS
Ref. [11]	5.0	155	HVOF
Ref. [12]	5.5	166	EB-PVD

Table 4.2 – Mechanical properties of as-sprayed CoNiCrAlY coatings fabricated using different manufacturing methods.

It should be noted that Zotov *et al.* [12] have used the same maximum load during Nanoindentation tests, while Kwon *et al.* [11] used continuous stiffness measurements with h_{max} = 2000 nm. Zotov *et al.* [12] have also reported some diagrams showing the effects of high-temperature annealing (at 1000 °C for different times) on the mechanical properties of EB-PVD coatings.

We also employed Impulse Excitation Technique (IET) for measuring the global elastic modulus of as-sprayed CoNiCrAlY coatings, by using a novel set-up arranged and optimized at University of Calabria (Department of Mechanical Engineering) in a bi-layer configuration (substrate and coating). The mean value obtained herein is somewhat higher with respect to

those reported in other works for APS coatings with similar composition and obtained using vibration-based iterative procedures [14,15]. This value is comparable to that measured by Choi *et al.* [13] on similar coatings by using tilted indentation technique. Micromechanical methods were employed to check the consistency of results obtained by NI and IET.

So, APS CoNiCrAlY coatings exhibited very promising properties and, to this purpose, it would be interesting to evaluate their performance during long-term exposures in real environments, especially in thermal cycling conditions. In our opinion, a high-temperature pre-treatment (a few hours) or a surface remelting in vacuum after plasma spraying are able to further enhance the anti-oxidation properties of these coatings.

In this work, two different zirconia-based porous thermal barrier coatings were deposited by APS, *i.e.* ceria-yttria co-stabilized zirconia coatings (CYSZ) and yttria stabilized zirconia coatings (YSZ). YSZ is the material currently adopted in some industrial applications.

CYSZ coatings showed very good thermal and mechanical properties compared to typical YSZ coatings, in terms of higher phase stability, higher microhardness, higher thermal expansion coefficient and similar high-temperature heat capacity.

The evolution of phase composition was different in CYSZ and YSZ systems. Indeed, during thermal aging of YSZ coatings at 1315 °C a gradual decomposition of metastable t’ phase occurred and a corresponding increase in the amount of tetragonal t, cubic c and monoclinic m phases was noticed. However, after 50 h of heat treatment a high percentage of t’ phase was also present. On the contrary, in CYSZ coatings, the presence of cubic phase in as-sprayed state provided very strong phase stability. Indeed, no monoclinic phase was found after 50 h of isothermal exposure. The different starting phase compositions of CYSZ and YSZ systems had a great influence on their high-temperature behaviour. The presence of relatively large amount of monoclinic phase at room temperature has been previously noticed in YSZ coatings annealed or thermally shocked at 1300 °C (up to 20 %) [16,17]. Table 4.3 shows the

values of total porosity measured by Image Analysis on different CYSZ and YSZ coatings. The end-users typically require that the coating porosity is of about 10 %. Indeed, the ceramic TBCs have to possess a proper value of porosity in order to reduce the heat transfer from the coating surface to the metallic substrate.

The microstructural properties of CYSZ and YSZ coatings changed during high-temperature isothermal exposure, due to the partial sintering of the porous microstructure, *i.e.* the closure of fine pores and microcracks. After 50 h at 1315 °C, CYSZ and YSZ coatings showed similar porosity values, even if it should be noted that the as-sprayed YSZ coatings were more porous than CYSZ ones (12.2 % against 10.2 %) and exhibited a sharper sintering rate in the first hours of thermal aging.

Coating	Average porosity [%]
CYSZ, this study	10.2
YSZ, this study	12.2
YSZ, Ref. [18]	10.8
CYSZ and YSZ, Ref. [19]	7-9
YSZ, Ref. [20]	15
YSZ, Ref. [21]	12
YSZ, Ref. [22]	15
CYSZ, Ref. [23]	18.4
YSZ, Ref. [23]	20.7

Table 4.3 – Average porosity of various plasma sprayed CYSZ and YSZ coating.

The sintering effect tended to stabilize with increasing the aging time.

The thermal expansion coefficient values (in-plane and out-of-plane) obtained for CYSZ coatings were higher than those reported in literature, thus involving a lower mismatch between the CTE values of substrate and coating, while the values measured for YSZ coatings were comparable to those reported in literature. Table 4.4 shows the values of in-plane thermal expansion coefficients for various plasma sprayed CYSZ and YSZ coatings.

In turn, the heat capacity of YSZ coatings was lower than that reported in previous published works. The C_P value is found to be 0.49 $J*K^{-1}*g^{-1}$ at 100 °C and 0.52 $J*K^{-1}*g^{-1}$ at 1250 °C. As mentioned above, these values are lower than those reported by other authors for YSZ sintered samples and plasma sprayed coatings [27,28]. For as-sprayed CYSZ coatings, the C_P value is around 0.44 $J*K^{-1}*g^{-1}$ at 100 °C and 0.71 $J*K^{-1}*g^{-1}$ at 1150 °C.

Coating	α_X (50-900 °C) $[10^{-6}K^{-1}]$
CYSZ, this work	12.6
YSZ, this work	10.7
YSZ, Ref. [24]	11.2
CYSZ, Ref. [25]	10.8
YSZ, Ref. [25]	9.9
YSZ, Ref. [22]	10-10.5
YSZ, Ref. [26]	10.87

Table 4.4 - In-plane thermal expansion coefficients for CYSZ and YSZ coatings.

To this purpose, it has been found that heat capacity and out-of-plane thermal expansion coefficient are affected by high-temperature sintering of the porous microstructure, while in-plane thermal expansion coefficient kept constant after thermal aging. Heat capacity

decreased with increasing the annealing time in the case of CYSZ coatings, while it increased in the case of YSZ coatings.

On the basis of these experimental results, CYSZ thermal barrier coatings seem to be preferable to YSZ ones, especially for extreme service conditions. However, both the coatings possess enhanced thermal and mechanical properties, in terms of low elastic modulus, high strain tolerance, high thermal expansion coefficient, high-temperature stability, low thermal conductivity and satisfactory protection against the entrainment of corrosive agents. To this purpose, it would be interesting to study their behaviour during long-term tests in real environments, where the coated components are subjected to thermal cycling and thermal shocks.

Moreover, further innovative TBC systems can be studied and developed. As an example, the development of multilayered TBCs can represent an alternative and novel solution. This solution would imply a ceramic TBC composed of a double layer: (a) an intermediate layer able to reduce the mismatch in CTE values between the overlapped layers and (b) an upper layer which should be more resistant to high temperature and to the penetration of oxygen and molten salts. A multilayered TBC is expected to better accommodate the thermal stresses, which notoriously promote TBC delamination. However, before developing multilayered systems, it is necessary to study the properties of the single layers.

Anyway, as mentioned above, it would be interesting to perform in-service long-term tests, especially for a TBC system composed of a substrate, a metallic bond coat and an upper ceramic coating. Unfortunately, this cannot be performed in research laboratories, due to some limitations of equipments as well as to the geometry of the samples. Test apparatus where only the upper surface of the ceramic coating is exposed to heat and oxygen should be arranged.

In addition, preliminary investigations about plasma sprayed nanostructured YSZ coatings were also performed and revealed that these coatings showed unique microstructural and mechanical properties. Indeed, the heterogeneous melting of nanoparticles agglomerates produced a very porous microstructure (about 20 %) composed of well-melted splats and unmelted or partially melted regions, respectively. As a consequence, a bimodal distribution of mechanical properties was noticed. Previous works have reported lower values of porosity for similar coatings, *i.e.* in the range from 7 % and 9 % [20, 21, 29]. These values have been measured by Image Analysis, but the authors probably used only low magnifications to acquire coatings micrographies. Low magnifications are surely representative of large regions of coating microstructure, but are not probably suitable to appreciate the fine intrinsic porosity of these unique coatings. Anyway, the values measured for coating porosity are higher than those obtained on microstructured coatings with similar composition and, therefore, nanostructured coatings are less harder.

On the basis of these first experiments, we can suppose that the properties of nanostructured coatings can be tailored for multi-functional applications, by controlling the degree of melting of nanostructured agglomerates and the density of the final coating. Indeed, these coatings are promising to be applied as TBCs as well as abradable coatings. To this purpose, in the next, we are going to perform further experiments, in order to optimize the main plasma spraying parameters (plasma energy and spraying distance) which can have a significant influence on the final properties. A Design of Experiment (DOE) could be a useful tool for process optimization.

It is evident that the research topic is rather wide and the constant advancements in this field provide new ideas and guidelines for the choice of alternative materials, their processing, the development and the characterization of coatings. To this purpose, new investments in research and development activities are needed, as well as further studies and new contributes.

References

[1] P. Poza and P. S. Grant, Microstructure evolution of vacuum plasma sprayed CoNiCrAlY coatings after heat treatment and isothermal oxidation, Surf. Coat. Technol. 201 (2006) 2887-2896.

[2] F. Tang, L. Ajdelsztajn, G. E. Kim, V. Provenzano and J. M. Schoenung, Effects of surface oxidation during HVOF processing on the primary stage oxidation of a CoNiCrAlY coating, Surf. Coat. Technol. 185 (2004) 228-233.

[3] P. Richer, M. Yandouzi, L. Beauvais and B. Jodoin, Oxidation behaviour of CoNiCrAlY bond coats produced by plasma, HVOF and cold gas dynamic spraying, Surf. Coat. Technol. doi: 10.1016/j.surfcoat.2010.03.043 (2010).

[4] V. Higuera, F. J. Belzunce and J. Riba, Influence of the thermal-spray procedure on the properties of a CoNiCrAlY coating, Surf. Coat. Technol. 200 (2006) 5550-5556.

[5] H. Waki, K. Ogura, I. Nishikawa and A. Ohmori, Monotonic and cyclic deformation behavior of plasma-sprayed coatings under uni-axial compressive tests, Mater. Sci. Eng. A 374(1-2) (2004) 129-136.

[6] L. Zhao, M. Parco and E. Lugscheider, High velocity oxy-fuel thermal spraying of a NiCoCrAlY alloy, Surf. Coat. Technol. 179 (2004) 272-278.

[7] F. J. Belzunce, V. Higuera and S. Poveda, High temperature oxidation of HFPD thermal-sprayed MCrAlY coatings, Mater. Sci. Eng. A 297 (2001) 162-167.

[8] S. Saeidi, K. T. Voisey and D. G. McCartney, The effect of heat treatment on the oxidation behavior of HVOF and VPS CoNiCrAlY coatings, J. Therm. Spray Technol. 18(2) (2009) 209-216.

[9] C. H. Lee, H. K. Kim, H. S. Choi and H. S. Ahn, Phase transformation and bond coat oxidation behavior of plasma-sprayed zirconia thermal barrier coatings, Surf. Coat. Technol. 124 (2000) 1-12.

[10] W. Brandl, G. Marginean, D. Maghet and D. Utu, Effects of specimen treatment and surface preparation on the isothermal oxidation behaviour of the HVOF-sprayed MCrAlY coatings, Surf. Coat. Technol. 188-189 (2004) 20-26.

[11] J. Y. Kwon, J. H. Lee, Y. G. Jung and U. Paik, Effect of bond coat nature and thickness on mechanical characteristic and contact damage of zirconia-based thermal barrier coatings, Surf. Coat. Technol. 201 (2006) 3483-3490.

[12] N. Zotov, M. Bartsch and G. Eggeler, Thermal barrier coating systems – analysis of nanoindentation curves, Surf. Coat. Technol. 203 (2009) 2064-2072.

[13] W. B. Choi, L. Prchlik, S. Sampath and A. Gouldstone, Indentation of metallic and cermet thermal spray coatings, J. Therm. Spray Technol. 18(1) (2009) 58-64.

[14] S. Patsias, N. Tassini and K. Lambrinou, Ceramic coatings: effect of deposition method on damping and modulus of elasticity for yttria-stabilized zirconia, Mater. Sci. Eng. A 442 (2006) 504-508.

[15] N. Tassini, K. Lambrinou, I. Mircea, M. Bartsch, S. Patsias and O. Van der Biest, Study of the amplitude-dependent mechanical behavour of yttria-stabilized zirconia thermal barrier coatings, J. Eur. Ceram. Soc. 27 (2007) 1487-1491.

[16] U. Schulz, Phase transformation in EB-PVD yttria partially stabilized zirconia thermal barrier coatings during annealing, J. Am. Ceram. Soc. 83(4) (2000) 904-910.

[17] C. H. Lee, H. K. Kim, H. S. Choi and H. S. Ahn, Phase transformation and bond coat oxidation behavior of plasma-sprayed zirconia thermal barrier coatings, Surf. Coat. Technol. 124 (2000) 1-12.

[18] Z. Chen, J. Mabon, J. G. Wen and R. Trice, Degradation of plasma-sprayed yttria-stabilized zirconia coatings via ingress of vanadium oxide, J. Eur. Ceram. Soc. 29 (2009) 1647-1656.

[19] S. Y. Park, J. H. Kim, M. C. Kim, H. S. Song and C. G. Park, Microscopic observations of degradation behaviour in yttria and ceria stabilized zirconia thermal barrier coatings under hot corrosion, Surf, Coat. Technol. 190 (2005) 357-365.

[20] B. Liang and C. Ding, Thermal shock resistances of nanostructured and conventional zirconia coatings deposited by atmospheric plasma spraying, Surf. Coat. Technol. 197 (2005) 185-192.

[21] H. Chen, Y. Zhang and X. Ding, Tribological properties of nanostructured zirconia coatings deposited by plasma spraying, Wear 253 (2002) 885-893.

[22] W. Ma, D. E. Mack, R. Vassen and D. Stöver, Perovskite-type strontium zirconate as a new material for thermal barrier coatings, J. Am. Ceram. Soc. 91(8) (2008) 2630-2635.

[23] S. Ahmaniemi, M. Vippola, P. Vuoristo, T. Mantyla, F. Cernuschi and L. Lutterotti, Modified thick thermal barrier coatings: thermophysical characterization, J. Eur. Ceram. Soc. 24 (2004) 2669-2679.

[24] H. B. Guo, R. Vassen and D. Stover, Thermophysical properties and thermal cycling behavior of plasma sprayed thick thermal barrier coatings, Surf. Coat. Technol. 192 (2005) 48-56.

[25] S. Ahmaniemi, P. Vuoristo, T. Mantyla, F. Cernuschi and L. Lorenzoni, Modified thick thermal barrier coatings: thermophysical characterization, J. Eur. Ceram. Soc. 24 (2004) 2669-2679.

[26] D. Schwingel, R. Taylor, T. Haubold, J. Wigren and C. Gualco, Mechanical and thermophysical properties of thick PYSZ thermal barrier coatings: correlation with microstructure and spraying parameters, Surf. Coat. Technol. 108-109 (1998) 99-106.

[27] R. Vassen, X. Cao, F. Tietz, D. Basu and D. Stover, Zirconates as new materials for thermal barrier coatings, J. Am. Ceram. Soc. 83 (8) (2000) 2023-2028.

[28] F. Cernuschi, L. Lorenzoni, S. Ahmaniemi, P. Vuoristo and T. Mantyla, Studies of the sintering kinetics of thick thermal barrier coatings by thermal diffusivity measurements, J. Eur. Ceram. Soc. 25 (2005) 393-400.

[29] H. Chen and C. X. Ding, Nanostructured zirconia coating prepared by atmospheric plasma spraying, Surf. Coat. Technol. 150 (2002) 31-36.

Annex

Some of the results herein reported have been presented at International and National Conferences or published on International Journals with Impact Factor. For knowledge, these scientific and technological works are reported below.

- M. Alfano, G. Di Girolamo, L. Pagnotta, D. Sun, J. Zekonyte, R.J.K. Wood, The influence of high temperature sintering on microstructure and mechanical properties of APS CeO_2-Y_2O_3-ZrO_2 coatings, J. Mater. Sci. 45(10) (2010) 2662-2669.
- M. Alfano, G. Di Girolamo, L. Pagnotta, D. Sun, Processing, microstructure and mechanical properties of air plasma-sprayed ceria-yttria co-stabilized zirconia coatings, Strain 46 (2010) 409-418.
- G. Di Girolamo, C. Blasi, L.Pagnotta, M. Schioppa, Phase evolution and thermophysical properties of plasma sprayed thick zirconia coatings, Ceram. Int. doi: 10.1016/j.ceramint.2010.07.035 (2010).
- M. Alfano, G. Di Girolamo, C. Blasi, L. Pagnotta, G. Stigliano, Structural analysis and elastic characterization of air plasma sprayed ceria-yttria co-stabilized zirconia coatings, WSEAS Trans. Appl. Theor. Mech. 2(10) (2007) 201-208.
- M. Alfano, G. Di Girolamo, L. Pagnotta, Analisi di rivestimenti in zirconia co-stabilizzata. XXXVII Convegno Nazionale AIAS, Roma, 2008, Atti del convegno, Memoria n. 279, pp. 1-9.
- M. Alfano, G. Di Girolamo, D. Sun, Effect of isothermal annealing on hardness and Young's modulus of free-standing plasma sprayed CeO_2-Y_2O_3-ZrO_2 coatings, XXXVIII Convegno Nazionale AIAS, Torino, 2009, Atti del convegno, Memoria n. 175, pp. 1-10.
- M. Alfano, G. Di Girolamo, C. Blasi, L. Pagnotta, G. Stigliano, Measurement of the elastic modulus of ceria-yttria co-stabilized zirconia coatings. 3rd WSEAS International Conference on Applied and Theoretical Mechanics, Tenerife, 2007. (+ atti del congresso, pp. 1-6).
- G. Di Girolamo, M. Alfano, L. Pagnotta, Microstruttura e proprietà meccaniche di rivestimenti CoNiCrAlY realizzati mediante plasma spray, AIMAT 2010, Capo Vaticano, 2010, Atti del convegno, pp. 1-4
- G. Di Girolamo, M. Alfano, C. Blasi, L. Pagnotta, G. Stigliano, L. Capodieci, T. Nocco, Microstructural and elastic properties of ZrO_2-CeO_2-Y_2O_3 thermal barrier coatings, Technical Report, RT-TEC(2007)15Rev0, pp. 1-23.
- G. Di Girolamo, M. Alfano, L. Pagnotta, J. Zekonyte, R .J. K. Wood, Microstructure and mechanical properties of plasma sprayed CoNiCrAlY coatings after early-stage isothermal oxidation, submitted to J. Therm. Spray Technol. (2010).
- M. Alfano, G. Di Girolamo, L. Pagnotta, J. Zekonyte, R. J. K. Wood, Depth sensing indentation of oxidized plasma sprayed CoNiCrAlY coatings, in preparation (2010).

Acknowledgments

I wish to thank Prof. Leonardo Pagnotta for encouragement, valuable and useful suggestions and ideas about the planning of the experimental work, the preparation and the writing of this doctoral thesis.

I wish to thank Marco Alfano for IET measurements, useful discussions and valuable cooperation.

I would like to extend special thanks to Jurgita Zekonyte and Dan Sun for Nanoindentation measurements, Caterina Blasi for technical contribution during plasma spray processing, Monica Schioppa for thermal measurements, Laura Capodieci, Donato Cannoletta, Luciano Pilloni, Emanuele Serra and Pierangela Caliandro for technical assistance during SEM observations.

I wish to thank Eng. Domenico Umbrello for useful discussions and suggestions about the manuscript.

Finally, I wish to thank my family for continuous support and encouragement through the years spent in this work: my mother Anna Maria, my father Pietro and my brother Antonino.